Wire Array Infrared Metamaterial Fibres: Fabrication and Applications

A thesis submitted in fulfilment
of the requirements for the degree of
Doctor of Philosophy

by

Juliano Grigoleto Hayashi

School of Physics
Faculty of Science
University of Sydney
Australia

January/2018

Statement of originality

To the best of my knowledge, I certify that this thesis contains no copy of work published by another person. This thesis has not been submitted for any degree or other purposes.

Juliano Grigoleto Hayashi

Acknowledgements

The submission of this thesis represents the conclusion of a long journey, and a large number of people must be remembered and thanked.

Firstly, I would like to thank my supervisors (the Jedi council, as I call them on my head): Alex Argyros, Simon Fleming, Boris Kuhlmey and Alessio Stefani, for all their support, advice, patience and teachings throughout these last four year. Without their help, this work would not have been possible. I had a fantastic experience through their supervision, and I cannot properly quantify the lessons I will always take with me in my future academic career. Many thanks (we finally got here).

A special acknowledgement must be made to my friend Richard Lwin from his many contributions. Thank you, Richard, for all your help with the tower, the drawing, the purchases, paperwork, the doubts about living in Australia, the advice and priceless lessons (many, many of the last one). I feel that part of this work is also yours, and I would like to dedicate this to you.

Throughout these nearly four years of research, various contributions have been made by other researchers, and these must be acknowledged here.

Stuart Jackson and several members of his team helped and supported the MIR subdiffraction imaging and lifetime experiments performed at Macquarie University. Thank you, Stuart, for opening your labs for me, for all the discussions, the expensive fibres, and your overall support on both experiments (I'm really sorry for the dead pixels). Your help was essential in the last part of my PhD. Thank you, Sergei Antipov, for your huge help with the fibre lasers. Thank you, Robert Woodward, Matthew Majewski and Darren Hudson for all your help and discussions. Regarding other colleagues from Macquarie University, I would also like to thank Benjamin Johnston and Alex Stokes for their laser micro-machining in the metallic foils employed in the embedding of our tapered hyperlenses (this was a crucial part in the fab-

rication of the final hyperlenses). Thank you for your time and contribution.

All the SEM imaging and FIB milling presented in this thesis were performed at the Australian Center for Microscopy and Microanalysis (ACMM - The University of Sydney). Therefore, I would like to thank their members for their technical support, particularly Patrick Trimby and Ashalatha Indiradevi. At the School of Physics, the filling of the metamaterial preforms was performed at the Applied and Plasma Physics Research Group. Thank you, Cenk Kocer for the use of your resistance oven.

On a more personal note, I cannot end without thanking friends and family.

Firstly, I would like to thank and dedicate this thesis to my former supervisor Cristiano Cordeiro from UNICAMP (where everything started), for all his teachings and support. These were crucial in my earlier formation, and his help was essential in the choice and acceptance to this PhD. Thank you, Cristiano.

I would like to thanks all my friend from the Legacy team, especially my great friend Ben Law for all the good times and "catch-ups" we had here in Sydney. Thanks, Franny (the best and cutest dog in Australia), for all your love and joy you brought me every day when I arrived late at home. Im sure I will miss you a lot.

Huge and special thanks must also be given to my dear fiancee Larissa Veiga, for all her love, laughs, trust, patience and support (apoio familiar) through these years (decades in my mind), since the old days back in Brazil. I would like to dedicate this thesis to her as well.

Since Im already getting a bit emotional, I would like to give giant thanks and also dedicate this thesis to my second mom, Dinha, that always believed in me and offered her support (always!). She always did everything to support me, especially in my education (my first English classes, my years through undergrad). Without a doubt, this thesis would not be possible without her, from whom I also have learned the meaning of hard work without complaining. Im extremely thankful for all that, and I know you are proud of this achievement (our achievement, because part of this thesis is yours as well). Thank you.

Finally, I would like to thank the program Science without Borders and CAPES for this incredible opportunity and the financial support of this PhD (scholarship 9468/13-7).

Included papers and attributions

The Chapter 3 of this thesis is strongly based on the peer-reviewed publication:

Metal selection for wire array metamaterials for infrared frequencies
Juliano G. Hayashi, Simon Fleming, Boris T. Kuhlmey and Alexander Argyros, *Optics Express* 23(23), pp. 29867-29881, (2015).

AA, SF and BTK conceived the idea of the work. JGH did all the simulations and wrote the manuscript with suggestions and additions from all authors. All authors contributed to discussions and interpretation of results.

Formal acknowledgement of the authors contribution and the publication are in Appendix C.

The preparation of other peer-reviewed publications with the content of Chapter 4, Chapter 5 and Chapter 6 are in progress.

Abstract

Metamaterials are artificial composite materials that exhibit exotic properties due to their components and sub-wavelength structure. During the past decades, several new materials have emerged from this research field with exciting new optical properties and applications. However, the fabrication of certain meta-structures remains a challenge, particularly with low cost and in large volumes. Fibre drawing is an interesting alternative approach to overcome such problems, but currently fabrication constraints restrict the size of the metal/dielectric drawn structures, limiting their operation to microwave/THz frequencies. In this context, this thesis concerns the fabrication, characterization, and employment of new soft-glass based wire array metamaterials fibres for applications in the infrared.

Numerical modelling of wire array structures is presented in order to understand which material combinations and structural parameters are more appropriate for infrared metamaterial fibres. The co-drawing process used is described, focusing on the adaptations performed to minimize fluctuation of the structure due to fluid dynamics. Metamaterial fibres with uniform structures containing wire diameter and spacing on the order of few hundreds of nanometers are produced, which are compatible with operation at mid-infrared frequencies.

The fabrication of metamaterial fibre tapers with steep transitions, generating magnifying hyperlenses, is also demonstrated. Far field imaging is attempted and the challenges regarding subdiffraction imaging are discussed. Feasible alternatives for future far field super-resolution imaging are proposed based on our numerical modelling and the typical structural transitions fabricated. Since the operational range of our hyperlenses is not limited to the infrared, subdiffraction focusing of 1/176 of the operational wavelength is reported at THz frequencies, achieved by combining a polymer hyperlens with our new infrared hyperlens.

Contents

Chapter 1

Introduction

Metamaterials are artificial composite materials that exhibit exotic properties due to their components and sub-wavelength structure. During the past decades, several new materials have emerged from this research field with exciting new electromagnetic, acoustic, thermal, elastic, and hydrodynamic responses. Regarding electromagnetic metamaterials, this resulted in the development of extraordinary new metadevices such as metalenses, metasurfaces, hyperlenses, and invisibility cloaks.

Despite improvement of the metamaterial fabrication methods over the years, the fabrication of certain types of meta-structures remains a challenge, particularly with low cost and in large volumes. Fibre drawing is an interesting alternative approach to overcome these problems, since one standard preform can generate kilometers of fibres and this technique also offers great control on the scaling down of the desired metamaterial structure. However, the Plateau-Rayleigh instabilities, which is the tendency of a liquid column to break into droplets, limits the size of the drawn metamaterial structure according to the rheological properties of the materials employed.

Currently, wire array metamaterial fibres based on polymer and indium are limited to structures with wire diameters around a few microns, which also restricts the size of the meta-structure and its operation range to microwave/terahertz frequencies. The fabrication of smaller uniform structures is possible by replacing the polymer with soft-glasses, which can lead to a decrease of the surface tension between the molten metal and the dielectric during the drawing, shifting down the Plateau-Rayleigh instability limit. In this context, this thesis concerns the fabrication, modeling, characterization of wire array metamaterial fibres based on soft-glass with structures that can

operate at frequencies as high as the mid-infrared (operational wavelength as short as $3\,\mu$m).

The co-drawing of uniform metallic structures embedded in a glass fibre represents a huge experimental challenge due its complexity and the several process constraints. The drawing is only possible if the rheological properties of the selected materials match and they are chemically compatible. In order to suppress the fluid dynamic instability, the drawing must also be adapted and performed under favourable conditions. In addition, care must be taken with the selection of the metal because it has, along with the structural parameters, a strong influence in the metamaterial's final optical loss.

Besides the low cost and large volume fabrication, drawn metamaterials offers the possibility to fabricate tapered samples, giving rise to wire array magnifying hyperlenses, which are considerably more difficult to fabricate with conventional planar techniques. Therefore, another main goal of the present thesis is the fabrication of tapered magnifying hyperlenses with structural parameters compatible with operational wavelengths as short as the mid-infrared, which opens the possibility of subdiffraction focusing and/or imaging in the near and far field for this spectral region. This is currently not possible with the polymer based metamaterial fibres presented in the literature.

The present thesis is organized as follows:

Chapter 2 is a general introduction on metamaterials, covering how it is possible to tailor the electromagnetic response of the medium with an elementary meta-structure. Hyperbolic metamaterials are discussed in detail, including their exotic optical properties, their basic structures, fabrication methods, and applications. An emphasis is given on wire array metamaterials and their hyperbolic dispersion, which allows the propagation of high spatial frequency modes and makes possible super-resolution imaging and lifetime engineering. The fibre drawing technique is introduced and a literature review regarding metamaterial fibres is presented, focusing on wire array fibres made of polymer and indium for applications at microwave/THz frequencies. The current fabrication limitations of this polymer/indium system related to the size of the drawn metallic structure is discussed. This limitation can be overcome by the replacement of the polymer by soft-glasses, which is the main novelty of this PhD project and represents a significant fabrication challenge due to the high complexity of metal/glass drawing.

Chapter 3 discusses metamaterial fibres for operation at the mid-infrared, beginning with a theoretical analysis of promising material candidates (metals and glasses), based on an optical quality argument (loss analysis) and their fabrication compatibility with the co-drawing method. Numerical modeling of an indefinite wire array metamaterial structure using finite element software (COMSOL) is presented, providing the optical response of such media for different material combinations, structural parameters (wire diameter and spacing), and wavelengths over the mid-infrared, from 1 to 10 μm. Based on this modeling, the materials, the structural parameters and the desirable operational range of wavelength of new infrared metamaterial fibre are selected.

Chapter 4 describes step-by-step the fabrication of our soft-glass wire array metamaterials, focusing on the adaptations performed to minimize the structural fluctuations on the metallic wire array due to fluid dynamics (Plateau-Rayleigh instability). The influence of the drawing parameters on the uniformity of the metamaterial structure is characterized and addressed. The fabrication of wire array metamaterial fibres with uniform structures compatible with operation at infrared frequencies is presented (wire diameter and spacing in the order of a few hundreds of nanometers).

Chapter 5 introduces the diffraction limit and subdiffraction imaging with metamaterials, focusing on metamaterial hyperlenses. The structural parameters and magnification factor required for far field subdiffraction imaging in the mid-infrared with wire array metamaterials are discussed. Numerical simulations are presented which describe the typical overall losses of the tapering transitions for different material combinations. The fabrication of a tin/soda-lime wire array magnifying hyperlens is reported, which includes the tapering of metamaterial fibres (generating a steep structural transition) and the selection of the desired transition based on the desired hyperlens's magnification factor and overall loss. The far field imaging experiment with our magnifying wire array hyperlenses is presented and the challenges regarding far field subdiffraction imaging are analysed. Feasible alternatives for future far field subdiffraction imaging with hyperlens in the infrared are proposed based on the modelling of the magnifying hyperlens and the typical losses of the structural transitions presented.

Chapter 6 discusses the use of the tin/soda-lime wire array metamaterial in the THz spectrum for extreme focusing and super-resolution imaging, since their operation is not limited to the infrared. The use of two different magnifying hyperlenses concatenated, called a hybrid hyperlens, is proposed and extreme focusing of 1/176 of the operating wavelength is reported at THz

frequencies. Future improvements and directions of such hybrid hyperlenses are discussed, including new possibilities regarding far field subdiffraction imaging.

Chapter 7 contains the concluding remarks with an overview of the main achievements reported in this thesis as well as a discussion of the future directions for our metamaterial fibres, including further improvements and applications.

Chapter 2

Metamaterials and fibres

This Chapter introduces metamaterials and discusses the tailoring of their electromagnetic response. Hyperbolic materials are reviewed, focusing on their properties and fabrication approaches. In particular, the electromagnetic response and the main optical properties of wire array metamaterials are discussed. Finally, the fabrication of wire array metamaterial fibres are also reviewed, with emphasis on their limitation and challenges to extend the actual achievable structure to operational frequencies in the mid-infrared.

2.1 Introducing Metamaterials

Metamaterials are artificial composite materials that exhibit exotic properties due to their components and sub-wavelength structure. Their electromagnetic response can be tailored by the design of such structure. Often, such optical properties are not available in nature at optical frequencies, which empowers metamaterials with remarkable new capabilities and applications.

During the past decades, several new materials have emerged from this research field with exciting new electromagnetic, acoustic, thermal, elastic, and hydrodynamic responses. Regarding electromagnetic metamaterials, this resulted in the development of incredible new metadevices such as metalenses, metasurfaces, hyperlenses, and invisibility cloaks.

In order to explain the unusual electromagnetic response of metamaterial, the electromagnetic response of conventional materials (dielectric and metal) is discussed below. Subsequently, the idea of controlling such electromagnetic response with sub-wavelength inhomogeneities (or elementary meta-

structure) is also reviewed.

2.1.1 Electric and magnetic responses of conventional materials

When an electromagnetic wave interacts with a material, the incident electric and magnetic fields can alter the organization of its electrical charges and magnetic dipoles, inducing a polarization and magnetization field. The electromagnetic properties of the medium are defined by this response to incident electric and magnetic fields, which, for linear media, are described by its electric permittivity (ϵ) and magnetic permeability (μ). On the macroscopic scale, the overall optical response of a medium can be obtained with Maxwell's equations, ϵ, μ, and other related parameters - the refractive index $n = \sqrt{\epsilon\mu}$ and the impedance $Z = \sqrt{\mu/\epsilon}$.

Fig. 2.1 shows a "parameter space diagram" that classifies conventional materials according to the values of ϵ and μ, extracted from Ref. [1]. The upper right quadrant (I) contains materials with simultaneously positive ϵ and μ, which includes most transparent dielectric materials. The upper left quadrant (II) covers materials that exhibit negative ϵ for certain frequencies, which is the case for metals and semiconductors below their plasma frequency. Region IV includes some ferrite materials with negative magnetic permeability below microwave frequencies.

A negative value of ϵ (μ) means that the electric (magnetic) field induced inside the material is in the opposite direction to the field of an incident eletromagnetic wave. When one of the parameters is negative (quadrant II and IV), the refractive index ($n = \sqrt{\epsilon\mu}$) is purely imaginary, which means the waves are evanescent (decay exponentially). Regarding quadrant III, there are no natural materials with simultaneously negative electric permittivity and magnetic permeability at optical frequencies and over a sufficient bandwidth. This is only achievable with metamaterials.

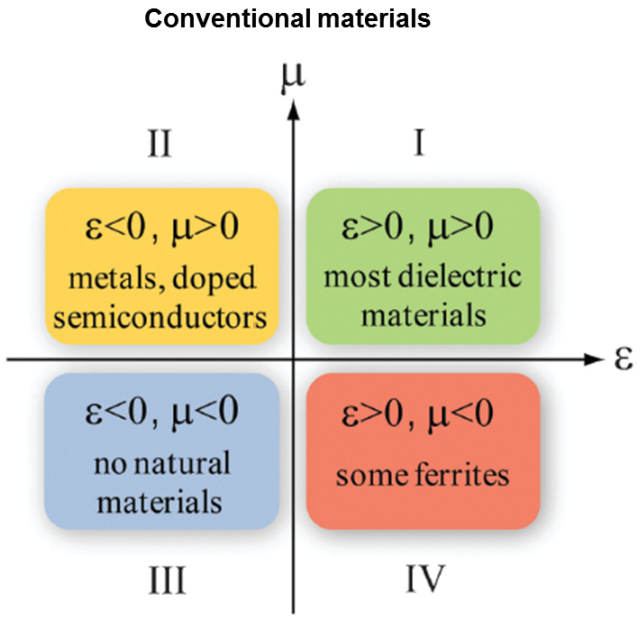

Figure 2.1: Electric permittivity and magnetic permeability of conventional materials, extracted from Ref. [1].

Usually, using the classic electromagnetic theory [2], the electromagnetic response of a medium can be well described by the Drude-Lorentz model, which treats electrons or fictitious magnetic charges as damped harmonically bounded particles when driven by external electric or magnetic fields, respectively. From the oscillation equation of electric charges and fictitious magnetic particles, the frequency-dependent permittivity and permeability for a medium with one electric and one magnetic atomic resonances (ω_0) are given by [1]

$$\epsilon(\omega) = \epsilon_0 \left(1 - \frac{\omega_{p,e}^2}{\omega^2 - \omega_{0,e}^2 + i\gamma_e\omega}\right) \tag{2.1}$$

$$\mu(\omega) = \mu_0 \left(1 - \frac{\omega_{p,m}^2}{\omega^2 - \omega_{0,m}^2 + i\gamma_m\omega}\right) \tag{2.2}$$

where ϵ_0 (μ_0) is the permittivity (permeability) of free space, ω_p is the plasma frequency (or the numerical equivalent for dielectrics), ω_0 is the natural frequency of the oscillator (restoring force acting on the bound electron or

fictitious magnetic charge), γ is the damping factor related to material losses (friction force on the damped oscillator model), and the subscripts e and m correspond to the electric and magnetic response, respectively. Note that Eq. (2.1) and Eq. (2.2) are derived considering the oscillation of the particle in the presence of an electromagnetic field $\mathbf{E(t)} = \mathbf{E}_0 e^{-i\omega t}$ and $\mathbf{B(t)} = \mathbf{B}_0 e^{-i\omega t}$, respectively.

Manipulating Eq. (2.1) and separating it into real and imaginary parts, the real (ϵ') and imaginary (ϵ'') part of the electric permittivity are given by

$$\epsilon'(\omega) = \epsilon_0 \left(1 - \omega_{p,e}^2 \frac{(\omega^2 - \omega_{0,e}^2)}{(\omega^2 - \omega_{0,e}^2)^2 + \gamma_e^2 \omega^2}\right) \tag{2.3}$$

$$\epsilon''(\omega) = \epsilon_0 \omega_p^2 \frac{\omega \gamma_e}{(\omega_0^2 - \omega^2)^2 + \omega^2 \gamma_e^2}. \tag{2.4}$$

Equations (2.3) and (2.4) are good approximations for the electric response of a dielectric with one atomic electric resonance (ω_0), and their typical behavior can be seen in Fig. 2.2. Note that the electric response of the medium depends on its atomic properties and the real part of the permititivity can be negative for frequencies around ω_0. It is also important to emphasize that, in real dielectric materials, the atoms/molecules possess multiple resonant frequencies, which must be taken into account with their respective oscillator strength for a more realistic model [3, 4].

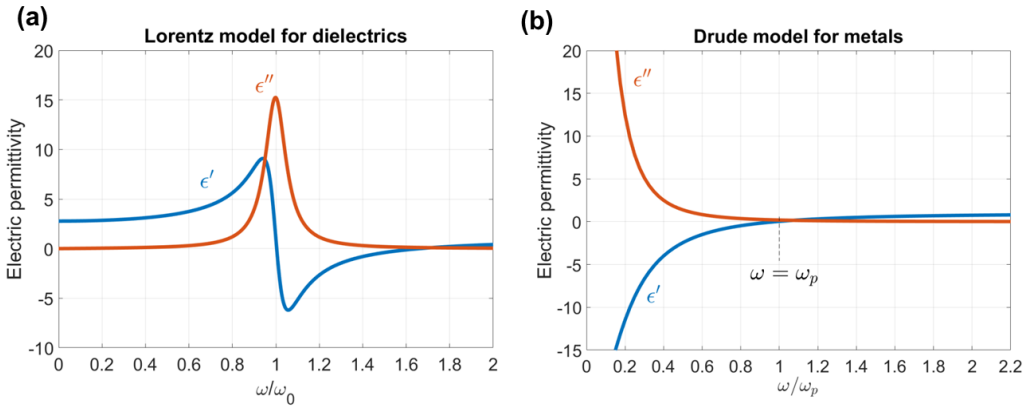

Figure 2.2: Typical electric response: (a) Lorentz model for dielectric with one electric resonance (Eqs. (2.3, 2.4)), (b) Drude model for metals (Eqs. (2.7, 2.8)).

In metals, some electrons are not bound to the nucleus, which means that the atomic restoring force is negligible in the system. Therefore, the free electron approximation can be assumed ($\omega_{0,e} = 0$), and Eq. (2.1) becomes the Drude model

$$\epsilon(\omega) = \epsilon_0 \left(1 - \frac{\omega_p^2}{\omega^2 + i\gamma_e\omega}\right) = \epsilon'(\omega) + i\epsilon''(\omega), \tag{2.5}$$

where ω_p the natural resonant frequency of the electron gas, the plasma frequency is given by

$$\omega_p^2 = \frac{N_e e^2}{m_e^* \epsilon_0}, \tag{2.6}$$

where N_e is the density of electrons, e is the elementary charge and m_e^* is the effective mass of the electron. Consequently, the real and imaginary part of the metal's permittivity become

$$\epsilon'_{metal}(\omega) = \epsilon_0 \left(1 - \frac{\omega_p^2}{\omega^2 + \gamma_e^2}\right) \tag{2.7}$$

$$\epsilon''_{metal}(\omega) = \epsilon_0 \frac{\omega_p^2 \gamma_e}{\omega(\omega^2 + \gamma_e^2)}, \tag{2.8}$$

and their typical behaviour is illustrated in Fig. 2.2(b).

According to Eq. (2.7), the real part of the permittivity of metals is negative below their plasma frequency, which is determined by the atomic properties of the material (density and effective mass of the electron), having values limited to ultra-violet (UV) frequencies for most metals and infrared frequencies for semiconductors [5, 6].

Regarding the magnetic response, natural materials that exhibit negative permeability are rare, especially at high frequencies. This happens because the flow of orbital currents or unpaired electron spins that can generate the magnetic polarization only respond to electromagnetic waves at low frequencies. As a consequence, all natural materials have $\mu \simeq \mu_0$ at optical frequencies [7].

Note that the electromagnetic response of a medium is characterized by its resonances, which are imposed (and consequently limited) by the properties of atoms/molecules. Electromagnetic responses beyond those of conventional

materials discussed can be obtained and tailored with sub-wavelength inhomogeneities or elementary meta-structures. These approaches are reviewed and discussed below.

2.1.2 Engineering electric and magnetic responses with metamaterials

Structured materials present an alternative to expand such limitations on the electromagnetic response of conventional materials. Arguably, this approach dates back to the Egyptian and Roman times, when metallic particles were used to dope glass and achieve different colors [8]. However, the understanding of the physics of electromagnetic composite materials behind this phenomenon is a lot more recent [8–10].

Optical composite materials are generally employed in the quasi-static limit, where the particle size is much smaller than the wavelength of interest. In this limit, the sub-wavelength inhomogeneities (embedded structures) cannot be individually resolved by the incident electromagnetic radiation, and the medium's optical response is characterized by the "average" of the collective response of the whole assembly. In other words, on the macroscopic level, the optical response of the artificial structured medium can be characterized by an equivalent homogeneous material with an effective electric permittivity (ϵ_{eff}) and effective magnetic permeability (μ_{eff}). This approach is called homogenization and, as a rule of thumb, can be applied if the spatial scale of the structured material is smaller than about 5 times the wavelength in the host material [11].

Metamaterials employ sub-wavelength inhomogeneities, the elementary meta-structures, to design and tailor both the electrical and magnetic response of the composite medium without precedent, typically with periodic and resonant structures. Fig. 2.3(a) and (b) show the two basic metamaterial structures used to implement artificial plasmonic and magnetic responses, wire media and split ring resonators, respectively.

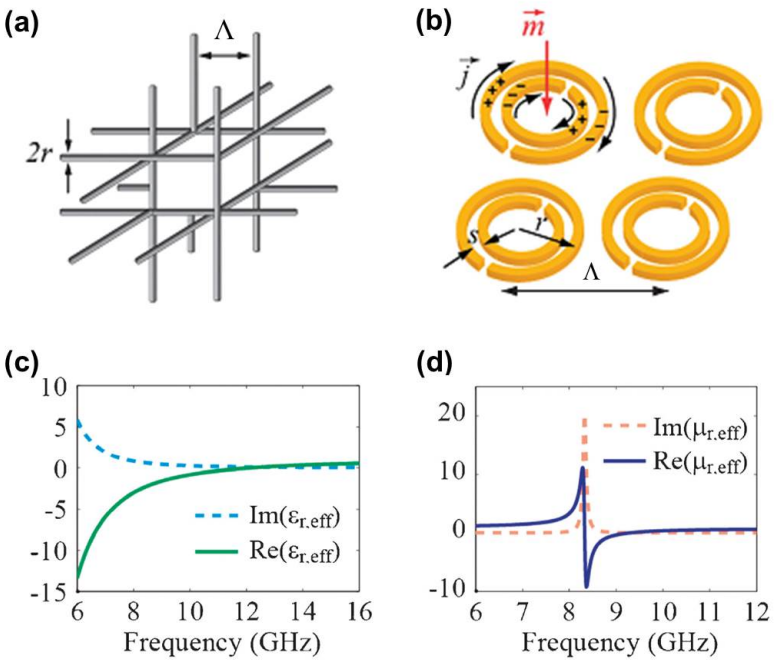

Figure 2.3: Elementary metamaterial structures used to achieve artificial plasmonic (a) and magnetic responses (b). (a) Schematic of a periodic arrangement of metal wires (wire mesh) with radius r and lattice constant Λ. (b) Schematic of split ring resonators and the current density $\vec{j}$ induced by an incident magnetic field, generating a magnetic dipole $\vec{m}$. (c) Effective electric permittivity of a wire mesh, behaving like a metal with extremely low plasma frequency. (d) Effective magnetic permeability of the split ring resonators around the resonance frequency. Figure adapted from Ref. [1].

Due to the sub-wavelenght size of the meta-structure, metamaterials can be homogenized and represented as an equivalent effective medium, with an effective electric permittivity and effective magnetic permeability. The control on the design of the elementary meta-structure allows the tailoring of the macroscopic electromagnetic responses, providing exciting opportunities for tunability. For example, a wire mesh with very thin wires (Fig. 2.3(a)), according to Pendry [12], possesses an effective electric permittivity as

$$\epsilon_{eff,wm}(\omega) = \epsilon_0 \left(1 - \frac{\omega_{p,eff}^2}{\omega^2 + i\gamma_{eff}\omega}\right), \tag{2.9}$$

which still behaves like a metal (obeys the Drude model, Eq. (2.7)), but with an effective plasma frequency that depends on the wire mesh's geometry and is approximately given by

$$\omega_{p,eff}^2 = \frac{N_{e,eff}e^2}{\epsilon_0 m_{e,eff}} = \frac{2\pi c^2}{\Lambda^2 ln(\Lambda/r)} \tag{2.10}$$

and a damping factor of

$$\gamma_{eff} = \frac{\epsilon_0 \Lambda^2}{\pi r^2 \sigma_c}, \tag{2.11}$$

where $N_{e,eff}$ is the effective electron density, $m_{e,eff}$ is the effective electron mass, r is the radius of the wire, Λ is the lattice constant of the structure, and σ_c is the conductivity of the metal, c is the speed of light.

Note that, according to Eq. (2.9), the effective plasma frequency of such media can be tailored with the structural parameters of the lattice (r and Λ). In other words, the metallic behaviour of the wire medium ($\epsilon < 0$ for $\omega < \omega_{p,eff}$) can be tuned along the electromagnetic spectrum by changing its structural parameters. Fig. 2.3(c) shows the relative effective permittivity ($\epsilon_{eff,wm}/\epsilon_0$) of a 3D wire array mesh, as seen in Fig. 2.3(a), behaving like a metal with extremely low plasma frequency (extracted from Ref. [1]).

An artificial magnetic response can be created by a current loop, similarly to orbital currents present in natural magnetic materials. By Faraday's law, a time-varying magnetic field through a conducting coil induces a loop current that generates a weak magnetic moment. Such response can be greatly enhanced with resonances in the coil.

Split-ring resonators (SRRs), one of the first magnetic meta-structures proposed [13], employ such an approach to achieve a strong artificial magnetic response. Figure 2.3(b) illustrates four SRRs, formed by two concentric rings split with a small opening at opposite directions. The behaviour of such a structure is analogous to an LC circuit, with a natural resonance of $\omega_{0,SRR} = \sqrt{1/LC}$, where L and C are the inductance and capacitance of the elementary meta-structure, respectively. When a magnetic field within a certain frequency region around the natural resonance $\omega_{0,SRR}$ propagates throught the SRR, it induces a strong current loop ($\vec{j}$), which generates a magnetic dipole $\vec{m}$, as illustrated in Fig. 2.3(b). This induced magnetic moment can be in or out of phase with the incident magnetic field and, if

it is strong enough, can generate a negative effective magnetic permeability (μ_{eff}), as shown in [13], defined by

$$\mu_{eff}(\omega) = \epsilon_0 \left(1 - \frac{F\omega^2}{\omega^2 - \omega_{0,SRR}^2 + i\Gamma\omega}\right), \tag{2.12}$$

where F is the SRR's filling fraction

$$F = \frac{\pi r^2}{\Lambda^2}, \tag{2.13}$$

$\omega_{0,SRR}$ is the resonance frequency

$$\omega_{0,SRR} = \sqrt{\frac{3sc^2}{\pi^2 r^3}}, \tag{2.14}$$

and Γ is the damping factor

$$\Gamma = \frac{2\rho}{r\mu_0}, \tag{2.15}$$

where Λ is the distance between two adjacent SRR, r is the radius of the outer ring, s is the gap between the rings, c is the speed of light in vacuum, and ρ is the resistivity of the material of which the rings are made. Figure 2.3(d) illustrates the typical effective magnetic permeability of a SRR around its resonance frequency ($\omega_0/2\pi$), which exhibits a resonant feature, as expected from Eq. (2.12) due to its Drude-Lorentz like behaviour.

The tailoring of both the electric and magnetic response opens a vast range of new possibilities to realize artificial materials with exotic behaviour and optical properties. For example, both meta-structures discussed can be combined to obtain both negative ϵ_{eff} and μ_{eff} in the same frequency region, resulting in a left-handed material (quadrant IV).

As theoretically discussed by Veselago in his seminal work [14], a left-handed medium can be described by a negative refractive index, which gives rise to a variety of counter-intuitive phenomena such as negative refraction, reverse Doppler and reverse Cherenkov effect. In 2000-2001, Smith and Shelby experimentally demonstrated the first left-handed material, overlapping the negative electric and magnetic response of wire arrays and SRR in the microwave region and observing a negative refraction [15, 16], which

brought the so far hypothetical consideration of metamaterials to experimental reality.

Through the almost two decades following Smith's seminal work, a vast number of other elementary meta-structures were developed, characterized, and employed for different applications and metadevices (invisibility cloak, hyperlens, superlens). An overview of the area can be found in several books [17–19] and review papers [1, 11, 20–25].

This thesis is focused on hyperbolic metamaterials for subdiffraction imaging and lifetime engineering. Therefore, a short literature review and a detailed description of their optical response, optical properties and fabrication approaches will be presented next.

2.2 Hyperbolic Metamaterials

The initial studies on metamaterials focused on structures with negative electric permittivity and magnetic permeability in the same range of frequencies, in order to achieve media with negative refractive index (left-hand materials) [15, 16]. After this initial trend, the research focus changed to active and tunable metamaterials, with arguably simpler structures but still with unusual optical properties and functionalities. One particular class, hyperbolic metamaterials, received a lot of attention due to the exotic hyperbolic dispersion relation [26].

Hyberbolic metamaterials are uniaxial composite materials which are described by an extremely anisotropic permittivity and/or permeability tensor [26–28]

$$\bar{\bar{\epsilon}} = \begin{pmatrix} \epsilon_{xx} & 0 & 0 \\ 0 & \epsilon_{yy} & 0 \\ 0 & 0 & \epsilon_{zz} \end{pmatrix}, \bar{\bar{\mu}} = \begin{pmatrix} \mu_{xx} & 0 & 0 \\ 0 & \mu_{yy} & 0 \\ 0 & 0 & \mu_{zz} \end{pmatrix} \tag{2.16}$$

where ϵ_{xx}=ϵ_{yy}=$\epsilon_{\perp}$, and ϵ_{zz} are the electric permittivity component, while μ_{xx}=μ_{yy}=$\mu_{\perp}$, and μ_{zz} are the magnetic permeability, both the along the principal axis.

For an ideal electric hyperbolic medium described by Eq. (2.16) with $\mu_{\perp} = \mu_{zz} > 0$, the dispersion relation of the extraordinary waves, *i.e.*, the dispersion relation for waves with non-zero electric field component along the axis of anisotropy (or principal axis), is described by [26, 27]

$$\frac{k_x^2 + k_y^2}{\epsilon_{zz}} + \frac{k_z^2}{\epsilon_\perp} = \left(\frac{\omega}{c}\right)^2, \tag{2.17}$$

where ω is the angular frequency of the radiation, c is the vacuum speed of light, and $\vec{k} = [k_x, k_y, k_z]$ is the wavevector of the propagating wave.

If $\epsilon_{zz} \cdot \epsilon_\perp < 0$, the isofrequency surfaces solution to Eq. (2.17) are hyperboloids in k-space, in contrast to the closed spherical isofrequency surface of an isotropic medium given by the dispersion equation $k_x^2 + k_y^2 + k_x^2 = \epsilon(\omega/c)^2$ (Fig. 2.4(a)). Electric hyperbolic metamaterials are classified in two categories, depending on the number of negative components of the dielectric tensor (Eq. (2.16)). If $\epsilon_{zz} < 0$, the isofrequency surfaces generate an open hyperboloid as shown in Fig. 2.4(b) (HMM1). In contrast, if $\epsilon_{xx} = \epsilon_{yy} < 0$, the isofrequency surface generates a closed hyperboloid as shown in Fig. 2.4(c) (HMM2).

The mentioned conditions require that the medium behaves like a metal in one (HMM1) or two directions (HMM2), and operates like a dielectric (insulator) in the complementary directions, which does not occur in natural materials at optical frequencies, and/or in a broadband operation window. Some natural materials, such as bismuth and graphite, exhibit hyperbolic dispersion in narrow and specific frequency ranges [29]. On the other hand, metamaterials can exhibit broadband hyperbolic dispersion and the tuning in their structure allows the tailoring of such optical response over the electromagnetic spectrum.

An ideal medium with a hyperbolic dispersion as described in Eq. (2.17) allows the propagation of waves with unbounded large wavevectors ($k^2 > k_0^2 = (\omega/c)^2$) known as high-$k$ modes or high-k waves [31], which would be evanescent in conventional isotropic and low anisotropy media with a spherical and elliptical k-space topology, respectively.

In hyperbolic metamaterials composed of periodic elementary meta-structures, such high-k waves are bounded by the finite size of the elementary meta-structure, where its lattice acts like a natural cut-off. The maximum wavevector component allowed in the metamaterial corresponds to the edge of their Brillouin zone. In addition, the exact dispersion of their extraordinary waves must be calculated by numerical modeling due to spatial dispersion. A detailed description of this behaviour for wire array metamaterials will be presented in the next section.

The hyperbolic dispersion and the presence of high-k modes lead to a

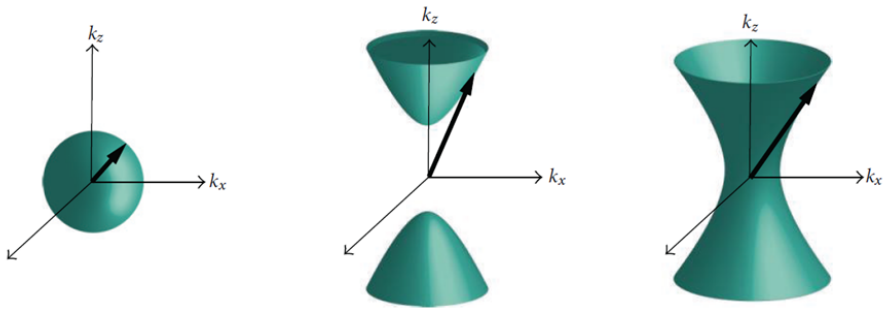

Figure 2.4: Isofrequency surfaces. (a) Isotropic medium. For extraordinary waves in highly anisotropic uniaxial medium, the isofrequency surface can be a open or closed hyperboloid, depending on the number of negative electric permittivity components. (b) Hyperbolic medium with negative electrical permittivity on the z axis (HMM1). (c) Hyperbolic medium with negative electrical permittivity on the x and y axes (HMM2). Figure extracted from Ref. [30].

high photonic density of states (PDOS) in the metamaterial [32, 33]. The PDOS describes the number of modes allowed in a certain energy interval (frequency interval), and can be obtained by a mode counting procedure in k-space from the dispersion relation ($\omega(k)$) [34]: the PDOS is related to the differential volume between two isofrequency surfaces ($\omega(k)$ and $\omega(k)$+dω), as represented in Fig. 2.5 for an isotropic dielectric and a hyperbolic type I metamaterial.

In free-space and isotropic media, the photonic density of states will be proportinal to ω^2, while in a hyperbolic metamaterial it will be proportional to k^3_{max} [33,35], which is the maximum propagating wavevector allowed. Even with the cut-off from the limited size of the meta-structure, the metamaterial can exhibit a PDOS enhancement of a factor of 10^3-10^5 compared to vacuum [36]. However, when losses and propagation lengths are taken into account, a large number of those high-k modes are not useful for most applications [37].

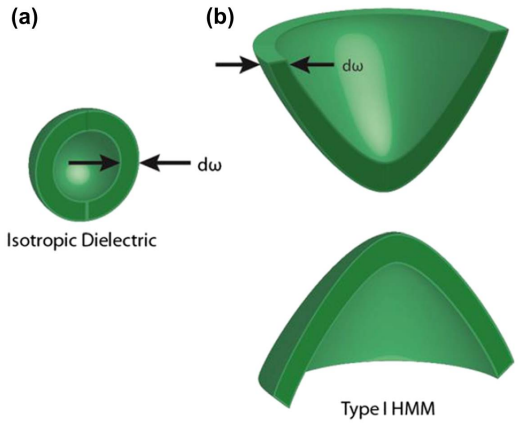

Figure 2.5: Two isofrequency surfaces corresponding to slightly different frequencies ($\omega(k)$ and $\omega(k)$+dω) for an isotropic dielectric (a) and a type I hyperbolic metamaterial (b). The enclosed volume between the two surfaces is proportional to the photonic density of states of the medium. Figure extracted from Ref. [38].

The presence of high-k modes and the high PDOS can be exploited in several applications related to spontaneous emission lifetime engineering of an emitter [30, 32, 39–43] and thermal emission engineering [44–46].

In particular, the high-k modes of hyperbolic metamaterials allow the development of a range of metadevices for subdiffraction imaging in the near and far field (straight and magnifying hyperlenses) [31, 47–50] and subdifraction focusing [50–53].

2.2.1 Origin and characteristics of the high-k modes

When an eletromagnetic wave propagating in a medium couples with a "quasi-particle" that polarizes the medium (plasmon, phonon, exciton), it gives rise to a hybrid mode called a polariton. [54, 55]. For example, an oscillating electric field can couple with infrared optically active phonons in dielectrics, giving rise to a vibrational-electromagnetic mode, called phonon-polariton mode [56]. Similarly, in the presence of metal, a plasmon-photon excitation originates a plasmonic-electromagnetic mode, called plasmon-polariton mode [57]. The characteristics of such hybrid modes are strongly dependent on how the energy is distributed between the excitation components and on the structural properties of the medium.

In hyperbolic metamaterials, the metallic/dieletric interfaces in the elementary meta-structure allow the excitation of plasmon-polariton modes. Therefore, the metamaterial's high-k modes can be considered artificial hybrid modes that obtain their large momentum ($\mathbf{p} \propto \mathbf{k}$) from their hybrid light-matter coupling [30]. Such modes are also called Bloch modes, because they are the solutions of Maxwell's equations in conjunction with Bloch's theorem due to the medium periodicity.

2.2.2 Realization of hyperbolic metamaterials: effective medium theory and fabrication approaches

As discussed previously, the two types of electric hyperbolic metamaterials (see Fig. 2.4) have one (HMM1) or two (HMM2) negative electric permittivity tensor components. Metals below their plasma frequency have a negative permittivity because the polarization response of their free electrons is in the opposite direction of the incident electric field. Therefore, one or two negative components of the permittivity tensor can be obtained by having a metallic component in the metamaterial structure that restricts the movement of the free electrons in those desired directions.

The most common meta-structures employed to fulfil these conditions are the multilayer metal-dielectric structure and wire media, as seen in Fig. 2.6 (a,b). According to effective medium theory, such configurations can achieve the desired extreme anisotropy response and lead to both types of hyperbolic metamaterials. Figure 2.6(c,d) present the effective medium constants calculated using a homogenization model based on a generalized Maxwell-Garnett approach [38], showing the limits where both structures exhibit hyperbolic dispersion of type I and II.

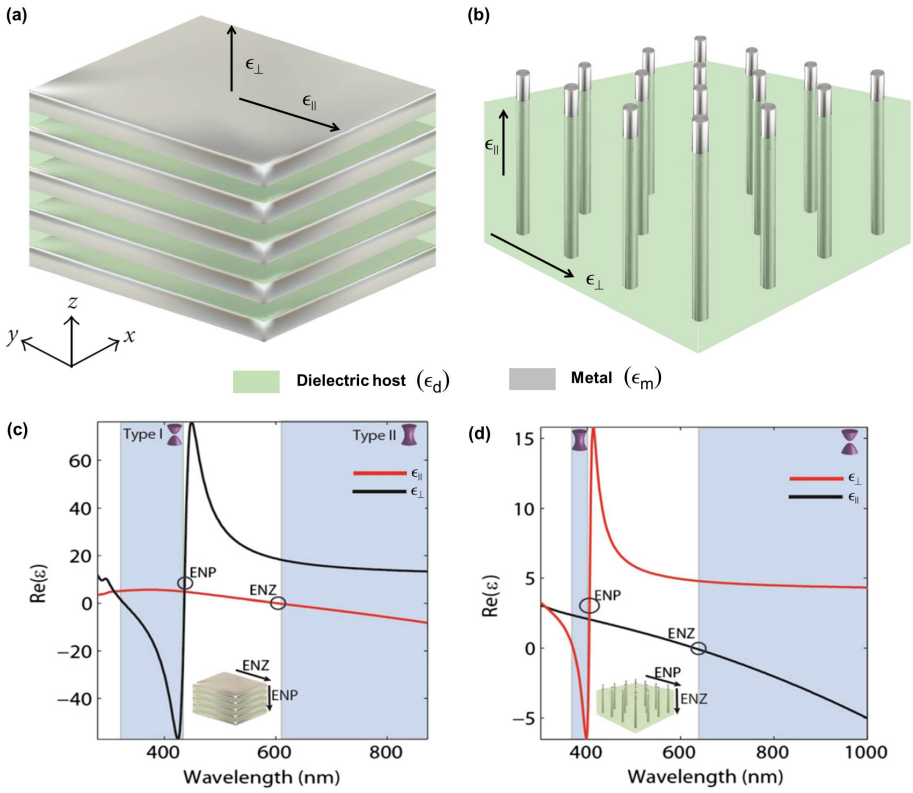

Figure 2.6: Schematic of the two most common structures employed to achive different types of electric hyperbolic metamaterials. (a) Multi-layer metamaterial. (b) Wire array metamaterial. Real part of the effective electric permittivity calculadted from effective medium theory. (c) Ag-TiO_2 multilayer structure with 35 % of Ag filling fraction. (d) Wire array of silver embedded in Al_2O_3, with 15 % of silver filling fraction. Figure extracted and adapted from Ref. [38].

The analytical calculation of the effective electric response of these two types of hyperbolic metamaterials is discussed below, using the effective medium and generalized Maxwell-Garnett approach (see appendix of Ref. [38]), followed by their respective fabrication techniques. Note that there are also other more complex meta-structures used to achieve hyperbolic metamaterials, such as the nanolayered meta-dielectric pyramid [42, 58], multilayer graphene-dielectric [59–61], and the fishnet structure (for both eletric and magnetic hyperbolic metamaterial) [62, 63].

Multilayer metal-dielectric metamaterials

In the local effective medium approach, the effective electric response of the medium is determined by the relationship between the macroscopic space average incident electric field ($\mathbf{E}$) and the macroscopic space average electric displacement field ($\mathbf{D}$), given by

$$\mathbf{D} = \bar{\bar{\epsilon}}_{eff}\mathbf{E} \tag{2.18}$$

where $\bar{\bar{\epsilon}}_{eff}$ is the effective permittivity tensor. From Maxwell's equations, the tangential component of the electric field at the interface of a medium must be continuous. Therefore, in a multilayer metamaterial, as illustrated in Fig. 2.6(a), we have

$$\mathbf{E}_m^{\parallel} = \mathbf{E}_d^{\parallel} = \mathbf{E}^{\parallel} \tag{2.19}$$

where $\mathbf{E}_m^{\parallel}$ and $\mathbf{E}_d^{\parallel}$ are the electric field component parallel to the metal and dielectric interface, respectively. The average of the electric field displacement in the direction parallel to the interface can be found by averaging the displacement field contribution from the metal ($\mathbf{D}_m^{\parallel}$) and dielectric ($\mathbf{D}_d^{\parallel}$), as

$$\mathbf{D}^{\parallel} = \rho_m\mathbf{D}_m^{\parallel} + (1-\rho_m)\mathbf{D}_d^{\parallel} \tag{2.20}$$

where ρ_m is the filling fraction of the metal in the multilayer metamaterial structure, given by

$$\rho_m = \frac{b_m}{b_m + b_d} \tag{2.21}$$

where b_m and b_d are the thickness of the metal and dielectric, respectively. Replacing Eqs. (2.18) and (2.19) in Eq. (2.20), we have

$$\epsilon_{eff}^{\parallel}\mathbf{E}^{\parallel} = \rho_m\epsilon_m\mathbf{E}^{\parallel} + (1-\rho_m)\epsilon_d\mathbf{E}^{\parallel}. \tag{2.22}$$

where ϵ_m and ϵ_d is the real part of the permittivity of the metal and dielectric, respectively. Cancelling the common $\mathbf{E}^{\parallel}$ component in Eq. (2.22), the

effective electric permittivity component parallel to the multilayer interface is given by [64–66]

$$\epsilon_{eff}^{\parallel} = \rho_m \epsilon_m + (1-\rho_m)\epsilon_d = \frac{\epsilon_m b_m + \epsilon_d b_d}{b_m + b_d}. \tag{2.23}$$

A similar approach can be employed to derive the effective permittivity perpendicular to the metal-dielectric interface. The electric displacement vector component normal to the metal/dielectric interface must be continuous, thus

$$\mathbf{D}_m^{\perp} = \mathbf{D}_d^{\perp} = \mathbf{D}^{\perp}. \tag{2.24}$$

The total magnitude of the normal electric field component in the multilayer system is the superposition of the respective components in the metal ($\mathbf{E}_m^{\perp}$) and in the dielectric ($\mathbf{E}_d^{\perp}$) layers. As a result,

$$\mathbf{E}^{\perp} = \rho \mathbf{E}_m^{\perp} + (1-\rho)\mathbf{E}_d^{\perp}. \tag{2.25}$$

Using Eq. (2.18) in Eq. (2.24), the boundary conditions become

$$\mathbf{E}_m^{\perp} = \epsilon_{eff}^{\perp} \frac{\mathbf{E}^{\perp}}{\epsilon_m}, \quad \mathbf{E}_d^{\perp} = \epsilon_{eff}^{\perp} \frac{\mathbf{E}^{\perp}}{\epsilon_d}. \tag{2.26}$$

Substituting Eq. (2.26) in Eq. (2.25) and eliminating the common $\mathbf{E}^{\perp}$, we obtain the effective electric permittivity component normal to the metal/dielectric interface [66]:

$$\epsilon_{eff}^{\perp} = \frac{\epsilon_m \epsilon_d}{\rho_m \epsilon_d + (1-\rho_m)\epsilon_m} \tag{2.27}$$

As seen in Eq. (2.23) and Eq. (2.27), both effective structural parameters in a metal dielectric superlattice can be tailored with the thickness of the layers and/or the response of the materials, which can be exploited to obtain hyperbolic dispersion ($\epsilon_{zz} \cdot \epsilon_{\perp} < 0$). Figure 2.6(c) shows the real part of these effective parameters, calculed with Eq. (2.23) and Eq. (2.27) in Ref. [38], for an Ag-TiO_2 multilayer structure with 35 % of Ag filling fraction. The regions where the medium exhibits both types of hyperbolic dispersion are indicated in blue. Other examples can be found in Ref. [67] (see Fig. 4).

It is important to emphasize that Eq. (2.23) and Eq. (2.27) are approximations of the electric response of the metamaterial, even when the structure's dimensions are on the sub-wavelength scale, and may only be valid for a

certain region of the spectrum. The main assumption in the preceeeding derivation is that fields do not change over the thickness of layers. However, surface plasmons can be excited at the metal/dielectric interfaces, leading to fast spatial variations of the fields within layers. Furthermore, at oblique incidence spatial dispersion becomes important [68, 69]. As a result, isofrequency curves can differ from those estimated by this model, and are not necessarily elliptical or hyperbolic.

The fabrication of multilayer metamaterials relies on the deposition of ultrathin and smooth films of the selected materials. Care must be taken with the quality of the deposited surface to avoid the increase of material loss and light scattering. The methods employed for the deposition of the metal-dielectric layer vary according to the selected materials.

Several groups have deposited gold and silver along titanium oxide or alumina by electron beam evaporation [33, 40], with typical layer thickness around few tens of nm. Other oxides and nitrites, alternative plasmonic options for optical frequencies, can be made by reactive sputtering or deposited by pulsed laser [70]. Silicon carbide (SiC) can be grown by chemical vapor deposition, and silica can be deposit by plasma enhanced chemical vapor deposition (PECVD) [71]. Alternatively, molecular beam epitaxy can be employed to grow alternating layers of undoped and highly doped semiconductors (which behaves like a metal) [72].

It is important to emphasize that multilayer metamaterials are easy to fabricate but also possess drawbacks or limitations related to high losses and high reflectivity due to their significant metal fraction. Ideally, high transmission can be obtained if the operational region is close to the metal's plasma frequency, where their reflectivity decreases. Alternatively, a dielectric with high refractive index can be employed to compensate the metal's high reflectivity, such as TiO_2 or SiN [22].

Metamaterials based on wire media

As discussed previously in Section 2.1.2, a wire array mesh with very thin perfectly conducting metallic wires behaves like an artificial medium with a Drude-like electric response characterized by a geometrically dependent plasma frequency (see Eq. (2.9) and Fig. 2.3(a,c)). Below this effective plasma frequency, the medium exhibits a negative electric permittivity.

Similarly, an array of vertically aligned non-ideal metal wires embedded in a dielectric, as seen in Fig. 2.6(b), exhibits a metal-like behaviour in the

direction of the wires ($\epsilon_{\parallel} < 0$) for frequencies below its effective plasma frequency. If the filling fraction volume of the metal is small, meaning that the size of the array lattice (Λ) is much larger than the wire diameter (d), the medium behaves like a dielectric in the plane transverse to the wires ($\epsilon_{\perp}$). Therefore, in this scenario, it is intuitive to expect a hyperbolic dispersion type I in this regime ($\epsilon_{\parallel} \cdot \epsilon_{\perp} < 0$).

Analytical calculations based on effective medium theory and homogenization models can lead to relations for the effective electric response of this type of wire array media. However, it is quite complicated to obtain a strict general analytic solution, which must include a nonlocal model to take into account the spatial dispersion [73,74], particularly for modes with high wavevector component, as will be discussed in Section 2.3.1. However, for nearly normal incidence and for small filling fraction of metal and poorly conducting wires (thin wire approximation, and moderate $|\epsilon_m|$ so that the field can be approximated as a constant within the wire), the vertically aligned wire medium is adequately described by Maxwell-Garnett approaches [67], where the electric permittivity components are given by [38] (note that Ref. [38] uses the opposite convention for $\parallel$ and $\perp$ directions),

$$\epsilon_{eff}^{\parallel} = \frac{(1+\rho'_m)\epsilon_m\epsilon_d + (1-\rho'_m)\epsilon_d^2}{(1+\rho'_m)\epsilon_d + (1-\rho'_m)\epsilon_m}, \tag{2.28}$$

$$\epsilon_{eff}^{\perp} = \rho'_m\epsilon_m + (1-\rho'_m)\epsilon_d, \tag{2.29}$$

where ρ'_m is the metallic filling fraction of the medium, defined as

$$\rho'_m = \frac{\text{wire area}}{\text{unit cell area}} = \frac{\pi r^2}{A_{cell}}, \tag{2.30}$$

with $A_{cell} = \Lambda^2$ for a square wire array, and $A_{cell} = \sqrt{3}\Lambda^2/2$ for hexagonal wire arrays. A more detailed derivation can be found in Appendix 2 of Ref. [38]. The requirement for $|\epsilon_m|$ to be moderate means this approximation is best suited for optical frequencies, whereas models using perfectly conducting wires are better suited at microwaves frequencies. Other regimes will be discussed in more detail in the next section.

As seen in Eqs. 2.28 and 2.29, the wire medium also exhibits effective parameters that can be tailored with the filling fraction of the metal and/or

with the response of their material components, which can be explored to obtain hyperbolic dispersion ($\epsilon_{zz} \cdot \epsilon_{\perp} < 0$).

Figure 2.6(d) shows the real part of these effective parameters, calculed with Eqs. 2.28 and 2.29 in [38], for a wire array structure with silver wires embedded in Al_2O_3, with 15 % of silver filling fraction. The regions where the medium exhibits both types of hyperbolic dispersion are indicated in blue. Somewhat counter-intuitively, besides the broadband hyperbolic dispersion of type I, wire media also exhibits hyperbolic dispersion type II in a small region where $\epsilon_{\parallel} > 0$ (true for frequencies larger than the effective plasma frequency) and $\epsilon_{\perp} < 0$ (true for a short region around the resonant pole), as seen in Fig. 2.6(d).

A common technique employed in the fabrication of wire metamaterials is electrochemical deposition of gold or silver on a porous alumina substrate [75], created by anodization of aluminium in a required template [76, 77], which can also be purchased commercially [78]. Typical dimensions achieved with such technique include gold wires with diameters from 10 to 50 nm, spacing of the wires between 40 to 70 nm, and lengths from 20 to 700 nm [77]. Structures as large as 1 cm x 1 cm x 50 μm have been fabricated with silver wires with diameter of 35 nm [78]. Other techniques like micromachining [79] and photolithography [80] are limited to micron-sized structures. Focused ion beam (FIB) and electron beam lithography can fabricate sub-10 nm structures, but they are too slow and expensive to produce structures over large areas or reasonable lengths and depths.

Recently, fibre drawing has been used as a mass-production and low-cost alternative to fabricating wire array metamaterials [50, 81–84]. The use of polymer as the dielectric material allows the fabrication of uniform wires down to diameters around 5 μm, achieving metamaterials for operational frequencies in the THz spectrum. However, problems with fluid instability makes the fabrication of smaller uniform wire array structures in polymer fibres difficult [84], which limits their operational ranges to low frequencies (THz). This thesis is focused on the fabrication of wire array metamaterials fibre for the infrared, which is made possible using soft-glass instead of polymer.

Besides the low cost and mass-production, fibre drawing also makes possible the fabrication of tapered wire array metamaterials, which generate magnifying wire array hyperlenses. Such wire-based metadevices are difficult to fabricate with the standard planar techniques discussed above. A literature review of metamaterial fibres and the current structural limita-

tions is presented in the last section of this Chapter and discussed in detail in Chapter 4.

In the next Section, the electromagnetic response of wire array metamaterials is discussed in detail, particularly how their response varies for different frequency regimes (visible, infrared and THz), the origin and influence of their spatial dispersion, and their modal structure.

2.3 Wire array metamaterials

As previously discussed, a sub-wavelength array of metallic wires embedded in a dielectric matrix behaves as a homogeneous artificial medium with extreme optical anisotropy and ehxibits unusual optical properties, such as hyperbolic dispersion and negative refractive index [85].

Wire array metamaterials, in contrast to other bulk metamaterials, do not rely on resonances, which means that they do not exhibit resonant losses or resonant frequency dispersion, and can achieve broadband response. The small fraction of metal in their meta-structure decreases reflections and can lead to a high figure of merit regarding transmission (high $Re(n_{eff})/Im(n_{eff})$). The simplicity in their structure facilitates their fabrication and offers large wavelength tunability.

The electromagnetic response of this type of metamaterial is complex and strongly related to three factors:

(1) The behaviour of the metal in the selected operational frequency range.

(2) Structural parameter of the wire medium (wire diameter, wire spacing, lattice arrangement, and the degree to which the elementary meta-structure is sub-wavelength).

(3) Spatial dispersion.

Below, the behaviour of a metal is described according to the operational frequency range, followed by a detailed description of the electromagnetic response of a wire array metamaterial and its spatial dispersion.

2.3.1 Electromagnetic response of wire array metamaterials

Wire media were studied in the 1950-60s to achieve artificial plasma in microwave frequencies [86–88], *i.e.*, artificial materials with negative electric permittivity. More recently, wire media have been studied more deeply [12, 89, 90], particularly in the context of metamaterials [15, 91].

From homogenization models, the electromagnetic response of a wire array medium formed by vertically aligned thin metal rods in a dielectric matrix, as illustrated in Fig. 2.7, can be described in terms of a dyadic permittivity as

$$\bar{\bar{\epsilon}} = \begin{pmatrix} \epsilon_{xx} & 0 & 0 \\ 0 & \epsilon_{yy} & 0 \\ 0 & 0 & \epsilon_{zz} \end{pmatrix} \tag{2.31}$$

where $\epsilon_{xx} = \epsilon_{yy}$ is the permittivity transverse to the wires (ϵ_t) and ϵ_{zz} is the effective permittivity in the direction along the metal wires.

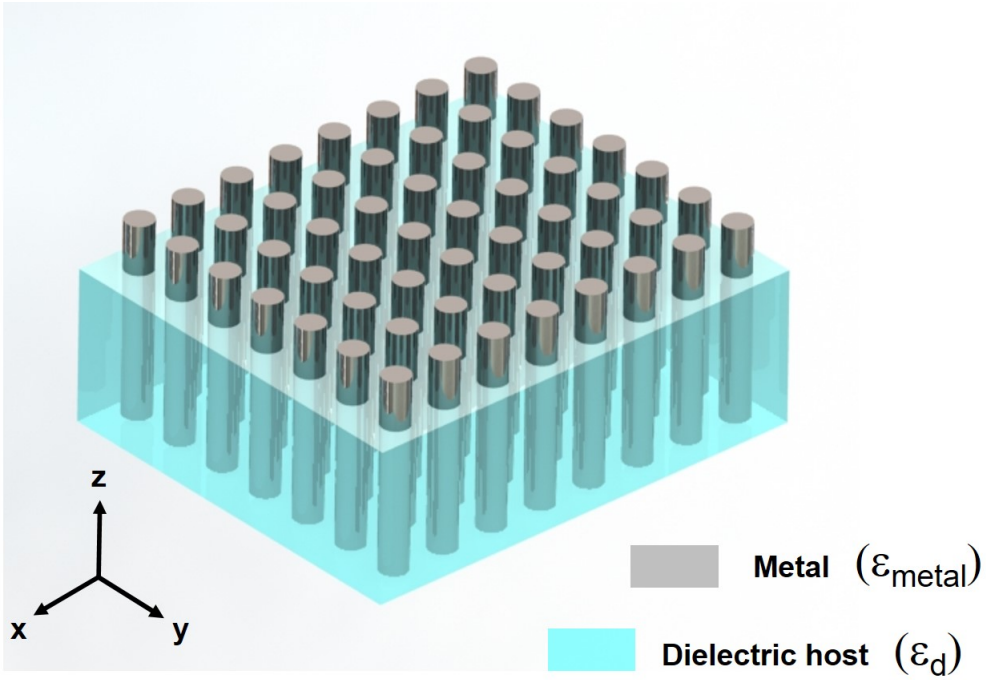

Figure 2.7: Schematic of the wire array medium.

According to early models analyzed in [87, 89], the wire medium can be described with a local permittivity tensor, *i.e.*, with electric permittivity components only depending on frequency. In this local model, which does not consider spatial dispersion, a wire medium with perfect electric conducting wires (PECs, zero resistivity and ϵ=-∞) exhibit an effective medium parameter ϵ_{zz} as [12, 92]

$$\epsilon_{zz}(\omega) = \epsilon_d \left(1 - \frac{\omega_{p,eff}^2}{\omega^2(\epsilon_d/\epsilon_0)}\right), \tag{2.32}$$

where $\omega_{p,eff}$ is the effective plasma frequency of the structure. Note that the above equation indicates a Drude-like behaviour with a geometrically dependent plasma frequency. Over the years, several homogenization approaches derived different formulae for this effective plasma frequency ($\omega_{p,eff}$), which will be discussed in detail in Section 2.3.1.

Defining $k_{p,eff} = (\omega_{p,eff}/c)$ as an effective structural wave number corresponding to the effective plasma frequency, Eq. (2.32) can be rewritten as

$$\epsilon_{zz}(\omega) = \epsilon_d \left(1 - \frac{k_{p,eff}^2}{k^2}\right), \tag{2.33}$$

where $k = \sqrt{\epsilon_{d,r}}\ \omega/c = n_d\, k_0$, c is the speed of light and considering a non-magnetic metal ($\mu = \mu_0$). For frequencies lower than $\omega_{p,eff}$, this local model describes a hyperbolic metamaterial with Re($\epsilon_{zz} < 0$) and Re($\epsilon_{xx} = \epsilon_{yy} > 0$), with an ideal hyperbolic dispersion as shown in Fig. 2.4(b).

Recently, the local model presented in Eq. (2.33) has been shown in Ref. [73] to lead to incorrect and unphysical results for propagating modes containing a wavevector component along the wires, *i.e.*, the extraordinary waves/modes with $E_z \neq 0$. Belov *et al.* proposed the use of a non-local model for ideally conducting wires (PECs), replacing Eq. (2.33) with a spartially dispersive permittivity component, given by [73]

$$\epsilon_{zz}(\omega, k_z) = \epsilon_d \left(1 - \frac{k_{p,eff}^2}{k^2 - k_z^2}\right), \tag{2.34}$$

where k_z is the wavevector component along the wires of the propagating extraordinary mode. Note that, as discussed before, the PEC approximation describes well the behaviour of a metal for low frequencies. Therefore,

Eq. (2.34) is a good approximation for wire media operating at THz frequencies.

The non-local homogenization model was generalized for wire media containing ϵ-negative wires (not perfect conductors as Eq. (2.34)) by Silveirinha in Ref. [93]. According to this model, the electric response of wire media can be described with the permittivity tensor (Eq. (2.31)), with components

$$\epsilon_t(\omega) = \epsilon_d \left(1 + \frac{2}{\dfrac{\epsilon_m + \epsilon_d}{\rho'_m(\epsilon_m - \epsilon_d)} - 1} \right) \tag{2.35}$$

$$\epsilon_{zz}(\omega, k_z) = \epsilon_d \left(1 + \frac{1}{\dfrac{\epsilon_d}{\rho'_m(\epsilon_m - \epsilon_d)} + \dfrac{k_z^2 - k^2}{k_{p,eff}^2}} \right), \tag{2.36}$$

where ρ'_m is the metal filling fraction (Eq. (2.30)). This non-local model has been studied and tested with full-wave simulations in [94], and was validated over the whole infrared region under the following conditions:

(1) The skin depth of the metal needs to be no larger than half the wire diameter.

(2) The structure needs to be sub-wavelength in comparison with the effective wavelength propagating in the medium.

Note that these conditions are fulfilled for micron and sub-micron wires at THz and mid-infrared frequencies, respectively. In addition, in the case that $\epsilon_m \to -\infty$ (a low frequency limit where the wires can be considered PECs), Eq. (2.36) becomes Eq. (2.34), showing that both non-local models are in agreement.

In a uniaxial medium, i.e., an anisotropic medium containing one optical axis (one component of the permittivity tensor is different to the other two), the modes can be classified as transverse electric (TE) and transverse magnetic modes (TM), when the electric or magnetic field is transverse to the axis of anisotropy, respectively. For wire array media, the solution of the TM dispersion equation ($k_\perp = \epsilon_{zz}(k_0^2 - k_z^2)$), where z is the direction of the wire) with the spatially dispersive permittivity component ϵ_{zz} (Eqs. 2.34

or 2.36), leads to two different solutions, and hence two TM modes are allowed to propagate besides the TE mode [93, 94]. One of these TM modes can exhibit a dispersion similar to a transverse electromagnetic mode (TEM, $k_z^2 \approx k_0^2$), being dispersionless in respect to $k_\perp$ and possessing a nearly flat isofrequency surface in k-space. As a consequence, these modes can propagate along the wires with the same (or nearly the same) phase velocity for all possible transverse spatial frequencies, being ideal for imaging. This approximation is called the canalisation regime. In this canalization regime, wire media behave like a multi-wire transmission line, and such modes are called transmission-line modes. Since they are not strictly TEM, they are also called quasi-TEM modes.

Note that the isofrequency surfaces of the quasi-TEM mode of the wire array medium can be significantly different from the hyperbola due to spatial dispersion. Figure 2.8 illustrates this with a comparison between the isofrequencies surfaces for the quasi-TEM modes of an ideal hyperbolic medium with no spatial dispersion (described by Eq. (2.36) ignoring the term $k_z^2/k_{p,eff}^2$), a spatially dispersive wire array of vertically aligned PECs (described by Eq. (2.34)), and a spatially dispersive wire array of conventional metallic wires with finite negative permittivity (described by Eq. (2.36)).

As seen in Fig. 2.8, the quasi-TEM mode in the spatially dispersive model with PECs (a good approximation for metals in the THz) exhibits a flat isofrequency surface, while the spatially dispersive model with finite negative ϵ (a good approximation for metals in the infrared) exhibits an intermediate behaviour between the PEC and the ideal non-spatially dispersive hyperbolic medium.

Effective plasma frequency of wire array medium

The geometrically dependent effective plasma frequency of the wire medium employed in the local (Eq. (2.33)) and non-local (Eq. (2.34)) analitycal models is analogous to the conventional plasma frequency of the metals (Eq. (2.6)), and it is the reason this type of medium is usually called "artificial plasma". Through the literature, it is possible to find different formulae for such homogenized parameter [12,95–97]. For example, the effective plasma frequency of a square array in the thin PEC wires approximation, *i.e.*, for d and $\Lambda \ll \lambda$, is derived in [96] (see Eq. (40)) as

$$k_{p,eff}^2 = \frac{2\pi/\Lambda^2}{0.5275 + \ln\left(\frac{\Lambda}{2r\pi}\right)}, \tag{2.37}$$

where r is the radius of the metal wire.

Another expression for square arrays of thicker wires was derived in Refs. [97, 98] as

$$k_{p,eff}^2 = \frac{2\pi/\Lambda^2}{\ln\left(\frac{\Lambda^2}{4r(\Lambda - r)}\right)}. \tag{2.38}$$

and gives a qualitatively correct result in the limit where two wires nearly touch ($r \to \Lambda/2$). Regarding their accuracy, comparison with full-wave numerical simulations [99, 100] shows that Eq. (2.38) is more accurate than Eq. (2.37) for $r \geq 0.1\Lambda$, but even Eq. (2.38) is a poor approximation when r $\gtrsim 0.2\Lambda$. However, the opposite behaviour is observed for $r < 0.05\Lambda$. Note

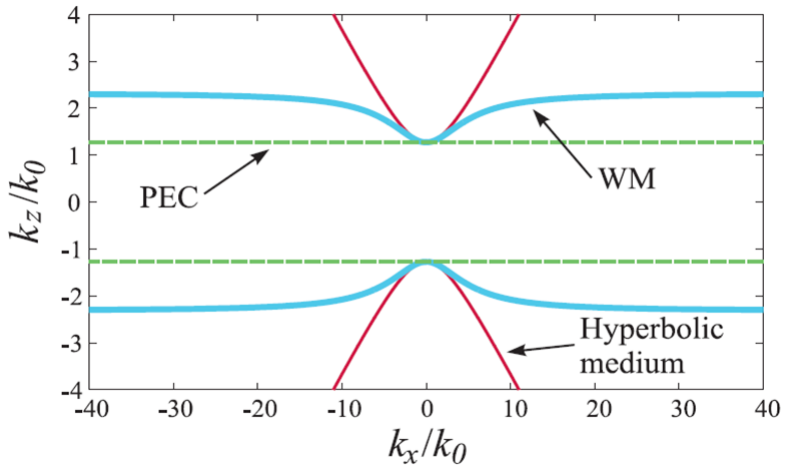

Figure 2.8: Comparison between isofrequency surfaces of the extraordinaty modes between an ideal hyperbolic medium (red curve), described by Eq. (2.17), and two vertically aligned wire array structures: perfect electrical conductor (green doted line), metallic rods with negative permittivity (blue curve). Figure extracted from Ref. [74].

that another expression commonly cited and derived in [12, 90] as

$$k_{p,eff}^2 = \frac{2\pi/\Lambda^2}{\ln(\Lambda/r)}, \tag{2.39}$$

presents a worse accuracy in comparison to Eqs.(2.37, 2.38), even for rather small wire diameters. In addition, it does not give a qualitatively sensible result for the limit where $r \to \Lambda/2$, where $k_{p,eff}$ should tend to infinity.

For hexagonally arranged thin wires, the effective plasma frequency from the model for Eq. (2.38) is given by

$$k_{p,eff}^2 = \frac{(2\pi/\Lambda)^2}{\sqrt{3}\pi\ln(\Lambda^2/(d(2\Lambda - d)))}. \tag{2.40}$$

A general model for the effective plasma frequency was developed in Ref. [98] using a quasi-static homogenization model and a thin wire approximation, as

$$k_{p,eff}^2 = \frac{\mu_0}{A_{cell}L_{eff}}, \tag{2.41}$$

where A_{cell} is the area of the unit cell (square array: $A_{cell} = \Lambda^2$, hexagonal array: $A_{cell} = \sqrt{3}\Lambda^2/2$), and L_{eff} is the effective inductance of the wire medium.

2.4 Metamaterial fibres

Fibre drawing is an interesting alternative method to fabricate metamaterials since it allows mass production (which reduces the cost) and possesses a remarkable flexibility in the scaling down of different types of structures. However, the required presence of metal in the fibre's structure to achieve hyperbolic metamaterials introduces extra constraints and challenges in the drawing process, due to the different rheological properties of the selected material. Fluid dynamics also affects the quality of the metallic structure fabricated by co-drawing, depending on the materials selected, the drawing parameters and the dimensions required.

The drawing of structured fibres is introduced and a review of metamaterial fibres is presented below, with emphasis on the materials employed

and the dimension of the structures that were successfully fabricated, which limits the metamaterials to operating at THz frequencies.

The co-drawing of structures including metal (multimaterial drawing) is discussed in details in Chapter 4, along with a review of glass/metal drawing and the fabrication of our MIR wire array metamaterial fibre.

Fibre drawing technique

The method used to fabricate microstructured fibres containing air holes along their lenght is well established since the invention of photonic crystal fibres (PCFs) in the 1990's [101–103]. The general process is commonly divided in two steps: the preform fabrication and the fibre drawing.

The preform, a macroscopic version of the fibre containing the desired structure, can be produced by different methods, depending on the dielectric employed and the type of structure desired. The most common methods are: stack-and-draw [101, 103, 104], extrusion [105, 106], casting [107, 108] and ultrasonic or regular drilling [105].

After its fabrication, the preform is scaled down to fibre in a fibre drawing tower. Figure 2.9 shows a general schematic of a conventional drawing tower that consists of a feeding unit, a furnace and a drawing unit. Initially, the preform is heated to a temperature around the softening point of its constituent material (glass or polymer), where the dielectric softens and it drops by gravity. The drop is attached to the pulling system and the feeding (v_{feed}) and pulling (v_{draw}) velocities are adjusted according to the desired reduction factor of the original preform and the range of velocities available on both units. Under a steady state regime, the relation between the diameter of the fibre (d_{fibre}) and preform (D_p) is imposed by the volume conservation equation

$$d_{fibre}^2 = D_p^2 \frac{v_{feed}}{v_{draw}}. \tag{2.42}$$

The steps described above are a general outline of the drawing process, which can be quite sophisticated depending on the type of geometry desired and materials employed [109–111]. The main advantages of the fibre drawing technique are the low cost, the large volume production, and the great control in the scaling down of the fibre's structure. One conventional preform can generate kilometers of fibre, and the drawing process can scale down the

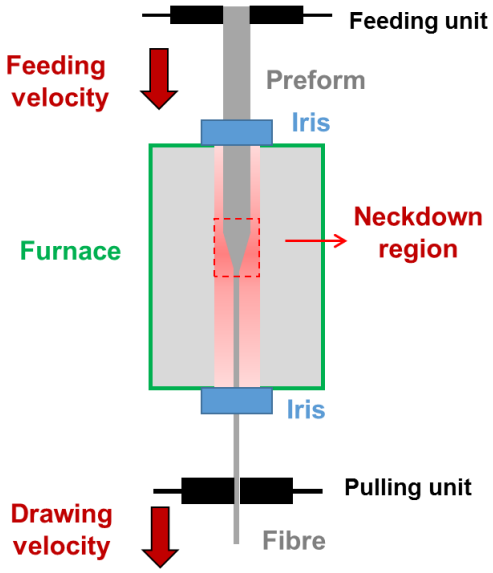

Figure 2.9: Schematic of the fibre drawing process.

original structure by several orders of magnitude with great precision and control.

Polymer metamaterial fibres for applications at THz frequencies

The fabrication of metamaterial fibres based on metallic structures embedded in dielectric can be achieved by incorporating metals in the fibre's microstructure. In particular, split-ring resonators (SRRs) and wire arrays structures have been fabricated using polymers (PMMA, polycarbonate, Zeonex) and indium.

Single split-ring resonators were fabricated by drawing in [82]. The SRR's preform was set up by rolling an indium sheet around a PMMA tube together with a PMMA rod to produce a slotted cylinder, and introducing the set into a polycarbonate (PC) jacket. Figure 2.10(a) shows the cross section pictures of two drawn split ring fibres with outside diameters around 300 μm and 250 μm. The split-rings were stacked and drawn again in a Zeonex slab, as seen in Fig. 2.10(b), forming a rectangular fibre containing an array of 6 or 7 SRRs. Resonators with outside diameters as small as 100 μm were obtained,

and exhibited magnetic resonances between 0.3 and 0.4 THz, characterised by a reduction in the transmittance, as seen in Fig. 2.10(c), when the incident magnetic field is parallel to the slotted resonators (Fig. 2.10(d)).

A similar approach was employed in Ref. [83] for the fabrication of double SRR fibres. Figure 2.10(e) shows the cross-section of a drawn double SRR indicating its constituents materials. The use of a large Zeonex jacket was required to preserve the structure of the two rings, which was later removed with cyclohexane by chemical etching, as seen in Fig. 2.10(f). Double SRRs as small as 100 μm were achieved, exhibiting resonances around 0.25 THz, when the incident magnetic field is parallel to the slotted resonators.

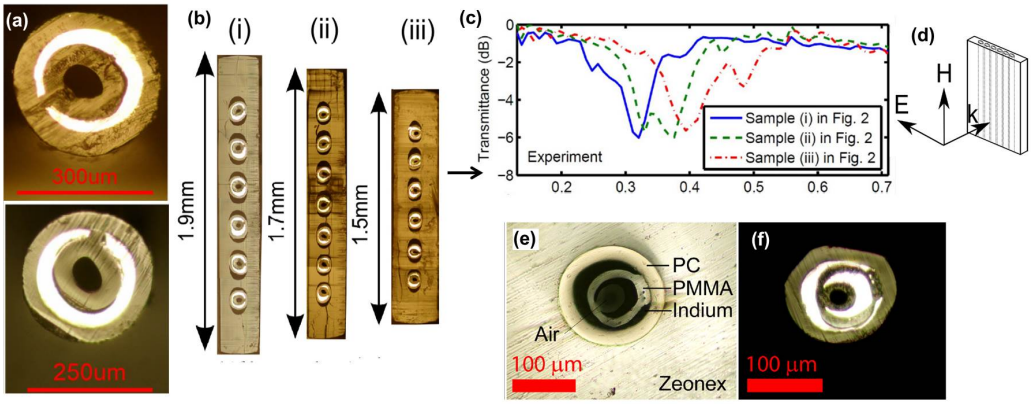

Figure 2.10: (a) Cross-section pictures of split ring resonator fibres made of PMMA/PC and indium. (b) Rectangular array fibres obtained after the stacking and drawing of the split rings in a Zeonex slab. (c) The experimental transmitance of the array fibres showed in (b), with magnetic resonances between 0.3 and 0.4 THz, when the incident magnetic field is parallel to the slotted resonators (as seen in (d)). (e-f) Cross-section picture of a double SRRs fibre before and after the etching of the Zeonex cladding, respectively. Figures (a-d) were adapted from Ref. [82], while Figs. (e-f) were extracted from Ref. [83].

Tuniz *et al.* presented in Ref. [81] the fabrication of wire array metamaterial fibres using a stack-and-draw approach. PMMA capillaries filled with indium were drawn, similarly to a Taylor wire process [112], stacked into a PMMA jacket and drawn to fibre. Fibres containing wires of approximately 8 μm diameter and 100 μm spacing were reported (Fig. 2.11(a)), exhibiting a plasma frequency around 0.2 - 0.3 THz dependent on the geometry as expected, as seen Fig. 2.11(b), from a lateral transmittance (Fig. 2.11(c)).

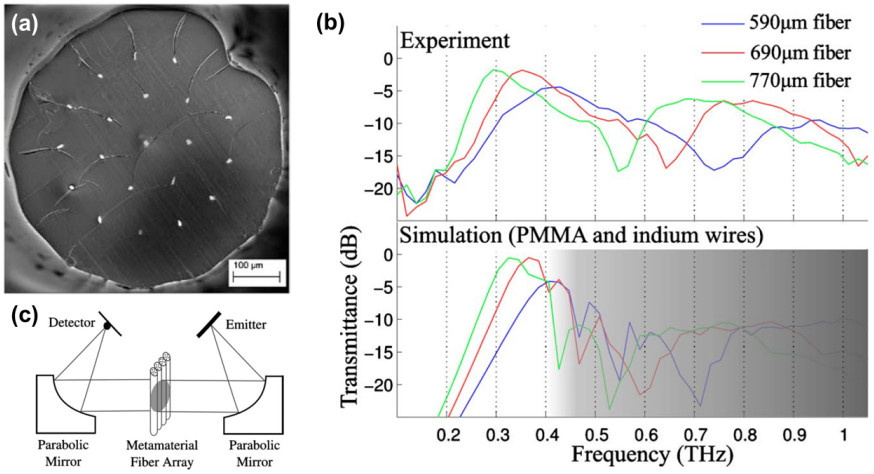

Figure 2.11: (a) SEM micrograph of an indium/PMMA wire array metamaterial fibre and (b) the experimental and the simulation side transmission exhibiting a plasma frequency around 250 GHz depending on the size of the fibre (measuring setup seen in (c)). Figures extracted and adapted from Ref. [81].

Denser and tapered wire array metamaterial fibres made of PMMA/Zeonex and indium were demonstrated in Ref. [50], with wire diameter as small as 10 μm and distance of 50 μm, and employed for subdiffraction imaging at THz frequencies. A detailed review of such work will be presented in Chapter 5.

Naman *et al.*, using the same stack-and-draw approach, demonstrated the fabrication of wire array fibres (PMMA/indium) with denser wires and plasma frequencies varying from the THz through the MIR (1 to 20 THz, corresponing to $\lambda = 300$ - 15 μm) [84]. Fluctuations of the metallic structure due to Plateau-Rayleigh instability [113] were observed, for fibres with wire diameter smaller than 10 μm.

Adjusting the drawing parameters to perform drawing at the highest possible viscosity of the polymer, Plateau-Rayleigh instability was minimized, and the fabrication of wires with diameter as small as 1 μm was achieved (Fig. 2.12(a)). However, even with such favourable drawing conditions, the fluctuation on the diameter exponentially grows for diameters smaller than 5 μm. This behaviour is illustrated in Fig. 2.12(b), where the variation in the wire diameter (standard deviation divided by the average diameter) as a function of the wire diameter is presented. Figure 2.12(a) shows the smaller-scale fibre fabricated, with wire diameter of approximately 1 μm, spacing of

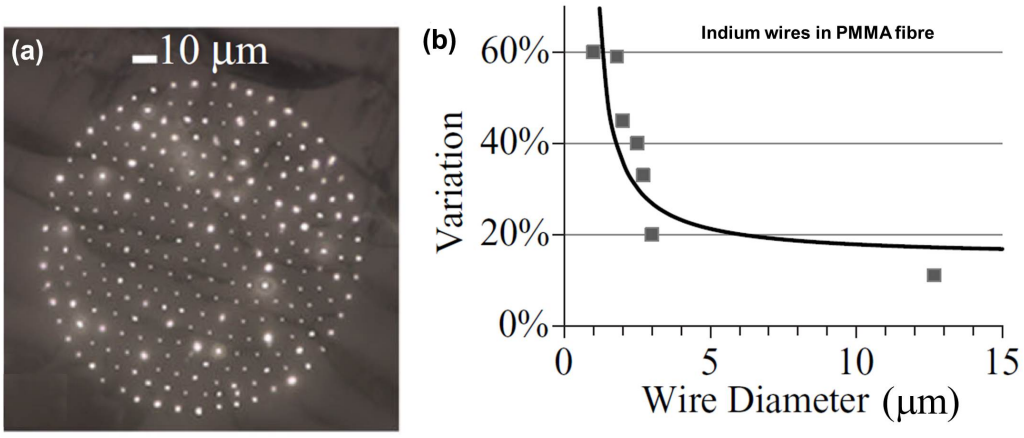

Figure 2.12: (a) Smaller-scale PMMA/indium metamaterial fibre fabricated in Ref. [84], with wire diameter of approximately 1 μm, spacing of 7 μm. (b) The standard deviation in diameter divided by average diameter for a larger set of wire array metamaterial fibres based on PMMA/in. Figures extracted from Ref. [84].

7 μm, and a fluctuation on the wire diameter around 60 %.

Consequently, Fig. 2.12(b) indicates that, even with optimized drawing conditions, the fabrication of uniform drawn wire array structures in polymer is limited to wire diameters larger than a couple of microns. This also restricts the possible values for the distance between the wires ($\sim 7\,\mu$m for the smallest structured showed in Fig. 2.12(a)), which is the size of the meta-structure.

Considering that metamaterials must have an elementary meta-structure smaller than 1/10 of the operational wavelength ($\Lambda < \lambda_0/10$ for wire arrays), the limit imposed by the Plateau-Rayleigh instability restricts the operational range of these polymer metamaterial fibre to the microwave and THz spectrum or far infrared. However, according to the literature [114, 115], drawn wires with smaller structures (diameters as small as 50 nm) can be achieved by replacing the polymer for glasses, due to the different rheological properties of such materials and the typical interfacial tension obtained during the drawings. A detailed literature review of the co-drawing of metal and glasses and the Plateau-Rayleigh instability is presented in Chapter 4.

In this context, the main goal of this thesis is the use of soft-glasses to produce wire array metamaterial fibres with wire diameters of a few tens of nanometers, which leads to metamaterial fibres with operational wavelength in the mid-infrared.

Chapter 3

Material selection for IR metamaterial fibres

This Chapter discusses the material selection for the fabrication of infrared wire array metamaterial fibres based on optical performance and drawing feasibility. Firstly, a figure of merit for the optical losses of the selected metals in the infrared region is established, which provides a measure to compare their optical performance. The drawing feasibility of some metal/dielectric combinations is also analyzed based on material chemical compatibility and the requirements for multimaterial drawing. Finally, after the selection of promising material combinations, the optical losses of the high-spatial frequency quasi-TEM modes for the full indefinite wire array metamaterial media are presented (numerically simulated with a finite-element software - COMSOL). The optical loss as a function of the structural parameters (wire diameter and spacing) is evaluated in three different regions of the infrared spectrum and their feasibility for different applications is assessed.

This Chapter is strongly based on the publication:

Metal selection for wire array metamaterials for infrared frequencies
Juliano G. Hayashi, Simon Fleming, Boris T. Kuhlmey and Alexander Argyros, *Optics Express* 23(23), pp. 29867-29881, (2015).

Appendix C contains the contributions, authors' signatures, and the original version of this publication.

3.1 Material selection for IR hyperbolic metamaterial fibres

The drawing of hyperbolic metamaterial fibres composed of a metallic structure embedded in a dielectric matrix is considerably more difficult than the fabrication of conventional microstructured optical fibres (Holey fibres, PCFs [102] and mPOFs) due to the presence of the metal. This type of drawing possesses extra requirements and the correct material selection is essential for the fabrication feasibility.

In a co-drawing process of metals and glasses, the rheological properties of the selected materials must match and they must be chemically compatible: The melting point of the metal must be lower than the minimum drawing temperature of the dielectric to allow them to be drawn together. Chemically, the selected materials must not react since the formation of any oxide or new component can be extremely detrimental to the fabrication process: if such a new component has a melting point higher than the drawing temperature, it will not be drawable or/and will lead to deformations of the metallic structure.

Besides the fabrication feasibility aspect, the selection of the metal must also consider its influence on the optical properties of the final metamaterial device. The presence of its metallic structure has a huge contribution on such optical losses due to ohmic losses, which is the heat dissipation when a current flows through a conductor (Joule heating). Such contribution is particularly high in the infrared and optical frequencies, where the skin depth of the metals is larger than at lower frequencies, which results in a deeper penetration of the electromagnetic field in the metallic structure [116].

In the following sections, the optical quality of the metals is analyzed and the possible material combinations for metamaterials in the near infrared (NIR) and mid-infrared (MIR) region are discussed. Firstly, in Section 3.2, the bulk properties of the metals is studied and a figure of merit for their optical quality specific to wire arrays is presented. Based on optical quality and fabrication feasibility arguments, interesting material combinations are proposed for operation around $1\,\mu$m, $3\,\mu$m and $10\,\mu$m wavelengths. In Section 3.3, a loss study is extended to parameters such as wire diameter (d), operational wavelength (λ) and the index of the dielectric host (n_d). In Section 3.4, the loss of high-spatial frequency quasi-TEM modes is presented for hexagonal wire array structures with specific material combinations, varying

wire diameter, wire spacing and index of the dielectric, in the NIR and MIR. Finally, in Section 3.5, the use of such wire array structures is assessed for different applications in the infrared spectral region.

3.2 Bulk metal losses and figure of merit for wire array media

The optical loss of a wave reflecting from, or propagating along, a bulk metal is determined by the imaginary and real parts of the metal's permittivity (ϵ'' and ϵ'), which vary with free space wavelength (λ). The imaginary part of the dielectric constant ϵ'' is related to the metal's absorption, while the ϵ' is related to the penetration of the wave in the bulk metal. Figures 3.1(a) and 3.1(b) show experimental values of ϵ'' and ϵ', respectively, for several metals in the NIR and MIR (data extracted from Refs. [5,117]). For all the metals presented, except bismuth, ϵ'' and the absolute value of ϵ' increases with λ. In a wire array, or even in a single metal wire plasmonic waveguide, ϵ'' is not sufficient to estimate propagation loss of waves in these structures. The optical loss of each mode is also strongly related to the energy distribution between the metal and the surrounding dielectric, meaning that the real part of permittivity (ϵ') of both materials and the geometry also influence the loss. An appropriate figure of merit for this type of structure is the loss of the fundamental TM mode in a single metal wire waveguide. While these losses also depend on the wire diameter used, setting a nominal diameter enables comparison between metals. The mode condition equation for the 0^{th} order TM mode of a single wire can be found analytically as [118],

$$\frac{\gamma_2 I_1(\gamma_1 a) K_0(\gamma_2 a)}{\gamma_1 I_0(\gamma_1 a) K_1(\gamma_2 a)} = -\frac{\epsilon_2}{\epsilon_1}, \tag{3.1}$$

where I_m and K_m are the modified Bessel functions of order m, a is the radius of the metal wire, and ϵ_1 and ϵ_2 are the complex permittivities of the metal and dielectric, respectively. The factor γ is defined by,

$$\gamma_j = k_0 (n_{\text{eff}}^2 - \epsilon_j)^{1/2}, \tag{3.2}$$

where n_{eff} is the effective index of the mode, k_0 is the vacuum wavenumber

($k_0 = 2\pi/\lambda$). The root of the transcendental Eq. (3.1) can be found numerically and provides the n_{eff} of the TM mode, which can be used to calculate the loss in dB/μm using,

$$\alpha = \frac{40\pi\kappa}{\lambda \ln 10}, \tag{3.3}$$

where κ is the imaginary part of n_{eff} and λ is the wavelength in microns.

Figures 3.1(c) and 3.1(d) illustrate the loss of the lowest order TM mode calculated using Eqs. (3.1-3.3), for wire diameters of 250 nm and 500 nm, respectively, embedded in vacuum, as a function of wavelength. The representative metals were chosen for their good optical properties (gold, silver, aluminium, copper) or their convenience for fabrication due to availability and relatively low melting temperature (bismuth, tin, indium). As expected, Figs. 3.1(c) and 3.1(d) show that the absolute value of the loss changes with wire diameter but the relative loss of the different metals is not qualitatively affected. Consequently, the loss for a nominal diameter is a good figure of merit for a metal's optical quality. As such, Figs. 3.1(c) and 3.1(d) show that loss decreases for longer wavelengths and gold, silver, aluminium and copper are clearly the best metals as far as loss is concerned for the wavelength range between 1 to 10 μm.

Considering Fig. 3.1(c), aluminium is the best metal in terms of optical quality over almost all the wavelength range considered. However, experimental tests with common silica-based glasses (borosilicate, soda-lime and SiO_2) showed high reactivity resulting in the production of silicon, through the reaction [119–121].

$$4\text{Al} + 3\text{SiO}_2 \rightarrow 2\text{Al}_2\text{O}_3 + 3\text{Si}. \tag{3.4}$$

Copper is compatible with glass and Cu/SiO_2 fibres have been reported in the literature [122], however its strong tendency to oxidize when molten can be a problem, especially during preform fabrication. According to the TM mode figure of merit (Fig. 3.1(c,d)), both gold and silver have similar and high optical quality, but silver presents higher reactivity. Therefore, among the metals with lowest losses, gold remains the best option once compatibility with the glass drawing process is considered.

The second group of metals, having poorer optical quality, is considered for practicality. Of these, tin presents low oxidation when molten and high

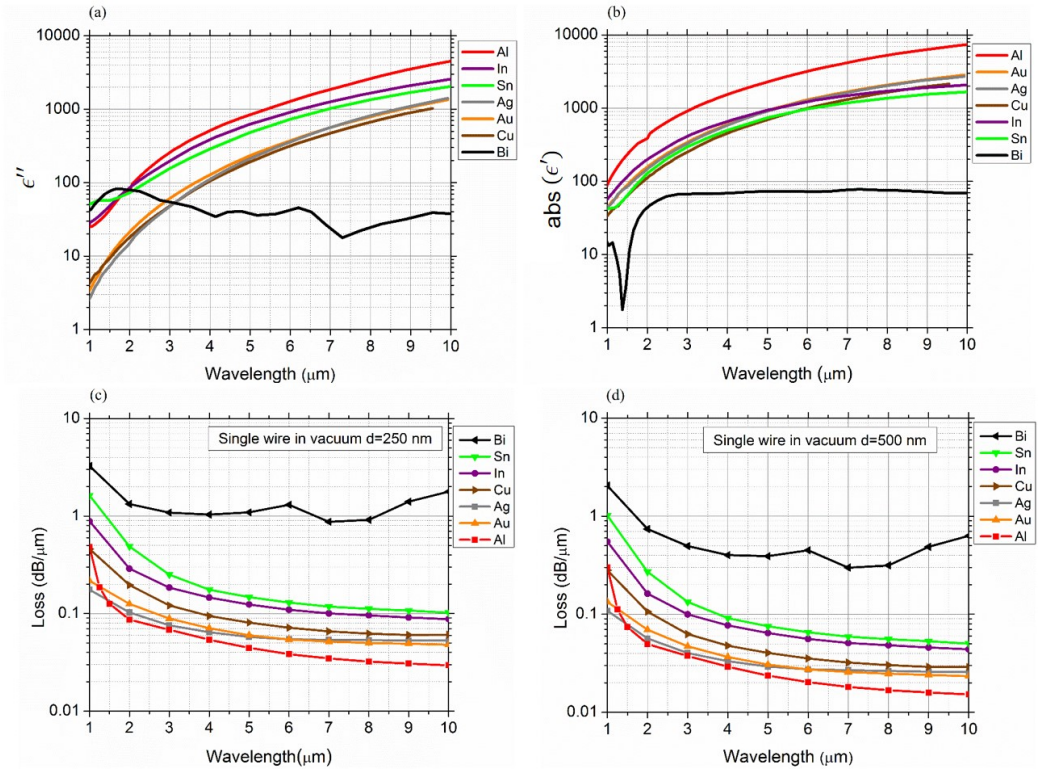

Figure 3.1: Measured values of (a) the imaginary and (b) the real part of the permittivity for bulk metals [5, 117], in the NIR and MIR. Figure of merit: the 0^{th} order TM mode loss of a single metal wire waveguide embedded in vacuum for wire diameters of (c) $d = 250\,\text{nm}$, (d) $d = 500\,\text{nm}$.

compatibility with common glasses, especially with soda-lime and borosilicate. This compatibility is commercially employed in the fabrication of float soda-lime and borosilicate by the Pilkington process or microfloat process [123–125]. This feature, combined with an optical quality similar to indium, low cost and low melting point, motivates a deeper analysis of its use in drawn wire arrays. We thus focus further analysis on gold and tin, as cases of high optical quality (gold) and practicality (tin). Figures 3.1(c) and 3.1(d) show that losses for wire arrays using other interesting metals (silver and copper) are expected to lie between these two cases.

In the next section, the loss study of the 0^{th} order TM mode of the single wire waveguide is extended to other parameters such as wire diameter (d), wavelength, and the refractive index of the dielectric host (n_d), before

studying losses of the full wire array in Section 3.4. Such analyses of a simpler waveguide will provide some qualitative insights into the behaviour of the more complex indefinite wire array metamaterial media.

3.3 Single metal wire waveguide: Optical loss as function of wavelength, wire diameter and refractive index of the dielectric

The loss of the TM mode of a single metal wire depends on the wire diameter, the wavelength and the index of the surrounding dielectric. Figures 3.2(a) and 3.2(b) present this loss for gold and tin wires with several diameters (from 10 nm to 2.5 μm), in the wavelength region between 1 to 10 μm, calculated with Eqs. (3.1-3.3) using the complex permittivity of the metals from Figs. 3.1(a) and 3.1(b). Vacuum is selected as the dielectric medium in order to analyze, in the first instance, the influence of the metal in isolation.

Figure 3.2 shows that the losses are higher for the tin wires, as expected from the figure of merit and because tin has larger ϵ'' (Fig. 3.1(a)). In addition, the optical losses decrease with longer wavelength and larger wire diameter. This is somewhat counter intuitive in that ϵ'' increases with wavelength (Fig. 3.1(a)), and one could naively expect losses to diminish with wire diameter, as the amount of metal is reduced. In order to clarify this

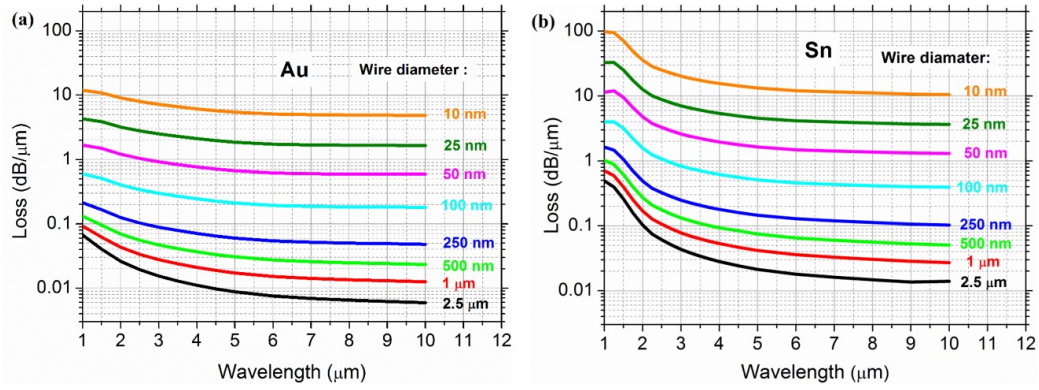

Figure 3.2: The 0^{th} order TM mode loss of single metal wire waveguides with different diameters, embedded in vacuum, as a function of wavelength. (a) gold, (b) tin.

behaviour, the field distribution in the metal is calculated. The fractional energy in the metal is defined as,

$$\eta = \frac{\iint\limits_{metal} W(\mathbf{r})\, dA}{\iint\limits_{All} W(\mathbf{r})\, dA}, \tag{3.5}$$

where W is the mode energy density given by [126, 127],

$$W(\mathbf{r}) = \frac{1}{2}\left(\frac{d(\epsilon(\mathbf{r})\omega)}{d\omega}|\mathbf{E}(\mathbf{r})|^2 + \mu_0|\mathbf{H}(\mathbf{r})|^2\right), \tag{3.6}$$

and μ_0 is the vacuum permeability, ϵ is the complex permittivity, and ω is the angular frequency.

Figure 3.3(a) illustrates how fractional energy in the wire varies with wire diameter for gold and tin wires embedded in vacuum, for a fixed wavelength of 3 μm. As seen in Fig. 3.3(a), smaller wire diameters lead to an extremely confined mode, which increases loss [126]. This behavior is consistent with Figs. 3.1(c) and 3.1(d). Note that the bulk permittivity of the metals were used for this calculation, which becomes increasingly inapplicable for very thin wires with diameters below tens of nanometers [128, 129]. Thus, these results should be treated as an approximation.

The fractional energy analysis cannot be used to explain the wavelength dependence of loss as it does not take into account the dispersion and group velocity. From perturbation theory [130], the difference in the imaginary part of the mode effective index for the TM mode of a single wire with and without the metallic loss can be expressed to first order as,

$$\Delta\kappa = \left(\frac{\epsilon_0}{\mu_0}\right)^{1/2} \frac{\int\limits_{metal} \epsilon_i|\mathbf{E}|^2\, dA}{\int\limits_{All} 2(|E_r H_\phi|)\, dA}, \tag{3.7}$$

where E_r and H_ϕ are the radial and azimuthal components of the electric and magnetic field, respectively.

Figure 3.3(b) shows the factor $\Delta\kappa/\lambda$, which is proportional to the loss per unit length, for 250 nm gold and tin wires in vacuum, as a function of wavelength. This is consistent with the loss calculated directly from the complex mode effective index in Fig. 3.1(c) and Fig. 3.1(d), showing again that loss decreases for longer wavelengths and that tin is lossier than gold.

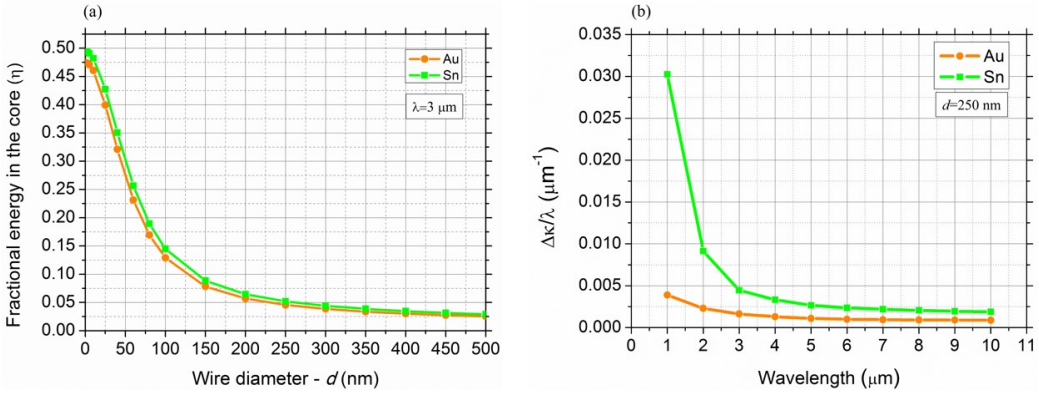

Figure 3.3: (a) Fractional energy in the metal for the lowest order TM mode in the single wire waveguide in vacuum, as a function of the wire diameter, for gold and tin, at $\lambda = 3\,\mu$m. (b) Difference in the imaginary part of the mode effective index for the TM mode of a single wire with and without the metallic loss, normalized by the wavelength.

The refractive index of the dielectric surrounding the metal also influences the modal energy distribution. For this reason, for a specific material combination, any loss analysis as a function of wavelength must include the dispersion of the complex dielectric index. However, for a fixed wavelength, it is interesting to understand how the loss behaves if only n_d varies, which simulates a change of the dielectric. Figure 3.4 illustrates the loss of the gold and tin wire with $d = 250\,$nm, at $\lambda = 3\,\mu$m, for n_d varying from 1 to 3. This range covers the refractive indices of SiO_2 (1.41925 [131]), soda-lime (1.4849 [132]), borosilicate (around 1.5), and some chalcogenide glasses (up to 3 [133]) commonly used for the wavelengths in the range of 1-10 μm. In order to simplify the analysis, the loss of the dielectric was omitted, as with appropriate choice of dielectrics the loss of the metal should dominate.

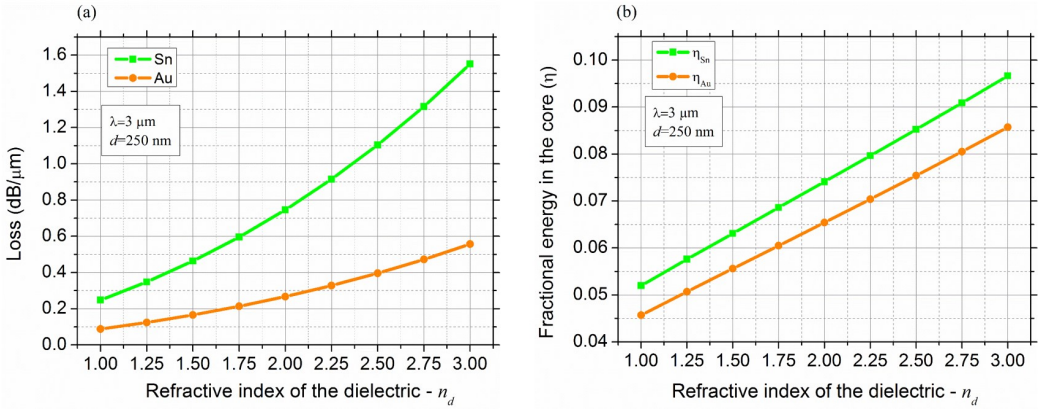

Figure 3.4: (a) Loss and (b) fractional energy in the metal core as a function of the refractive index of the dielectric for gold and tin wires ($d = 250\,\mathrm{nm}$), at $\lambda = 3\,\mu\mathrm{m}$.

As seen in Fig. 3.4, the loss and fractional energy in the metal increase for higher dielectric index n_d. Consequently, the selection of the dielectric must not only consider its transparency but also the real part of its refractive index. As the loss of the metal is usually much higher than that of the dielectric, the selection of an optically poorer dielectric could result in a lower modal loss if the real part of the dielectric index is lower, through reducing the fractional energy in the metal.

In the next section, the loss of the high-spatial frequency quasi-TEM mode for the full hexagonal wire array metamaterial media is discussed. Some material combinations for operational wavelengths in the NIR and MIR are proposed, and consider the effect of varying structure parameters such as wire diameter and wire spacing.

3.4 Indefinite wire array metamaterial media

The indefinite wire array metamaterial media constitutes a spatially dispersive hyperbolic medium for frequencies below the effective plasma frequency of the structure [20], and has three types of modes: TE, TM and quasi-TEM (a second TM mode) [93]. When this hyperbolic metamaterial is considered for super-resolution imaging, it is the propagation of high spatial frequency modes that is most important, as these contain the sub-wavelength information usually restricted to the near field. In the absence of spatial

dispersion, the extraordinary mode of hyperbolic media has the dispersion relation [20, 26, 27, 50],

$$\frac{k_{\parallel}^2}{\epsilon_{\perp}} - \frac{|k_{\perp}|^2}{|\epsilon_{\parallel}|} = \left(\frac{\omega}{c}\right)^2, \tag{3.8}$$

where $k_{\perp}$, $k_{\parallel}$, $\epsilon_{\perp}$ and $\epsilon_{\parallel}$, are the wave vector and permittivity components transverse and parallel to the wires, respectively, and c is the speed of light. The isofrequency surface generated by Eq. (3.8) is hyperbolic, and has no high spatial frequency cut-off, enabling subdiffraction imaging. However, because of spatial dispersion not one but two extraordinary modes exist (the TM and quasi-TEM), and isofrequency surfaces are best calculated numerically. Figure 3.5(a) shows isofrequency curves for the modes in a hexagonal wire array shown in Fig. 3.5(b), based on tin and soda-lime, with $d = 100\,\text{nm}$, wire spacing $\Lambda = 600\,\text{nm}$ and $\lambda = 3\,\mu\text{m}$, calculated using a commercial finite element solver (COMSOL). As it can be seen, the quasi-TEM mode (black dots) allows propagation of high transverse spatial frequencies with $(k_{\perp}/k_0 > n_{\text{d}})$, which can enable imaging beyond the diffraction limit. Figure 3.5(c) shows an example of a calculated quasi-TEM mode with high spatial frequency, where the white arrows represent the E field distribution in the xy plane and the color scale represents the normalized time averaged energy flow in the wire direction.

From homogenization theory [93], the TE mode (red dots) in this structure does not have a hyperbolic dispersion of the form of Eq. (3.8) because its polarization is transverse to the anisotropy axis, corresponding to an ordinary wave. As a result, the wire array behaves like a dielectric and the dispersion relation is given by [134],

$$k_{\perp}^2 + k_{\parallel}^2 = \epsilon_d \left(\frac{\omega}{c}\right)^2, \tag{3.9}$$

matching the numerical results in Fig. 3.5(a). The TE mode is evanescent for $(k_{\perp}/k_0 > n_{\text{d}})$, which corresponds to $k_{\perp}/k_0 > 1.4849$ in Fig. 3.5(a). The dispersion relation of the TM modes (blue dots), can be approximated from spatially dispersive homogenization models [134] as,

$$k_{\perp}^2 + k_{\parallel}^2 + k_p^2 = \epsilon_d \left(\frac{\omega}{c}\right)^2 \tag{3.10}$$

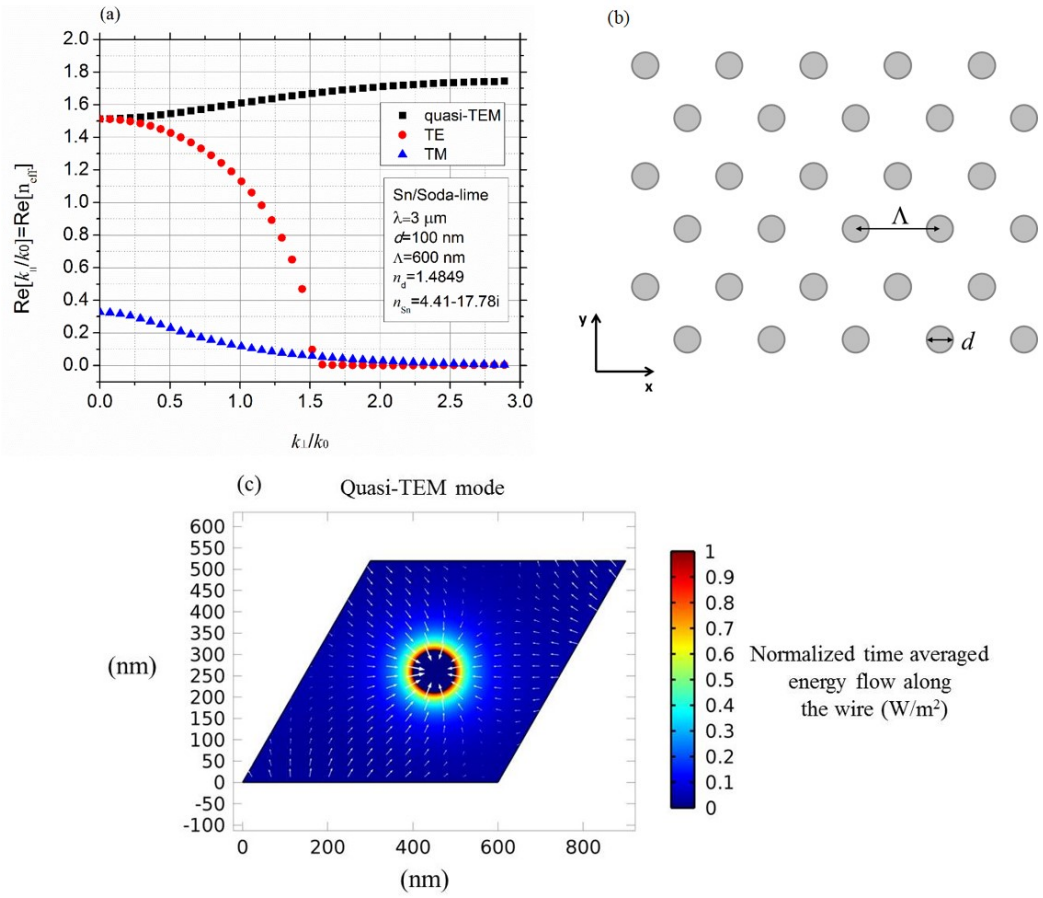

Figure 3.5: (a) Isofrequency curves of the modes in the wire array, tin/soda-lime system, $d = 100\,\text{nm}$, $\Lambda = 600\,\text{nm}$ and $\lambda = 3\,\mu\text{m}$. (b) Schematic of the hexagonal wire array. (c) Field distribution of the calculated quasi-TEM mode with high spatial frequency ($k_\perp = \frac{\pi}{\Lambda}\frac{2}{\sqrt{3}}$).

where k_p is the effective plasma frequency of the wire array [84,96]. According to Eq. (3.10), the TM mode is evanescent for all $k_\perp$ when $k_p^2 > \epsilon_\text{d}(\omega/c)^2$, a condition that is fulfilled in the structure of Fig. 3.5.

The wire array is more complex than the single wire waveguide as the propagation loss also depends on the distance between the wires Λ and the mode field distribution, in addition to the other parameters already discussed. In the following subsections, some possible material combinations for wire ar-

rays in the MIR and NIR are discussed and their loss for a range of structural parameters are analysed. Any effect relying on the hyperbolic nature of the material (e.g. density of states enhancement, subdiffraction imaging), will require low loss for high transverse spatial frequencies $k_\perp/k_0 > n_\mathrm{d}$. COMSOL was used to calculate the isofrequency curves, loss and modal fields of the wire array with a hexagonal lattice as in Fig. 3.5(b), using Bloch-Floquet boundary conditions, since the high-k modes are the Bloch modes of the metal-dielectric periodic structure. From the complex effective index (n_eff) of the simulated quasi-TEM mode, Eq. (3.3) is used to calculate the propagation loss. For each specific structure and material combination, two cases of the quasi-TEM mode were considered, $k_\perp = 0$ being the lowest transverse spatial frequency, corresponding to k oriented along the wires, and $k_\perp = \frac{\pi}{\Lambda}\frac{2}{\sqrt{3}} = k_{\perp max}$ which corresponds to the edge of the Brillouin zone for the hexagonal wire array in the Γ-M direction, and thus one of the highest transverse spatial frequency that can propagate. Consequently, $k_{\perp max}$ approximately corresponds to the highest resolution possible with the structure for a given Λ. The range of the geometric parameters (d and Λ) for each material combination varies with the operational wavelength and the refractive index of the dielectric host. The study was limited to structures capable of subdiffraction propagation and thus keep the distance between the wires below the diffraction limit ($\Lambda < \lambda/2n_\mathrm{d}$). The wire diameters are selected in order to achieve d/Λ between 0.1 and 0.9. The mesh size in the metal wire was set as $d/100$, while the mesh in the dielectric was set smaller than $\Lambda/50$.

3.4.1 Near infrared (1 μm), Gold/SiO_2

Gold wires in SiO_2 are considered as the case study for the NIR. Gold was shown above to be favorable, and SiO_2 is chosen for its high transmission at 1 μm and known compatibility with gold with both co-drawing techniques [135] and the pressure-assisted melt-filling method [136–138].

Figure 3.6 presents the loss in dB/μm of the quasi-TEM mode with lowest loss as a function of Λ, for $\lambda = 1\,\mu$m and different wire diameters. In Figs. 3.6(a) and 3.6(b), the modes have $k_\perp = 0$ and $k_{\perp max}$, respectively. The refractive indices used were 1.45042 [131] for SiO_2 and 0.25-6.66i [117] for gold, considering its bulk complex permittivity from Figs. 3.1(a) and 3.1(b). It is important to emphasize that this becomes increasingly inapplicable for very thin wires with diameters below tens of nanometers. According to the

literature, the loss of thin gold films is expected to increase or decrease as a function of thickness, depending on the type of film [128, 129]. Thus, further work will be required and these simulations at 1 μm wavelength must be treated as an approximation. The study is limited to structures with $\Lambda < 345$ nm, which corresponds to the diffraction limit ($\lambda/2n_{\mathrm{d}}$).

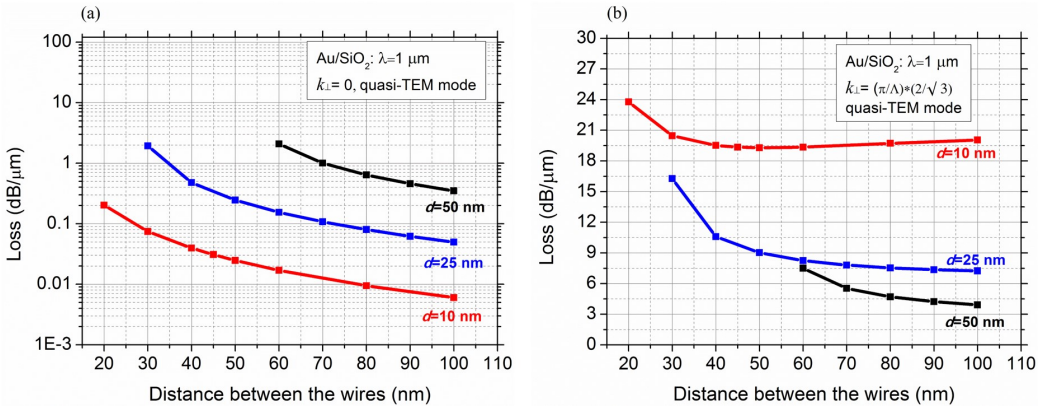

Figure 3.6: Quasi-TEM mode loss for the wire array (gold/SiO_2 system) as a function of d and Λ, at $\lambda = 1\,\mu$m, for (a) $k_\perp = 0$, and (b) $k_{\perp max}$ (corresponding to the edge of the Brillouin zone).

As shown in Fig. 3.6(a), the loss of the quasi-TEM mode decreases with increasing Λ for $k_\perp = 0$. This is expected since the metal fraction in the unit cell decreases for a fixed wire diameter. When the distance between the wires is constant, the loss increases for larger wire diameters, showing the opposite behaviour compared to the single wire case (Figs. 3.2(a) and 3.2(b)). This indicates that, for $k_\perp = 0$, the influence of the metal fraction on the loss is more significant than the influence of the mode confinement when d is changed.

On the other hand, the modes with $k_\perp = k_{\perp max}$ follow the behaviour of the single wire waveguide, presenting higher loss for smaller wire diameter. This indicates that, for $k_{\perp max}$, the variation on the mode confinement is more significant than the change in metal fraction when d increases. Indeed, for $k_\perp = 0$ the quasi-TEM modal fields are predominantly between wires, while for large $k_\perp$ fields localize more strongly at the wire interface. Figure 3.7(a) shows the profile of the normalized electric field across the small diagonal of the unit cell (red line of the inset) of the quasi-TEM modes with $k_\perp = 0$ and $k_{\perp max}$, for the cases with $d = 10$ nm (Figs. 3.7(b,c)) and $d = 25$ nm

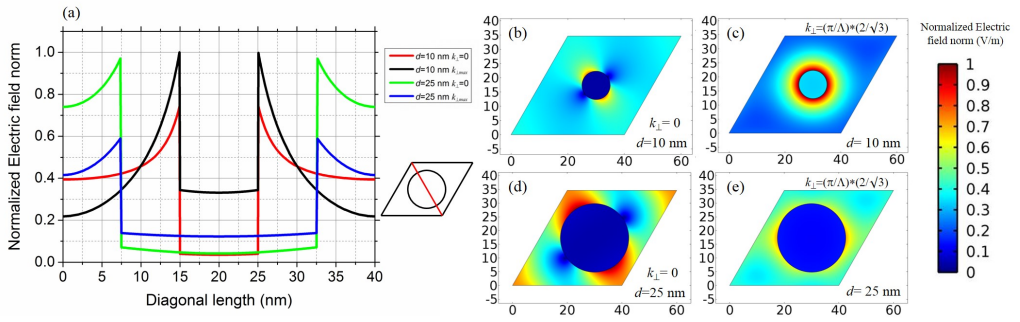

Figure 3.7: (a) Profile of the normalized electric field norm across the small diagonal of the unit cell (red line of the inset) from the four quasi-TEM modes shown in (b-e), gold/SiO_2 system, $\Lambda = 40$ nm, at $\lambda = 1\,\mu$m. Normalized electric field for the quasi-TEM modes with $k_\perp = 0$ and $k_{\perp max}$, $d = 10\,$nm (b,c) and $d = 25\,$nm (d,e), respectively.

(Figs. 3.7(d,e)), for $\Lambda = 40$ nm, gold/SiO_2 system, at $\lambda = 1\,\mu$m.

According to Figs. 3.7(a-e), the concentration of electric field in the metal wire for the modes with $k_{\perp max}$ is higher than their respective modes with $k_\perp = 0$, which explains the difference in the losses between Figs. 3.6(a,b). In addition, Fig. 3.7(a) also shows that, for $k_\perp = 0$, there is slightly more electric field in the metal for the case with $d = 25\,$nm than the one with $d = 10\,$nm. This explains the unusual behaviour presented in Fig. 3.6(a), where the loss increases for larger wire diameters. From the E and H field distributions and using Eqs. (3.5-3.6), the energy density inside the metal for the all the four cases presented in Figs. 3.7(b-d) are calculated. The fractional energies in the metal found were 0.004 (Fig. 3.7(b)), 0.242 (Fig. 3.7(c)), 0.0325 (Fig. 3.7(d)) and 0.229 (Fig. 3.7(e)), which are also in agreement with the losses presented in Fig. 3.6.

Importantly our results show that while the loss of the quasi-TEM mode with k oriented parallel to the wires ($k_\perp = 0$) can be low enough to propagate over hundreds of wavelengths, this is not the case for modes with $k_\perp > n_d k_0$, which are the modes most relevant to any subdiffraction physics such as hyperlenses and density of states enhancement.

For an imaging application, considering 20 dB as the maximum acceptable propagation loss, Fig. 3.6(b) shows that the maximum propagation length for the gold/SiO_2 system at $\lambda = 1\,\mu$m is around 1, 3 and 7 μm for wire diameters of 10, 25 and 50 nm, respectively. These maximum propagation

lengths of approximately 1, 3, and 7 wavelengths make straight metamaterial hyperlenses based on wire array unlikely to be of use at 1 μm wavelength.

3.4.2 Mid-infrared (3 μm), Systems: gold/SiO_2 and tin/soda-lime

For the MIR, the gold/SiO_2 system was considered again. In addition, tin was also considered due to its low melting point (232 °C), which makes possible the use of drawing methods using common soft glasses such as soda-lime (drawing temperature around 700 °C), and borosilicate (800 °C). Both have similar optical quality at 3 μm, with a transmission around 50 % for 1 mm thickness [139,140]. Soda-lime was selected for our simulations because of its lower drawing temperature and well known compatibility with tin [123–125].

Figure 3.8(a,b) present the loss for the gold/SiO_2 system at $\lambda = 3\,\mu$m, for the quasi-TEM modes with $k_\perp = 0$ and for $k_{\perp max}$. Similarly, Figs. 3.8(c,d) show the equivalent results for the tin/soda-lime system. The refractive indices used were 1.41925 [131] for SiO_2, 1.63-18.6i [117] for gold, 1.4849 [132] for soda-lime and 4.41-17.78i [5] for tin. The structure is limited to $\Lambda < 1\,\mu$m, which corresponds to the diffraction limit for $\lambda = 3\,\mu$m, given the indices of the glasses.

As shown in Figs. 3.8(a,b), the loss of the quasi-TEM modes at 3 μm for both $k_\perp = 0$ and $k_{\perp max}$, presents the same behaviour as the modes at 1 μm when wire diameter and separation are varied. Considering again 20 dB as the maximum acceptable loss, Fig. 3.8(b) shows that the maximum propagation lengths of the high $k_\perp$ mode for the gold/SiO_2 system at $\lambda = 3\,\mu$m are around 33 μm ($d = 100$ nm), 100 μm ($d = 250$ nm) and 110 μm ($d = 500$ nm), when the distance between the wires approaches the diffraction limit. These maximum propagation lengths of approximately 10, 30, and 33 wavelengths make the use of wire arrays much more compelling at 3 μm than at 1 μm wavelength. In this regime, depending on the combination of d and Λ, even distances between the wires around half of the diffraction limit have reasonable propagation lengths. For instance, for $\Lambda = 500$ nm and $d = 250$ nm, the 20 dB propagation length is around 50 μm.

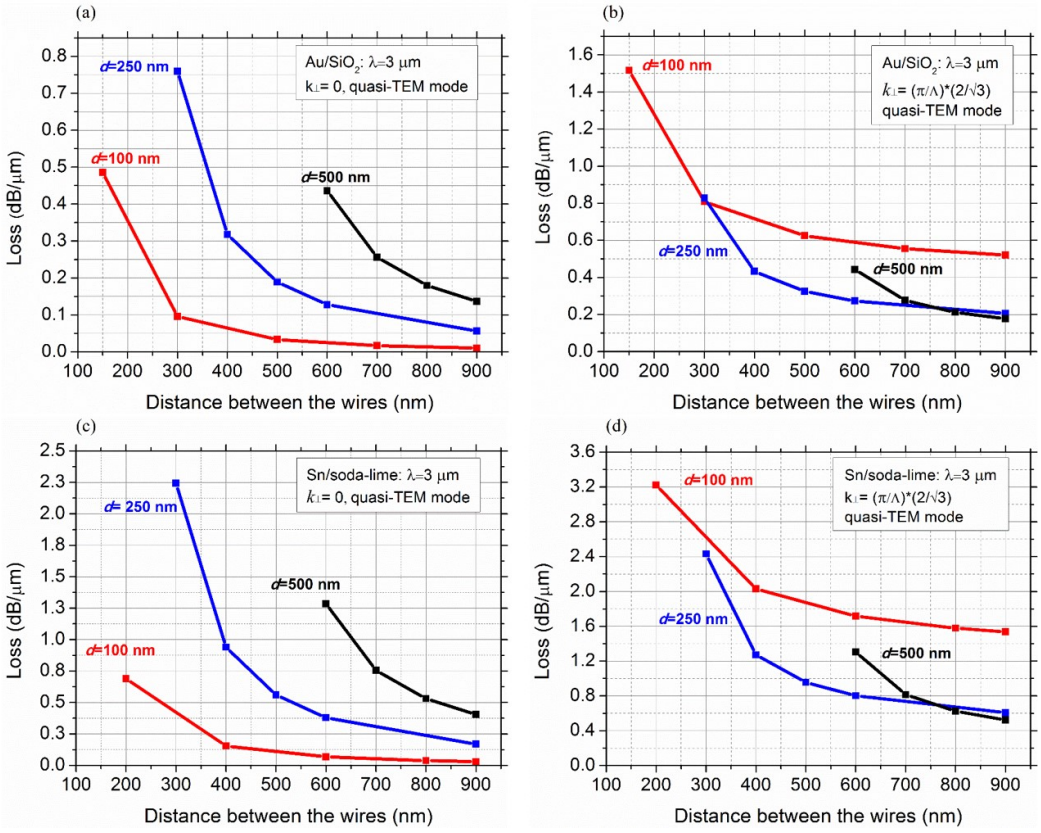

Figure 3.8: Quasi-TEM mode loss for wire arrays as functions of d and Λ, at $3\,\mu$m wavelength, for (a,c) $k_\perp = 0$ and (b,d) $k_{\perp max}$(corresponding to the edge of the Brillouin zone). (a,b) gold/SiO_2 and (c,d) tin/soda-lime.

Regarding the tin/soda-lime system, Fig. 3.8(d) shows that the maximum propagation length at $\lambda = 3\,\mu$m is around $13\,\mu$m ($d = 100\,$nm), $33\,\mu$m ($d = 250\,$nm), and $40\,\mu$m ($d = 500\,$nm). As expected from the single wire waveguide analysis, gold is optically better than tin. However, the propagation lengths of approximately 4, 11 and 13 wavelengths described above make this an interesting option for large wire diameters and wire separation.

3.4.3 Mid-infrared (10 μm): Gold and tin embedded in a glass with n_d=2.8

At the operational wavelength of 10 μm, the loss of the dielectric also needs to be taken into account in the selection of the materials. Because of their low transparency, silica-based glasses must be excluded. Chalcogenide glasses such as IRG 22 (Schott, $Ge_{33}As_{12}Se_{55}$) [141], GLS (Gallium Lanthanum Sulphide) [105], As_2Se_3 and As_2S_3 are better choices because they have a transmission higher than 50 % at $\lambda = 10\,\mu$m, for 2 mm samples. Therefore, a material with $n_\mathrm{d} = 2.8$ is considered as the dielectric, which is representative of the above examples. The low minimum drawing temperature of the chalcogenide glasses, between 300 to 700 °C, makes the co-drawing of these glasses with high melting point metals such as gold, copper and silver impossible. This limitation emerges from the fabrication requirement that the minimum drawing temperature of the dielectric must be higher than the melting point of the metal. According to our figure of merit (Fig. 3.1(c)), apart from these high melting point metals, the best options at $\lambda = 10\,\mu$m are tin and indium. Because their optical quality is very similar, tin was selected due its low oxidation and low cost. Even though it is impossible to co-draw chalcogenide glasses with molten gold, this metal was nevertheless considered as an ideal scenario for comparison.

Figures 3.9(a,b) present the loss for tin wires at $\lambda = 10\,\mu$m, for the quasi-TEM modes with $k_\perp = 0$ and for $k_{\perp max}$, respectively. Figures 3.9(c,d) show the equivalent results for gold wires. The indices used were 22-46.41i [5] for tin and 12.36-55.04i [117] for gold. The structure is limited to $\Lambda < 1.785\,\mu$m, which corresponds to the diffraction limit for $\lambda = 10\,\mu$m in a dielectric with $n_\mathrm{d} = 2.8$.

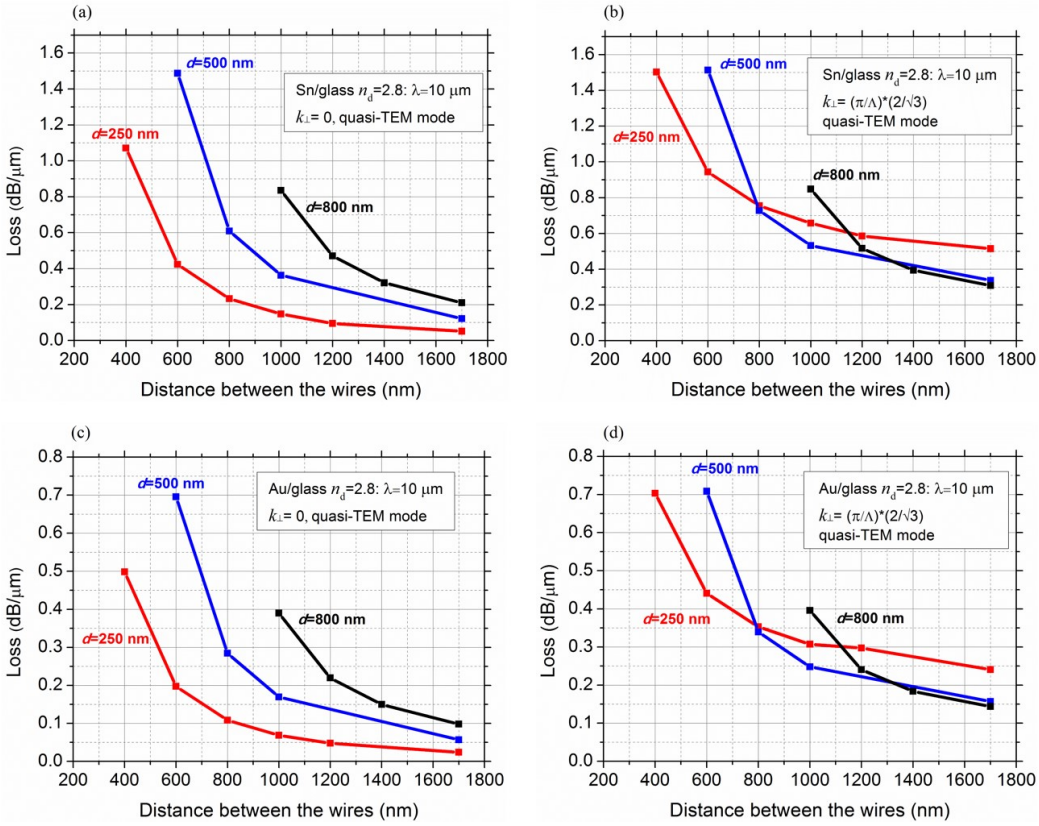

Figure 3.9: Quasi-TEM mode loss for wire array as functions of d and Λ, at 10 μm wavelength, for (a,c) $k_\perp = 0$ and (b,d) $k_{\perp max}$ (corresponding to the edge of the Brillouin zone). (a,b) tin and (c,d) gold embedded in a glass with $n_\mathrm{d} = 2.8$.

Considering again 20 dB as the maximum acceptable loss of the high $k_\perp$ modes, Fig. 3.9(b) shows that the maximum propagation lengths for the tin/glass with $n_\mathrm{d} = 2.8$ system at $\lambda = 10\,\mu$m are around 38 μm ($d = 250$ nm), 60 μm ($d = 500$ nm), and 65 μm ($d = 800$ nm). These propagation lengths of approximately 3.8, 6 and 6.5 wavelengths are not as encouraging as the propagation lengths at $\lambda = 3\,\mu$m. Regarding the gold wires, Fig. 3.9(d) shows that the maximum propagation lengths are around 83 μm (8 wavelengths, $d = 100$ nm), 127 μm (12 wavelengths, $d = 250$ nm), and 140 μm (14 wavelengths, $d = 500$ nm). As expected by the single wire waveguide analysis, gold is optically better than tin for the wire array at $\lambda = 10\,\mu$m, presenting a factor of 2 improvement on the loss. Although the metals have lower loss at this wavelength compared to 3 μm, the higher index of the dielectric re-

sults in an overall increase in the loss due to higher mode confinement in the metal.

3.4.4 Loss as a function of n_{d}

The refractive index of the dielectric (n_{d}) influences the mode energy distribution in the wire array and, consequently, also affects the mode loss. Therefore, the best dielectric in terms of the metamaterial optical performance is not necessarily the one with the lowest extinction coefficient (i.e. the highest transparency). Figure 3.10 illustrates the loss of the quasi-TEM modes ($k_{\perp} = 0$ and $k_{\perp max}$ as functions of n_{d} at $\lambda = 3\,\mu$m, for a fixed structure with tin wires ($d = 250\,$nm, $\Lambda = 500\,$nm). The refractive index of the dielectric is varied from 1 to 3, covering SiO_2(1.41925 [131]), soda-lime (1.4849 [132]), borosilicate (around 1.5), and some chalcogenide glasses (up to 3 [133]).

Figure 3.10 shows the loss increasing for larger n_{d} for both modes. This behavior is in agreement with the single wire waveguide (Figs. 3.4(a,b)) and indicates that larger n_{d} increases the mode confinement in the metal. As a result, if the transparency of the glass candidates is equivalent, the best option is the dielectric with the lower refractive index. Since lower refractive

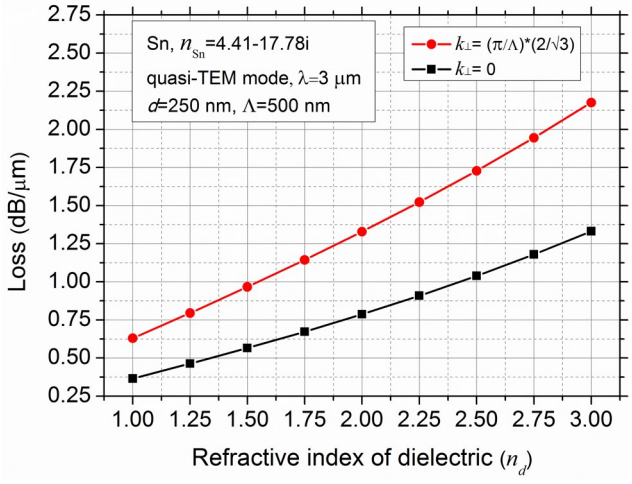

Figure 3.10: Quasi-TEM mode loss for a wire array with tin wires as a function of the refractive index of the dielectric n_{d}, $d = 250\,$nm and $\lambda = 500\,$nm, at $3\,\mu$m wavelength, for $k_{\perp} = 0$ (black curve) and for $k_{\perp max}$ (red curve), corresponding to the edge of the Brillouin zone.

indices lead to lower losses, it is tempting to artificially reduce the effective refractive index of the glass e.g. by adding holes between wires. Simulations to that effect (adding a hole between wires in the unit cell) show this only reduces loss by $\sim$1 %, because electric fields are weakest at the half-way point between wires, where it would be practical to add holes in the structure. Further simulations showed that reducing the amount of metal by replacing wires by metallic coated holes do not reduce loss at all, but rather lead to an increase in losses when the metal thickness is below the skin depth - which can be understood in terms of the effective resistance increases when reducing the metal cross section.

3.5 Conclusion, assessment of the systems and feasible applications

Promising metal/glass combinations were investigated considering optical quality and drawing feasibility for the fabrication of wire array metamaterial media for the MIR and NIR. The figure of merit based on the 0^{th} order TM mode loss of a single metal wire waveguide provides a qualitative comparison between the optical quality of the metals. The single wire analysis shows that loss decreases for longer wavelengths, larger wire diameter and smaller refractive index of the surrounding dielectric due to the variations in the mode confinement. Simulations of the full wire arrays show that the loss for the quasi-TEM mode varies greatly with transverse spatial frequency. While it is the high spatial frequency modes that give hyperbolic media their most interesting properties, the propagation loss of the highest spatial frequency (at the Brillouin zone edge) can be orders of magnitude higher than for propagation parallel to the wires. At $\lambda = 1\,\mu$m the loss of high spatial frequency modes are high for all material combinations considered. With 20 dB-propagation lengths of a few microns at most among all configurations simulated, wire media are unlikely to yield many applications in the NIR.

The situation is considerably better at longer wavelengths. At $\lambda = 3\,\mu$m, gold is optically the best option yielding 20 dB-propagation lengths for high spatial frequency modes up to 110 μm, depending on the wire diameter and the distance between the wires. Reasonable losses are still achieved for distances between the wires smaller than half of the diffraction limit, so that subdiffraction limited wire-array based hyperlenses are in principle feasible

at this wavelength. Tin is optically poorer but still usable for large wire diameters and distance between the wires, with maximum 20 dB-propagation lengths up to 40 μm in this limit.

For an optical wavelength of 10 μm, losses are relatively higher, even for gold wire arrays, because of the increased refractive index of suitable host dielectrics. At this wavelength, tin wire arrays with relatively large wire diameters and distance between the wires marginally below the diffraction limit could also prove useful, with maximum propagation lengths up to 65 μm.

In all cases, the loss of the high spatial frequency modes diminishes rapidly for a structure with fixed d/Λ and increasing wire-to-wire spacing. Therefore, magnifying hyperlenses based on tapered wire arrays will suffer much lower losses than those calculated here - as long as the taper angle is steep from the outset. Note that the hyperlenses' resolution is inversely proportional to the wire-to-wire spacing. Thus, the increase of the wire-to-wire spacing to compensate the losses is not desirable. Such configurations require further study and will be presented in Chapter 5. Our study shows the practical spectral limits of wire array metamaterial media, considering the properties of feasible material combinations, and assuming the need to propagate distances of multiple wavelengths. We conclude there is little possibility for operational wavelengths of 1 μm or shorter for applications relying on transmission of high spatial frequencies, but have identified material combinations that will permit operation in the near infrared to wavelengths as short as 3 μm.

Based on the loss analyses presented in the conclusion of the last section, the system tin/soda-lime was selected for our wire array metamaterial fibres for applications in the mid-infrared (3 μm). The intended structure for the final metamaterial is composed of 500 tin wires with diameter and spacing of 250 and 500 nm, respectively. According to our simulations, the quasi-TEM mode with high spatial frequency will have an optical loss around 1 dB/μm at $\lambda = 3\,\mu$m in such a structure, which is acceptable for our applications involving lifetime engineering (discussed in Appendix A) and subdiffraction imaging (Chapter 5).

Chapter 4

Fabrication of mid-infrared wire array metamaterial fibres

The required sub-wavelength metallic structure in hyperbolic metamaterials presents a huge challenge in the fabrication of such metamaterial fibres since the co-drawing of metal and glasses is not trivial due to their different rheological properties. Uniform metallic structures along the length of the fibre are only achievable for certain dimensions and if the drawing is performed under favourable conditions.

In the present Chapter, the challenges and extra material constraints of multimaterial fibre drawing are discussed, and a literature review of the co-drawing of metal and glasses is presented. Special attention is given to the Plateau-Rayleigh instability and how it can be minimized in the drawing of soft-glass based metamaterial fibres.

The soft-glass fibre tower used to fabricate these new mid-infrared metamaterial fibres is presented and characterized. Our developed/adapted fabrication process is fully described, step-by-step, from the metamaterial preform fabrication to the final wire array metamaterial fibre. The influence of the fabrication parameters on the quality of the structure is assessed and optimized. The final result of the work presented in this Chapter is a tin/soda lime wire array metamaterial fibre with a remarkably uniform metallic structure on the scale of a few hundred nm. This represents an operational wire array metamaterial in the mid-infrared.

4.1 Multimaterial Fibre Drawing

The obvious advantage of using fibre drawing for the fabrication of metamaterials is mass production and the remarkable flexibility in the scaling down of the desired microstructure, for example, of a metallic wire array. A conventional preform can generate kilometers of fibre, and the drawing process allows the reduction of the preform's structure over a range of several orders of magnitude. However, this type of multimaterial drawing is more complex than the traditional single dielectric and structured fibre drawing, commonly employed for the production of conventional step index silica fibres [142], PCFs [109] and microstructured polymer optical fibres (mPOFs) [111].

In conventional single material drawing, the viscosity of the selected dielectric at the drawing temperature dictates the fabrication parameters such as the drawing speed, feed speed and pulling tension. Practically, the dynamic viscosity of the dielectric lies between 10^7 to 10^3 dPa.s [143, 144]. On the other hand, the drawing of multimaterials fibres presents additional constraints due to the different mechanical, chemical and rheological properties of the selected material [145, 146].

In the multimaterial drawing, at least one amorphous material (glass or polymer) should be used as external cladding to contain the other inner material (metal, semiconductor, or glass) and maintain the cross-sectional structure of the fibre. The inner material must have a lower or similar viscosity in comparison to the cladding material at the drawing temperature. In this regime, the high viscosity of the cladding material avoids deformations in the fibre structure during the scaling down process, if the fabrication parameters are carefully selected.

Figure 4.1 shows the viscosity as a function of temperature for a variety of metals/semiconductors (a) and amorphous materials (b), extracted from Ref. [146].

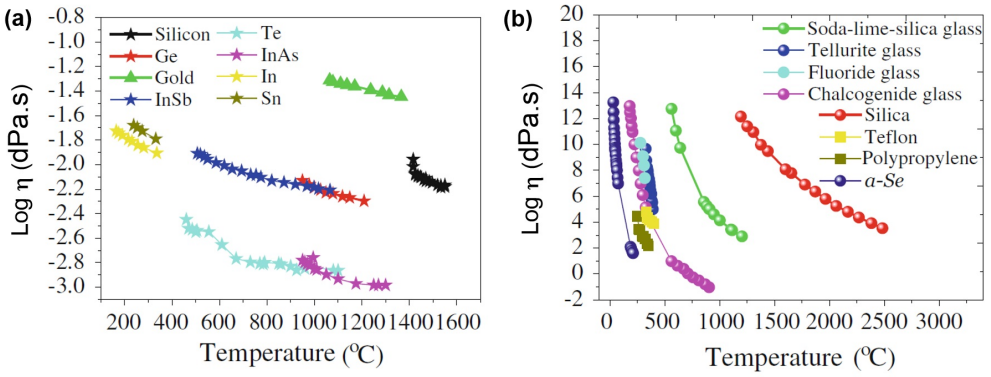

Figure 4.1: Logarithm of the dynamic viscosity η as a function of the temperature for several metals/semiconductures (a) and amorphous materials (b). Both graphics were extracted from Ref. [146].

According to Fig. 4.1, tin and soda-lime glass have compatible dynamic viscosities for the co-drawing process (η of the inner material $<$ η of the cladding material). Tin has a dynamic viscosity around $10^{-1.7}$ dPa.s above its melting point temperature of 232 °C (Fig. 4.1(a)), which is smaller than the dynamic viscosity of the soda-lime glass in the conventional fibre drawing region (10^7 to 10^3 dPa.s) [143, 144], corresponding to temperatures between 750°C and 1250 °C (Fig. 4.1(b)).

The selected materials must also not react during the drawing process, which can lead to oxide formation and the change in the glass composition. Such new oxide can be extremely detrimental for the drawing process and the quality of the metallic structure. Care must also be taken with the matching of the thermal expansion of the materials, which could result in fractures or gaps in the multimaterial structure. Ideally, a similar thermal expansion is preferable, but a mismatch is also acceptable in some systems and under special drawing conditions. In addition, the drawing parameters must be optimized to avoid Plateau-Rayleigh instability, particularly when the surface tension (high curvatures presented in smaller structures) between the two material are high. This constraint is discussed more deeply in Section 4.1.2.

Despite the challenges involved, a considerable amount of metal/glass co-drawing has been reported in the literature for several different applications. A literature review of this type of multimaterial drawing is presented below.

4.1.1 Taylor wire process: Fabrication of single glass-encapsulated metallic wires

The co-drawing of metal and glass was firstly reported by Taylor in 1924 [112] and employed to produce single metallic filaments with a diameter as small as 200 nm, embedded in glass fibres as small as 1 μm. The resultant glass-encapsulated metallic wire, also called Taylor wire, could be removed by acid etching (using HF) and used for a range of different applications such as resistance thermometers [147], thermocouples [148, 149], and bolometers [150]. Conventional metal wire drawing through a die [151], without using the glass jacket as in the Taylor process, is quite expensive for producing metallic filament smaller than 100 μm since requires repeated drawings and annealing stages [152].

In Taylor's original fibre drawing method, a piece of the selected metal to be drawn is placed in the bottom of a glass tube previously closed at one end. The closed bottom and the metal are heated with a flame until the glass softens and the metal melts. The soften glass is squeezed with pliers, causing the molten metal to flow up the tube, separating itself from the oxidation residue formed in the initial melting. The bottom of the tube containing the oxidation layer is discarded and the process repeated, until an inner metal column without any evidence of oxidation is obtained.

The resultant preform is drawn to fibre using a heated copper cylinder. This rudimentary furnace, described in Fig. 4.2(a), is composed of a steel rod attached to a copper rod containing a row of holes. The copper cylinder is heated by a flame and the fibre is drawn in one of the available holes with the use of a feeding and pulling system.

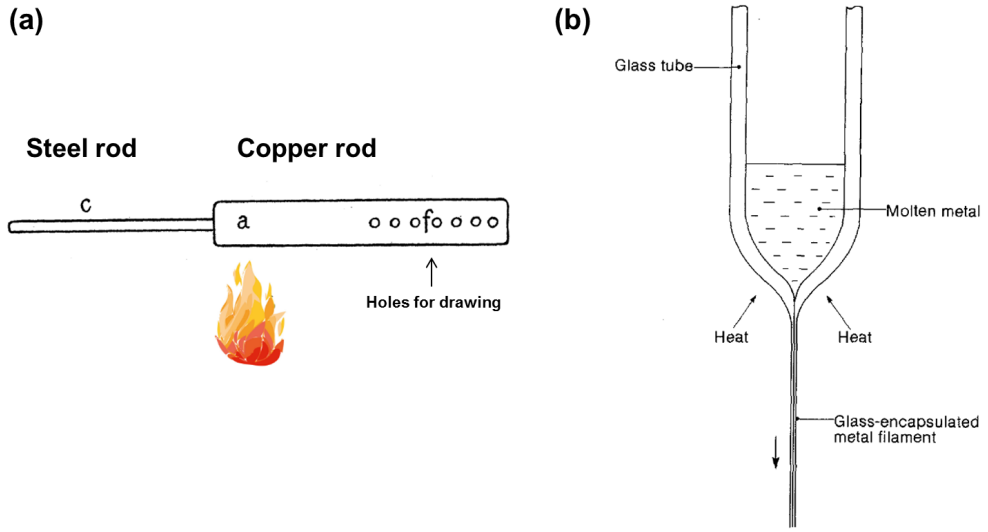

Figure 4.2: (a) Schematic of the rudimentary furnace used by Taylor in the first glass/metal drawing reported in 1924, extracted and adapted from Ref. [112]. (b) Schematic illustration of the Taylor wire technique, extract from Ref. [152].

This method was successfully used to produce metallic filaments with high tensile strength of Pb, Sb, Bi, Au, Ag, Cu, Fe, Sn, Tl, Cd, Co, Ga and In with a variety of glasses [112]. Since Taylor had no means of directly measuring the diameter of the small wires (this was in 1924!), he calculated their respective sizes by measuring the resistance of a known length and assuming that the filament had the same resistivity as the bulk metal. The smallest achieved wire was a Sb filament with 200 nm of diameter, and Taylor stated that *"No limit has been found to the smallness of filaments which can be produced"* [112].

During the next decades after Taylor's seminal work and patent [153], a considerable amount of research was dedicated to the improvement of his method, to produce longer wires and to characterize them, with no apparent effort to produce filaments smaller than 200 nm. A detailed review about the development of this co-drawing method can be found in Ref. [152].

Twenty five years ago, Ayers *et al.* reported a new method for producing submicron metallic fillaments by re-drawing a Taylor wire with an extra thick-walled glass capillary [154], as shown in Fig. 4.3(a). In theory, the original metallic wire would experience the same diameter reduction of the extra glass capillary. However, it was stated that the metallic wire breaks into spheres

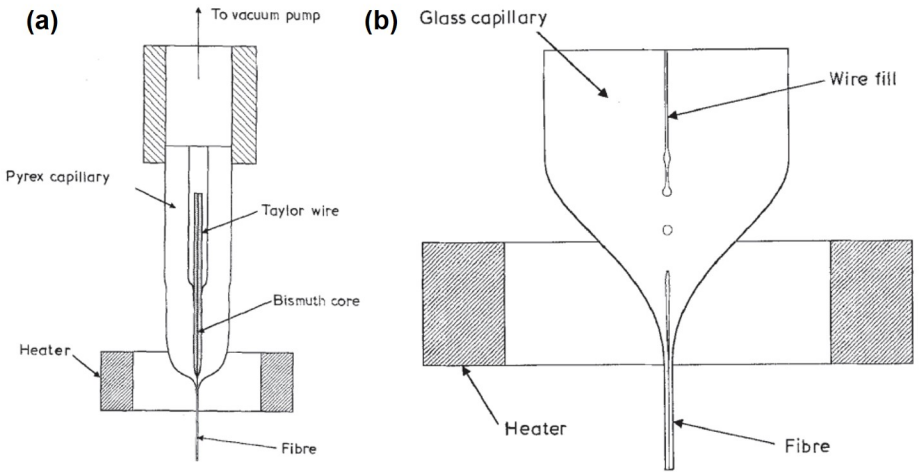

Figure 4.3: (a) Schematic of the re-drawing of a Taylor wire with an extra jacket by Ayres [154]. (b) Schematic of the breaking of the wire into droplets due to surface tension. Both figures were extracted from Ref. [154].

below a certain dimension due to the high surface energy of the liquid metal column, as described in Fig. 4.3(b), a phenomenon called Plateau-Rayleigh instability [113].

4.1.2 Plateau-Rayleigh Instability

Ideally, during the drawing of a preform formed by a metallic structure embedded in a dielectric matrix (amouphous material), the metal is liquid and the dielectric has a dynamic viscosity within the drawable range. In this scenario, the multimaterial preform is a complex fluid dynamic system under competing forces [155].

The surface tension, which tend to minimize the surface area of the inner material, competes with inertial and viscous forces, which tends to mantain the cylindrical shape of the system [156]. If this interfacial surface tension between the materials dominates, it causes any small fluctuations on the liquid metal column to grow over time, a phenomenon known as Plateau-Rayleigh instability [156, 157], and represented in Fig. 4.4(a) (extracted from Ref. [158]). Such perturbations growing exponentially with time can greatly deform the structure and eventually break the inner liquid material into droplets, as seen in Fig. 4.4(b) (extracted from Ref. [156]).

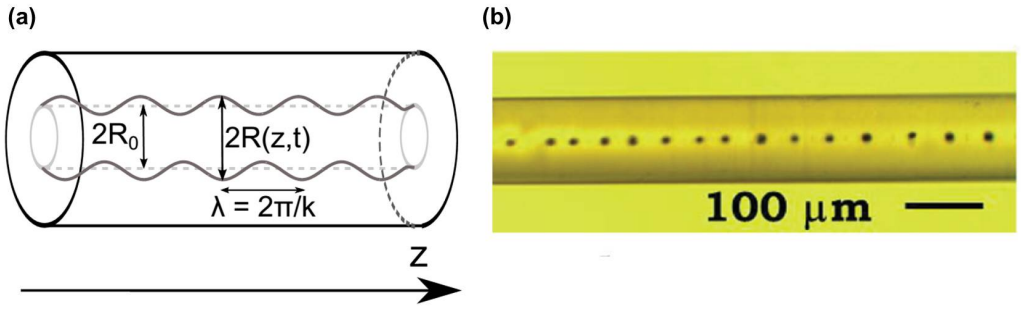

Figure 4.4: (a) Schematic of pertubations in a viscous cylinder generated by Plateau-Rayleigh instability, from Ref. [158]. (b) Example of core breakup in a multimaterial fibre due to the Plateau-Rayleigh instability, from Ref. [156].

According to Tomotika's formalism [113, 157], the periodic perturbation in diameter for an incompressible fluid cylinder surrounded by an unbounded viscous fluid will grow over time and along length as,

$$R(z,t) = R_0 + A_0 e^{gt} cos(kz), \tag{4.1}$$

where R_0 is the initial cylinder's radius, z is the position along the column's length, A_0 is the initial amplitude, and k is the spatial frequency of the perturbation. The growth of the perturbation is dictated by the gain term g, defined by [84, 113, 157],

$$g = \frac{\sigma}{2R\mu}(1 - x^2)\Phi(x, \mu'/\mu), \tag{4.2}$$

where σ is the interfacial surface tension between the inner fluid cylinder and the unbound surrounding viscous fluid (Fig. 4.4(a)), R is the radius of the perturbed inner cylinder, $x = kR$, μ is the viscosity of the unbound surrounding viscous fluid, μ' is the viscosity of the inner fluid cylinder, and Φ is a complex function composed of Bessel functions and can be found in Ref. [113]. This theory assumes an unbounded surrounding viscous fluid, therefore will only be accurate if the outside diameter of the surrounding fluid is considerably larger than the outer diameter of the inner fluid cylinder.

For liquid indium in PMMA, $\mu'/\mu \sim 10^{-8}$ [159, 160]. According to Ref. [84], in such regime no particular frequency dominates, and the term $(1 - x^2)\Phi(x, \mu'/\mu) \approx 1$ when the term x is small ($R << \lambda$ and k close to 0), which

means that perturbations with long wavelength all possess similar gain. In other words, Eq. (4.2) can then be simplified to

$$g \approx \frac{\sigma}{2R\mu}. \tag{4.3}$$

In the multimaterial drawing context, Eq. (4.3) states that the instabilities grow more rapidly for smaller wires, for a smaller viscosity of the external dielectric, and for larger surface tension between the materials. The surface tension can only be minimized with the selection of favourable materials, or potentially by nanostructuring of the surface - but this would be likely destroyed once materials are molten or softened. On the other hand, the viscosity of the external dielectric can be maximized if the drawing is performed at the lowest possible drawing temperature, which is limited by the tensile strength of the dielectric.

Figure 4.5(a) illustrates how the Plateau-Rayleigh instability generates breaks in the core of a multimaterial fibre (glass core/polymer cladding) for different drawing temperatures, which considerably changes the viscosity of the polymer cladding, as seen in Fig. 4.5(b) (from Ref. [156]). As expected from Eq. (4.3), drawings performed at higher temperature and, consequently, lower viscosity of the dielectric cladding (μ_g), leads to stronger fluctuations and breaks in the fibre's core.

According to Eq. (4.1), another alternative to minimise the instability is to reduce the dwelling time that the fibre is above the softening temperature of the external dielectric. This can be achieved by increasing the drawing speed and cooling (quenching) the fibre as close as possible to the neck-down region. In such a scenario, the instabilities do not have enough time to grow considerably.

Such approaches have been used in the fabrication of uniform Taylor wires with no gaps [112, 152]. However, it is a complex process, depending on the materials employed, the position of quenching, a high pulling velocity, and the cooling rate achieved. According to Ref. [152], successful quenching was employed in the Taylor wire process using cooling rate as high as 10^5 K/s.

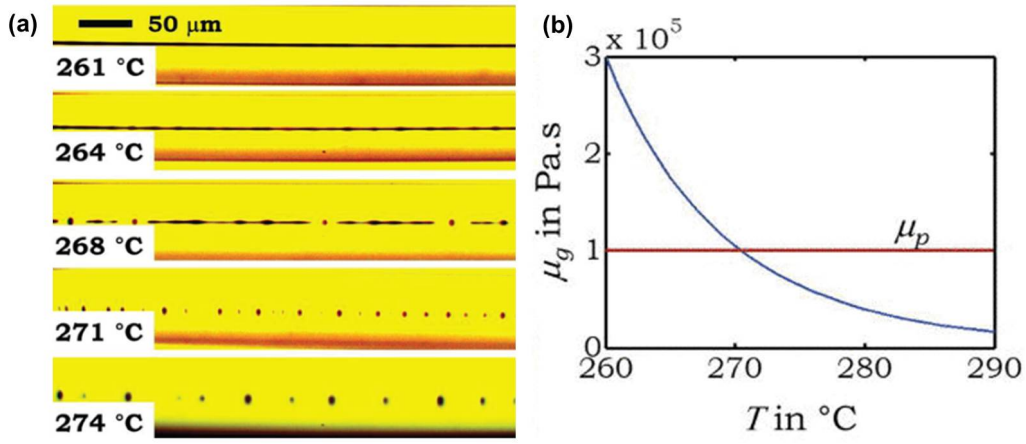

Figure 4.5: (a) Optical micrographs side view of multimaterial fibres (glass core/polymer cladding) fabricated by tapering at different temperatures, showing different stages of the core breakup due to the Plateau-Rayleigh instability. (b) Glass viscosity of the inner glass (μ_g) and polymer cladding (μ_p) as a function of the temperature. Both figures were extracted from Ref. [156].

4.1.3 Co-drawing of metallic wires in microstructured optical fibres

Over the last two decades, the invention of photonic and microstructured fibres made possible the fabrication of fibres with air hole channels at the nanometric scale [101, 102]. A considerable amount of work has been done in the incorporation of metallic wires in such structures, after or before the drawing of the fibre, for the development of PCF-based plasmonic structures with a variety of attractive applications [161].

The fabrication of silica PCFs contaning metal electrodes by co-drawing was firstly reported by Hou in [122]. The Taylor wire process was used to produce six silica-coated copper rods, which were stacked in a preform with 114 hollow capillaries and a single solid rod. Figure 4.6(a) shows a SEM micrograph of the fabricated PCF with one ring of copper rods with diameter around 4.2 μm. Figure 4.6(b) shows a SEM micrograph after the polishing of the fibre, where the copper wires are clearly distinguishable (bright dots). An electrical conduction experiment confirmed the continuity of the copper wires for a 50 cm sample. The authors also stated that further attempt to fabricate the same structure with copper wires smaller than 2 μm was not

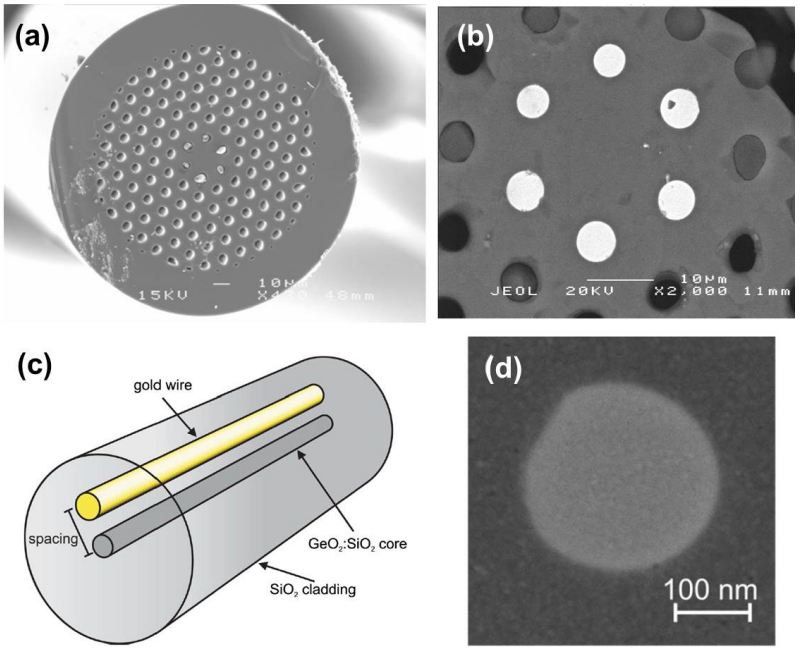

Figure 4.6: (a) SEM cross section picture of a PCF fibre with a ring of holes filled with copper, fabricated by drawing. (b) SEM picture showing the six copper wires with diameter around 4.2 μm, both extracted from reference [122]. (c) Schematic of the gold-filled cane used as an alternative to the stacking of Taylor wires approach. (d) Smallest gold single wire fabricated by direct drawing of the gold filled cane, diameter of 260 nm, both extracted from reference [135].

successful due to instabilities on the structure.

Further improvement on the fabrication of microstructured fibres with metallic inclusion by drawing was reported by Tyagi *et al.* in [135]. Instead of a Taylor wire, the authors fabricated a cane with an empty hole (diameter around 90 μm), which was filled with molten gold by applying vacuum at one end (Fig. 4.6(c)). In the final stage, the gold-filled cane was inserted in a silica tube and drawn to fibre. Single gold wires were produced with diameters as small as 260 nm, as seen in Fig. 4.6(d). However, at such dimensions, the gold wires are continuous only over lengths around 20 μm, separated by micro-sized gaps formed during the drawing. Samples with continuous wire longer than 5 cm were found only with wire diameter bigger than 1 μm.

Alternative methods to achieve metallic wires in microstructured fibres

In view of the difficulties in the drawing of sub-micron metallic wires in glass fibres due to fluid instabilities, other post-drawing metal filling approaches have been exploited and reported [136–138, 162]. These techniques are worth mentioning because, besides their limitations, they could offer an alternative fabrication route for material combinations that are not compatible in the drawing technique.

One option is the pressure-assisted technique with a pressure cell, where the air channels of the PCF/microstructure fibres are filled by pumping molten metal at high temperate and high pressure [136, 162]. Figure 4.7(a) shows an example of silica PCF filled with Au (diameters of 1.52μm, over 40 mm length) using a pressure cell at 1100 °C and pressure of 60 bars, extracted from [136]. The original PCF structure drawn has been well preserved because the melting temperature of Au (1064 °C) is well below the softening temperature of silica.

The second option is an adaptation of the previous process, called the spliced-fibre pressure-filling technique [137], described step-by-step in Fig.4.7 (b). Such an approach is more flexible, safe, reduces the amount of metal required, and can be employed for selective channel filling of the structure. Figure 4.7(c) contains an example of the selected filling of two 1 μm holes with gold, after applying a pressure of 50 bars, reported in [137].

These metal-filling options produce wires with high optical quality, but the required high pressure limits their length to a few cm. Depending on the size of the holes, the required pressure could be as high as 300 bar. Figure 4.7(b) shows the smallest gold wire fabricated with the splice-filling technique, with a diameter of 120 nm (filling length of 3 cm), obtained with a pressure of 300 bar over 20 min.

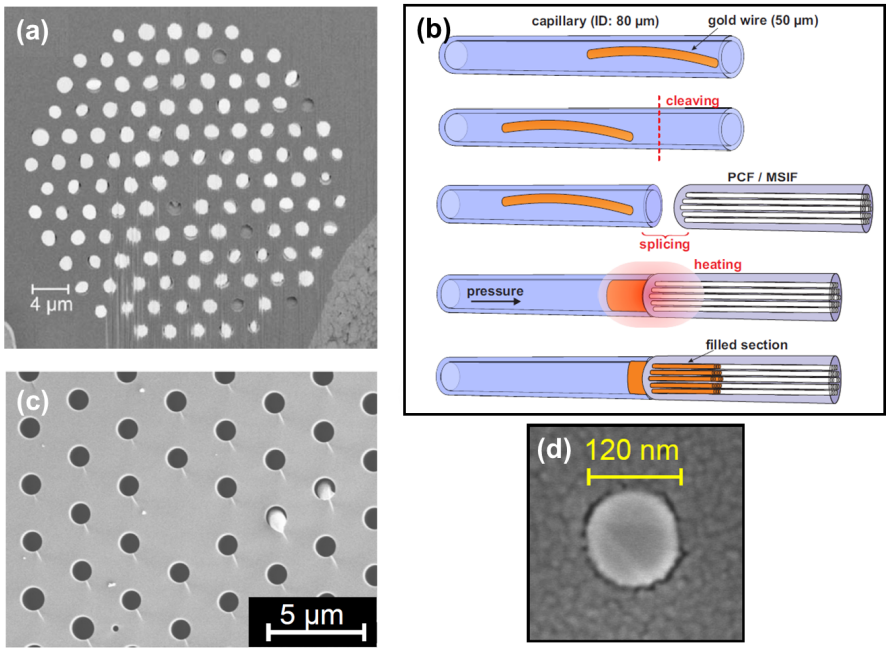

Figure 4.7: (a) PCF filled with gold by the pressure-assisted technique, hole diameter of 1.52 μm, hole spacing of 2.9 μm, typically filled length around 40 mm, extracted from [136]. From reference [137]: (b) Schematic of the spliced-fibre pressure-filling technique. (c) SEM micrograph of a PCF after the selective filling of two 1 μm holes with gold nanowire (pressure applied $\approx$ 50 bars). (d) SEM micrograph of the smallest gold wire obtained so far with the splice-filling technique, diameter of 120 nm, (filling length of 3 cm using 300 bar over 20 min).

4.1.4 Fibre drawing for the production metallic micro and nanowires

The mass production of ordered metalic/semiconductor micro and nano wires have been reported in the literature by drawing [114,115,163], for application related to microelectronics and chemical/biological sensing.

Zhang reported in [115] the drawing of copper/phosphorus alloy wires embedded in borosilicate glass (Pyrex) by repeating the draw-cut-stack process of a Taylor wire several times (Fig. 4.8(a)). Figure 4.8(b)) shows a SEM micrograph of a 500 nm CuP(92.75/7.25%) nanowire obtained after three consecutive drawings and the etching of the glass. It is worth noticing that the author reported some problems in the drawing related with the migra-

tion of phosphorus to the glass due to its high vapor pressure, leading to a change in the mechanical and thermo-physical properties of the set during the drawing.

Badinter *et al.* have fabricated a densely packed bundles of bismuth and lead/tin alloy nanowires embedded in borosilicate glass [114]. Firstly, Taylor wires were drawn, stacked in a large jacket tube, and the set was drawn again to a single bundle, as seen in Fig. 4.8(c). Several bundles were stacked again in a second jacket tube and stretched several times down to fibre (Fig. 4.8(d)). The authors have claimed the fabrication of bismuth and lead/tin nanowires with diameters as small as 50 nm over a 1 m length.

It is important to note that the former reported wire array structures with metallic nanowires were not employed, and are not ideal, for metamaterial applications. According to our simulations of Chapter 3, bismuth wires will not have good optical properties in the infrared. Regarding the mentioned alloys, the lack of characterization of their optical constants in the infrared prevents a reliable theoretical estimation of the metamaterial losses.

Assuming that Pb/Sn (90/10%) alloy has optical losses similar to pure lead, a figure of merit analysis with the values presented in Fig. 3.1(c) shows that such an alloy would have a loss slightly higher than tin. For a 250 nm lead single wire in air, the loss of the 0^{th} TM mode at $\lambda = 3\,\mu$m is around $0.3\,\mathrm{dB}/\mu$m, while the tin wire would have a loss of $0.25\,\mathrm{dB}/\mu$m. In a similar evaluation, assuming that the CuP (92.75/7.25%) alloy has a behaviour similar to pure copper, its optical loss ($\approx 0.12\,\mathrm{dB}/\mu$m) would be better than tin. However, the influence of the phosphorus, a non-metal element, on the electric permittivity of the alloy must be investigated. According to Ref. [164], a small amount of phosphorus in the copper alloy decreases considerably its conductivity, which increases the penetration of the electromagnetic field in the metal wire. Consequently, higher optical losses for the CuP alloy (92.75/7.25%) are expected in comparison with pure copper.

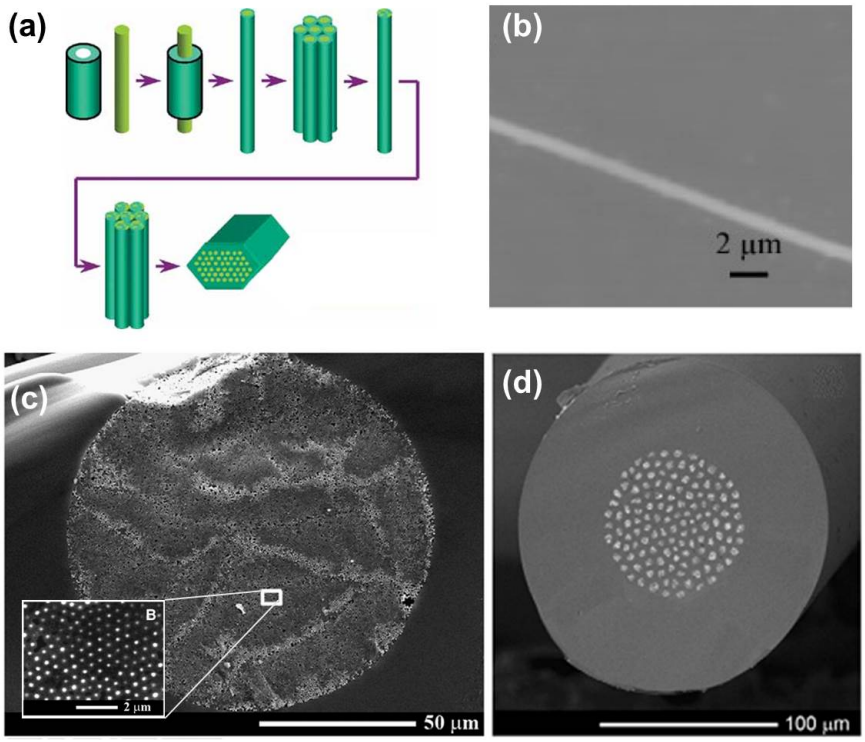

Figure 4.8: (a) Schematic of the draw-stack-cut fabrication process employed in [115] to achieve metallic nanowires embedded in a borosilicate fibre. (b) A SEM micrograph of a 500 nm CuP (92.75/7.25%) nanowire obtained after three consecutive drawings and the etching of the glass. Both pictures were extracted from Ref. [115]. (c) Cross sectional SEM micrograph of a densely packed bundle of PbSn (90/10%) wires embedded in borosilicate glass. Inset: zoom in the white region delimited, showing wires with diameter around 200 nm. (d) SEM micrograph of a final fibre containing approximately 1 million 50 nm bismuth wires seperated in several bundles, as seen in (c), and embedded in a borosilicate fibre. Pictures (c) and (d) were extracted from Ref. [114].

Other fabrication aspects discourage the use of the mentioned alloys for the production of wire array infrared metamaterial fibres. Lead is highly toxic and care must be taken with phosphorus, especially because of its low boiling point (280 °C), which is an issue if an alloy with non-eutectic composition is used. The impact of the phosphorus migration on the rheological properties of the glass during the drawing, as reported in [115], should also be better evaluated. A change in the viscosity of the glass and in the thermal expansion

of the alloy could be detrimental for uniformity of the drawn wire array structure and could generate gaps along its length.

In summary, the fabrication of soft-glass fibres containing metallic nanowires with a diameter down to 50 nm were reported using favourable drawing parameters and for specific material combinations. However, because they were developed for microelectronics applications, their optical response, optical quality and structural uniformity were not assessed, characterized, optimized or explored in metamaterial applications, which is the focus of this thesis.

Amorphous nanowires fabricated by fibre drawing.

For completeness, it is important to mention that the fabrication of smaller nano structures by drawing has been reported in the literature with the combination of amorphous materials.

The drawing of uniform amorphous structures can be easier to achieve in comparison with the metallic arrays because the viscosity of the selected materials can be similar, and the surface tension between them is smaller in magnitude, which greatly reduces the effects of the Plateau-Rayleigh instability for wires above the nanoscale.

For instance, the fabrication of semiconducting chalcogenide nanowires by drawing was reported in [165]. Figure 4.9(a) shows a example of As_2Se_3 wires encapsuled in a PVDF shell (polyvinylidene fluoride) and embedded in a PES polymer fibres (polyethersulfone), with diameters of 66, 41 and 14 nm, adapted from [165]. Even smaller As_2Se_3 nanowires in PES fibres were reported in [166], where the authors combined drawing and tapering to achieve sub-5 nm wires. They drew ≈ 4000 wires with diameters between 20 and 500 nm, the continuity of which was confirmed by etching of the polymer and SEM imaging. Further reduction to sub-5 nm As_2Se_3 nanowires was demonstrated by an extra fibre tapering process. The continuity of such nanowires can be seen in the high-resolution SEM micrographs of Fig. 4.9(b-d) after the etching of the polymer, adapted from the supplementary information of reference [166]. Below these dimensions, the Plateau-Rayleigh instabilities in this system grows at a faster rate than can be overcome by increasing the drawing speed.

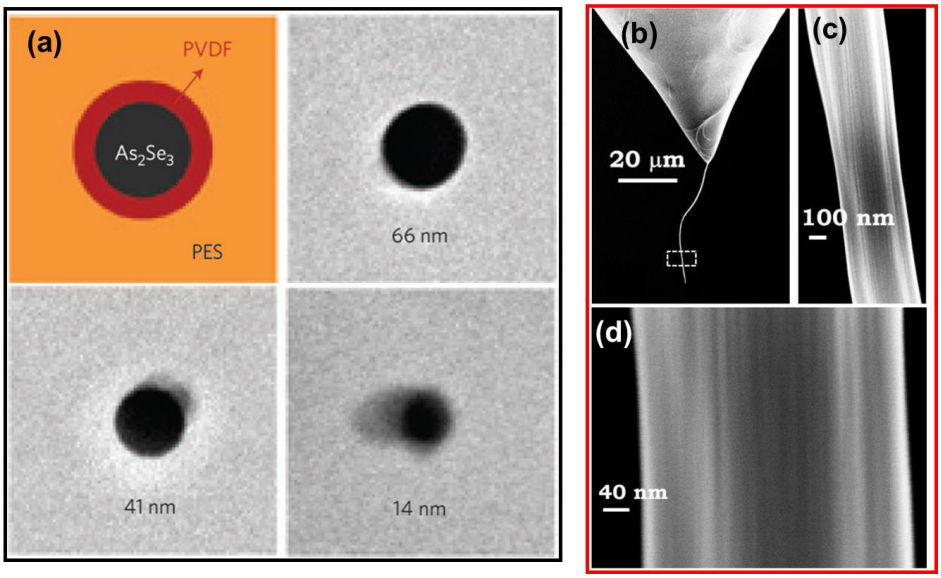

Figure 4.9: (a) As_2Se_3-PVDF core-shell semiconducting nanowires embedded in a PES polymer fibre, with diameters of 66, 41 and 14 nm, adapted from Ref. [165]. Further reduction in size of As_2Se_3 achieved in Ref. [166], extracted from its supplementary information: "2.5 nm-diameter high-density nanowire arrays produced by tapering a fiber containing 20-nm-diameter nanowires. (b) SEM micrograph of an intact exposed bundle of 2.5 nm-diameter nanowires emerging from the tapered fibre tip. (c) SEM micrograph of the dashed white box in (b), and (d) a zoomed-in SEM micrograph of (b), both showing continuous bundles of nanowires. The visible strands are most likely the sets of 12 2.5 nm-diameter nanowires".

In the next section, the fabrication of tin/soda-lime wire array fibres is discussed. This work leads to workable structures with dimensions as small as 143 nm, ideal for metamaterial applications in the MIR.

4.2 Fabrication of wire array infrared metamaterial fibres

The fabrication of our new mid-infrared metamaterial fibre can be divided into four steps:

(1) The fabrication of the preform, containing a hole array structure embedded in a soda-lime matrix, called the hole array cane.

(2) The filling of the hole array cane with the desired metal, generating the wire array cane.

(3) The sleeving and stretching of the wire array cane giving a metamaterial preform containing wires with $d \approx 10\mu$m.

(4) The scaling down of the metamaterial preform into fibre through a final stretching process (drawing or tapering).

The section below will first describe the upgrade performed to the custom-built Heathway polymer draw tower (IPOS - The University of Sydney) which allowed the fabrication of the soft-glass fibres described in this thesis. The fibre tower is described and its furnace characterized. In sequence, all the four steps in the fabrication of the new wire array infrared metamaterial fibre mentioned above are presented and discussed in detail. The influence of the drawing process on the quality of the wire array structure is assessed, and an uniform wire array with d and Λ on the scale of a few hundreds of nm is reported.

4.2.1 Soft-glass drawing and the employed fibre tower

Dielectric materials (glasses and polymers) are usually drawn in the temperature range where their viscosity lies between 10^3 and 10^7 dPa.s [143, 144]. Drawing under higher tension (viscosity larger than 10^7 dPa.s) is possible and limited by the tensile strength of the selected material. For soft-glasses, the temperature region corresponding to this drawable viscosity window greatly varies according to their composition.

Figure 4.10 shows the viscosity as a function of temperature for several commercial soft-glasses available from Schott [143]. According to the material selection analysis of Chapter 3, soda-lime glass is a promising candidate

for infrared metamaterial fibres due to its low cost and high chemical compatibility with tin. From Fig. 4.10, the conventional drawable window (10^3 and 10^7 dPa.s) for soda-lime corresponds to temperatures between 750 and 1250 °C (gray curve number 5).

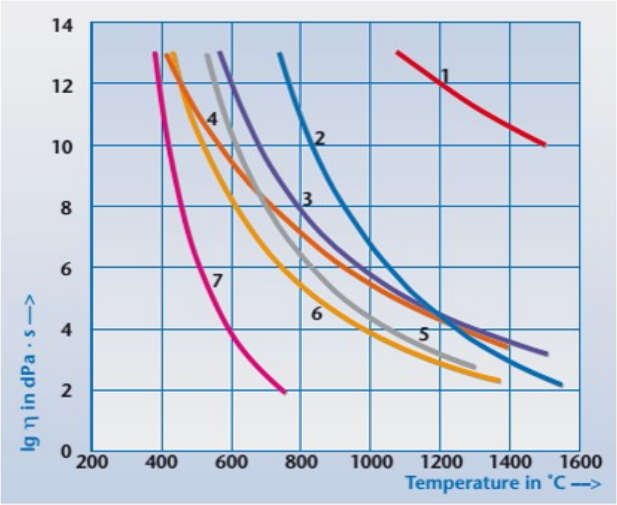

Figure 4.10: Viscosity as a function of temperature curves for several commercial soft-glasses from Schott [143]: fused silica (line 1), glass 8409 (Supremax ®, line 2), glass 8330 (borosilicate glass Duran ®, line 3), glass 8248 (borosilicate glass with high B_2O_3 content, line 4), glass 8350 (soda-lime AR glass ®, line 5), glass 8095 (lead glass with 28 % of PbO, line 6), glass 8465 (line 7).

In order to make the fabrication of soda-lime fibres viable, a resistance furnace with an operational range up to 1200 °C was installed in the custom built Heathway polymer draw tower (IPOS, School of Physics, the University of Sydney, Australia). Figure 4.11(a) shows the resistance furnace purchased. A stainless steel casing was developed to contain an extra layer of ceramic insulation, to support two irises on its two extremities, and to attach the set to the main frame of the fibre tower, as seen in Fig. 4.11(b). The operation of the furnace requires a power supply with a PID control, which was developed and enclosed in an electrical cabinet (Fig. 4.11(c)).

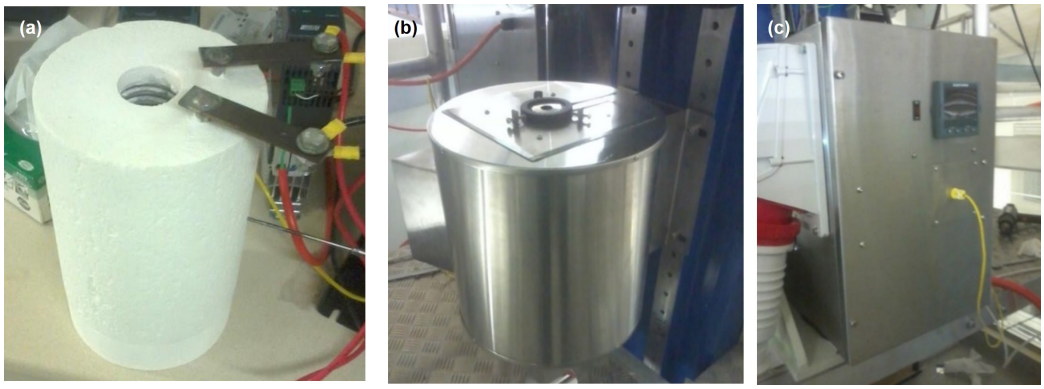

Figure 4.11: (a) Original resistance furnace for the soft-glass fibre drawing, operational temperature up to 1200 °C. (b) Furnace covered in a stainless steel casing and attached to the main frame of the fibre tower. (c) Electrical cabinet containing the power supply and the PID controller required for the operation of the soft-glass furnace.

The fibre tower is composed of a feeding unit, a furnace, a diameter monitor system and pulling units. Figure 4.12(a) shows a picture of the fibre tower with the description of all these components. Figure 4.12(b) shows a schematic of the tower as employed for soft-glass drawing.

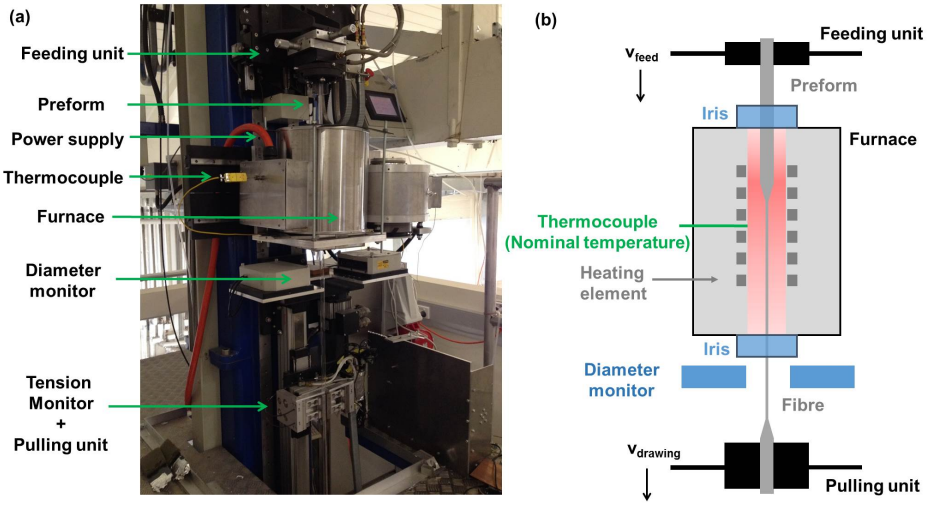

Figure 4.12: (a) Photograph and (b) schematic of the soft-glass tower illustrating all its components and the drawing process.

In the drawing process, the top of the preform is initially attached to the feeding unit, which is an adjustable chuck coupled to a step-motor, and aligned with the furnace. The furnace temperature is increased with the PID controller until the softening of the glass is achieved (above its softening temperature, where $\eta = 10^{7.6}$ dPa.s). For the soda-lime glass (AR-Glas ® from Schott), the softening temperature is around 700 °C. In this regime, the bottom end of the preform slowly drops due to gravity. When the drop reaches the pulling system, the clamp is closed and both the feeding (v_{feed}) and pulling (v_{draw}) velocities are adjusted according to the desired reduction factor of the original preform and the range of velocities available on both units.

Under the steady state regime, the relationship between the diameter of the fibre (d_{fibre}) and preform (D_p) is imposed by the volume conservation equation (Eq. (2.42)), repeated below for convenience.

$$d_{fibre}^2 = D_p^2 \frac{v_{feed}}{v_{draw}}. \tag{2.42}$$

The fibre diameter is monitored by a laser-based system and both velocities can be changed via a computer controller. In the case of a microstructured preforms or metamaterial fibre drawing, more complicated aspects of the drawing process must be taken into account. Drawing variables such as feed rate, drawing rate, pulling tension and temperature have a huge influence on the quality of the structure in the final fibre.

In addition, the viscosity of the dielectric during drawing and the surface tension between both materials play an important role in the degree of uniformity of the metallic structures due to the Plateau-Rayleigh instability. Such aspects will be discussed in detail throughout this Chapter.

Furnace Characterization: Temperature Profiles

The heating of the preform inside the furnace is a complex process involving heat conduction, convection, radiation absorption and heat dissipation. The temperature profile inside the furnace has a strong influence on the fibre fabrication since the length, position and shape of its hot zone influences the neckdown shape [167–169] and the heat transfer processes to the preform. Such parameters can affect the quality of the drawn microstructure or influence the instability in the metallic structure in the co-drawing scenario.

As a result, a full characterization of the temperature profile inside the

furnace is required in order to optimize the fibre fabrication and for the selection of the optimum drawing parameters. Furthermore, any modeling of the co-drawing based on the heat transfer process requires an accurate measure of such profiles.

The subsections below describe three different experiments performed to characterize different aspects of the complex heat transfer process. A K-type thermocouple was fed inside the furnace in different positions to measure the temperature profile along its center, its wall, and inside and outside a preform. A reflective shield surrounding the thermocouple was also used to minimize the radiation contribution in some of the cases.

The air temperature inside the furnace plays a strong role in conduction and convection. The temperature profile was obtained by feeding a K-type thermocouple mounted inside a tapered borosilicate tube (Fig. 4.13(a)) along the length of the furnace, as shown in Fig. 4.13(b). The thermocouple head is immersed in air and the tapering region of the borosilicate tube ensures alignment and minimizes the convection of air inside the glass tube. However, note that the temperature of the probe is also affected by its radiative exchange with the furnace's radiative elements. Consequently, the measured temperature also depends on the emissivity of the probe, and thus cannot be understood as a perfect measure of the air-temperature.

Figure 4.13(c) shows the temperature profiles for three different nominal temperatures (400, 450 and 500 °C), as a function of the distance from the top iris (top entrance of the furnace). The nominal temperature used for feedback by the PID controller is measured with another thermocouple permanently positioned in the middle of the furnace's wall, shown in Fig. 4.13(b) as the green line.

According to Fig. 4.13(c), the maximum temperature of the air in the center of the furnace is around 5% lower than the nominal temperature, and positioned around 90 mm below the furnace entrance (top iris). Considering the hot zone as the region presenting a temperature above 95% of the maximum temperature, Fig. 4.13(c) indicates a hot zone's length around 110 mm for our soft-glass furnace, which slightly decreases for higher nominal temperatures. Such information is useful to estimate the position of the neckdown transition and the ideal alignment for the bottom holder, which is usually attached to the preform as a pulling weight for the initial drop. The position of this bottom holder and its joint with the glass preform is restricted according to the range of temperature that they can withstand.

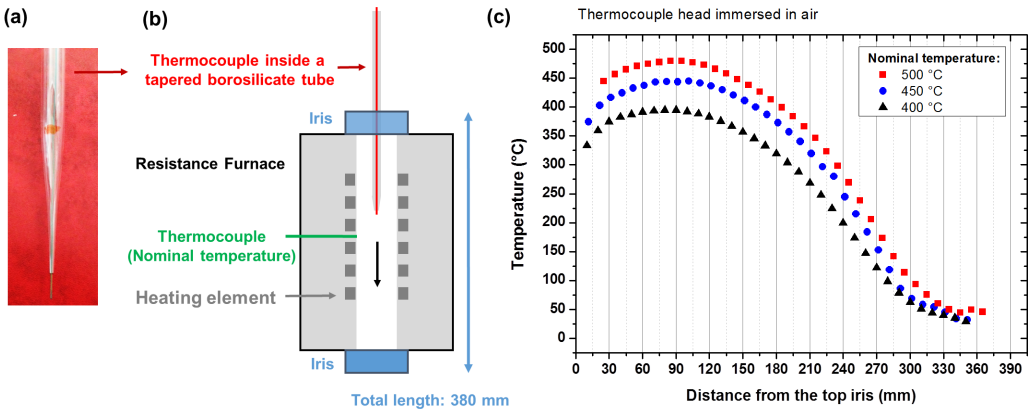

Figure 4.13: (a) Picture of the thermocouple mounted inside a tapered borosilicate tube. (b) Schematic of the furnace and the feeding of the thermocouple through the center. (c) Temperature profile of the air along the center of the furnace for three different nominal temperatures: 400, 450 and 500 °C, as a function of the distance from the top iris.

An important indicator of the efficiency of the heat transfer process during the drawing is the temperature profile along the furnace's length in the center of a preform. Such temperature profile depends on the size of the glass preform, the glass composition, the presence or not of a microstructure (air holes or other materials), and the selected feeding velocity.

In order to simplify such characterization, a test preform composed of a K-thermocouple, a soda-lime tube and a soda-lime rod was employed, as represented and pictured in Fig. 4.14(a). Figure 4.14(b) shows a schematic of the measurement, where such a test preform with the central thermocouple was fed through the center of the furnace along all its length. Figure 4.14(c) and (d) show the temperature profiles with feed velocities varying from 5 to 50 mm/min, for two different nominal temperatures of 400 and 500 °C, respectively.

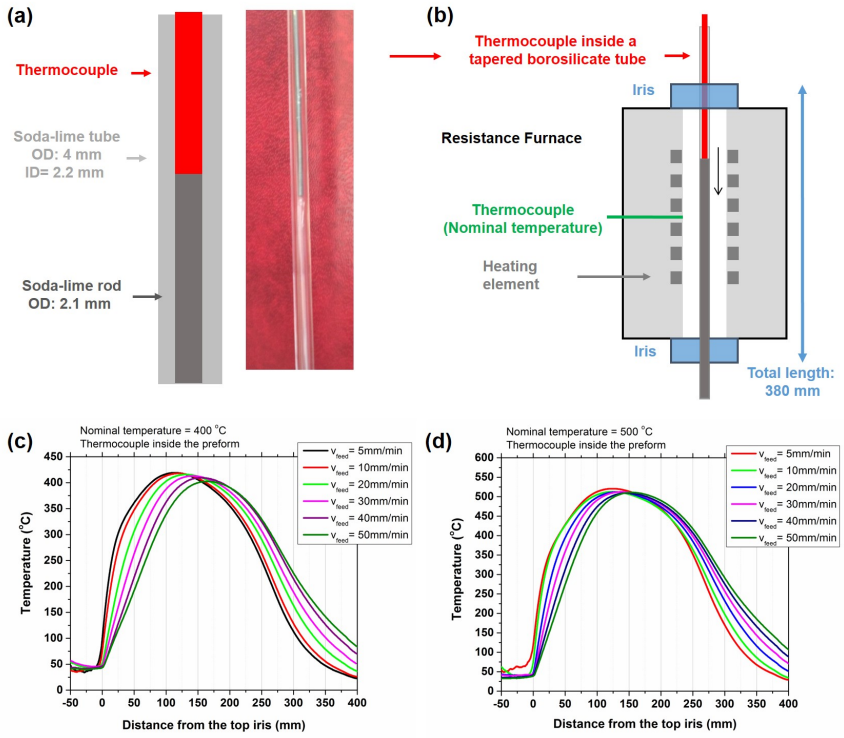

Figure 4.14: (a) Schematic and picture of the testing preform with the attached thermocouple. (b) Schematic of the temperature characterization. Temperature profile in the center of the preform for different feed velocities (from 0 to 50 mm/min), with nominal temperatures of 400 °C (c) and 500 °C (d).

As expected, the temperature profile inside the solid soda-lime preform differs from the air temperature profile in the center of the furnace. Note in particular that the maximum temperature measured here is slightly higher than temperature measured by the thermocouple without preform, which can be attributed to the different emissivity and radiation balance, including a "greenhouse effect" within the preform. As viewed in Fig. 4.14(c) and (d), the maximum temperature decreases and the general profile shifts to the right as the feeding velocity increases, which is related to the dynamics of the heat transfer and the time required to heat the full preform.

For the nominal temperature of 400 °C, the maximum temperature varies from 420 °C (black curve) to 402 °C (dark green curve). Such a decrease with increasing feeding velocity is expected because more material is supplied in a given time for a fixed heat transfer rate. For the nominal temperature of

500 °C, the maximum temperature varies from 520 °C (red curve) to 511 °C (dark green curve).

According to Fig. 4.14(c) and (d), the hot zone's length varies with nominal temperature, from 81 mm (400 °C) to 93 mm (500 °C), but both do not vary with the feeding speed.

4.3 Metamaterial Preform Fabrication

Over the years, different methods for the fabrication of preforms of microstructured fibres have been reported, depending on the dielectric material employed and the structure desired. The most common are: stack-and-draw [101, 103, 104], extrusion [105, 106], casting [107, 108] and ultrasonic drilling [105].

When glass is selected as the dielectric, and commercial tubes are available in a range of dimensions at reasonable prices (which is the case for soda-lime glasses), the stack-and-draw technique is generally preferred: This method has a high flexibility in the achievable structural parameters and generates remarkably uniform hole array structures, commonly used for the fabrication of PCFs and microstructured fibres [101,102]. In addition, it can produce large preforms (that can be drawn to kilometers of fibre) and holes with high surface quality (minimizing scattering loss in the final fibre), which are not the possible in the drilling approach.

For the fabrication of hyperbolic metamaterial preforms, the conventional stack-and-draw technique must be adapted to include the metallic structure. As a result, the fabrication of our wire array metamaterial preform is divided in the following three steps:

(1) The fabrication of a hole array cane, which is the macroscopic version of the desired structure without metal, by the drawing and stacking of empty capillaries.

(2) The filling of the hole array cane with the selected metal by a pressure-assisted technique, giving a wire array cane.

(3) The sleeving (addition of a glass jacket) and stretching of the wire array cane until the diameter of the wires scales down to sizes around 10 μm, generating the metamaterial preform.

Below, the mentioned steps are described in detail and the fabrication of two tin/soda-lime wire array preforms is presented. One containing around 50 wires (testing structure for the characterization of the Plateau-Rayleigh instability and drawing parameters), and a second one containing around 500 wires (ideal for the imaging applications due to its larger wire array region).

4.3.1 Hole array cane fabrication

The hole array cane fabrication starts with the production of glass capillaries from the drawing of a large tube in the fibre tower, as illustrated in Fig. 4.15(a). When soda-lime glass is employed, the tube is heated around its softening point ($T = 720\,^{\circ}C$, corresponding to a viscosity of $10^{7.4}$ dPa.s), until its bottom end drops due to gravity. The drop is attached to the pulling system of the tower and the feed and pulling velocities are adjusted to achieve the desirable reduction, which is dictated by the volume conservation Eq. (2.42).

The resultant capillaries are stacked in a hexagonal pack with an adjustable 3D printed hexagonal stacker (Fig. 4.15(b)) and inserted inside a large soda-lime tube, called a jacket. The selected jacket must have an inner diameter matching the size of the hexagonal pack. The remaining air gaps are filled with solid soda-lime rod supports, forming the stacked preform (Fig. 4.15(c)). If a circular hole array structure is desired, the solid rod supports are replaced by corresponding hollow capillaries.

The stacked preform is then stretched to a hole array cane in the fibre tower. Vacuum is applied between the capillaries during this process in order to collapse the interstitial air gaps. Figure 4.15(d) shows a schematic of a resultant hole array cane, showing no air gaps and a slight reduction in the outside diameter of the overall structure.

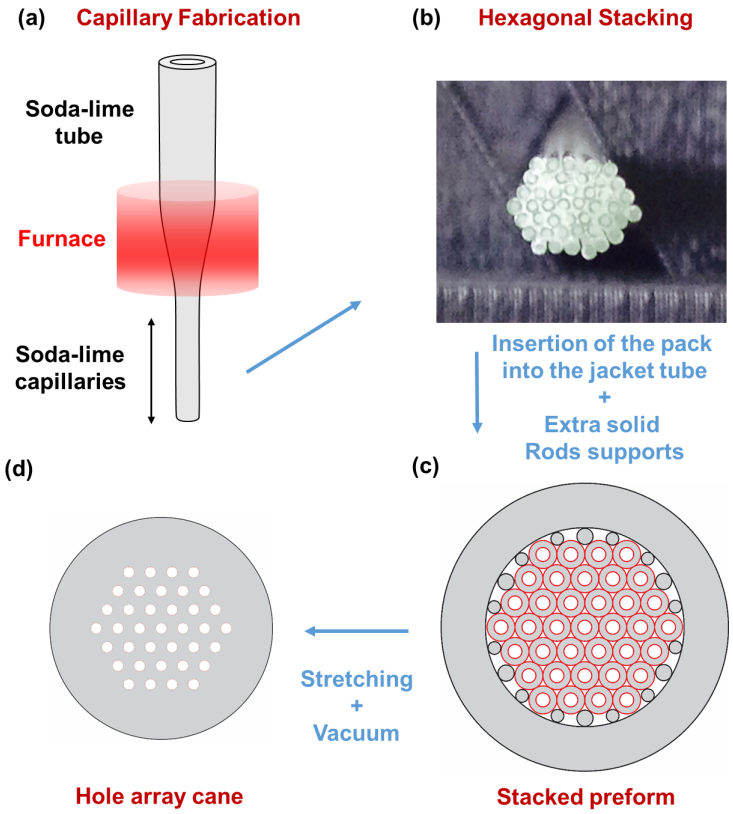

Figure 4.15: Schematic of the hole array cane fabrication. (a) Stretching of a hollow soda-lime tube to smaller capillaries in the fibre tower. (b) The capillaries are stacked in a hexagonal arrangement. (c) The hexagonal stacking is inserted into another soda-lime (jacket tube) and additional solid rod supports are employed to fill the outer air gaps, forming the stacked preform. (d) The stacked preform is stretched in the fibre tower with vacuum applied between the capillaries to collapse the interstitial air gaps, generating the hole array cane.

The selection of the soda-lime tubes used to make the stacked capillaries depends on the structural parameters desired in the final metamaterial fibre, as the structure presented in the hole array cane will merely be scaled down. The ratio between the hole diameter (d) and the distance between two neighbouring holes (Λ) in the hole array cane is determined by the ratio between the inside and outside diameter of the stacked capillaries. For example, in order to fabricate a metamaterial structure with $d/\Lambda = 0.5$, it is necessary to stack capillaries with a ratio between outside diameter (OD) and inner

diameter (ID) of 0.5. When the desired ratio is not available commercially, several tubes can be combined in a process called sleeving. In this process, one tube is inserted inside another, stretched in the fibre tower with vacuum applied only between the tubes, resulting in a tube with a new ID/OD ratio.

In the final metamaterial fibre, the wire diameter and spacing have a huge influence on the overall optical loss (as discussed in Chapter 3), and also on the density of photonic states, and the resolution of metamaterial hyperlenses. When imaging applications with these metamaterials are considered, a large number of wires is also required to maximize the imaging area and avoid edge effects. Ideally, if the wire array region is much bigger than the imaging object, the metamaterial can be considered infinite, leading to a better agreement between the modeling and experimental results. For these reasons, the fabrication of a hole array cane with around 500 holes is described below. This will be used as standard structure for applications presented in this thesis.

Hole array cane with around 500 holes

The selected metamaterial structure for our imaging applications and lifetime engineering in the MIR is composed of approximately 500 tin wires with $d/\Lambda = 0.5$ and $d = 250\,\mu$m. Figure 4.16(a) shows the stacking plan for such preform.

A large soda-lime tube (OD = 4 mm and ID = 2 mm) is stretched to hundreds of capillaries with OD=500 μm and ID=250 μm. These capillaries are stacked in a hexagonal shape and introduced inside a soda-lime jacket tube with OD = 12 mm and ID = 10 mm. Extra capillaries with different dimensions are introduced in the air gap between the inner diameter of the jacket and the original hexagonal pack to avoid structural deformations, as shown in the stacking plan in Fig. 4.16(a). Figure 4.16(b) shows a picture of the resultant stacked preform.

The hole array cane is then fabricated by stretching the stacked preform in the drawing tower. During this process, as mentioned above, vacuum is applied only between the capillaries in order to collapse the interstitial air gaps presented between them. Figure 4.16(c) shows a picture of the resultant hole array cane, with an OD $\approx$ 6 mm and an average hole diameter $d \approx 100\,\mu$m.

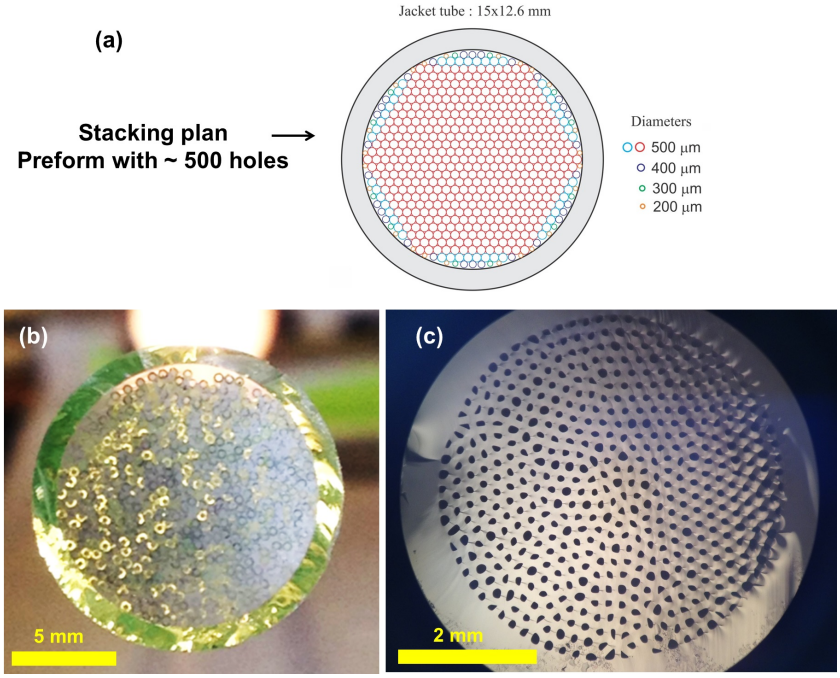

Figure 4.16: (a) Stacking plan for the fabrication of hole array cane composed by approximately 500 holes. (b) Stacked preform after the insertion of the stacked pack into the jacket tube. (c) Resultant hole array cane after the drawing of the stacked preform.

The deformations in the structure observed in Fig. 4.16(c) are caused by imperfections in the stacking pack, which arises from the high flexibility and small size of the employed capillaries (OD = 500 μm). Static forces make a perfect stacking impossible and there is a small reorganization of the capillaries when the whole hexagonal pack is inserted in the jacket tube due to its high flexibility.

After the hole array cane is fabricated (Fig. 4.16(c)), its air holes are filled with tin using a novel pressure-assisted filling technique. In this process, it is important to avoid the sucking of any metal oxide inside the cane, which could be detrimental for the co-drawing due to its different melting point and could generate deformations on the final metallic structure. Care must also be taken to fill the length of the cane and to avoid the formation of gaps.

In the next section, a novel pressure-assisted filling process that addresses all the issues mentioned above will be described step-by-step.

4.3.2 Filling of the hole array cane with the selected metal

The hole array cane is positioned inside a resistance oven through a ceiling hole until its bottom end is positioned a few millimeters above the bottom of an empty beaker (Fig. 4.17(a)). Several small pieces of pure tin wire are placed in a second beaker (Fig. 4.17(b)) and positioned beside the empty beaker. The oven is heated up to 280 °C, which is a few tens of degrees above the melting point of pure tin (232 °C), and the metallic wires melt (Fig. 4.17(c)).

When the tin is completely molten, the furnace is opened and the liquid metal is transferred to the empty beaker until the bottom of the hole array cane is completely submersed in the molten metal (Fig 4.17(d)). This transfer process is essential to separate any metal oxide that existed on the original tin wires or was generated from the original melting, so as to prevent it from blocking or filling the holes of the cane. As emphasized in the literature [112], such oxides could also be extremely detrimental to the co-drawing process. Figure 4.17(e) shows an example of the remaining oxide residue after the molten tin was transferred.

After transferring the pure tin, a vacuum pump is attached to the top end of the cane that is outside the oven. The vacuum system is turned on and the pressure inside the air holes of the hole array cane is slowly reduced by the closing of a leaking valve, until the maximum vacuum of -800 mbar is achieved. The resultant positive pressure induced by the vacuum inside the cane and the capillary forces pull up the liquid metal through the holes of the cane until the liquid metal columns reach the outside of the oven and solidify (Fig. 4.17(f)).

According to Ref. [137], the required time for the filling can be calculated by

$$L = \frac{1}{2}\sqrt{(d_{\text{hole}}\gamma_{\text{st}}\cos\phi + \frac{d_{\text{hole}}^2}{4}p)\frac{t_f}{\eta_{dv}}}, \tag{4.4}$$

where d_{hole} is the hole diameter, γ_{st} is the surface tension, p is the applied relative pressure (atmospheric pressure - vacuum pressure in our filling method), ϕ is the contact angle of the molten metal, t_f is the filling time, and η_{dv} is the metal's dynamic viscosity. Table 4.1 lists these parameters for tin and gold.

Table 4.1: Filling parameters for tin and gold

	Dynamic viscosity η_{dv} (Pa.s)	Surface Tension γ_{st} (N/m)	Contact angle ϕ (degree) in silica
Tin	1.54 x 10^{-3}, at 280 °C [170]	0.54, at 280 °C [171, 172]	112.5 °, at ∼900 °C [173]
Gold [137]	5.13 x 10^{-3}	0.75	122.5 °

In view of Eq. (4.4), and the parameters listed in Table 4.1, a vacuum of -800 mbar (which is equivalent to a filling pressure $p = 800$ mbar), and a length of 50 cm, the estimated filling time for holes with $d = 100\,\mu$m is around 9 s for tin. Because the contact angle for liquid tin presented in Table 4.1 was calculated in contact with silica (instead of soda-lime glass) and at ∼900 °C in Ref. [173], this filling time should be treated as an approximation. After that period, the oven's temperature is slowly decreased to room temperature, and the vacuum pump is turned off and the filled hole array is removed from the oven.

Note that, for such dimensions and pressure, a hole array cane made of silica would be easily filled with gold as well (filling time around 32 s). However, this would not be true for a hole diameter below 20 μm. According to Eq. (4.4), because the $\cos\phi$ of the liquid metal in glass is negative, there is a minimum pressure ($p_{min} = (4\gamma_{st}/d_{hole})\cos\phi$) required to initiate the filling process. Using the parameters presented in Table 4.1, and a p_{min} of 1 bar (the maximum equivalent pressure achieved with a perfect vacuum), the smallest hole diameter that could be filled with a vacuum pump is around 20 μm (for gold) and 8.3 μm (for tin).

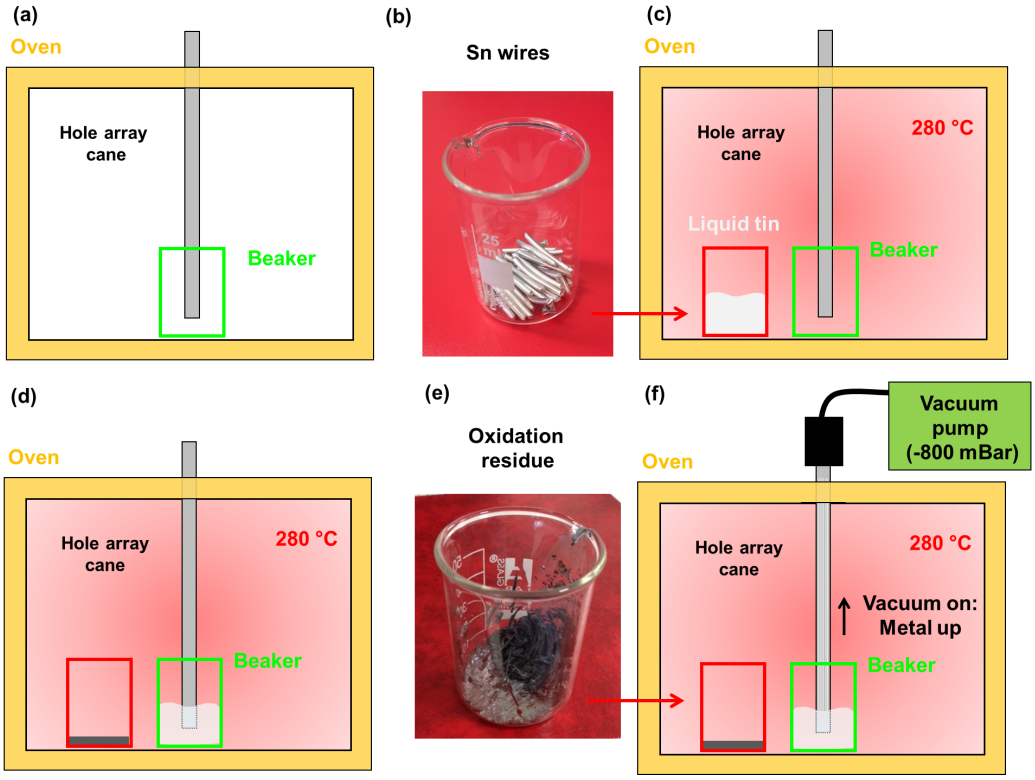

Figure 4.17: Schematic of the pressure assisted filling process develop to fill our hole array canes with tin. (a) A hole array cane is aligned inside an oven, with its bottom end positioned a few millimeters above the bottom of an empty beaker. (b) A pure tin wire is cut in small pieces and introduced inside a second beaker. (c) The beaker containing the tin wires is placed beside the empty one inside the oven and the temperature is set to 280 °C. (d) The liquid tin is transferred to the empty beaker, separating the molten metal from the oxidation residue, shown in (e), as the darker region). (f) Vacuum inside the air holes of the hole array cane pulls up the liquid metal though the structure, until the metal columns reach the outside of the oven and solidify.

Figure 4.18(a) and Fig. 4.18(b) show an example of a hole array cane with a few tens of holes before and after filling with tin, respectively. Such a process is also successful with a large number of holes. Figure 4.18(c) and Fig. 4.18(d) show a hole array cane with a few hundred holes, before and after filling with tin, respectively. In both preforms the filling length achieved was around 50 cm, corresponding to the vertical size of our resistance oven.

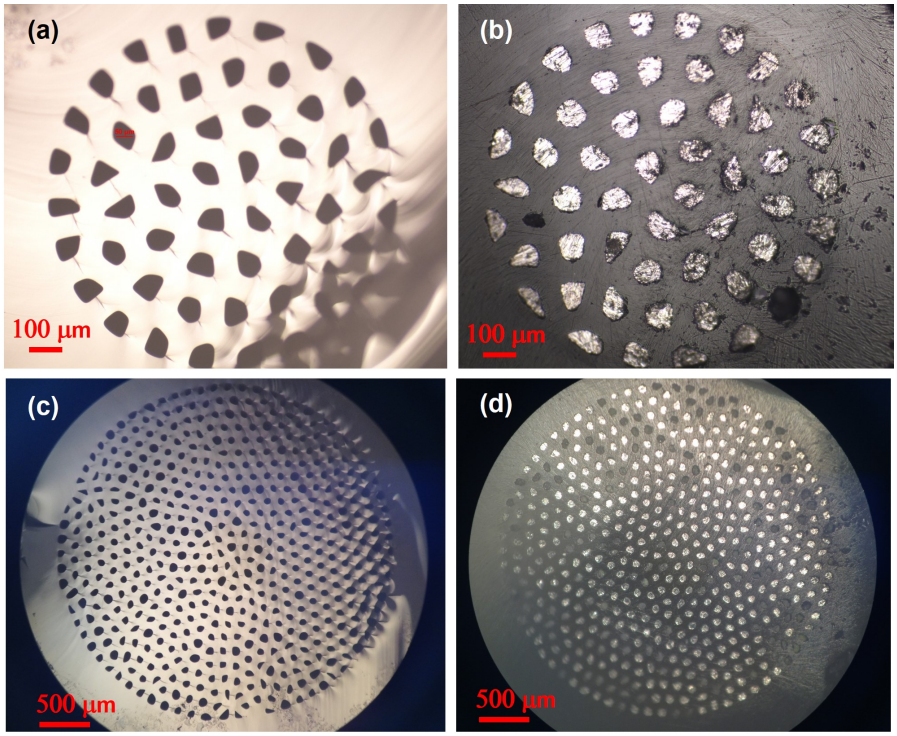

Figure 4.18: Hole array canes before (a,c) and after their filling with tin (b,d). The preform containing few tens of wires has $d_{\text{avg}} \approx 50\,\mu$m, $\Lambda \approx 100\,\mu$m, while the one containing few hundreds of wires has $d_{\text{avg}} \approx 100\,\mu$m, $\Lambda \approx 200\,\mu$m.

Note that the bright regions in Fig. 4.18(b) and Fig. 4.18(d) are the tin wires. The dark regions indicate that the filling of some of the holes was not completely successful (the molten metal column has not reached the top of the hole array cane). This problem likely arises from the blocking of these holes with oxidation residue or other dust fragments, which obstructs the positive pressure applied with the vacuum pump. However, such samples can still be used if a considerable length of the hole array cane is completely filled with metal and the defected region is discarded.

4.3.3 Sleeving and stretching of the wire array cane to a metamaterial preform

After the filling process, the metamaterial preform is obtained by the sleeving and stretching of the wire array cane in the fibre tower. Figure 4.19 shows a schematic of such drawing developed for our soft-glass fibres.

In this process, the top side of a wire array cane is heated by a butane flame and collapsed with pliers, in order to avoid any overflowing of the metal when vacuum is employed during the sleeving. Such a cane is inserted inside an additional soda-lime jacket with an inner diameter slightly larger than the outside diameter of the cane, as shown in Fig. 4.19(a). The bottom of this set is also heated with a butane flame and the gap between the jacket tube and the cane is collapsed with pliers, as shown in Fig. 4.19(b).

In the fibre tower, vacuum is applied from the top, in the gap between the original preform and the jacket tube, and the assembly is stretched whilst drawing (Fig. 4.19(c)). As a result, the metamaterial preform is obtained containing a scaled down version of the wire array cane structure and an extra layer of dielectric material on its outside, as represented in Fig. 4.19(d). The typical draw ratio achieved in this process varies between 5 and 10x, depending on the size of the jacket tube and the intended outside diameter for the stretched sample.

Since this stretching process involves the co-drawing of metal and glass, care must be taken with the selected drawing temperature and final diameter of the wires. According to the literature, the metallic structure starts to fluctuate greatly for wire diameters around $3\,\mu$m in polymer (indium/PMMA-Zeonex, Fig. 4.4, [84]) and below $1\,\mu$m for metallic wires embedded in glass [154]. As a result, in order to avoid instabilities in this first co-drawing, the final size of the wires should not be smaller than $5\,\mu$m and high drawing temperatures must be avoided.

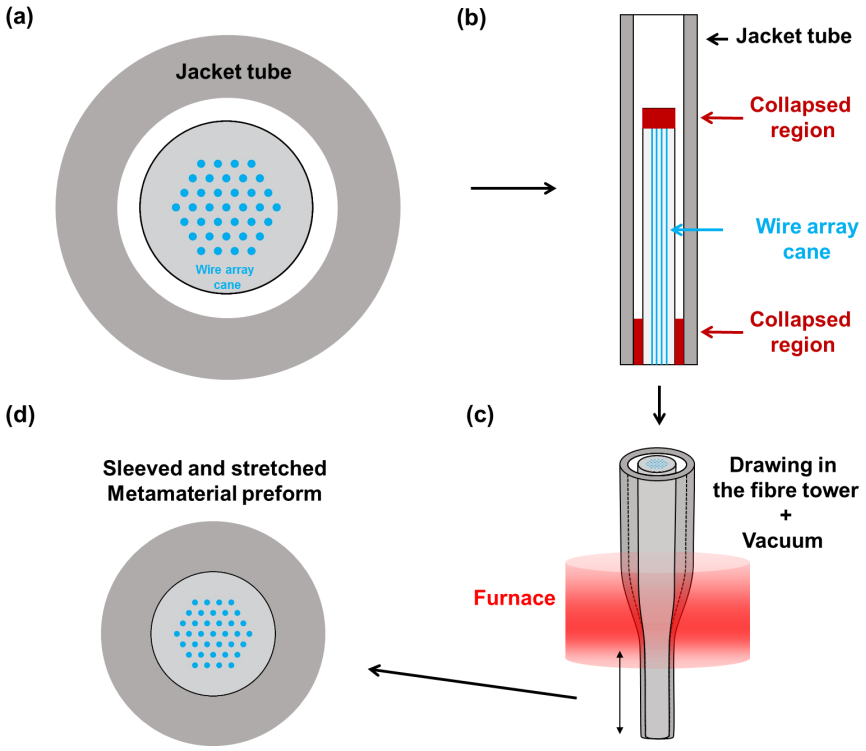

Figure 4.19: Schematic of the sleeving and stretching process. (a) The wire array cane with one of its extremities collapsed is inserted inside a soda-lime jacket tube. (b) The bottom of the set is closed with a butane flame and pliers. (c) The stretching is done in the drawing tower with vacuum applied in the air gap between the inner cane and the jacket tube. (d) The resultant metamaterial preform after the stretching and sleeving process.

Figure 4.20(a) shows a micrograph of the cross section of the original wire array cane with few tens of wires ($d \approx 85\,\mu$m, $\Lambda \approx 170\,\mu$m, and an OD=1.8 mm) while Fig. 4.20(b) and (c) show the resultant metamaterial preform after the sleeving and stretching process ($d \approx 10\,\mu$m, $\Lambda \approx 20\,\mu$m and OD = 1 mm).

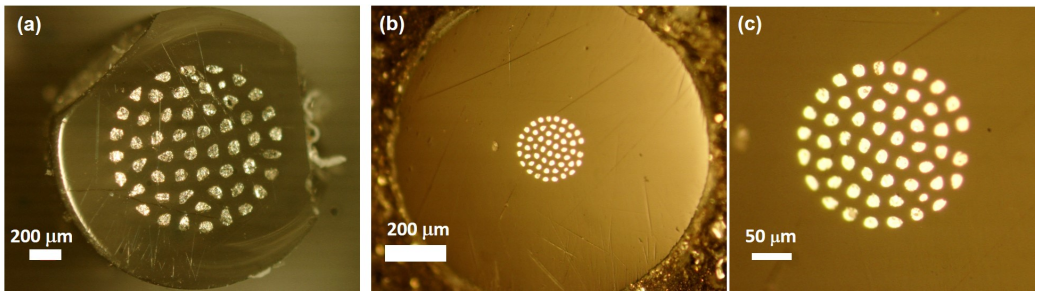

Figure 4.20: (a) Original wire array cane with few tens of wires with $d \approx 85\,\mu$m, and $\Lambda \approx 170\,\mu$m, and OD$= 1.8$ mm. (b) Resultant metamaterial preform after the sleeving and stretching of the wire array cane, using a soda-lime jacket tube with OD$= 5.2$ mm and ID$= 1.9$ mm. (c) Zoomed-in picture in the wire array region, showing a metallic structure with $d \approx 10\,\mu$m, $\Lambda \approx 20\,\mu$m and OD$= 1$ mm.

Figure 4.21(a) shows a picture of the metamaterial preform containing a few hundred wires, obtained with the sleeving and stretching process of the filled cane seen in Fig. 4.18(d), performed under favourable conditions (low drawing temperature and high tension). Figure 4.21(b) shows a zoomed pictured in the wire array region, with $d_{\text{avg}} = 9.34\,\mu$m and $\Lambda \approx 18\,\mu$m.

With a high resolution cross section micrograph, as the one presented in Fig. 4.21, it is possible to characterize the fluctuation of the wire diameter in the structure measuring the diameter of each hole and calculating the standard deviation of the wire diameter distribution σ_d. The metamaterial

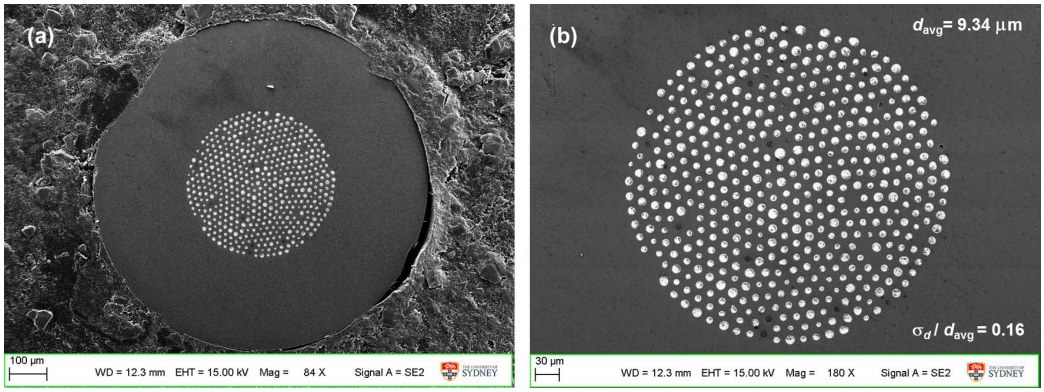

Figure 4.21: (a) Metamaterial preform fabricated by the sleeving and stretching of the few hundred wires metamaterial preform (Fig. 4.18(d)), with OD $\approx 900\,\mu$m. (b) Zoom of the wire array region, showing a $d_{\text{avg}} = 9.34\,\mu$m and $\Lambda \approx 18\,\mu$m.

preform shown in Fig. 4.21 has a $\sigma_d/d_{\text{avg}} = 0.16$, which represents a small fluctuation in the metallic structure. Besides, note that the respective hole array cane after the filling, shown in Fig. 4.18(c), already presents a small degree of fluctuation in its holes due to imperfections in the stacking, indicating that the first co-drawing of metal and glass (sleeving and stretching) did not create any detrimental fluctuation. Such a scenario is essential to achieve a uniform structure in the second and final stretching process (by drawing or tapering).

After the fabrication of the uniform wire array preform, the next step is the final drawing to fibre, which must be performed under certain conditions to avoid wire diameter fluctuations caused by the Plateau-Rayleigh instability.

4.4 Drawing of the metamaterial preform to fibre

The final metamaterial fibre is fabricated by a last sleeving and stretching of the metamaterial preform where the wires are scaled down from diameters around 10 μm to a few hundred nanometers. Due to the exponential growth of the Plateau-Rayleigh instability, the quality of the drawn metallic structure is very sensitive to the drawing parameters such as temperature, pulling tension, feeding and drawing velocities.

According to the Plateau-Rayleigh instability gain term, $g = \sigma/(2R\mu)$ (Eq. (4.2)), the fluctuations in the metallic wires grow more rapidly for lower viscosity of the dielectric matrix (μ). As a result, they can be minimized if the drawing process is performed with the highest possible viscosity of the dielectric matrix, *i.e.*, at the minimum temperature for which drawing is still possible (which we shall call the minimum drawable temperature, corresponding to highest pulling tension before the preform or fibre breaks).

The minimum drawable temperature varies with the size of the preform, draw ratio and the feeding velocity. Larger preforms and fast feeding shift up the minimum drawable temperature because they change the heat transfer dynamics. For a specific size of preform and draw ratio, such temperature is limited by the maximum drawing tension that the fibre can withstand before breaking, which is determined by the tensile strength of the glass.

Figures 4.22(a) and (b) show two different wire structures with hundreds

of wires fabricated under low and high drawing tension, respectively. Both fibres were drawn from the metamaterial preform presented in Fig. 4.21, with jacket tubes with OD = 10 mm, ID = 1.2 mm, v_{feed} = 5 mm, but with 25 °C of difference in the drawing temperature (710 °C and 685 °C, respectively). It is clear from Fig. 4.22 that a small difference in the drawing temperature ($\approx 3.5\%$) produced a huge variation in the uniformity of the final drawn wire array structure. The structures fabricated under low and high tension presents a $\sigma_d/d_{avg} = 0.68$ and 0.42, respectively.

The Plateau-Rayleigh instability limit for the tin/soda-lime system can be established by a set of controlled drawings attempt performed at the limit of the pulling tension and the analysis of σ_d/d_{avg} values of thus obtained metallic structures. Several metamaterial preforms with a few tens and a few hundreds of wires (Fig. 4.20(b) and Fig. 4.21) were sleeved with a jacket tube with OD = 10 mm, ID = 1.2 mm, and drawn into fibres with outside diameter from 100 μm to 1 mm, resulting in wires with diameters from 100 nm to 1 μm. For every fibre with different outside diameter (different draw ratio), the drawing parameters were adjusted to achieve values close to the maximum drawing tension (experimentally determined by trial and error based on breakage) and, consequently, close to the minimum drawable temperature. Since the fibre tower does not have a system to measure the pulling tension, the values employed in the drawings must be considered experimental

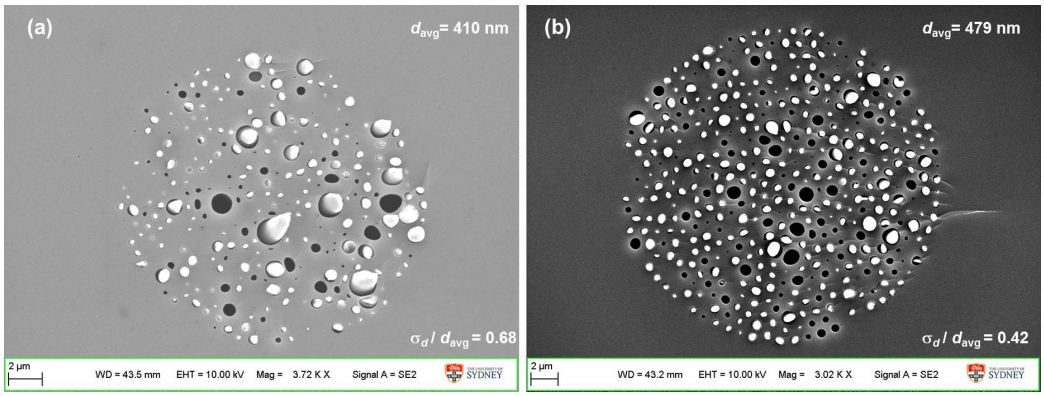

Figure 4.22: SEM micrographs of wire array metamaterial fibres drawn from the metamaterial preform of Fig. 4.21. (a) Drawing performed under low pulling tension, T = 710 °C, structure with d_{avg} = 410 nm and $\sigma_d/d_{avg} = 0.68$. (b) Drawing preformed under high pulling tension, T = 685 °C structure with d_{avg} = 479 nm and $\sigma_d/d_{avg} = 0.42$.

approximations to the maximum drawing tension.

Figure 4.23 shows two sets of high resolution cross section micrographs for several fibres drawn under such conditions with different final structures. Figure 4.23(a-c) shows wire array structures drawn from the metamaterial preform with a few tens of wires (Fig 4.20(b)), and Fig. 4.23(d-f) with a few hundreds of wires (Fig. 4.21). The increase in fluctuation on the wire array structures (σ_d/d_{avg}) is evident as the d_{avg} decreases, for both set of structures. Note that the black regions consist of empty holes or wires that had their top extremities removed in the cleaving process.

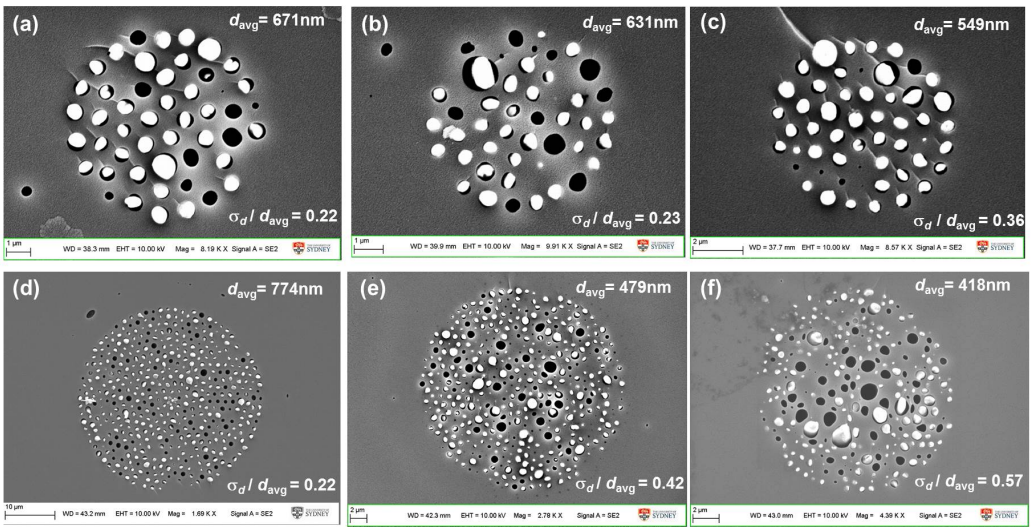

Figure 4.23: Examples of fibres drawn under the limit of tension from the two metamaterial preforms from Fig. 4.20 and Fig. 4.21, respectively. (a) $d_{\text{avg}} = 671\,\text{nm}$, $\sigma_d/d_{\text{avg}} = 0.22$. (b) $d_{\text{avg}} = 631\,\text{nm}$, $\sigma_d/d_{\text{avg}} = 0.23$. (c) $d_{\text{avg}} = 549\,\text{nm}$, $\sigma_d/d_{\text{avg}} = 0.36$. (d) $d_{\text{avg}} = 774\,\text{nm}$, $\sigma_d/d_{\text{avg}} = 0.22$. (e) $d_{\text{avg}} = 479\,\text{nm}$, $\sigma_d/d_{\text{avg}} = 0.42$. (e) $d_{\text{avg}} = 418\,\text{nm}$, $\sigma_d/d_{\text{avg}} = 0.57$.

The Plateau-Rayleigh instability limit for the tin/soda-lime (red and black curve) and the indium/PMMA-Zeonex system (blue curve - data from Ref. [84]) is illustrated in Fig. 4.24. The term σ_d/d_{avg} is plotted as a function of the averaged wire diameter measured for several tin/soda-lime wire array structures drawn on the limit of tension, with d_{avg} from 380 nm to 1 μm. The points with d_{avg} around 10 μm are the respective preforms. The blue curve contains the same factor similarly calculated in ref. [84] for wire array structures drawn in polymer fibres (indium/PMMA-Zeonex). The lines cor-

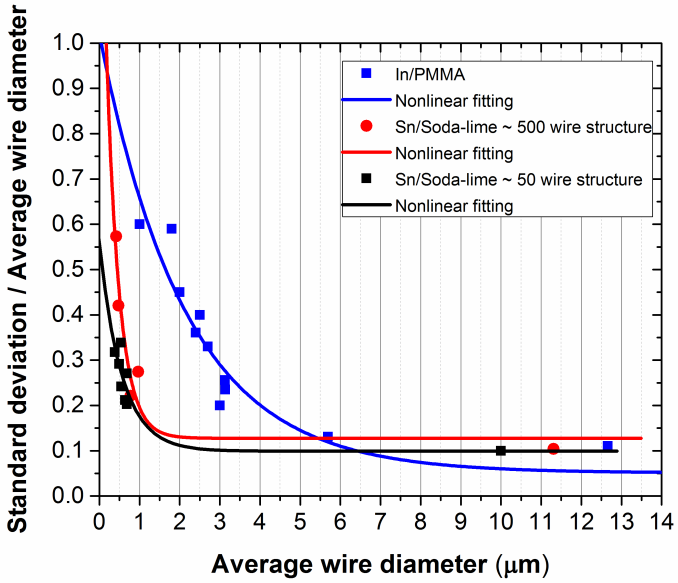

Figure 4.24: Comparison of the standard deviation divided by the average wire diameter between the indium/PMMA-Zeonex system (blue dots) and the tin/soda-lime system for the ~ 50 wires (red dots) and ~ 500 wires (black dots) structures. The indium/PMMA-Zeonex data was extracted from Ref. [84]. The lines correspond to nonlinear fittings, which were selected according to their agreement with the experimental points (nonlinear functions that minimize the residual sum of squares).

respond to nonlinear fittings, which were selected according to their agreement with the experimental points (nonlinear functions that minimise the residual sum of squares (RSS)).

Considering the Plateau-Instability limit as the wire diameter corresponding to $\sigma_d/d_{\text{avg}} = 1/\text{e}$ (≈ 0.37), Fig. 4.24 indicates that such limit for drawn structures shifts from wire diameter around 2.5 μm for the indium/polymer system, to wire diameter around 600 nm ($\sim$500 wire structure, red line) and 300 nm ($\sim$50 wire structure, black line) for the tin soda-lime system, respectively.

It is important to emphasize that small fluctuations in the wire diameters are already seen in the metamaterial preforms before the last drawing (Fig. 4.20 and Fig 4.21), which are due to inconsistent capillary sizes employed in the hole array stacking or appearing during the hole array cane drawing

due to assymetries and vacuum (they are not from Plateau-Rayleigh instability). This type of structural fluctuation varies between the different preforms used to fabricate the different fibres. Therefore, the Plateau-Rayleigh instability limit shown in Fig. 4.24 should be treated as an approximation. A more precise result could be achieved if drawing at the limit of the drawing tension is ensured, which is possible if the pulling tension is monitored during the drawing process. This is not available on the draw tower used.

How to obtain even better structures stretching the preform under extreme conditions is described in the next section.

4.4.1 Avoiding Plateau-Rayleigh instability: Last stretching under extreme conditions

Instead of drawing in the fibre draw tower, the last stretching of the metamaterial preform to fibre can be replaced by a quick, high-tension pulling process, referred to here as tapering. The shorter timescale of this process and the possibility of applying higher pulling tension can result in a shift of the Plateau-Rayleigh limit, which leads to more uniform wire array structures.

The tensile strength of the preform is strongly related to the quality of the glass surface and, according to [143], it can vary from 20 to 200 MPa ($\approx$ from 2 to 20 $\mathrm{kg/mm^2}$) for soda-lime glass. When continuous drawing is employed, high pulling tension is hard to maintain because some defect on the surface of the glass eventually breaks the fibre. In the tapering process, because only a small portion of the preform is heated and stretched, it is possible to achieve pulling tensions by area higher than those effectively obtained in a continuous draw process. Consequently, the preform can be stretched under higher viscosity of the glass in comparison with the drawing.

In addition to the higher viscosity of the glass during the stretching, the smaller hot zone and faster pulling velocity of the tapering process decreases the cooling time of sample. According to Eq. (4.1), both higher viscosity and smaller dwell time decrease the Plateau-Rayleigh instability.

In our developed tapering setup, the metamaterial preform is locally heated by a butane torch while a weight previously attached to its bottom end stretches it, as illustrated in Fig. 4.25(a). This process yields three samples: two conical transition regions, called tapered metamaterial fibre, and a straight fibre between them, as seen in Fig. 4.25(a). The tapered fibre can

be used as magnifying hyperlens, as will be discussed in the next Chapter.

It is important to emphasize that the straight region possesses a slight variation in the outside diameter along its length, which will not be detrimental for applications that are limited to short samples with length smaller than 200 μm, such as imaging with a straight hyperlens (the length is in practice limited by the overall optical loss) or lifetime engineering with metamaterials.

Figure 4.25(b) and (c) show an example of tin/soda-lime metamaterial fibre (straight fibre) fabricated by tapering in the last stretching process. The resultant structure has $d_{\text{avg}} = 532\,\text{nm}$, Λ around 1.06 μm and $\sigma_d/d_{\text{avg}} = 0.14$, which represents a remarkable uniformity for such dimensions.

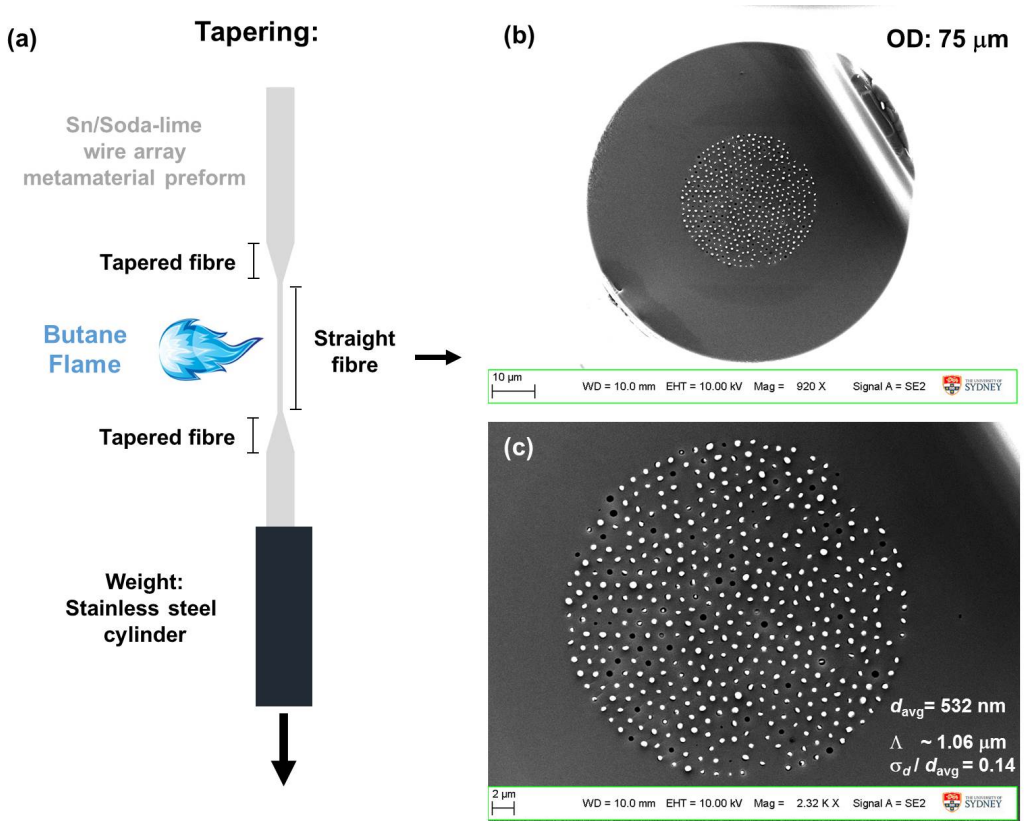

Figure 4.25: (a) Schematic of the tapering process and the resultant samples: two tapered and one straight fibre. (b) Final tin/soda-lime metamaterial fibre with $d_{\text{avg}} = 532\,\text{nm}$ and $\Lambda \approx 1.06\,\mu$m, fabricated by tapering the few hundred wire metamaterial preform (Fig. 4.21). (c) Zoom into the wire array region of the straight metamaterial fibre.

The improvement in the quality and uniformity of the wire array becomes evident when two equivalent structures, with a similar d and Λ, are fabricated by the two methods and compared. Figure 4.26 shows such structures fabricated from a similar 500 wires metamaterial preform (Fig. 4.21), by drawing and by tapering, respectively. The wire array made by drawing has $d_{\text{avg}} = 479\,\text{nm}$ and $\sigma_d/d_{\text{avg}} = 0.42$, while the one made by tapering has $d_{\text{avg}} = 532\,\text{nm}$ and $\sigma_d/d_{\text{avg}} = 0.14$.

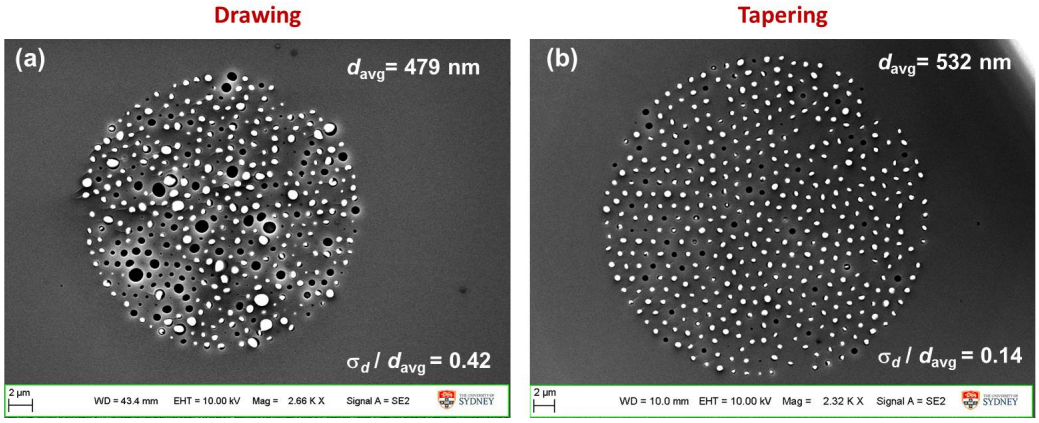

Figure 4.26: Comparison between similar structures fabricated by drawing (a) at the minimum drawable temperature (highest tension and viscosity) and by tapering (b). Both fabricated from the metamaterial preform showed in Fig. 4.21.

In the drawing process, the metamaterial preform is sleeved and pulled with a jacket tube with $\text{OD} = 10\,\text{mm}$ and $\text{ID} = 1.2\,\text{mm}$, and the drawing parameters are adjusted to the limit of pulling tension (experimentally determined by trial and error based on fibre's breakage). In the tapering process, the metamaterial preform is not sleeved. A 50 g weight is attached to its bottom, a hand butane torch heats a short piece of the preform (around 1 cm). After a few seconds of heating, the weight tapers the preform by gravity. Such weight of 50 g generates an initial pulling tension by area of $63.6\,\text{g}/mm^2$ in the metamaterial preform ($\text{OD} = 1\,\text{mm}$).

In the straight fibre region of the taper ($\text{OD} = 75\,\mu\text{m}$ for the sample showed in Fig. 4.25), such weight produces a pulling tension by area of $11.32\,\text{kg}/mm^2$. In order to achieve the same tension by area on the fibre by drawing, it is necessary to have a pulling tension equivalent to 5 kg, because the extra jacket increases the area by a factor of 100. Such tension

seems much higher than the one usually employed during our drawings (the measurement of the pulling tension is not available in our fibre tower).

A better visualization of the improvement due to the replacement of the drawing by the tapering can be seen in Fig. 4.27, containing the σ_d/d_{avg} as a function of the average wire diameter for two sets of nearly 500 wires structures fabricated by the two different methods. Even structures with d_{avg} around 200 nm presented a σ_d/d_{avg} smaller than 0.2.

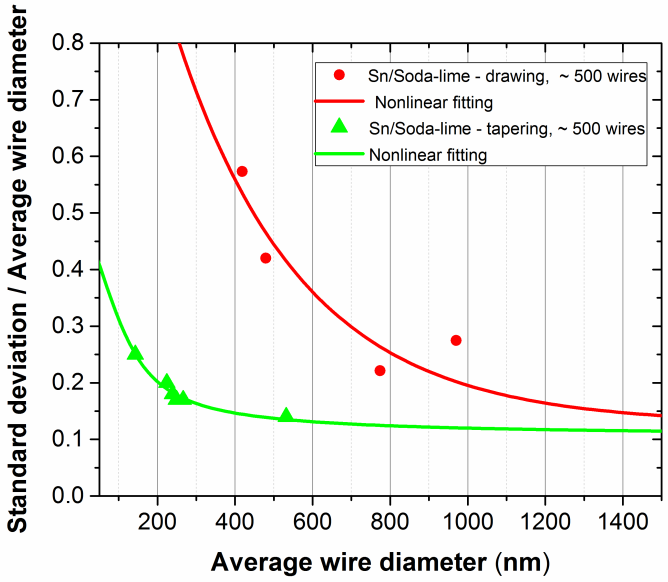

Figure 4.27: Comparison of the standard deviation divided by the average wire diameter for tin/soda-lime wire array structures made by drawing at the limit of the pulling tension (red curve) and by tapering (green curve) for the last fabrication step. All samples fabricated from a metamaterial preform with few hundreds of wires (Fig. 4.21). The lines correspond to nonlinear fittings, which were selected according to their agreement with the experimental points (nonlinear functions that minimise the residual sum of squares).

Figure 4.28(a-c) show other examples of metamaterial fibres fabricated, having uniform wire array structures with σ_d/d_{avg} smaller than 0.18, with d_{avg} varying from 266 nm to 239 nm. Figure 4.28(d) shows the smallest structure fabricate, with $d_{\text{avg}} = 143$ nm, $\Lambda \approx 285$ nm, $\sigma_d/d_{\text{avg}} = 0.25$.

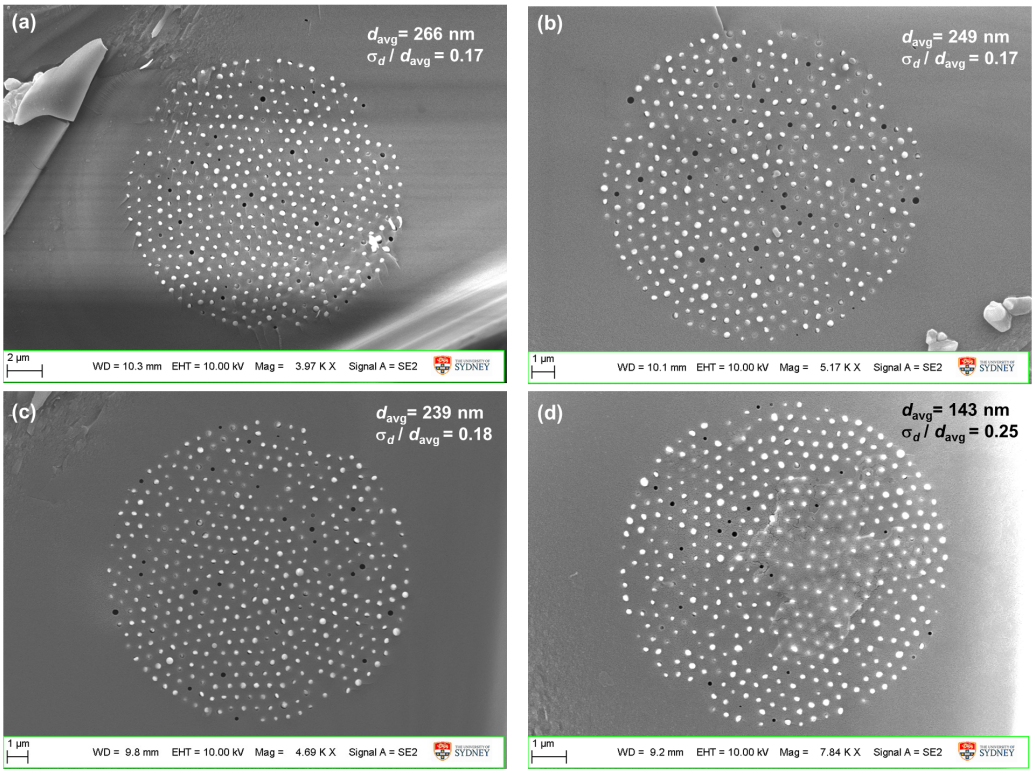

Figure 4.28: Other examples of tin/soda-lime wire array metamaterial fibres fabricated by the tapering of the stretched metamaterial preform showed in Fig. 4.21. (a) $d_{\mathrm{avg}} = 266\,\mathrm{nm}$, $\Lambda \approx 530\,\mathrm{nm}$, $\sigma_d/d_{\mathrm{avg}} = 0.17$. (b) $d_{\mathrm{avg}} = 249\,\mathrm{nm}$, $\Lambda \approx 500\,\mathrm{nm}$, $\sigma_d/d_{\mathrm{avg}} = 0.17$. (c) $d_{\mathrm{avg}} = 239\,\mathrm{nm}$, $\Lambda \approx 480\,\mathrm{nm}$, $\sigma_d/d_{\mathrm{avg}} = 0.18$. (d) $d_{\mathrm{avg}} = 143\,\mathrm{nm}$, $\Lambda \approx 285\,\mathrm{nm}$, $\sigma_d/d_{\mathrm{avg}} = 0.25$.

4.5 Conclusion and discussion

Comparing the instabilities seen in the indium/polymer system (Fig. 4.24 and [84]) with our best structures, the level of quality $\sigma_d/d_{\mathrm{avg}} < 0.18$ reached for wires with diameter larger than 240 nm can be only obtained with wire diameters around $4.3\,\mu$m in the indium/PMMA system. Therefore, it is clear that the replacement of the polymer by soft-glasses and the use of the tapering process in the last fabrication step made possible the fabrication of a wire structure approximately 18x smaller with an equivalent quality, which is a remarkable improvement in such a complex co-drawing process.

Besides its slightly higher fluctuation in the wire diameters ($\sigma_d/d_{\mathrm{avg}} = 0.25$),

the smallest structure (seen in Fig. 4.28(d)) can still be employed for imaging and lifetime engineering applications. Comparing again with the instabilities seen in the indium/polymer system (Fig. 4.24 and [84]), the level of quality $\sigma_d/d_{\text{avg}} < 0.25$ can be only achieved in the indium/polymer system with wires larger than 3.36 μm. Therefore, for this size of structure, the use of soft-glass made possible the fabrication of a wire array structure ∼23x smaller with a equivalent quality.

Regarding the Plateau-Rayleigh instability limit (considered here the wire diameter corresponding to $\sigma_d/d_{\text{avg}} \approx 0.37$), the extrapolation of the nonlinear fitting (green line) presented in Fig. 4.27 indicates that such a limit has an expected value around 70 nm for the tin/soda-lime system, when the tapering is employed in the last stretching process, which is 34x smaller than the limit for the indium/PMMA system (around 2.4 μm according to Fig. 4.24 and [84]). Consequently, tin/soda-lime system and the tapering process could produce relatively uniform wire array structures even for wire diameters smaller than 140 nm. Such dimensions were not fabricated because this is outside the scope of this work. Indeed, the focus here is on MIR applications for which sub-250 nm wires exhibit huge optical losses, as concluded in Chapter 3.

A better control of the tapering process regarding the stretching ration and the profile of the transition region can be performed with conventional tapering setups and techniques commonly used for optical fibres. However, care must be taken with the heating method of the tapering region and the tension applied in the preform. In Chapter 5, another tapering setup using a commercial pipette puller adapted in a vertical configuration is presented, which provides more control over important parameters for the tapering process such as the length of the hot zone, the pulling temperature and heating time. Such control makes possible the fabrication of extremely steep tapers in short lengths, required for the production of tapered magnifying hyperlenses.

Chapter 5

Subdiffraction imaging with metamaterial fibres

This Chapter presents the fabrication of our tin/soda-lime wire array magnifying hyperlenses, their numerical modeling, and a far field subdiffraction imaging attempt with such metadevices in the mid-infrared. First, it is introduced the diffraction limit, how metamaterial-based lenses can be employed for near and far field subdiffraction imaging, and the use of metamaterial fibre hyperlenses for imaging at THz frequencies is reviewed. A discussion about magnifying hyperlenses for subdiffraction imaging in the mid-infrared is presented, including their requirement regarding structural parameters, magnification factor and the maximum acceptable overall losses.

The entire fabrication process of our tin/soda-lime wire array magnifying hyperlens is described, which includes the production of an extremely short taper from a wire array metamaterial preform (the preform fabrication was demonstrated in Chapter 4) and the selection of a specific taper section, according to the desired parameters for the hyperlens (overall loss, resolution and magnification factor).

The far field experimental setup is described, which includes the building of an Er-ZBLAN fibre laser for high output power at $2.8\,\mu$m. The far field imaging of a set of apertures, above and below the diffraction limit for an operational wavelength of $2.8\,\mu$m, is presented. The diffraction limit is characterized and confirmed with simulation (Fourier analysis). Finally, far field subdiffraction imaging with our magnifying hyperlenses is attempted and assessed. To conclude, possible improvements and future perspectives for far field super resolution imaging in the MIR and NIR using magnifying

metamaterial hyperlenses are discussed.

5.1 Diffraction limit and subdiffraction imaging with metamaterials

5.1.1 Diffraction limit

In an ideal optical system, every point of an object would be imaged as a point in the image plane. However, in real optical systems, light diffracts in the lens/objective and the image of a point becomes a blur. This diffraction blur resulting from the imaging of a point source is called the point spread function (PSF). In an optical system with a circular aperture, the PSF is also called the Airy disk or Airy pattern [174]. Figure 5.1 illustrates the cross-section of the intensity distribution and energy distribution of an Airy disc (a) and how it appears in the image plane (b), which can be described with a Bessel function of the first kind (J).

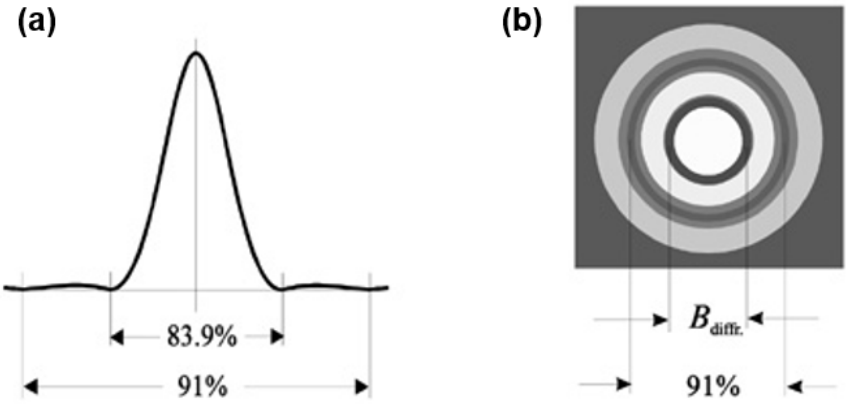

Figure 5.1: Airy disk. (a) Field and energy distribution. (b) Appearance in the image plane. Figures extracted from Ref. [175].

Two neighbouring point sources are considered resolvable if they are distinguishable in the image plane. In this scenario, the minimal distance between their center in which they are still resolvable is defined as the diffraction limit. However, this limit depends on the criterion used of what is a distinguishable blur, which leads to some arbitrariness in the definition of the

diffraction limit. Several different criteria have been proposed and employed since the last decades of the eighteenth century, and a historical overview can be found at Ref. [176].

In 1883, Ernst Abbe used diffraction theory to formulate the resolution limit of an imaging system illuminated by coherent light as [177]

$$l = \frac{\lambda_0}{\mathrm{NA}} \quad \text{(coherent illumination)}, \tag{5.1}$$

where λ_0 is the wavelength in free-space, NA$= n \sin\theta$ is the numerical aperture of the lens/objective used in the system, and n is the refractive index of the medium. Abbe argued that, under oblique coherent illumination, it is possible to collect higher diffraction orders [177,178]. Therefore, if the angles of incidence and collection are the same (the NA of the illumination lens and collection lens is the same), the diffraction limit becomes

$$l = \frac{\lambda_0}{2\mathrm{NA}} \quad \text{(Abbe diffraction limit)}, \tag{5.2}$$

which is the famous Abbe diffraction limit formula. One year after Abbe's famous work (which does not contain any mathematical notation), Hermann von Helmholtz published the same results containing a detailed mathematical derivation [179]. According to Helmholtz, Eq. (5.2) also holds for incoherent illumination, even when it is not oblique. In the scope of this thesis, we consider the Abbe limit (Eq. (5.2)) as the diffraction limit of our optical system.

Considering the Abbe limit and also the collection of all diffracted wavevectors ($sin\,\theta$=1), it is possible to define the diffraction limit of the medium as

$$l = \frac{\lambda_0}{2n}. \tag{5.3}$$

5.1.2 Overcoming the diffraction limit with metamaterials

The diffraction limit of an optical system in the far field arises from the nature of the light scattering and the spatial bandwidth of free-space. When an incident beam of light scatters on an object into a medium with refractive index n, the object's information is transferred to a wide spectrum of wavevector components (Fig. 5.2(a)), which can be propagating waves ($|k_\perp| < n|k_0| = 2\pi n/\lambda_0$, considering $\perp$ the plane transverse to the propagation direction z) or evanescent waves ($|k_\perp| > n|k_0|$, and k_z is imaginary). Because the evanescent waves possess larger transverse wavevector components, they carry finer details about the object than the scattered propagating waves. In a conventional optical system, such evanescent high $k_\perp$ waves decay exponentially, being effectively attenuated before reaching the image plane. Consequently, part of the information about the object is lost, and the resolution of the detected image is always "diffraction limited".

This resolution limit can be overcome with different approaches, such as near field scanning techniques [180] or fluorescence-based imaging methods [181,182]. However, both mentioned methods are slow and fluorescence-based methods are currently limited to the visible. Far field super-resolution imaging based on lens projection is an interesting alternative for high-speed imaging/microscopy. Several liquid and solid immersion techniques have been employed to enhance resolution (increasing the employed NA, which decreases the diffraction limit), but they are limited by the refractive index of conventional materials [183].

Nowadays, some types of metamaterial-based lenses offer alternative routes for subdiffraction imaging [22, 184, 185], such as perfect lenses, superlenses, metalenses, resonant metalenses, and hyperlenses. The behaviour and working mechanism of some of these metadevices are illustrated in Fig. 5.2(b), in comparison with a conventional lens.

Metamaterial perfect lens [91] and superlenses employ surface plasmon excitation to enhance the transmitted evanescent waves, which can compensate the evanescent attenuation due to the propagation outside the perfect/superlens [91, 184, 186]. If the image is detected in the near field, such compensation increases the number of evanescent modes detected, and improved super-resolution imaging is attained [186]. Far field subdiffraction imaging with superlenses is also possible if a coupling mechanism (diffraction grating) is employed to convert the high-$k_\perp$ waves [187,188], which do not usually

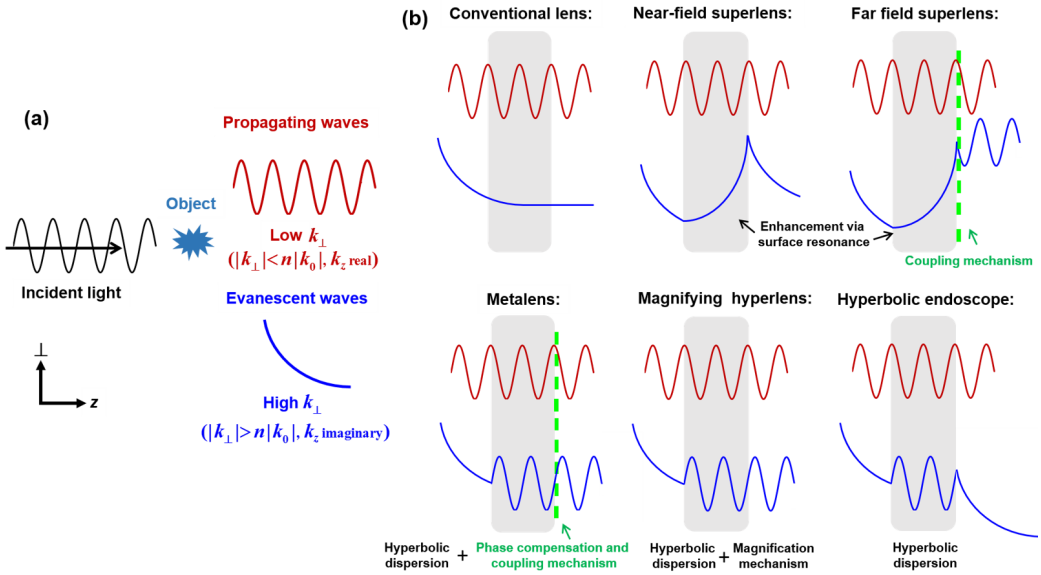

Figure 5.2: (a) Schematic of the light scattering at an object, generating propagating waves (low $k_\perp$ waves) and evanescent waves (high-$k_\perp$ waves, with $|k_\perp| > 2\pi n/\lambda_0$, and k_z imaginary). (b) Comparison of the behavior of several types of metamaterial-based lenses with a conventional lens: Near field superlenses, far field superlenses, metalenses, magnifying hyperlenses and hyperbolic endoscope.

couple from the metamaterial to free-space due to total internal reflection, into low $k_\perp$ propagating waves in free-space.

Due to their hyperbolic (or extremely elliptical) dispersion, metalenses and hyperlenses propagate waves with high spatial frequencies. Similarly to the far field superlens case, a mechanism at the end facet of the metamaterial that couples such high-$k_\perp$ modes into low $k_\perp$ propagating modes in free space (coupling mechanism) enables subdiffraction far field imaging with such metadevices, as illustrated in Fig. 5.2(b). In metalenses, such a coupling mechanism also provides a phase compensation that allows focusing of a plane wave below the diffraction limit. Over the years, different approaches were proposed for such a coupling mechanism: shaped metamaterial air interfaces (like conventional lenses) [189], diffractive structures to engineer the wavefront (plasmonic waveguide coupler) [190] and material refractive index variation (gradient-index metamaterial) [191]. Note that, a cluster of subwavelength resonators, called a resonant metalens, can also be employed for

far field subdiffraction imaging [192–194]. In addition, the term metalens is also employed by some research groups for far field metasurfaces [195–197].

In magnifying hyperlenses, the structural parameters of the metamaterial vary along the length and in the specific case of spherical magnifying hyperlenses, due to the conservation of angular momentum [31], the transverse components of the high spatial frequencies are transformed into low spatial frequencies. If the magnification factor is high enough to compress the high spatial frequencies to frequencies smaller than k_0, they become propagating waves after the hyperbolic medium, and subdiffraction far field imaging is attained [31]. Figure 5.3 shows two geometries that have been employed in the fabrication of magnifying hyperlenses, the curved multilayer metamaterial (Fig. 5.3(a)), and the tapered wire array (Fig. 5.3(b)).

In a hyperbolic endoscope form by a hyperbolic medium [50], there is no magnification effect and, consequently, the subdiffraction information is only transported away from its source and must be detected with near field techniques at the end of the hyperbolic endoscope.

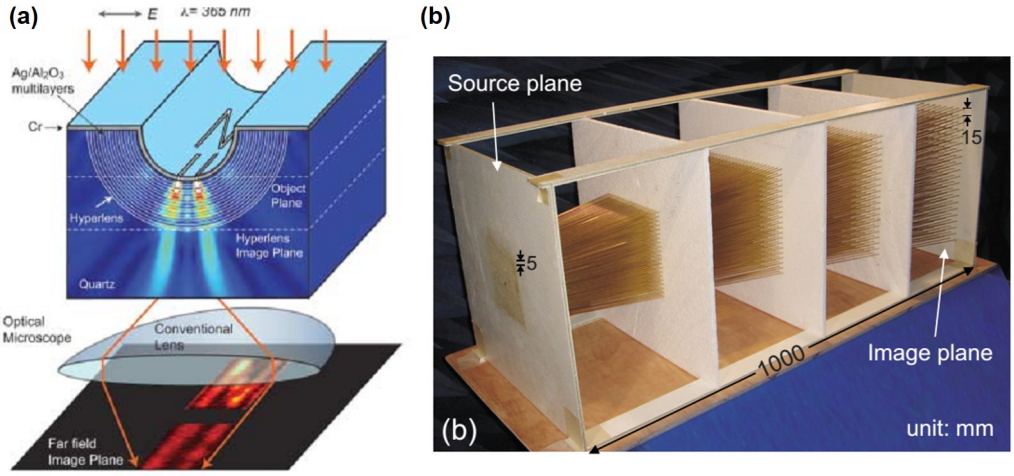

Figure 5.3: Examples of the two most common types of magnifying hyperlenses: (a) the curved multilayer metamaterial (Picture extracted from Ref. [48]); (b) the tapered wire array metamaterial (Picture extracted from Ref. [47]).

A more detailed review of those metadevices and the physics behind their operation can be found at Refs. [22, 184, 185].

Metamaterial fibre hyperlenses for imaging applications at THz frequencies

Wire array metamaterial fibres are an interesting platform for the fabrication of wire array metamaterial hyperlenses. The drawing technique allows large volume production of hyperbolic endoscope (straight hyperlens without magnification effect) and offers great control on the dimensions of the final fibre's structure. The neckdown region that results from the drawing of a preform generates a tapered magnifying hyperlens. In addition, tapering techniques commonly employed for optical fibres can be adapted and used to fabricate tapered magnifying hyperlenses from large-scaled metamaterial fibres, with great control in the transition profile (steepness and length).

In the past, our group has demonstrated the fabrication of straight and magnifying wire array metamaterial hyperlenses by fibre drawing, made of indium wires embedded in polymer (PMMA/Zeonex) [50], for imaging applications at THz frequencies. A metamaterial preform was fabricated by stacking indium wires embedded in Zeonex (proprietary name of a cyclo-olefin polymer with low absorption at THz frequencies) into a PMMA jacket tube. Figure 5.4(a) shows a schematic of the drawing of such a metamaterial preform, while Fig. 5.4(b) shows its cross-section, containing 453 indium wires ($d \sim 160\,\mu$m, $\Lambda \sim 800\,\mu$m). Figure 5.4(c) and (d) show a picture and a X-ray CT scan, respectively, of a 8x magnifying hyperlens selected from the neckdown region of the preform after drawing. Figure 5.4(e) shows a microscope cross-section image of the small facet of the hyperlens, containing a wire array with $d \sim 10\,\mu$m, $\Lambda \sim 50\,\mu$m.

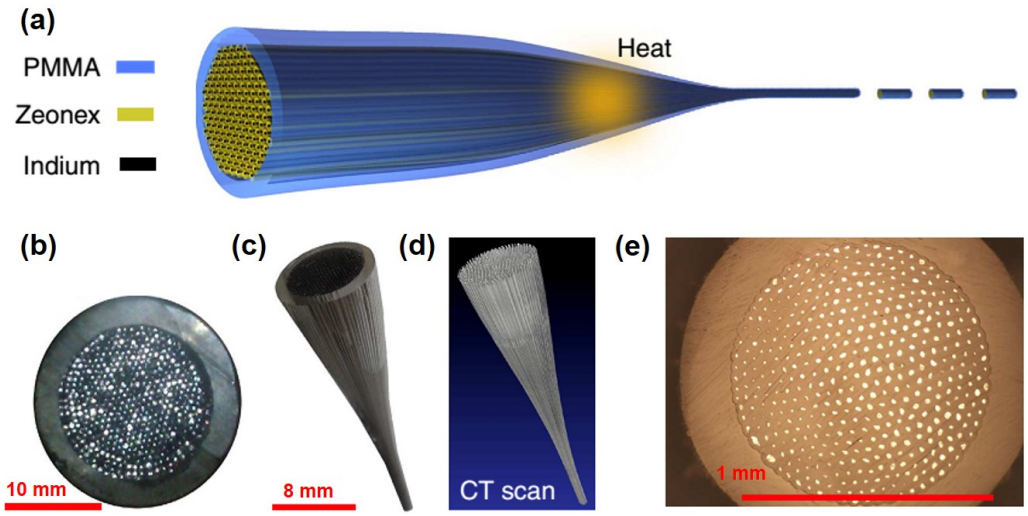

Figure 5.4: (a) Schematic of the wire array metamaterial preform composed of indium wires embedded in polymer (PMMA and Zeonex), and its drawing to fibre. (b) Cross-section picture of the preform containing 453 indium wires ($d \sim 160\,\mu$m, $\Lambda \sim 800\,\mu$m). Photograph (c) and X-ray CT scan (d) of the tapered wire array magnifying hyperlens, with magnification factor of 8x (ratio between the diameter of both facets). (e) Microscope image of the smallest facet of the hyperlens ($d \sim 10\,\mu$m, $\Lambda \sim 50\,\mu$m). Figures adapted from Ref. [50].

Tuniz *et al.*, using the above-mentioned hyperlens, demonstrated super resolution imaging in the THz spectrum, with propagation of subdiffraction information over hundreds of wavelengths. Figure 5.5(a,b) shows the measured and simulated image of two circular apertures ($d = 200\,\mu$m) with $100\,\mu$m inner-edge separation at 0.11 THz, after the propagation through 3.4 mm of metamaterial fibre. The experimental image was obtained by scanning a near field probe on the output facet of the fibre, and the simulated one was calculated $50\,\mu$m from the fibre output. The intensity cross-section profiles through the middle of the apertures along the x direction clearly indicate that the double aperture is resolvable with a resolution better than $\lambda/27$, as seen in Fig. 5.5(c).

In addition, focusing with an 8x magnifying hyperlens (Fig 5.4(c)) of a 75 GHz beam down to 1/28 of the wavelength in one direction was also demonstrated. Figure 5.5(d) shows the near field image of the signal coupled in the large facet of the magnifying hyperlens with a 1 mm circular aperture (circle in white), while Fig. 5.5(e) shows the focused beam after the hyperlens,

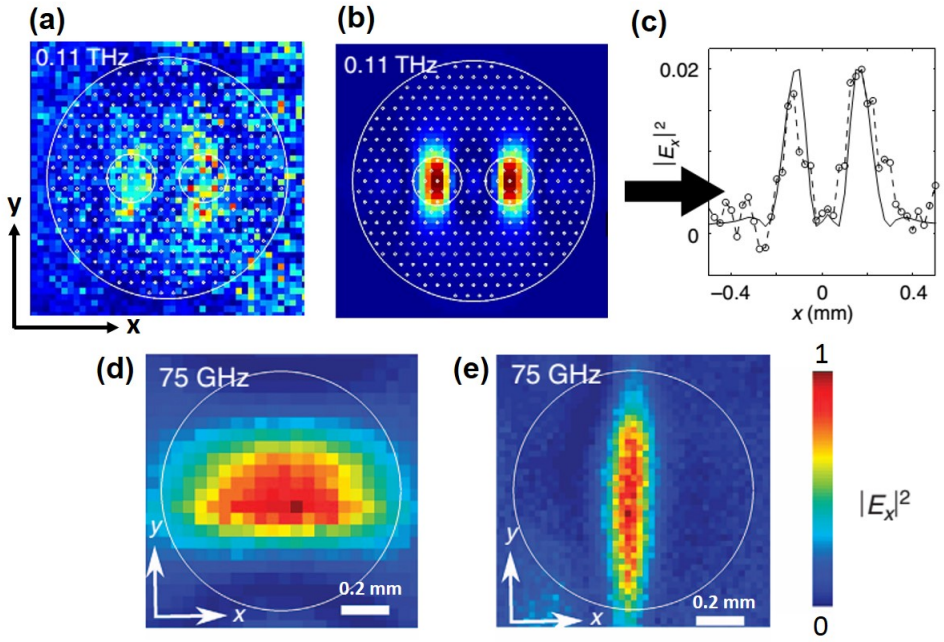

Figure 5.5: Experimental (a) and simulated (b) image of two circular apertures with $d = 200\,\mu$m and $100\,\mu$m inner edge separation, at 0.11 THz, after 3.4 mm of metamaterial fibre (straight hyperlens with the structure showed in Fig. 5.4(e)). (c) Intensity cross-section profile of the simulated and experimental image, in the x direction through the middle of the apertures, showing that they are resolvable, with a resolution better than $\lambda/27$. (d) Image of the input signal coupled into the large facet of the tapered hyperlens (Fig. 5.4(c)) with a 1 mm aperture (white circle), at 75 GHz. (e) Resultant subdiffraction focusing, acquired with near field scanning performed on the small facet of the tapered hyperlens, showing a strong focusing in the x direction, with full width at half maximum of $\lambda/28$. Figures adapted from Ref. [50].

measured with the near field probe scanning the small facet of the hyperlens.

As discussed before, the requirement for the meta-structures to be sub-wavelength, restricts wire array metamaterials to structures with wire diameter and wire spacing around a few hundred of nanometers if applications in the MIR are intended. However, due to the rheological properties of the materials, the Plateau-Rayleigh instability limits the drawing of wire arrays to those with wires with diameter around a few microns in the polymer/indium system [84]. In this context, the work presented in this thesis also aims to

fabricate tapered wire arrays metamaterial fibres based on tin and soda-lime to obtain MIR hyperlenses.

5.2 Wire array magnifying hyperlenses for operation in the MIR

In this section, the optical design and performance of magnifying wire array hyperlenses are discussed according to their structural parameters (material components, wire diameter, distance between the wires and overall length), for an operational wavelength of $\lambda = 3\,\mu$m. The high optical loss of the high-$k_\perp$ modes in such devices, due to the presence of the metal and Ohmic losses, represents a huge constraint in the design.

Firstly, the resolution is discussed, followed by the magnification factor, and overall optical loss of tapered wire array hyperlenses. Possible magnifying hyperlens designs of wire array structures based on gold/silica and tin/soda-lime systems are presented, which represent a high optical quality option (but expensive) and a lossy low cost option, respectively. Finally, the fabrication process of our tin/soda-lime wire array magnifying hyperlens is described and far field imaging in the MIR is attempted and discussed.

Achieving subdiffraction imaging with wire array metamaterial hyperlens

What conditions must be fulfilled in an imaging experiment in order to beat the diffraction limit?

A one-dimensional feature/object with size a in real-space can be represented by a spatial frequency equal to (π/a) in k-space. Therefore, we assume that it is necessary to detect a scattered/diffracted wave with $|k_{req}| \geq \pi/a$ to resolve this feature/object with an imaging device, where the $|k_{req}|$ is the spatial frequency component parallel to the dimension of the feature/object.

In vacuum, propagating waves have $|k_0| = \omega/c = (2\pi/\lambda_0)$. Thus, the maximum spatial frequency component parallel to our fictitious one dimensional object is $2\pi/\lambda_0$. Consequently, the condition ($|k_{req}| \geq \pi/a$) becomes

$$a \geq \frac{\lambda_0}{2}, \tag{5.4}$$

meaning that in free space, with an operational wavelength λ_0, it is only possible to resolve a feature/object equal or larger than $\lambda_0/2$. Not surprisingly, this is the equivalent condition obtained with the Abbe diffraction limit (Eq. (5.2)) considering $n = 1$ and that all the waves are collected ($sin\,\theta = 1$).

Similarly, if the feature/objective is immersed in a medium with refractive index n, the maximum spatial frequency component parallel to our fictitious one-dimensional object is nk_0. Thus, the condition ($|k_{req}| \geq \pi/a$) becomes

$$a \geq \frac{\lambda_0}{2n}, \tag{5.5}$$

which again is in agreement with the Abbe diffraction limit in the medium (Eq. (5.3)). Since Eq. (5.5) does not take into account the spatial cut-off of a lens/objective in the detection, we considered this the diffraction limit of the medium.

For a hyperbolic metamaterial, the modulus of the wavevector of propagating waves is not bounded by $n\omega/c$. As discussed previously, the hyperbolic dispersion allows the propagation of extraordinary modes (quasi-TEM) with $k_\perp > nk_0$ and k_z real (considering $\perp$ the plane transverse to the propagation direction z). In real wire array hyperbolic metamaterials, such propagating spatial frequencies are limited by the lattice size and arrangement of the wires (*i.e.* by the edge of the Brillouin Zone, see Fig. 5.6).

For a wire array metamaterial with vertically aligned wires squarely or hexagonally arranged, and embedded in a dielectric medium with refractive index n, the maximum propagating transverse spatial frequencies allowed in the medium ($k_{\perp max}$), matching the edge of the respective Brillouin zone [34], are approximately given by

$$|k_{\perp max}|_{sq} = \frac{\pi\sqrt{2}}{\Lambda}, \quad \text{(Square array)}, \tag{5.6}$$

$$|k_{\perp max}|_{hx} = \frac{2\pi}{\Lambda\sqrt{3}}, \quad \text{(Hexagonal array)}, \tag{5.7}$$

where Λ is the distance between the wires, as seen in Fig. 5.6.

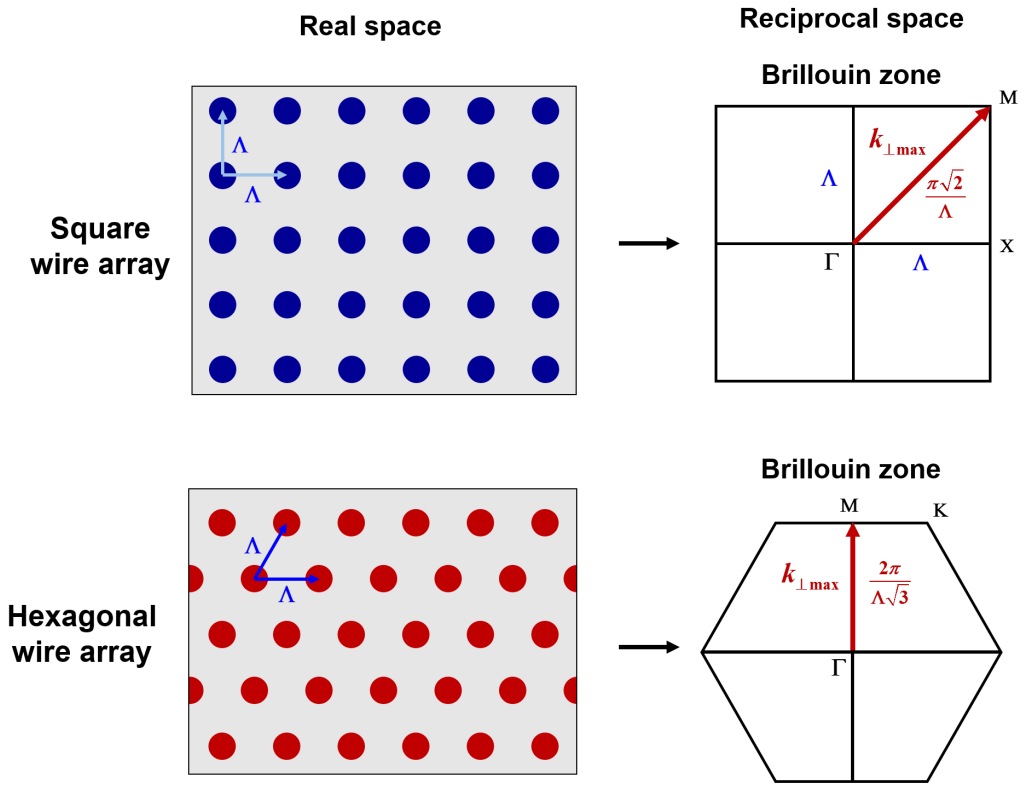

Figure 5.6: Schematic of the Brillouin zone and $k_{\perp max}$ for the square and hexagonal wire arrays.

Note that, strictly, the maximum propagating transverse spatial frequencies in the hexagonal lattice matches the edge of the Brillouin zone in the direction $\overline{\Gamma\mathrm{K}}$ ($4\pi/(3\,\Lambda)$), which is slightly larger than $2\pi/(\Lambda\sqrt{3})$. However, we consider here $k_{\perp max} = 2\pi/(\Lambda\sqrt{3})$ in order to be consistent with the periodic conditions employed in the simulations presented in Chapter 3 and throughout this Chapter.

Reversing the argument that a feature size of a can be detected with a spatial frequency π/a, the maximum spatial frequencies of Eqs. (5.6-5.7) can resolve features of

$$a_{sq} = \frac{\Lambda}{\sqrt{2}}, \qquad \text{(Square array)} \tag{5.8}$$

$$a_{hx} = \frac{\Lambda\sqrt{3}}{2}. \quad \text{(Hexagonal array)} \tag{5.9}$$

In order to overcome the diffraction limit obtained in a medium with refractive index n ($l = \lambda_0/2n$) using a wire array metamaterial with wires also embedded in a medium with n, it is required that a_{sq} or a_{hx} be smaller than a. Combining Eqs. (5.8-5.9) with Eq. (5.5), the structural requirement for subdiffraction imaging becomes

$$\Lambda_{sq} < \frac{\lambda_0}{(2/\sqrt{2})n}, \tag{5.10}$$

$$\Lambda_{hx} < \frac{\lambda_0}{\sqrt{3}n}, \tag{5.11}$$

for square and hexagonal arrays of wires, respectively.

Besides the minimum Λ given by the previous conditions, two other important factors must be taken into account for subdiffraction imaging in the far field to be feasible: the magnification factor and the overall loss of the high-$k_\perp$ modes.

Ideal magnification factor

Ideally, the magnification factor of the hyperlens must be large enough to transform all the high-$k_\perp$ modes propagating in the metamaterial into propagating waves in vacuum ($|k_\perp| < |k_0| = 2\pi/\lambda_0$, considering $\perp$ the plane transverse to the propagation direction z), at the end of the metadevice. Thus, the magnification factor (m_f) for the magnifying hyperlens must be

$$m_f \geq \frac{|k_{\perp max}|}{|k_0|}. \tag{5.12}$$

where $k_{\perp max}$ is the largest transverse wavevector component allowed to propagate in the metamaterial at the narrow end of the hyperlens.

Combining Eq. (5.6) and Eq. (5.7) with Eq. (5.12), the ideal magnification factor of the square ($m_{f,sq}$) and hexagonal ($m_{f,hx}$) wire array are given by

$$m_{f,sq} \geq \frac{\lambda_0\sqrt{2}}{2\Lambda}, \tag{5.13}$$

$$m_{f,hx} \geq \frac{\lambda_0}{\Lambda\sqrt{3}}, \tag{5.14}$$

where Λ is the center to center distance between the wires on the smallest side of a wire array magnifying hyperlens, which must also obey the conditions discussed in the previous section.

Maximum acceptable overall optical losses

Experimentally, the resolution achieved in an imaging experiment performed by a metadevice depends on the largest spatial frequency detected after the metamaterial. Therefore, besides the requirement regarding the allowed high spatial frequencies in the metamaterial and the minimum magnification factor needed to transform such spatial frequencies to propagating waves in vacuum, another important constraint is the overall optical loss of the high-$k_\perp$ the modes.

As discussed in the Chapter 3, the losses of the quasi-TEM modes in a hexagonal wire array metamaterial are strongly dependent on its material components, the structural parameters (wire diameter and lattice spacing), wavelength of operation, and the transverse wavevector component of the mode. Their typical losses can be around 1 dB/μm in the MIR. Consequently, the mentioned parameters and the length of the metadevice must be carefully selected to restrict the overall losses of the propagating high-$k_\perp$ modes to a detectable level.

In order to obtain an initial estimate of the typical optical losses of magnifying hyperlenses, an indefinite wire array structure was modeled with COMSOL [198], for different structures with a fixed d/Λ, emulating different cross sections along the length of a taper. For each structure, the effective refractive index of the quasi-TEM mode and Eq. (3.3) are used to calculate the modal optical loss in dB/μm.

Figure 5.7 shows the loss in dB/μm for the quasi-TEM mode with three different spatial frequencies as a function of d, with $d/\Lambda = 0.5$,for a hexagonal wire array, at $\lambda = 3\,\mu$m, where $k_{\perp max}$ corresponds to the transverse wave vector component matching the edge of the first Brillouin zone, which gives the maximum resolution of the hyperlens. Two different systems are considered, tin/soda lime (Fig. 5.7(a)), and gold/silica (Fig. 5.7(b)).

Using the losses presented in Fig. 5.7, the taper profile of the real samples

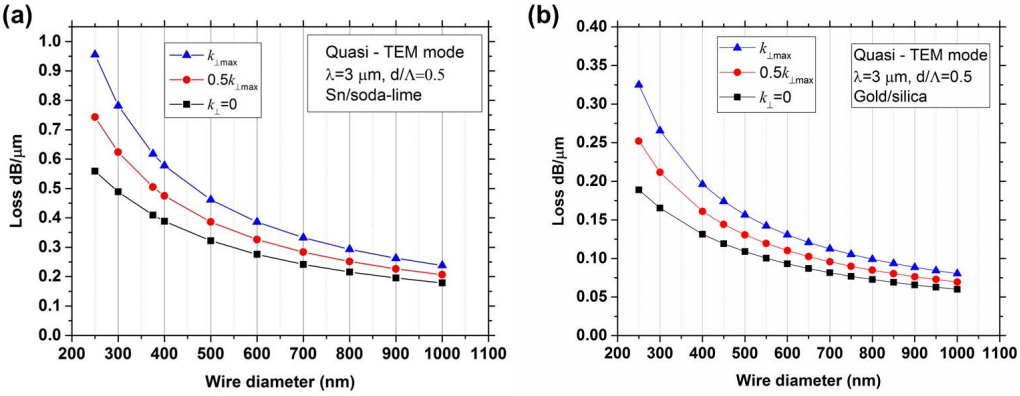

Figure 5.7: Loss in dB/μm for the indefinite hexagonal wire array structure with $d/\Lambda = 0.5$, as a function of the wire diameter, at $\lambda = 3\,\mu$m. The black, red and blue curves represent the modes with transverse wave vector equal to 0, $0.5k_{\perp max}$, and $k_{\perp max}$ respectively, where $k_{\perp max} = (\pi/\Lambda)(2/\sqrt{3})$ for a hexagonally arranged array. (a) Tin wire array embedded in soda-lime glass. (b) Gold wire array embedded in silica.

and their structural parameters scaled to their outside diameter, the overall optical loss can be estimated discretizing the tapering transition in several small slices along length and multiplying it with the loss of the respective cross section. The error of this approximation decreases with decreasing slice length, but assumes the transition is adiabatic. We define the nominal overall loss of the hyperlens as the loss of the quasi-TEM modes with $k_{\perp max}$, because they have the highest losses amongst the high-$k_\perp$ modes (Fig. 5.7) and they give the maximum resolution of the hyperlens.

In order to understand the typical length required to obtain a reasonable loss (low enough to make detection feasible), we propose a certain magnifying hyperlens and calculate the loss as a function of length considering a linear transition between the lens' two facets, as illustrated in Fig. 5.8(a). According to Eq. (5.11), a tapered wire array structure with $\Lambda < 1.17\,\mu$m in its smallest facet is required to beat the diffraction limit, when the operational wavelength is $3\,\mu$m and the wires are hexagonally arranged in a medium with $n = 1.4849$ (refractive index of soda-lime at $\lambda = 3\,\mu$m [132]). Therefore, the selected Λ for the smallest facet of this proposed linear hyperlens was 800 nm, which ensures subdiffraction imaging. The wire diameter was selected as 400 nm because of the typical $d/\Lambda = 0.5$ of the structures fabricated through-

out this thesis. According to Eq. (5.14), the ideal magnification factor for this proposed hyperlens (required to transform all the high-$k_\perp$ modes propagating in the metamaterial into propagating waves in free space) is around 2.16x. Therefore, the magnification factor selected for the proposed linear hyperlens was 2x, which results in a wire array structure with $d = 800\,\text{nm}$ and $\Lambda = 1.6\,\mu\text{m}$ on the hyperlens' largest facet (see Fig. 5.8(a)).

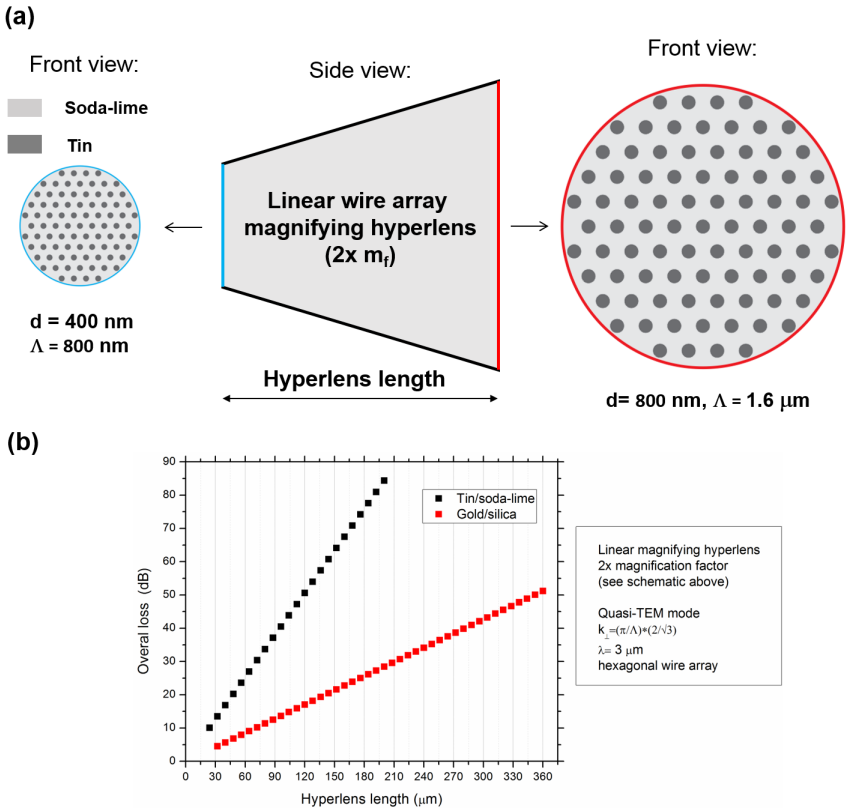

Figure 5.8: (a) Schematic of the proposed linear wire array magnifying hyperlens with 2x magnification and d varying from 400 nm to 800 nm, d/Λ =0.5, hexagonally arranged. (b) Overall loss in dB for the quasi-TEM mode ($k_{\perp max}$) for hyperlens illustrated in (a) with tin/soda-lime and gold/silica system, calculated with the losses of the respective indefinite wire arrays presented in Fig. 5.7.

Considering the limiting overall loss of the quasi-TEM mode with $k_{\perp max}$ as 50 dB (for a feasible detection attempt), Fig. 5.8(b) indicates that the proposed 2x magnifying hyperlens described in Fig. 5.8(a) must have an overall

length smaller than 120 μm for the tin/soda-lime system, or smaller than 360 μm for the gold/silica system. Note that these numbers are strongly related to the structural parameters selected for the magnifying hyperlens and how they vary over length. Therefore, these mentioned maximum overall lengths must be considered as mere indications of the transition required.

It is important to emphasize that, based on the tapering of optical fibres [199, 200], it is well known that an adiabatic transition is preferable in order to minimize the optical loss in a tapered waveguide, which is probably not the case for the linear transition analysed in Fig. 5.8(b). In such adiabatic transitions, the angle of the taper must be small enough that there is negligible power coupling between the modes. Consequently, a strict loss evaluation must take into account such modal coupling and is usually performed by numerical beam propagation methods, which are computationally difficult for this heavily multiscale problem. As a result, our method discussed above (and the losses of Fig. 5.8(b)) must be considered an approximation, simply employed to provide an estimation and a qualitative comparison between the different systems.

In the following section, the fabrication of our magnifying wire array hyperlens using tin/soda-lime is discussed, as is the selection of the desired transition region to form the final hyperlens.

5.2.1 Fabrication method: drawing or tapering with flame

As mentioned in Chapter 4, the final drawing or tapering of the metamaterial preform generates a straight fibre between two transition regions (see Fig. 4.25), called tapered fibres. Such tapered samples can be employed as magnifying hyperlenses.

Figure 5.9(a) shows a picture of a tapered region produced from the drawing of a metamaterial preform of OD = 1 mm ($d \approx 10\,\mu$m, $\Lambda \approx 20\,\mu$m), to a fibre with OD = 40 μm ($d \approx 400$ nm, $\Lambda \approx 800$ nm), while Fig. 5.9(b,c) shows the equivalent fibre fabricated by tapering the same preform with a butane flame under 170 g of tension (process described in Section 4.4.1).

The wire array magnifying hyperlens with a 2x magnification factor and a structure varying from $d = 400$ nm/$\Lambda = 800$ nm to $d = 800$ nm/$\Lambda = 1600$ nm, (as per the model presented in Fig. 5.8), corresponds to the structures in the region with OD varying from 40 to 80 μm of the real sample. According to

Fig. 5.9, the length of these regions is 20 mm and 2.5 mm, for the sample fabricated by drawing and tapering by flame, respectively. Clearly, from the simulated overall losses of the quasi-TEM mode with $k_{\perp max}$ presented in Fig. 5.8(b), both hyperlenses would present an overall loss larger than 50 dB, and are thus unsuitable for any super resolution imaging in the MIR.

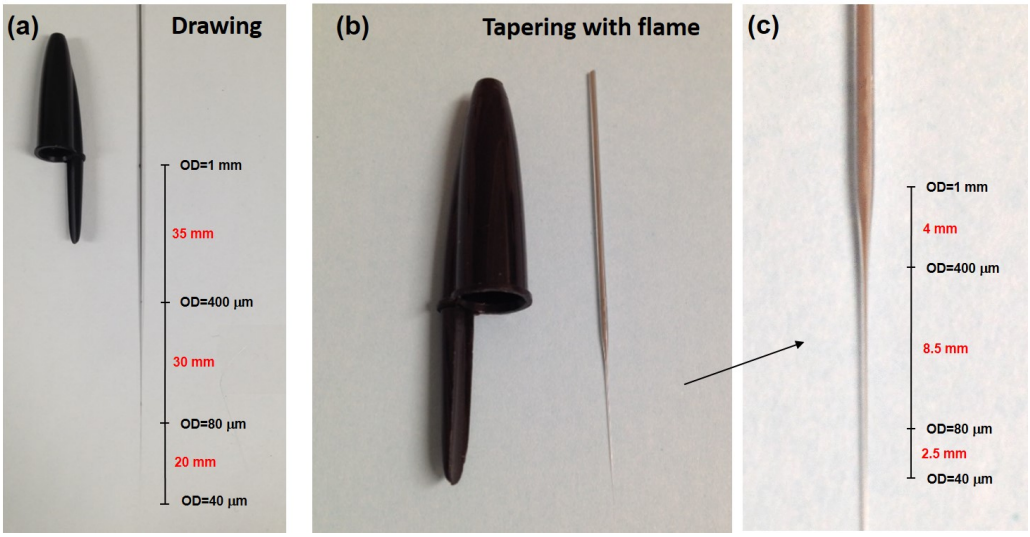

Figure 5.9: Example of tapered metamaterial fibre fabricated by (a) drawing, (b,c) tapering with flame + weight of 170 g. Both samples were stretched from a similar tin/soda-lime wire array preform with OD = 1 mm ($d \approx 10\,\mu$m, $\Lambda \approx 20\,\mu$m), containing a few hundreds of wires, as shown in Fig. 4.21.

Note that, even if the tapered metamaterial fibre presented were made of gold wires, such transition regions would still possess an overall optical loss larger than 50 dB. As was discussed previously, the proposed 2x magnifying hyperlens operating at $\lambda = 3\,\mu$m must have an overall length smaller than $120\,\mu$m. The reduction of the hot zone size from $\approx$ 11 cm (for our fibre draw tower furnace - see Section 4.2.1) to $\approx$ 5 mm (an estimation of the hot zone created by the butane flame), decreased the length of the proposed 2x magnifying hyperlens from 20 mm to 2.5 mm. In the next section, an alternative fabrication method that achieves such transition on the hundred micron scale is presented.

5.2.2 Magnifying hyperlens fabrication: extremely short tapers with acceptable overall optical losses in the MIR

In the stretching process of the metamaterial preform (drawing or tapering), the steepness and length of the transition regions is strongly related to the length and temperature profile of the hot zone employed in the process. When drawing with a fibre draw tower, these features are intrinsic to the furnace and are not easily tailored (without replacing the furnace). In a tapering process, the adjustment of the hot zone can be achieved with the reduction of the width of the flame or the employed heating element. In addition, it is not necessary a continuous process, as discussed earlier.

In order to produce extremely short tapers with overall length around $100\,\mu$m, a homemade tapering system was developed by adapting a conventional pipette puller in a vertical configuration. Figure 5.10(a) shows a schematic of this tapering setup, where the heating element is formed by a platinum/iridium alloy sheet of $50\,\mu$m thickness and with a center hole of 1.2 mm in diameter.

In this configuration, the hot zone length is proportional to the thickness of the filament, but also depends on several factors such as: the ratio between the size of the preform and that of the hole in the filament, the current employed in the heating element, the time of the heating process, and the heat dissipation of the system. Though it is hard to measure or simulate its length, the transitions achieved in such system indicates a hot zone region smaller than 1 mm.

Figure 5.10(b) shows a schematic of the tapering process, where the alloy element is heated by an electric current (supplied and controlled by the pipette puller), and a selected weight stretches down the preform with an adjustable and predetermined pulling tension (determined by the weight). Figure 5.10(c) shows a picture of the original pipette puller P-97 from Sutter Instruments [201]. Note that, in our tapering setup, the pipette puller serves as a current source with adjustable current profile, while none of its original mechanical parts are used.

A picture of the adapted setup is presented in Fig. 5.10(d), where the preform is held in two drill chucks. The alignment of the preform with the hole in the alloy filament is manually performed with three micrometric stages coupled to the top drill chuck.

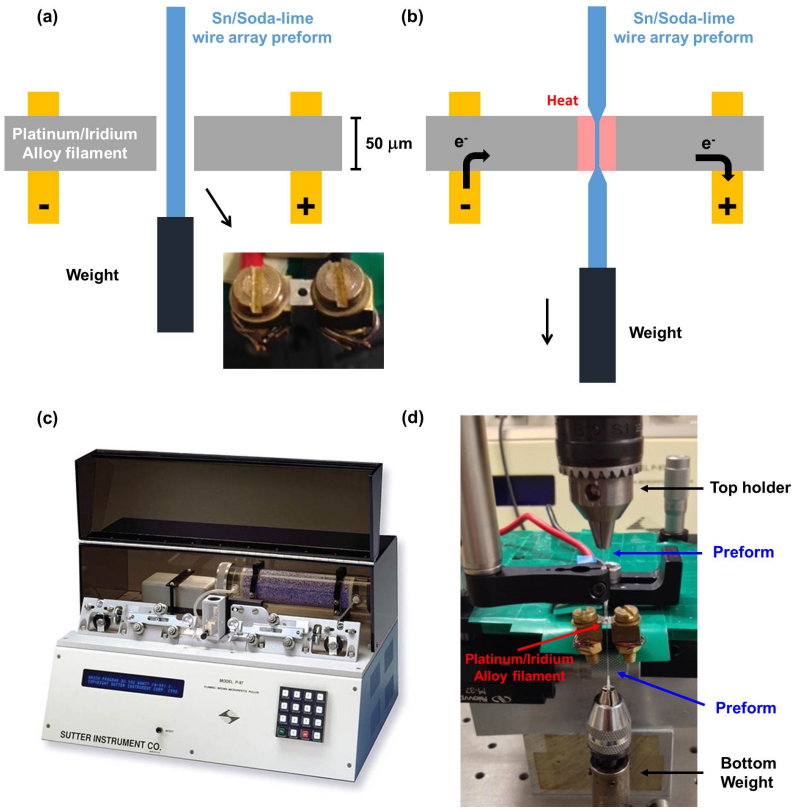

Figure 5.10: Schematic of (a) the tapering setup and (b) a taper fabrication. (c) Original micro pipette puller P-97 from Sutter Instruments (Picture extracted from Ref. [201]). (d) Picture of the adapted tapering setup in vertical orientation.

This adapted tapering setup has several advantages that allow the control of the taper profile, such as:

(1) High flexibility in the shape and length of the hot zone, which can be tailored with the shape of the platinum/iridium filament ($\approx 50\,\mu$m).

(2) Use of high pulling tension by adjusting the weight applied, which could lead to an initial tension per unit area as high as $6.5\,\mathrm{kg/mm^2}$ in the preform, or close to the tensile strength of the sample. According to [143], the experimental tensile strength of soda-lime glass can vary from 20 to 200 MPa ($\approx$ from 2 to $20\,\mathrm{kg/mm^2}$), depending on the quality of the glass surface.

(3) Fast cooling of the tapering region since the dwell time in the hot zone is small.

(4) It is a more controlled process in comparison with the flame tapering (see Section 4.4.1). The heating of the preform is more symmetric than with the flame. The temperature of the filament can be controlled with the current applied by the pipette puller to the alloy filament.

Initially, tapering of several solid soda-lime rods and wire array preforms was performed with various preform outside diameters (from 200 μm to 1.3 mm) and several hole sizes in the platinum/iridium alloy filament (see inset of Fig. 5.10(a) - diameter varying from 600 μm to 1.5 mm). From these range of parameters, the steepest transitions were obtained using a platinum/iridium filament with a central hole of 1.2 mm, and preforms with outside diameter around 400 μm. Those are the standard parameters used for the samples fabricated and discussed throughout this Chapter.

Figure 5.11(a) shows a cross-section of the tin/soda-lime wire array metamaterial preform employed in the fabrication of magnifying hyperlenses with the specially developed tapering setup. The standard preform has approximately 500 wires, OD $\approx 400\,\mu$m, $d \approx 4\,\mu$m and $\Lambda \approx 8\,\mu$m. Figure 5.11(b-d) shows examples of different transition regions obtained using similar heating parameters (heating time around 20 s) and different pulling tension by initial cross-section area (T_s), from a tin/soda-lime wire array metamaterial preform similar to the one in Fig. 5.11(a). The vertical arrows represent the region that could be selected to achieve a 3x magnifying hyperlens with a structure varying from approximately $d \approx 300$ nm and $\Lambda \approx 600$ nm (OD $= 30\,\mu$m) to $d \approx 900$ nm and $\Lambda \approx 1.8\,\mu$m (OD $= 90\,\mu$m).

The tips of the samples shown in Fig. 5.11 are not straight, which indicates a non uniform heating of the preform, probably caused by a misalignment of the sample in the filament or a non-uniform heating of the filament. However, such a feature is not detrimental to the final hyperlens device if this region is not selected, for example, selecting the region corresponding to the 3x magnifying hyperlens shown in Fig. 5.11.

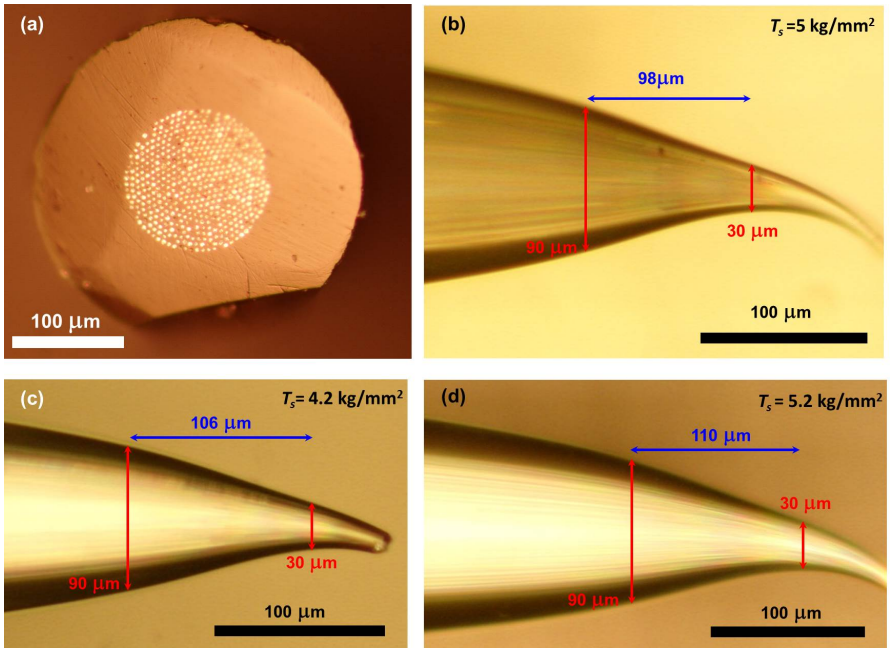

Figure 5.11: (a) Standard tin/soda-lime wire array metamaterial preform employed in the fabrication of magnifying hyperlenses with the tapering setup. Outside diameter of 400 μm ($d \approx 4\,\mu$m and $\Lambda \approx 8\,\mu$m), containing approximately 500 wires. (b-d) Examples of transition regions fabricated with our adapted taper system with different pulling tensions.

According to Fig. 5.11(b-d), it is evident that this method allows the fabrication of transitions steeper than the previous discussed approaches. For comparison, the intended 2x magnifying hyperlens proposed in Fig. 5.8, with d varying from approximately 400 to 800 nm and $d/\Lambda = 0.5$, had lengths of 62, 69, 70 μm in the examples shown in Fig. 5.11(b-d) (OD varying from 40 to 80 μm). As discussed before, the equivalent structural transition fabricated by drawing and flame tapering has length of 20 mm and 2.5 mm, respectively.

Using the side profiles of Fig. 5.11(b-d) and the simulated losses presented in Fig. 5.7(a), the expected overall losses of the transitions corresponding to the proposed 2x magnifying hyperlens are 27.8 dB, 30.5 dB and 32 dB, respectively ($\lambda = 3\,\mu$m, $k_{\perp max}$). Consequently, these magnifying hyperlenses exhibit losses that may be acceptable for super-resolution imaging in the MIR.

Similarly, it is possible to estimate the loss of the 3x magnifying region with d varying from 300 to 900 nm, $d/\Lambda = 0.5$, corresponding to the red ver-

tical arrows and overall length of 98, 106 and 110 μm in Fig. 5.11(b-d). The transitions shown possess an overall loss of 47.6 dB, 51.5 dB, and 54 dB, respectively. Although these losses are high, magnifying imaging could still be possible depending on the detection employed. In addition, smaller overall loss with 3x magnification factor could also be achieved by shifting the transition region to slightly larger wires, which also decreases the maximum resolution of the hyperlens. For example, the 3x magnifying hyperlens corresponding to OD varying from 35 μm to 105 μm from Fig. 5.11(b-d), has an expected loss of 40 dB.

Note that, if the same transitions were obtained for a gold/silica wire array, the overall losses in dB would decrease to one-third (see Fig. 5.8(b)), which represents a much better optical performance (losses in the 15 dB scale for the transitions shown). In this scenario, even higher magnifications could be possible.

In the next section, the final step to obtain the magnifying hyperlens, the extraction of the selected region from the tapered sample, is described.

5.2.3 Sample preparation: Selecting the desired transitions

After the fabrication of a tapered wire array metamaterial fibre with a steep transition and the desired range of structural parameters, the final step of the magnifying hyperlens sample preparation is the selection and extraction of the region of interest. This selection is based on the targetted magnification factor, resolution and total optical loss. The ratio between the outside diameters of both ends of the transition defines the magnification factor of the hyperlens device. The full length, the structural parameters of the wire array structure and the transition profile has a huge influence on its overall optical loss.

The sample preparation method described below was developed to produce the final hyperlens, which involves two steps: the embedding and the cutting/polishing of the tapered metamaterial fibre.

Embedding the hyperlens in a thin metallic foil

In order to extract the exact desired transition from the tapered metamaterial fibre, the sample was embedded in a thin metallic foil containing a hole. In such process, the alignment between the sample and the foil is crucial and

not trivial. Fig. 5.12(a) shows a schematic of the desired transition for a 3x magnifying hyperlens and where the metallic foil should be fixed (black dotted line).

Intending to avoid the necessity to perform such difficult alignment, a precise hole is fabricated in a metallic foil with a high power femto-second laser (laser machining facilities at Macquarie University, ANFF OptoFab node, Sydney, Australia - by Benjamin Johnson and Alex Stokes). The diameter of the hole matches the outside diameter of the tapered metamaterial fibre in the middle of the region of interest. The tapered sample stops at the correct position when introduced in the hole in the foil. Fig. 5.12(b) shows a 70 μm hole fabricated in a brass foil with thickness of 50 μm.

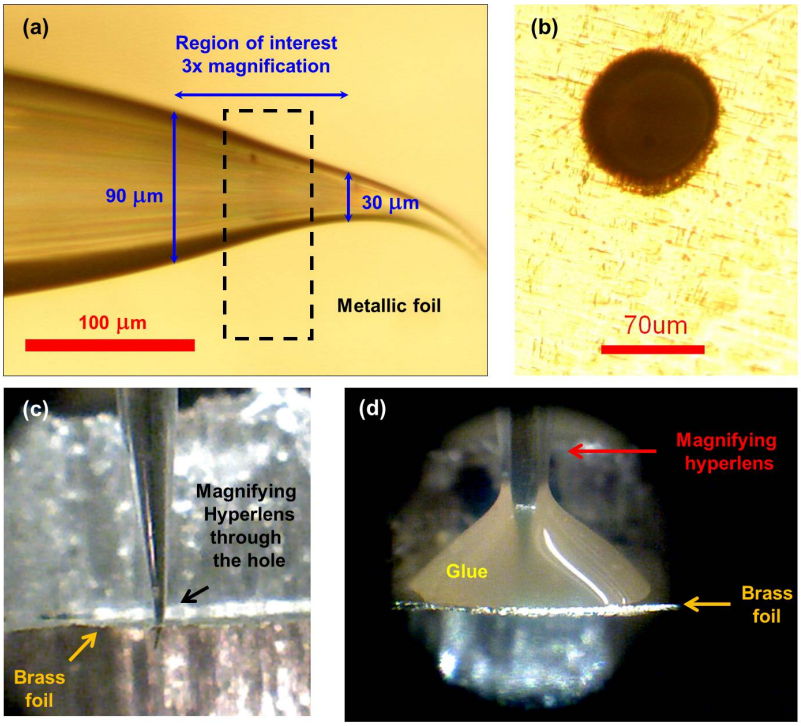

Figure 5.12: (a) Example of a tapered metamaterial sample and the region of interest for a 3x magnifying hyperlens, with the desired position of the metallic foil (black dotted rectangle) for the embedding process. (b) Picture of a 70 μm hole fabricated by a high power femto-second hole at Macquarie University (ANFF OptoFab node, Sydney, Australia), in a brass foil with 50 μm thickness. (c) Alignment of the tapered sample through the hole micro-machined in brass foil. (d) Gluing of the sample with an epoxy adhesive (yellow region).

The tapered sample is attached to a micrometer stage and, with the help of a microscope, introduced through the hole of the metallic foil, which is fixed in a support. Figure 5.12(c) shows a picture of this alignment process, where it is possible to visualize the brass foil and a small part of the hyperlens below it. After this alignment, a tiny portion of epoxy glue is manually deposited on the top of the foil, as seen in Fig. 5.12(d).

A different region of the tapered sample can be selected by adjusting the size of the hole micro-machined by the femto-second laser. Thinner metallic foils can also be used to embed shorter transition regions. For example, there are commercial stainless steel foils as thin as 13 μm (Starrett 667-1/2 feeler gauge) and brass foils as thin as 5 μm (Goodfellow, brass foil CU020200).

After embedding of the desired region, the final step is polishing/cutting of the glued sample.

Polishing/Cutting both sides of the hyperlens

Once embedding of the tapered metamaterial fibre in the metallic foil is concluded, it is necessary to extract the desired region from the glued sample. One easy and inexpensive method is polishing of both sides of the sample with a polishing sheet commonly employed to polish connectorized fibres.

The side containing the large amount of glue can be polished over several separated cycles using decreasing grit size. Commercial options are available with grit sizes varying from 20 nm to 30 μm (Thorlabs). For the small and more fragile facet of the magnifying hyperlens, a polishing cycle with the finest grit and low pressure is enough to achieve the desired result. Careful and slow polishing, combined with a regular visualization and measurement of the resulting structure with a microscope, allows the desired transition to be selected.

As an alternative method, focused ion beam (FIB) milling can be employed to cut the sample, especially the smallest side of the tapered region that is not covered by the epoxy. However, despite the lower risk of breaking the sample and the finer polishing offered, such a method is more expensive because it requires a long milling time with the ion beam. For example, the cutting of a tin/soda-lime metamaterial fibre with outside diameter of 30 μm takes around one hour with a high current (30 kV, 10 nA).

In the next section, the use of the best magnifying hyperlenses obtained by polishing for far field subdiffraction imaging in the MIR is discussed.

5.3 Far field imaging of apertures in the MIR

In this section, far field field imaging is presented and discussed. Firstly, the fibre laser built to generate high power at 2.8 μm wavelength is described, followed by the fabrication of the sub-wavelength apertures to be imaged. Before presenting the far field imaging with the magnifying hyperlens (Section 5.4), the imaging of a variety of apertures alone (sizes around the diffraction limit) is performed and discussed.

5.3.1 High power MIR light source (Er-ZBLAN fibre laser) and far field imaging setup

Because the tin/soda-lime hyperlenses discussed have huge overall loss in the MIR due to the presence of metal, the imaging experiment requires a high power laser with a good beam quality. In order to fulfil both requirements, a fibre laser with a ZBLAN fibre doped with high concentration of Er ions (7 mol%) was built at Macquarie University, in a collaboration with Prof. Stuart Jackson.

The fibre laser consisting of a 980 nm laser diode pump (CW, nLight Pearl^{TM} P14 series) and 3 m of single-mode ZBLAN fibre doped with Er (7 mol %) in a linear cavity configuration as illustrated in Fig. 5.13(a). Fig. 5.13(b) shows its output spectrum, measured with an optical spectrum analyser (Yokogawa AQ6376), with a peak power centered at 2.801 μm.

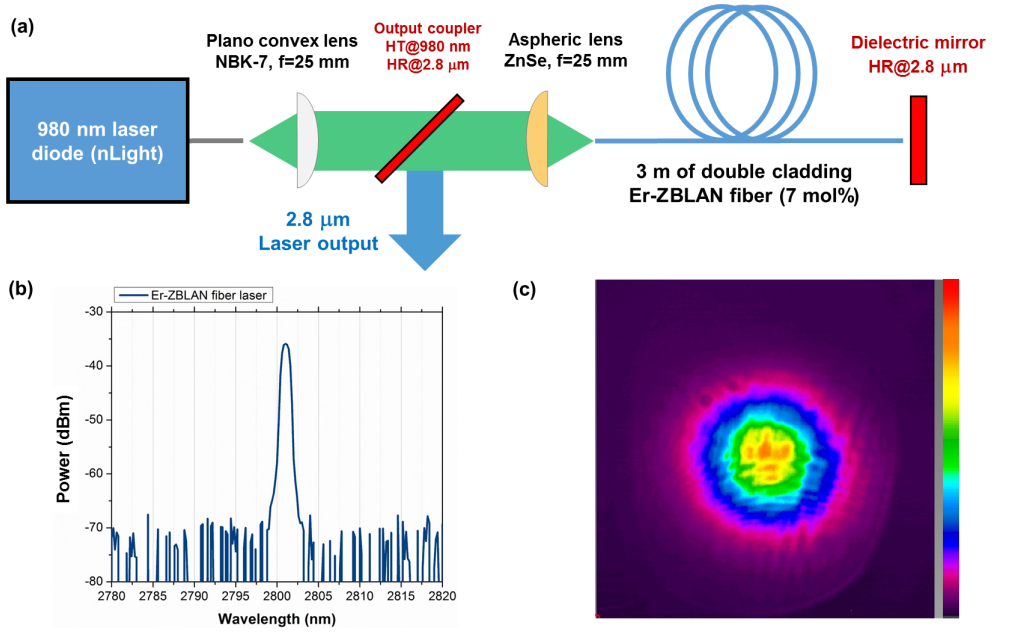

Figure 5.13: (a) Er-ZBLAN fibre laser built for the MIR imaging experiment. (b) Spectrum of the laser output centered at $\approx 2.8\,\mu$m. (c) Intensity profile of the collimated at $2.8\,\mu$m output beam.

The fibre laser described presented an efficiency around 20%, managing to deliver a CW output power of 2 W at $2.8\,\mu$m with a 980 nm pump of 10 W. The intensity profile of the Fig. 5.13(c) indicates a single-mode operation at $2.8\,\mu$m wavelength, as expected from the fibre's specifications. Note that the features in the image of the beam are artifacts due to the camera.

It is important to emphasize that the output wavelength of the fibre laser is slightly different from the $3\,\mu$m operational wavelength initially intended for the imaging applications. However, numerical modeling indicates a deviation smaller than 7 % in the optical loss of tin/soda-lime wire array structures between these two different operational wavelength. Consequently, these simulated losses must be considered as approximations when compared with the experimental results discussed below.

The typical experimental setup for far field imaging in the MIR based on transmission is illustrated in Fig. 5.14. The collimated output beam from the Er-ZBLAN fibre laser (Fig. 5.13) is focused with a ZnSe aspheric lens onto the aperture, which is positioned in the lens's focal point. The focal length of the lens is selected according to the desired spot size. Ideally, in order

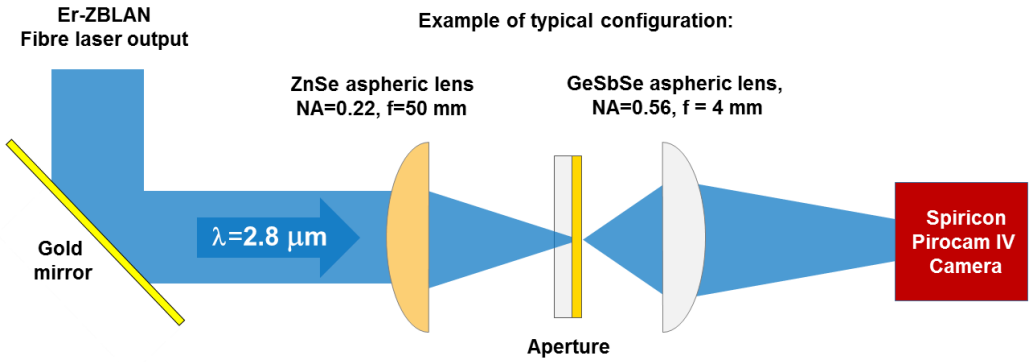

Figure 5.14: Far field imaging setup. Typical configuration: input ZnSe aspheric lens (NA = 0.22, $f = 50\,\text{mm}$), the apertures milled in a borosilicate microslide (thickness $\sim 150\,\mu\text{m}$), an output chalcogenide aspheric lens (glass GeSbSe, NA = 0.56, $f = 4\,\text{mm}$, Thorlabs), and a beam-profile solid-state/pyroelectric camera (Spiricon - Pirocam IV) for imaging in the infrared.

to maximize the power transmitted thorough the imaged aperture, the spot size on the focal point must be only slightly larger than the aperture size. A second aspheric lens is employed to collect the light diffracted through the aperture and to form an image in the image plane. An infrared beam-profile camera is aligned in the image plane. For our experiment, a Spiricon/Pirocam V solid-state/pyroelectric camera was employed (OPHIR Photonics), with sensitivity around 64 nW/pixel, an array of 320x320 pixels, and pixel size of $80\,\mu\text{m}$.

Note that the use of aspheric lenses is important to avoid spherical aberrations on the transmitted beam, which can affect the quality of the imaging. The focal length (f) and NA of the second lens can also be selected to change the diffraction limit of the system and the size of the image formed in the image plane.

The overall optical loss in the imaging setup depends on the lenses selected (transmission, clear aperture, reflection), the overlap of the focused beam with the aperture, and the absorption of the glass substrate. In the imaging discussed in this Chapter (wavelength operation at $2.8\,\mu\text{m}$), the typical coupling loss of the in-coupling lens can vary from 2 to 5 dB, while the coupling loss for the standard out-coupling chalcogenide lens (GeSbSe, NA = 0.56, $f = 4\,\text{mm}$, from Thorlabs) is around 1 dB. The absorption of the borosilicate coverslip with thickness around $150\,\mu\text{m}$ is $\sim 1.2\,\text{dB}$ at $2.8\,\mu\text{m}$

wavelength.

In order to be detected in the far field with an array camera, the size of the magnified image and the remaning power in the image plane must result in a power density per pixel higher than the noise limit of the employed camera. For the Spiricon Pirocam IV, this nominal noise limit is around 64 nW per pixel and the pixel size is 80 μm [202]. Consequently, for a certain input power, detecting the far field image of the aperture with fewer pixels increases the power density, which reduces the minimum input power required. However, detecting with fewer pixels also compromises resolution and quality of the far field image.

When a hyperlens is inserted between the aperture and the out-coupling lens in a far field super-resolution imaging system (as discussed in Section 5.4), the absorption of the hyperlens and the reflection of the light at both facets also affect the overall optical loss of the imaging setup, thus also changing the minimum input power required to detect the image.

It is important to emphasize that a strict estimation of the input power required to obtain a certain super-resolution image of an aperture is hard to obtain. The simulated loss of the hyperlenses discussed through this Chapter must be considered an approximation because the fabricated tapers are not adiabatic and the reflections on both facets of the hyperlens are not taken into account. In addition, a considerable amount of the incident power coupled into the hyperlens will excite ordinary waves. Although their losses are lower than the extraordinary waves, they will diffract and leak from the wire array region. This scenario will be further discussed in Section 5.4.

5.3.2 Fabrication of apertures

Another non trivial aspect of the far field subdiffraction imaging experiment with the magnifying hyperlenses is the fabrication of sub-wavelength apertures that will be imaged. In order to have sufficient control over the shapes, sizes and spacing of such apertures, FIB milling was selected as their fabrication method [203].

In an imaging experiment by transmission, as illustrated in Fig. 5.14, the light must be only transmitted through the aperture. Therefore, the apertures were FIB milled in a gold film deposited by sputtering (thickness $\approx$ 100 nm, highly reflective in the mid-infrared) on a borosilicate microslide (thickness $\approx$ 150 μm, from ProSciTech). The small thickness of the borosilicate slide ensures a small transmission loss due to the glass for the

incident 2.8 μm beam (attenuation around 1.2 dB).

Figure 5.15 shows examples of apertures with different shapes and sizes varying from 10 μm to 800 nm, fabricated at the Australian Center for Microscopy and Microanalysis (ACMM - The University of Sydney, Australia).

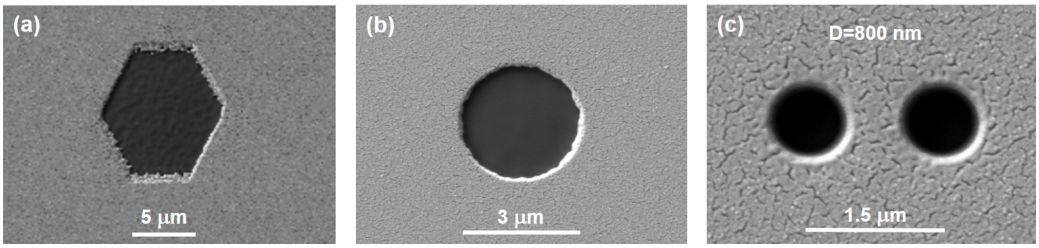

Figure 5.15: Examples of apertures milled with FIB in a gold film deposited on a borosilicate coverslip. (a) Hexagon, (b) Single circular aperture with d = 3 μm, (c) Double circular aperture with d = 800 nm and distance of 1.5 μm from center to center.

The milling parameters of the ion beam system must be optimized in order to fabricate sharp apertures with a pre-defined size [204], particularly for sizes smaller than 1 μm. The current employed in the FIB system alters the size of beam spot, which will affect in the resolution of the milling and the total milling time. A small dwell time is preferable to avoid problems related to re-deposition, which influences the precision of the milling (in comparison to the pre-defined size of the intended aperture), the sharpness of the edges, and how the profile of the aperture varies with the depth.

Table 5.1 lists the milling parameters employed successfully in the fabrication of the different types and sizes of apertures presented through this chapter.

Table 5.1: Aperture fabrication: FIB milling parameters.

Type of aperture	**Size**	**Ion beam Voltage/Current**	**Dwell time**	**Dose Spacing**	**Milling time**	**SEM micrograph**
Single hexagon	∼10 μm	30 kV, 50 pA	1 μs	100 nm	5 min	Fig. 5.15(a)
Single circle	d∼3 μm	30 kV, 25 pA	1 μs	50 nm	2 min	Fig. 5.15(b)
Double circle	d=800 nm	30 kV, 25 pA	0.1 μs	1 nm	30s each	Fig. 5.15(c)
Double circle	d=2 μm	30 kV, 50 pA	0.5 μs	30 nm	90s each	Fig. 5.16, column 1
Double circle	d=1.1 μm	30 kV, 50 pA	0.5 μs	10 nm	30s each	Fig. 5.16, column 2
Double circle	d=600 nm	30 kV, 50 pA	0.1 μs	1 nm	20s each	Fig. 5.16, column 3
Double circle	d=8.5 μm	30 kV, 1 nA	1 μs	235 nm	60s each	Fig. 5.21(a)
Anti-aperture I	OD∼15 μm, d=3.7 μm	30 kV, 1 nA	1 μs	90 nm	2 min	Fig. 5.22(a-c)
Anti-aperture II	OD∼15 μm, d∼1.75 μm	30 kV, 1 nA	1 μs	90 nm	2 min	Fig. 5.22(d-f)
Anti-aperture III	OD∼20 μm, d=7 μm	30 kV, 1 nA	1 μs	235 nm	2 min	Fig. 5.23(a)

5.3.3 Far field imaging of apertures with dimensions around the diffraction limit

Before subdiffraction imaging with the magnifying hyperlens is attempted, it is important to characterize the diffraction limit of the setup, which is strictly related to the degree of coherence of the light transmitted through the aperture, and the phase distribution. This is possible with the imaging of double apertures with a spacing varying around the nominal Abbe diffraction limit (Eq. (5.2)). As discussed before, this limit is considered the minimum distance at which two coherent point sources are distinguishable.

Figure 5.16 shows a set of double apertures fabricated for this type of characterization when the image is performed in an operational wavelength around 3 μm. Column 1 contains apertures with diameter around 2 μm and spacing varying from 4 to 2.1 μm. Column 2 contains apertures with diameter around 1.1 μm and spacing varying from 4 to 1.3 μm. Column 3 contains apertures with diameter around 660 nm and spacing varying from 1.2 μm to 800 nm.

The use of a highly sub-wavelength double circular aperture, as seen in column 3, provides a better spatial coherence for the transmitted light and, consequently, is a better approximation of two point sources. However, only a small amount of power can be transmitted through these small apertures, as the beam size diameter at the focal point is also limited by the diffraction limit, leading to a small overlap with the apertures, and power transmission through sub-wavelength apertures decreases with diameter as $(d/\lambda)^4$. On the

other hand, larger apertures, such as those seen in columns 1 and 2, provide a better coupling with the incident radiation, and more power is transmitted and detected. However, the transmitted light will somewhat vary in phase over the size of the aperture since the laser beam is not a perfect Gaussian beam.

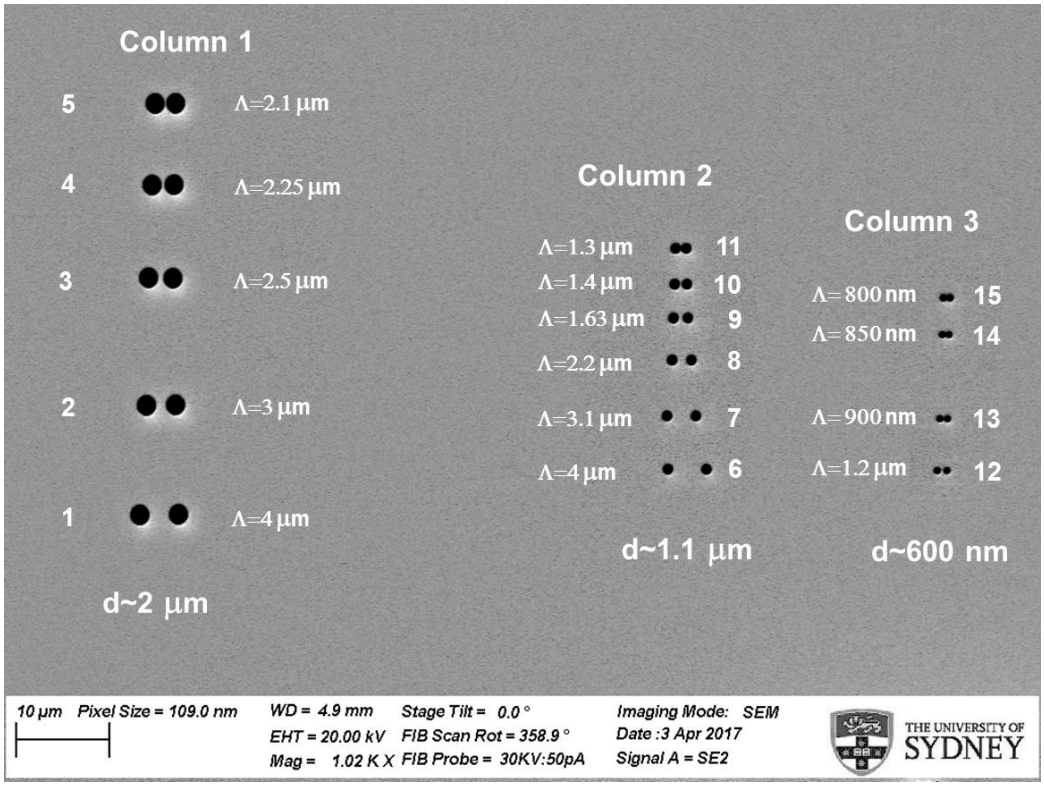

Figure 5.16: Three sets of circular double apertures fabricated with FIB for the diffraction limit characterization. Column 1 contains five apertures with d≈2 μm and distance between the center (Λ) from 4 to 2.1 μm. Column 2 contains six apertures with d≈1.1 μm and Λ from 4 to 1.3 μm. Column 3 contains four apertures with d≈600 μm and Λ from 800 nm to 1.2 μm.

Because the phase difference between the two apertures depends on the the size of the apertures, the diffraction limit of the system is expected to lie between $l = \lambda/2\text{NA}$ (Abbe limit for two out of phase point sources light) and $l = \lambda/\text{NA}$ (Abbe limit for coherent light). Therefore, an experimental characterization of the diffraction limit without hyperlens is required before

any subdiffraction imaging is attempted and claimed.

Figure 5.17(a) shows the far field imaging of the first three apertures of column 1, at $\lambda = 2.8\,\mu$m. The collimated beam from our Er-ZBLAN fibre laser was focused with a ZnSe lens, $f = 6\,$mm and NA $= 0.25$ (Innovation photonics, LFO-5-6), and the center of the double aperture was aligned with the center of the beam in the focal point, as illustrated in Fig. 5.17(b). An output aspheric chalcogenide lens with $f = 4\,$mm and NA $= 0.56$ (Thorlabs, glass GeSbSe, CM036TME-D) was employed to collect the light diffracted through the apertures and to form the image in the Spiricon camera (placed 80 cm away).

According to the imaging presented in Fig. 5.17(a), the double aperture number 1 ($\Lambda = 4\,\mu$m) is distinguishable, which is evident due to the two yellow dots. On the other hand, the second and third pairs ($\Lambda = 3\,\mu$m and $2.5\,\mu$m) are not resolvable. This indicates that the diffraction limit of the setup is between 3 and $4\,\mu$m, which agrees with the previous assessment that the experimental diffraction limit would lie between $\lambda/2$NA ($2.5\,\mu$m for $\lambda = 2.80\,\mu$m, NA $= 0.56$) and $\lambda/$NA ($5\,\mu$m), according to the phase difference of the light transmitted through the apertures.

A simulation of the far field imaging achieved by the system was performed using Fourier analysis (see Appendix B for the detailed description and the Matlab code). Figure 5.17(c) compares the cross-section intensity profiles of the original double aperture with its simulated and experimental far field imaging ($\lambda = 2.8\,\mu$m, NA $= 0.56$, aperture 1). The distance between the two peaks corresponding to the double aperture 1 detected experimentally ($\Lambda = 3.79\,\mu$m) is in agreement with the simulated one ($\Lambda = 3.75\,\mu$m), with a deviation of only 1%.

Due to the energy distribution of the focused beam and the typical overlap with the double aperture required to maximize the transmitted power (as illustrated in Fig. 5.17(b)), the illumination of the aperture cannot be considered uniform and with constant phase excitation, as would be the case with an ideal plane wave. This would only be a good approximation if the double aperture is smaller than the full width at half maximum (FWHM) of the focused beam, if they are aligned as seen in Fig. 5.17(b), and if the phase shift in a region corresponding to Λ is small.

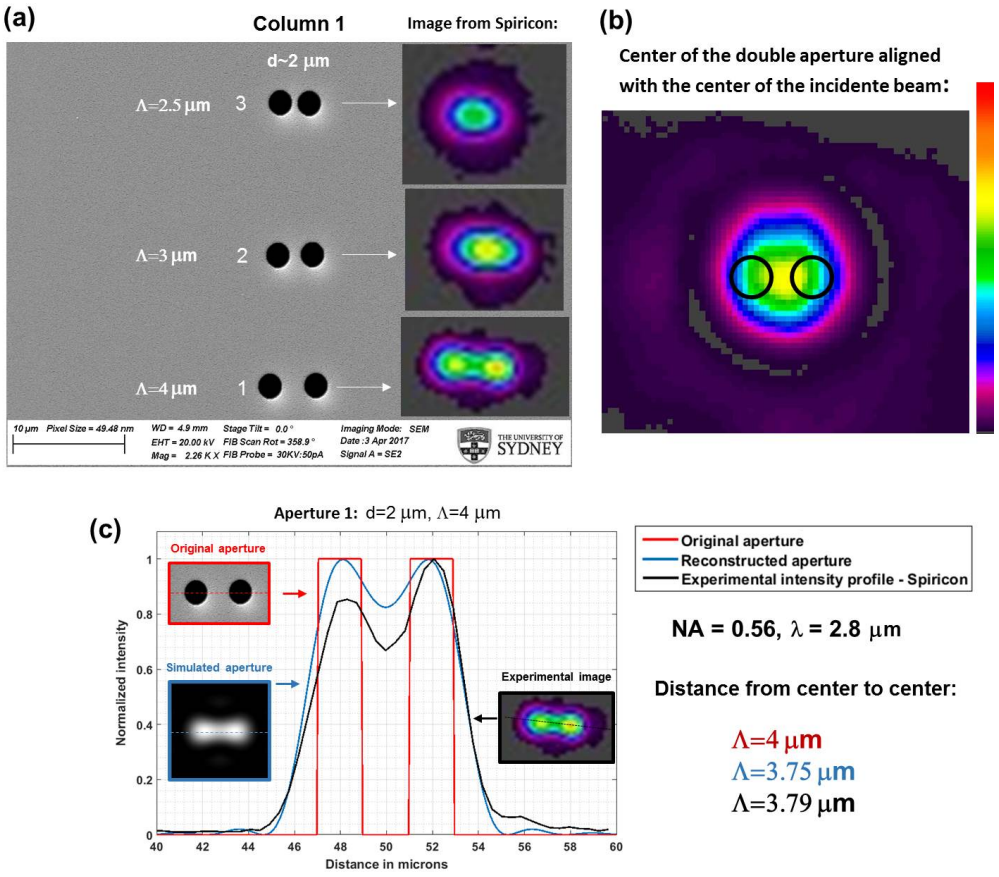

Figure 5.17: (a) Far field imaging of the first three double apertures of column 1 (Fig. 5.16). Experimental setup: input ZnSe lens ($f = 6$ mm and NA $= 0.25$, Innovation photonics, LFO-5-6), aperture on the focal point, output aspheric chalcogenide lens ($f = 4$ mm and NA $= 0.56$, Thorlabs, glass GeSbSe, CM036TME-D) and Spiricon-Pirocam IV camera placed 80 cm away from the output lens. (b) Schematic of the alignment employed, with the center of the double aperture aligned with the center of the beam. (c) Cross-section intensity profiles of the original double aperture with its simulated and experimental far field images ($\lambda = 2.8\,\mu$m, NA $= 0.56$, double aperture 1).

In order to gather information on the influence of a phase shift between the excitation of each aperture in the far field imaging, the imaging of the double apertures was repeated with slightly different coupling. Figure 5.18(a) illustrates this alternative alignment, with the center of the double aperture not aligned with the center of the incident beam.

Figure 5.18(b,d) presents the resultant imaging in this alternative alignment, showing that all double apertures of column 1 are resolvable in this configuration. The cross-section intensity profiles seen in Fig. 5.18(c) shows a good agreement between the experimental and simulated image of the double aperture 1, when the simulated case considers a uniform excitation and a phase shift of $\pi/2$ in one of the circular apertures.

Since even the double aperture 5 with $\Lambda = 2.1\,\mu$m is distinguishable, the diffraction limit of this configuration is smaller than $2.1\,\mu$m. Surprisingly, this value is smaller than the Abbe diffraction limit for an incoherent source ($2.5\,\mu$m for $\lambda = 2.8\,\mu$m, NA $= 0.56$, using Eq. (5.2)), indicating that a phase shift between the illumination of the apertures affects the diffraction limit. This can be understood if considering that two nearby out of phase dipolar sources (which these apertures can be approximated by) will have a quadrupolar emission pattern, and therefore have a dip at a direction orthogonal to the separation between dipoles. This gives the illusion of being able to resolve the dipoles, but in fact information of the distance between the apertures is lost. Care should be taken accordingly when claiming subdiffraction limited imaging is achieved when the excitation phase is not uniform.

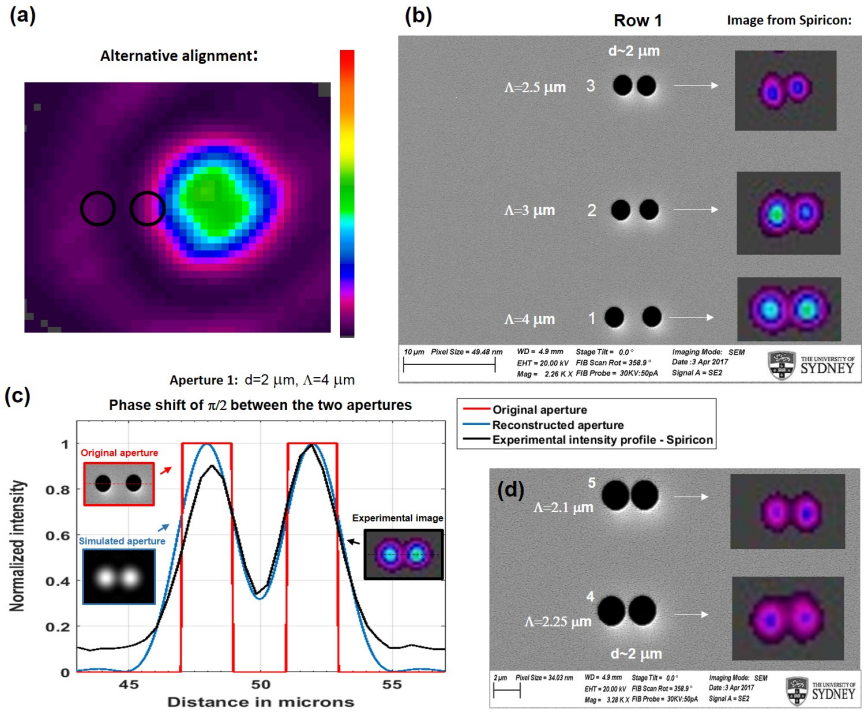

Figure 5.18: (a) Schematic of the alternative alignment, with the center of the double aperture not aligned with the center of the beam. (b) Far field imaging of the first three double apertures of column 1 (Fig. 5.16), with the alignment illustrated in (a), $\lambda = 2.8\,\mu$m. (c) Cross-section intensity profiles of the original double aperture 1 ($d = 2\,\mu$m, $\Lambda = 4\,\mu$m) with its simulated and experimental far field images, considering a phase shift of $\pi/2$ between the circular apertures. (d) Far field imaging of the double apertures four and five of column 1. Experimental setup: in-coupling ZnSe lens ($f = 6$ mm and NA $= 0.25$, Innovation photonics, LFO-5-6), aperture on the focal point, output aspheric chalcogenide lens ($f = 4$ mm and NA $= 0.56$, Thorlabs, glass GeSbSe, CM036TME-D) and Spiricon-Pirocam IV camera placed 80 cm away from the output lens.

Figure 5.19(a) shows a comparison between the simulated and the experimental cross section profile of the double aperture 2, with the simulated ones calculated considering a uniform excitation but with a phase shift of $(3/4)\pi$ between the neighbouring circular apertures. Note that, differently to the far field image presented in Fig. 5.17(a), aperture 2 is resolvable in the alternative configuration, and the experimental and simulated profiles exhibit excellent agreement. Similarly, aperture 5 is also resolvable and the

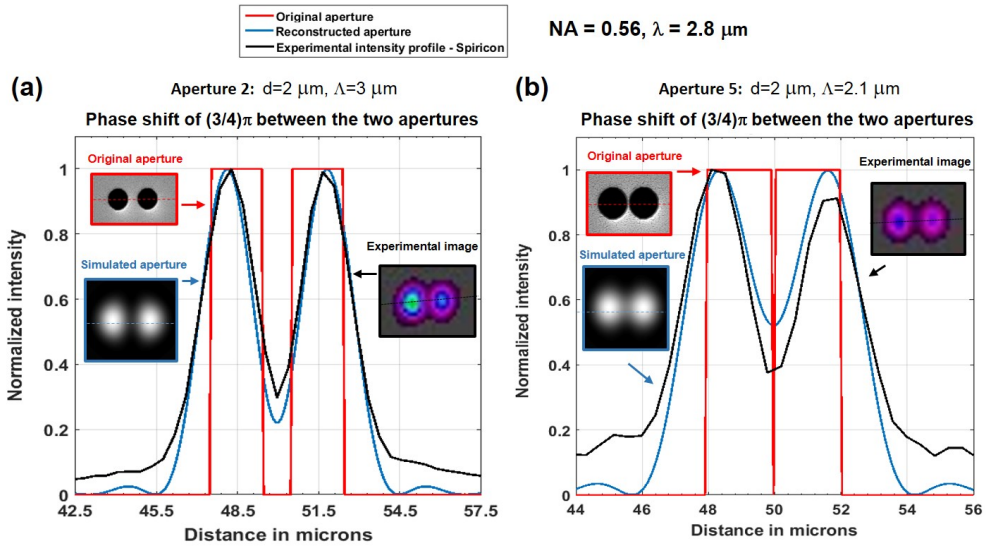

Figure 5.19: Cross-section intensity profiles of the original double aperture with its simulated and experimental far field images: (a) Aperture 2 ($d = 2\,\mu$m, $\Lambda = 3\,\mu$m), (b) Aperture 5 ($d = 2\,\mu$m, $\Lambda = 2.1\,\mu$m). Experimental setup: $\lambda = 2.8\,\mu$m, input ZnSe lens ($f = 6$ mm and NA $= 0.25$, Innovation photonics, LFO-5-6), aperture on the focal point, output aspheric chalcogenide lens ($f = 4$ mm and NA $= 0.56$, Thorlabs, glass GeSbSe, CM036TME-D) and Spiricon-Pirocam IV camera placed 80 cm away from the output lens.

simulated and experimental profile are in agreement, as seen in Fig. 5.19(b).

Given the influence of the phase excitation on the diffraction limit of the system, care must be taken regarding the alignment of the beam and the apertures before any claim of subdiffraction imaging (in our case with the magnifying hyperlens). Ideally, such claim could be made if the far field imaging of a certain unresolved double aperture becomes resolved if the magnifying hyperlens is inserted after the aperture, with no change in the in-coupling alignment.

In the next section, the far field subdiffraction imaging with the wire array tin/soda-lime magnifying hyperlens at the MIR is discussed.

5.4 Super resolution far field imaging with magnifying hyperlenses

Subdiffraction resolution can be obtained in a far field imaging experiment coupling a magnifying hyperlens after the imaged object, as illustrated in Fig. 5.20. In this configuration, the diffraction in the sub-wavelength aperture excites high spatial frequencies, which contain subdiffraction information, and are evanescent in isotropic media. If the hyperlens is aligned right after the aperture, in the near field, the high spatial frequencies couple into the metamaterial, where they excite propagating waves due to its hyperbolic dispersion. The tapered transition magnifies the propagating frequencies and, if the magnification factor is large enough, the initially high spatial frequencies become propagating waves with lower spatial frequencies after the hyperlens. Subdiffraction imaging is obtained if they are collected with a lens/objective and an image is formed in the far field, which can be detected with, *e.g.* single detector using a scanning technique, or using an array camera (as employed along this thesis).

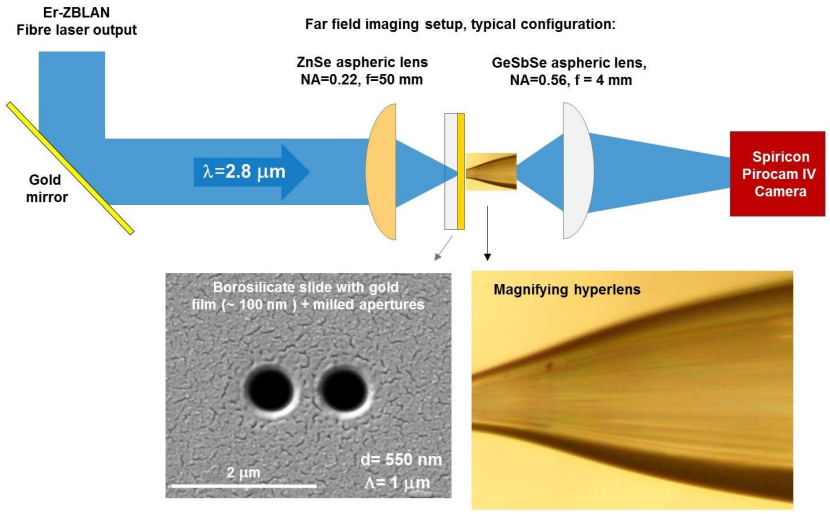

Figure 5.20: Typical far field imaging setup for subdiffraction imaging with magnifying hyperlens in the MIR: The collimated beam from the Er-ZBLAN fibre laser ($\lambda = 2.8\,\mu$m, see Fig. 5.13) is focused with an aspheric lens on the aperture, the hyperlens coupled with the aperture collects and magnifies the image, and an output aspheric lens projects the image in the far field, which is detected by a solid-state/pyroelectric camera (Spiricon - Pyrocam IV).

The first step in the imagining experiment is the alignment of the aperture without the hyperlens, using an experimental setup similar to the one illustrated Fig. 5.14. The NA of the first lens (in-coupling lens) is selected according to the size of the apertures to be imaged and the desired beam diameter at the focal plane. In order to optimize the coupling and maximize the light transmitted through the aperture, the beam diameter in the focal plane must be sightly bigger than the aperture. After the far field imaging of the aperture is obtained with the alignment of the second lens (out-coupling lens), the alignment of the first lens is not altered and the hyperlens is inserted after the apertures, as seen in Fig. 5.20.

The alignment of the hyperlens is performed with a 3D micrometer stage and the gap between the aperture and the hyperlens is monitored with a portable microscope. Initially, the hyperlens is placed a few millimiters from the aperture, and the alignment in the imaging plane is performed. Note that the focal point of the out-coupling lens must be adjusted because its focal plane must coincide now with the larger facet of the magnifying hyperlens, and not with the aperture. After the alignment in the focal plane, the hyperlens is carefully brought closer to the aperture until they touch, and a final focal adjustment of the out-coupling lens is performed.

In initial imaging attempts with the double apertures presented in Fig. 5.16, with diameters around $2\,\mu$m and low magnification hyperlenses, no light was detected from the wire array region, even after optimizing the coupling, the incident power, the detection settings of the Spiricon camera (set at maximum gain and sensitivity), and with a reduction of the number of pixels used in the imaging. Note that, this lower far field magnification concentrates the image on fewer pixels, thus the energy density is increased, achieving more power per pixel. As a result, far field imaging was attempted with larger double apertures, which are resolvable at $\lambda = 2.8\,\mu$m even without the hyperlens, in order to considerably improve the amount of light transmitted through the aperture and test the magnification effect of the hyperlenses.

Figure 5.21(a) shows the SEM picture of a double aperture with d and Λ around $8.5\,\mu$m. The far field imaging of the aperture alone can be seen in Fig. 5.21(b), using an in-coupling asphreric ZnSe lens with NA $= 0.67$, an out-coupling aspheric chalcogenide lens with NA $= 0.56$, at $\lambda = 2.8\,\mu$m, and the Spiricon camera 28 cm away from the out-coupling lens. As expected, the aperture with such dimension is resolvable and the detection settings of the camera must be set to low sensitivity to avoid saturation due to the better coupling of the beam to the aperture. Note that the image presented

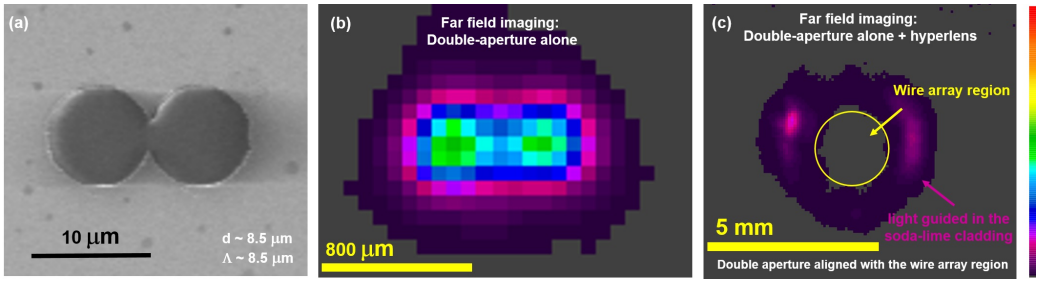

Figure 5.21: (a) SEM micrograph of a double-aperture fabricated by FIB milling with d and $\Lambda \sim 8.5\,\mu$m. (b) Far field image of the aperture alone, performed with an in-coupling asphreric ZnSe lens with NA $= 0.67$, an out-coupling chalcogenide aspheric lens with NA $= 0.56$, $\lambda = 2.8\,\mu$m, and the Spiricon camera 28 cm away from the out-coupling lens. (c) Typical far field image obtained coupling a magnifying hyperlens after the double aperture, where it is possible to visualize some light guiding in the soda-lime cladding of the hyperlens (purple region) and no light in the wire array region (yellow circle).

in Fig. 5.21 does not seem as good as the previous ones because the imaging was performed in a smaller area of the array camera, which results in the employment of fewer pixel, increasing the power/pixel ratio but compromising resolution. Figure 5.21(c) shows the far field image of the double aperture with a magnifying hyperlens coupled after the aperture (aperture aligned with the center of the wire array region), with the detection settings of the camera back to high gain and sensitivity.

As seen in Fig. 5.21(c), even with the double aperture with $d \sim 8.5\,\mu$m and more power transmitted through it, no light is detected from the wire array region (region marked in yellow), due to the high loss of the hyperlens. There is some light guided in the soda-lime cladding of the hyperlens (purple region), which is probably initially coupled into the glass or leaked from the wire region due to imperfections (gaps in the wires, for example) or for being ordinary waves (electric field transverse to the anisotropy axis, which do not "see" the wires and diffract).

In order to reduce the coupling loss in the aperture further, another type of aperture was developed and milled with a FIB. Figure 5.22 shows the SEM micrograph of two different sets of "anti-apertures", with different structural parameters, where the dark region is the glass and the lighter region is the gold film. The outside diameter of the milled region is slightly smaller than the typical outside diameter of the wire array region on the smallest facet

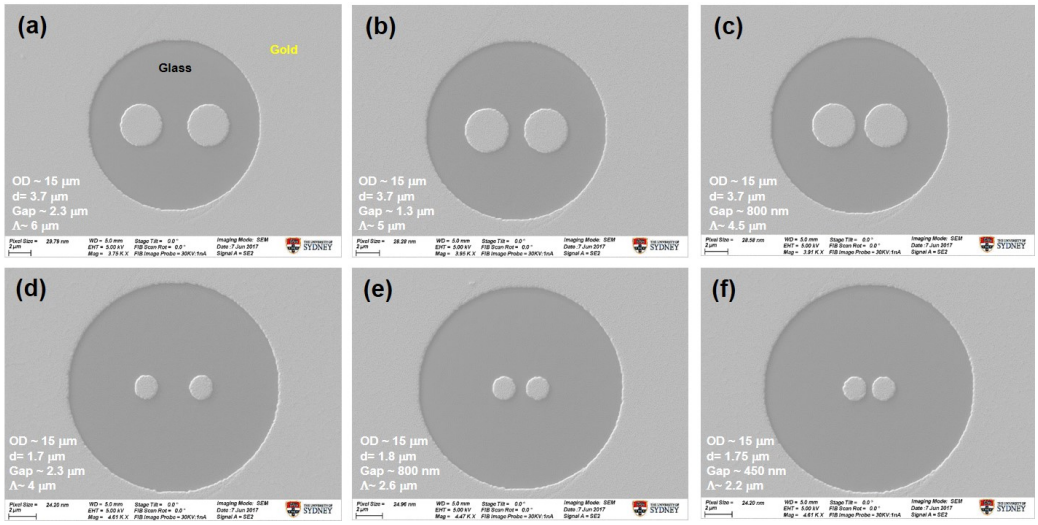

Figure 5.22: Two sets of anti-apertures fabricated by FIB milling on a borosilicate coverslip covered with a gold film ($\sim 100\,\text{nm}$). Different structural parameters: (a-c) OD of the circular milled region around $15\,\mu$m, $d \sim 3.7\,\mu$m, and Λ varying from 6 to $4.5\,\mu$m. (d-f) OD of the circular milled region around $15\,\mu$m, $d \sim 1.7\,\mu$m, and Λ varying from 4 to $2.2\,\mu$m.

of the hyperlens, in order to maximize the power coupled to and avoid any coupling of light to the soda-lime jacket cladding of the hyperlens.

It is important to emphasize that, due to their structural parameters, the anti-apertures presented in Fig. 5.22(a-c) are resolvable in a far field imaging experiment using $\lambda = 2.8\,\mu$m and an out-coupling lens with $\text{NA} = 0.56$ (no magnifying hyperlens is required), once Λ is larger than the diffraction limit in this configuration ($l = 2.5\,\mu$m). However, the large area without gold (defined by the OD of $15\,\mu$m) improves considerably the amount of power transmitted through the aperture, thus providing an excellent geometry to test the magnification of the magnifying hyperlens. Once the magnified far field image of such resolvable apertures are performed, the anti-aperture presented in Fig. 5.22(d-f) can be employed for a proof-of-concept of the subdiffraction imaging.

Figure 5.23(a) shows the SEM micrograph of the first anti-aperture employed in our imaging experiments, with $d = 7.5\,\mu$m, $\Lambda = 7.8\,\mu$m, and $\text{OD} = 20\,\mu$m. The experimental and simulated far field image of this anti-aperture is shown in Fig. 5.23(b) and Fig. 5.23(c), respectively. After the far field of

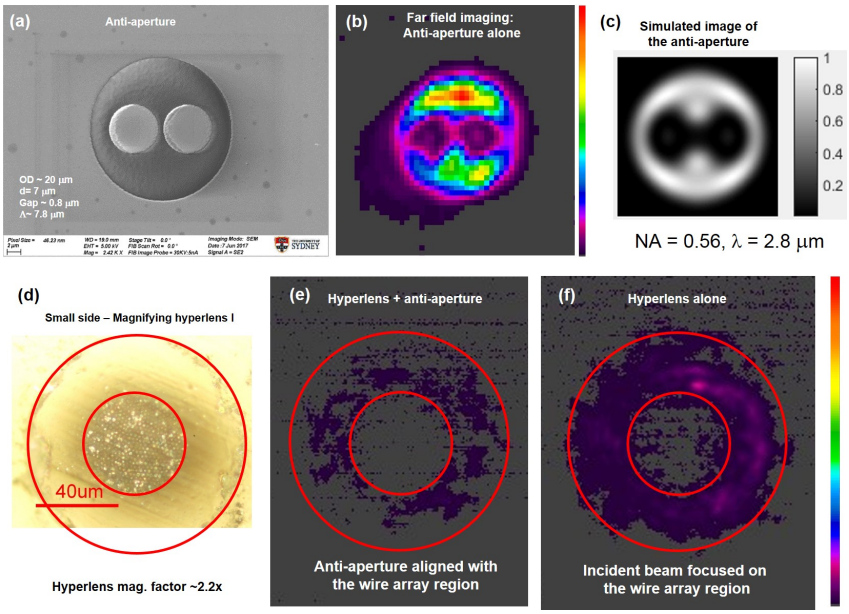

Figure 5.23: (a) SEM micrograph of anti-aperture with OD$\sim 20\mu$m, $d \sim 7\,\mu$m, and $\Lambda = 7.8\,\mu$m. (b) Far field imaging of the anti-aperture alone. (c) Simulated far field imaging of the anti-aperture considering an uniform plane wave excitation. (d) Cross section picture of the small side of hyperlens I, with magnification factor of ~ 2.2x, wire diameter varying from approximately 500 nm to 1.1 μm, $d/\Lambda = 0.5$. (e) Far field imaging of the anti-aperture and the hyperlens. (f) Far field imaging of the hyperlens alone. Experimental setup: ZnSe in-coupling lens with NA $= 0.25$, $f = 6$ mm (Innovation photonics), out-coupling chalcogenide aspheric lens with NA $= 0.56$, $f = 4$ mm, glass GeSbSe, Thorlabs), $\lambda = 2.8\,\mu$m, Spiricon camera 38 cm away from the out-coupling lens.

the anti-aperture was obtained, the magnifying hyperlens seen in Fig. 5.23(d) (magnification factor of 2.2x, d varying approximately from 500 nm to 1.1 μm, $d/\Lambda = 0.5$) was inserted and aligned after the apertures. The resultant magnified far field image obtained with the anti-aperture aligned with the center of the wire array region can be seen in Figure 5.23(e), where it is evident that no light from the wire array region is detected. The red lines define the wire array region and the jacket soda-lime cladding of the hyperlens.

Even with the anti-aperture removed and all the power focused on the wire array region (~ 200 mW), the amount of signal transmitted through the wire array region of the hyperlens is insufficient to be detected by the

camera, as seen in Fig. 5.23(f). This indicates that the power density by pixel in the image plane corresponding to the wire array region is smaller than the noise level of the Spiricon camera (64 nW/pixel). This is in agreement with our power density by pixel estimation. Experimentally, the coupling loss of the in-coupling and out-coupling lenses was measured as 4 dB and 1 dB, respectively, for the configuration used to obtain the image of Fig. 5.23(f). Adding the 30 dB loss of the hyperlens (simulated for the quasi-TEM with $k_{\perp max}$, $\lambda = 3\,\mu$m) to the coupling losses, the overall loss of the system is expected to be 35 dB. For an input power of 200 mW, an attenuation of 35 dB, and an image area with 3000 pixels (corresponding the area of the inner red circle of Fig. 5.23(f)), the power density by pixel is expected to be 21.1 nW/pixel, which is smaller than the noise level of the camera.

The power density by pixel in the image plane can be improved by increasing considerably the input power, improving the coupling, and/or using a hyperlens with lower overall loss (shorter and with lower magnification factor). Thus, higher input power and another shorter hyperlens with smaller overall loss were employed in the far field imaging of the anti-aperture presented in Fig. 5.23(a). Figure 5.24(a) shows the cross-section of the small side of this second sample (hyperlens II), with a magnification factor around 1.56x, wire diameter varying from approximately 500 nm to 780 nm, $d/\Lambda = 0.5$, and simulated overall loss of 27 dB (quasi-TEM mode with $k_{\perp max}$, $\lambda = 3\,\mu$m). The far field image of the aperture alone and with the hyperlens II is presented in Fig. 5.24(b) and (c), respectively.

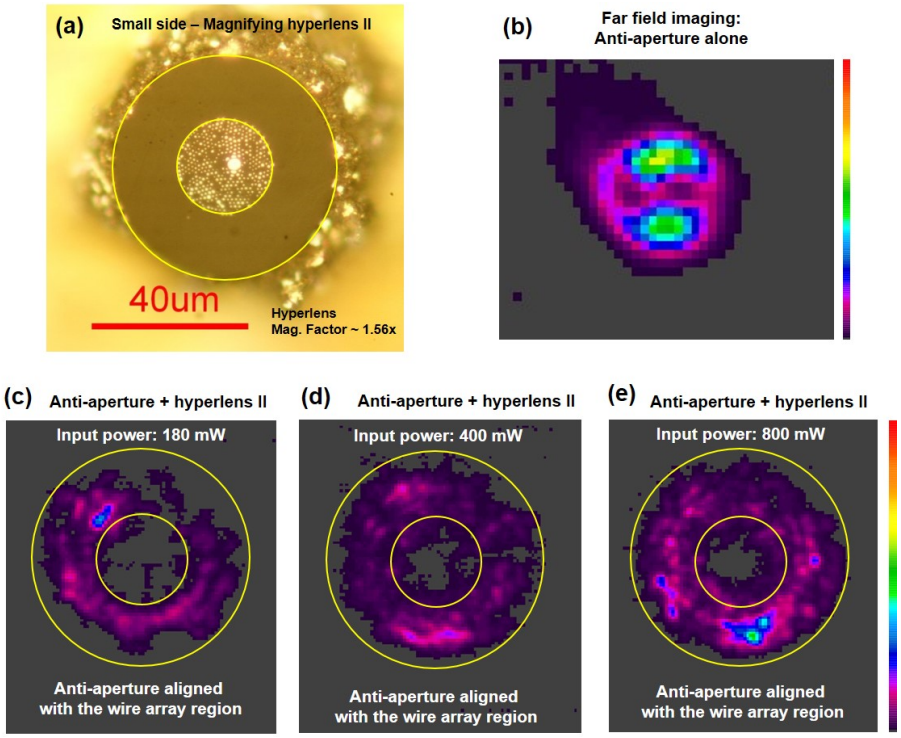

Figure 5.24: (a) Cross-sectional picture of the small side of this second sample (hyperlens II), wire diameter varying from approximately 500 nm to 780 nm, $d/\Lambda = 0.5$, with a magnification factor around 1.56x. (b) Far field imaging of the double aperture alone. Far field imaging of the anti-aperture with the hyperlens, for different input power (CW, $\lambda = 2.8\,\mu$m): (c) 180 mW; (d) 400 mW; (e) 800 mW. Imaging setup: In-coupling ZnSe lens with NA = 0.67, $f = 12.7$ mm, out-coupling aspheric lens with NA = 0.56, $f = 4$ mm (glass GeSbSe, Thorlabs), Spiricon camera 21 cm away from the out-coupling lens.

Firstly, using an input power of 180 mW, it is possible to distinguish a small amount of light in the wire array region (Fig. 5.24(c)), but there is not enough signal to identify the anti-aperture. Keeping the same alignment and increasing the power to 400 mw (Fig. 5.24(d)) and 800 mW (Fig. 5.24(e)), the amount of light in the outside region of the wire array increases, but even with such powers there is not enough light to identify the anti-aperture.

In the configuration employed in Fig. 5.24, the in-coupling lens exhibited a coupling loss of 2 dB (different lens than the one employed at Fig. 5.23), while the out-coupling lens exhibited a coupling loss of 1 dB. Adding the 27 dB loss

of the hyperlens (simulated for the quasi-TEM with $k_{\perp max}$, $\lambda = 3\,\mu$m) and the 8 dB loss due to the anti-aperture (Fig. 5.24(b)) to the coupling losses, the overall loss of the system is expected to be 38 dB. For input powers of 400 mW and 800mW, an attenuation of 38 dB, and an image area with 900 pixels (corresponding the area of the inner yellow circle of Fig. 5.24(d-e)), the power density by pixel is expected to be 70.4 nW/pixel and 140.8 nW/pixel, respectively. These values are both slightly above the noise level of the Spiricon camera (64 nW/pixel), and apparently in agreement with the visualization of some signal from the wire array region, as seen in Fig. 5.24(d-e). Thus, it is evident that an even higher power density by pixel in the image plane is required to properly image the employed anti-aperture, which means an improvement in the overall loss or in the input power.

After the imaging attempt with an incident power of 800 mW, a change in the optical response of the hyperlens was noticed, which could not reproduce anymore the same far field images than achieved with lower powers (Fig. 5.24(c) and (d)). Microscopy pictures of both facets of the hyperlens indicated that such high power melted the tin from the wires, bringing the metal up to the glass surface, as seen in Fig. 5.25(a,b). Consequently, increasing the power above a few hundred milliwatts is not a viable alternative to obtain detectable signal in the wire array region for the typical tin/soda-lime hyperlens fabricated. The remaining options are the improvement of the coupling, the reduction of the hyperlens loss, and/or the the improvement of the detection.

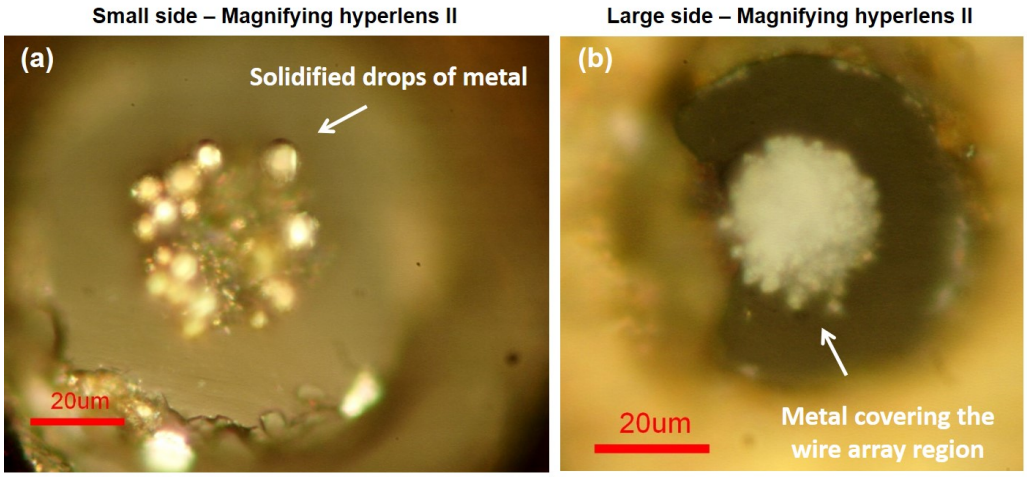

Figure 5.25: Micrograph of the cross section of both facets of the magnifying hyperlens II (Fig. 5.24(a)) after the imaging experiment using an input power up to 800 mW, (CW, $\lambda = 2.8\,\mu$m). The solidified drops of metal in (a) and the uniformed gray cover up to the wire array region in (b) indicate that the metal melted and came out of the hyperlens's surface.

The reduction of the overall optical loss of the hyperlens can be obtained by reducing even more the length of the metadevice. This is possible with the employment of a thinner metallic foil in the hyperlens's embedding process. The fabrication of such samples with stainless steel foil with 13 μm thickness is in progress. If successful, hyperlenses with lengths as small as 13 μm could be achieved, leading to overall losses in the 10-20 dB scale (quasi-TEM mode with $k_{\perp max}$, $\lambda = 3\,\mu$m), depending on the structural parameters of the sample. Calculations taking into account the input power limit, the typical overall coupling losses of our experimental setup, the sensitivity of the Spiricon camera, and the number of pixels employed, the image magnified by the wire array region should be detectable. However, without the improvement of the fabrication process to achieve steeper transitions, this alternative compromises the resolution and the magnification factor of the hyperlens, which means that subdiffraction far field imaging with such samples are not feasible.

The improvement of detection could be achieved by replacing the pyroelectric array camera, which has a noise equivalent power around $10^{-8}\,\mathrm{W}/\sqrt{Hz}$ [202], for a MCT solid state single detector (HgCdTe), which can have a noise equivalent power around $10^{-12}\,\mathrm{W}/\sqrt{Hz}$ [205]. However, there is no array option for this type of detector, meaning that a scanning approach should be

employed for imaging at the MIR. Note that imaging with a scanning technique has the disadvantage of long scanning times (few hours depending on the scanning parameters), and complications regarding the alignment and the cooling of the detector.

5.5 Conclusion and discussions

The main conclusion of the presented far field imaging attempt with our tin/soda-lime magnifying hyperlenses is that subdiffraction imaging is not feasible for short MIR wavelengths around 3 μm due to the high optical loss of the metadevices, even for samples with low magnification factor, extremely steep and short tapered transitions. Due to the tin's low melting point, the maximum input power that the metadevices withstand is also limited to a few hundred mW. Proof-of-concept far field imaging could be obtained by replacing the array camera with a solid-state single detector employing a scanning technique, but this introduces other problems related to alignment and long scanning times. Shorter tin/soda-lime hyperlenses, depending on the structural parameters selected, could present overall losses in the 10-20 dB scale, which makes detection feasible. However, without an improvement in the fabrication of steeper transitions, such samples will possess a minimal magnification factor, not suitable for any subdiffraction imaging at 3 μm operational wavelength. Alternatively, preliminary modeling indicates that the hyperlenses fabricated in this thesis could also exhibit overall losses in the 10-20 dB scale at slightly larger wavelengths (for example, losses $\sim$1.4x smaller in dB at 5 μm operational wavelength, in comparison to 3 μm operational wavelength). Therefore, subdiffraction imaging at such larger wavelengths could also be feasible and will be further studied and exploited.

According to our numerical simulations, the best scenario regarding loss for this type of metamaterial concerning far field subdiffraction imaging in the short MIR is wire array fibres made of gold wires embedded in silica, since its overall loss is one-third (in dB) compared to an equivalent structure in tin/soda-lime system (at 3 μm operational wavelength). Due to the higher melting point and glass transition temperature of gold and silica, respectively, this system would also allow the use of higher input power. In this context, having a considerable amount of signal after the gold/silica "low loss hyperlens", structural parameters that lead to higher resolution and higher magnification factor could be exploited. Note that, even with a high overall

loss in the 10-20 dB scale, the ideal gold/silica system would make possible the far field detection of modes with high-$k_\perp$ components, which leads to super-resolution imaging. Without the hyperlens, these high-$k_\perp$ modes would be evanescent in free-space, exhibiting much higher attenuation than 10-20 dB. In addition, other issues must be addressed, *e.g.* the filtering of the ordinary waves that leak from the wire array structure and usually have lower losses, adding considerably to the expected noise level [206].

Chapter 6

Tin/soda-lime wire array metamaterial fibres for applications at millimetre wave and THz frequencies

This Chapter concerns the use of the wire array metamaterial fibre hyperlenses made of tin/soda-lime for focusing and imaging applications at THz frequencies. Due to the lower penetration of the fields in the metal wires in such a regime, the overall loss of such metadevices is smaller in comparison to the unworkable losses seen at mid-infrared frequencies. Subdiffraction focusing of a THz signal down to 1/176 of its wavelength is demonstrated with the employment of two different concatenated hyperlenses. Future directions for such a promising configuration are discussed regarding subdiffraction focusing and near field and far field super-resolution imaging.

6.1 Subdiffraction focusing with magnifying hyperlenses

THz frequencies are of extreme interest for imaging and spectroscopy. However, one limitation that causes scepticism about THz is the size of the wavelength, when imaging applications are concerned. Because of the mm scale of the wavelength, the resolution is orders of magnitudes away from that of visible microscopy. In order to overcome this limitation, subdiffraction

focusing of THz waves has been reported in the literature using plasmonic waveguides [207–209] and metamaterial hyperlenses [50].

In an isotropic medium like free-space, the resolution of optical systems for imaging or focusing are limited by diffraction, to about half the wavelength of the light. As discussed before, such diffraction limit arises from the spatial frequency bandwidth of the medium that restricts the propagation of waves to transverse wavevector components smaller than $k_0 = 2\pi/\lambda_0$. Magnifying wire array metamaterials (hyperlenses) can beat this limit due to their hyperbolic dispersion, which arises from the highly anisotropic and sub-wavelength metallic structure. This allows the propagation of high spatial frequencies that contain the subdiffraction information and would be evanescent in an isotropic medium [47].

When the hyperlens is employed in a focusing configuration, coupling the light in its large facet, the tapered transition compresses all spatial frequencies, which still propagate due to the metamaterial's hyperbolic dispersion, making possible the focusing of the transmitted radiation below the diffraction limit. As discussed in Section 5.1.2, Tuniz *et al.* have demonstrated subdiffraction focusing at THz frequencies with a magnifying metamaterial hyperlens made of indium wires embedded in polymer fibre (PMMA and Zeonex) in Ref. [50]. The tapered transition with a magnification factor of 8x achieved a focusing of $\lambda/28$ in one direction for a 75 GHz signal (see Fig. 5.5(d,e)).

Further improvement in the focusing was impossible due to fabrication limitations of drawn metamaterial fibres based on polymer. Plateau-Rayleigh instability limits the size of the wires to a few microns in the indium/polymer system [84], consequently restricting the size of the meta-structure and its operational range. Below such structural limit, fluctuations of the wire diameters greatly deform the wire array structure, which can lead to the breaking of the wires and be highly detrimental to the metamaterial's optical response. As an alternative, as demonstrated in Chapters 4 and 5, our soft-glass metamaterial fibres and hyperlenses can be fabricated with smaller and still uniform structures, since their different rheological properties shifts down the Plateau-Rayleigh instability to wire diameters of hundreds of nm.

Since the operational range of our tin/soda-lime wire array hyperlenses is not limited to the infrared, subdiffraction imaging and focusing can be performed with them at THz frequencies. In this low frequency regime, the metal wires behave like perfect conducting wires, which result in a smaller penetration of the electromagnetic field in the metal, and the overall loss of

the infrared metamaterial fibres is expected to be smaller than their high losses in the mid-infrared (which are on the order of 1 dB/μm, quasi-TEM mode with $k_{\perp max}$, $\lambda = 3\,\mu$m).

Below, subdiffraction focusing with a combination of two wire array hyperlenses, the polymer/indium one from Ref. [50] and our tin/soda-lime hyperlens (Chapter 5), is demonstrated at THz frequencies. Such configuration has huge potential for extreme focusing and near and far field imaging.

6.1.1 Subdiffraction focusing with hybrid wire array hyperlens at millimetre wave and THz frequencies

In order to improve the subdiffraction focusing of THz radiation with metamaterial fibre-based hyperlens reported in the literature [50], two different metamaterial hyperlenses are combined (mechanically aligned with micrometre positioning stages), giving a hybrid hyperlens, as illustrated in Fig. 6.1.

The first hyperlens contains 473 hexagonally spaced indium wires embedded in a PMMA/Zeonex fibre (fabricated by Tuniz *et al.* in Ref. [50]). The wire diameter (d) through the tapered region reduces from 80 to 10 μm, while their separation (Λ) decreases from 400 to 50 μm (Fig. 6.1(b) and (c)). The second hyperlens contains 462 hexagonally spaced tin wires embedded in a soda-lime glass fibre. The wire diameter of this second tapered region reduces from 10 to 2.5 μm, while Λ decreases from 20 to 5 μm (Fig. 6.1(d) and (e)). The expected magnification factor of this hybrid hyperlens is 32x, calculated by the multiplication of the two separate magnification factors (8x for the polymer and 4x for the glass hyperlens). The lengths of the indium/polymer and tin/soda-lime hyperlenses are 38 mm and 3 mm, respectively.

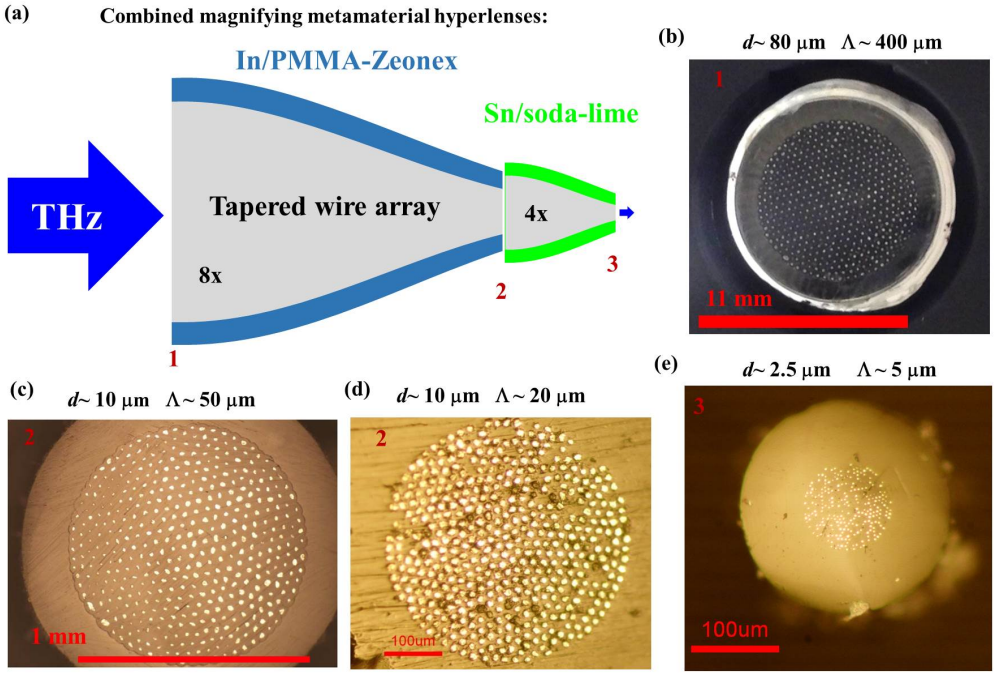

Figure 6.1: (a) Schematic of our combined polymer and glass metamaterial fibre magnifying hyperlenses used in the focusing experiment. Cross-section pictures of the fibres on every interface. (b) Region 1, $d \approx 80\,\mu$m, $\Lambda \approx 400\,\mu$m. (c) Region 2, $d \approx 10\,\mu$m, $\Lambda \approx 50\,\mu$m. (d) Region 2, $d \approx 10\,\mu$m, $\Lambda \approx 20\,\mu$m. (e) Region 3, $d \approx 2.5\,\mu$m, $\Lambda \approx 5\,\mu$m. (b,c) Indium/polymer hyperlens fabricated in Ref. [50]. (d,e) Tin/soda-lime hyperlens. Figure (c) was extracted from Ref. [50].

In order to characterize the overall focusing capability of our hybrid hyperlens, an experiment was set up with a THz time-domain spectroscopy system [210] to measure the transmitted (and focused) image through the metamaterial, as represented in Fig. 6.1(a). Figure 6.2(a) illustrates our THz time-domain spectroscopy system, composed of a Ti:Sapphire femtosecond pump laser (800 nm, 80 MHz, pulse width of 150 fs), a photoconductive emitter antenna from Ekspla, and a Teraspike near field photoconductive antenna from Protemics as the detector. The typical time-domain and frequency domain spectra generated and detected by this system (without any sample) are shown in Fig. 6.2(b) and (c), respectively.

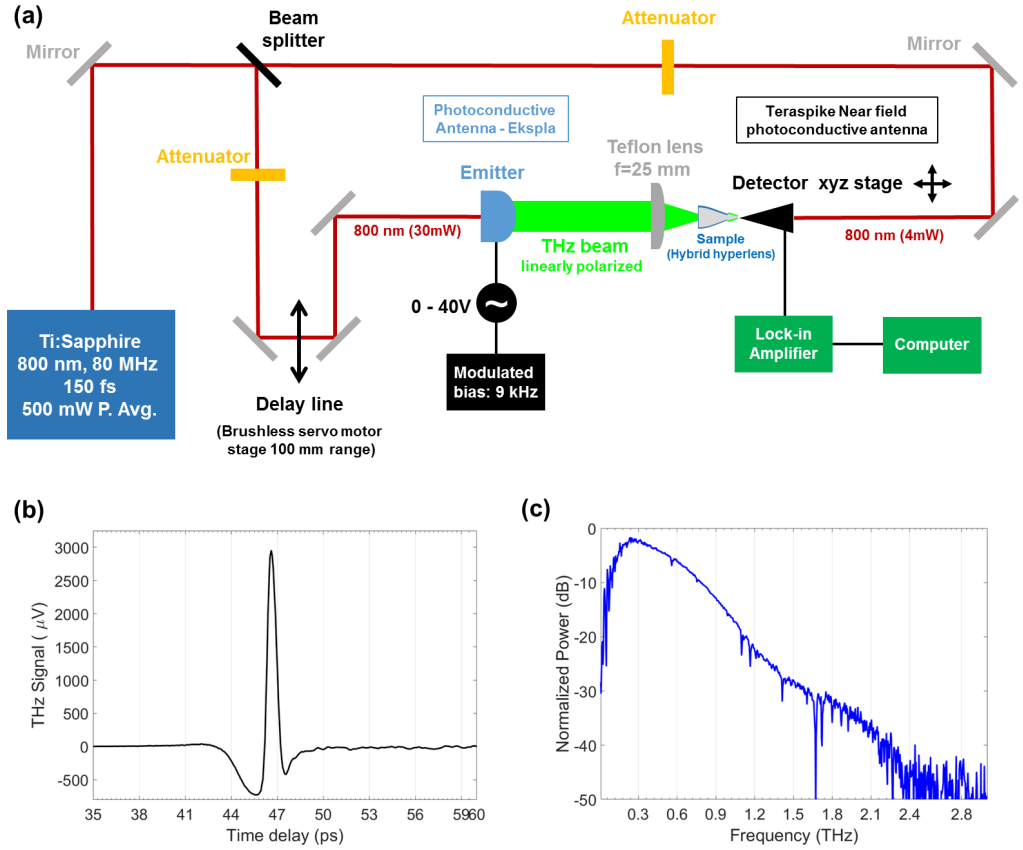

Figure 6.2: (a) Schematic of our THz-time domain spectroscopy system. Typical time-domain (b) and frequency domain (c) spectra of the generated and detected THz pulse.

A pinhole with diameter 1.5 mm was attached to the large side of the polymer hyperlens (Fig. 6.3(a)). The collimated and linearly polarized THz pulse was focused with a teflon lens, focal length of 25 mm, and aligned with the pinhole to maximize the power coupled and focused by the hybrid hyperlens. On the small side of the combined hyperlenses, a near field antenna performed 2D scans over an area of 200 x 200 μm, with a spatial step of 5 μm.

Figure 6.3(b-d) show the resulting focused images of the 1.5 mm pinhole after the hybrid hyperlens, for three different frequencies: 34 GHz (b), 58 GHz (c), and 72 GHz (d). As expected, the fields spread for all frequencies in the x-directions because the y-polarized input excites diffracting ordinary waves with x-wave vector components. On the other hand, the y-polarized

signal excites extraordinary waves in the y-direction that are confined by the metamaterial structure and consequently non-diffractive. Figure 6.3(e) shows the intensity profile in the y-direction for the three obtained images.

According to the full width at half maximum (FWHM) calculated from Fig. 6.3(e), the initial 1.5 mm circular energy distribution coupled into the hyperlens was focused in the y-direction to approximately 50 μm (at 34 GHz, $\lambda = 8.8$ mm), 60 μm (at 58 GHz, $\lambda = 5.2$ mm) and 70 μm (at 72 GHz, $\lambda = 4.2$ mm), with an error of $\pm 5\,\mu$m due to step size of the near field antenna. These correspond to subdiffraction focusing of approximately $\lambda/176$, $\lambda/87$, and $\lambda/60$, respectively. Note that these values must be treated as an approximation due to the low quality (high noise) of the curves presented in Fig. 6.3(e). New measurements with other samples and smaller step in the near field scan are currently in progress. Once smooth intensity profiles are obtained, the FWHM can be calculated with more precision from a Gaussian/Lorentzian like fitting.

If a perfect focus was performed, without any diffraction, the focused image of the original pinhole should have a width of $\sim$47 μm in the y-direction,

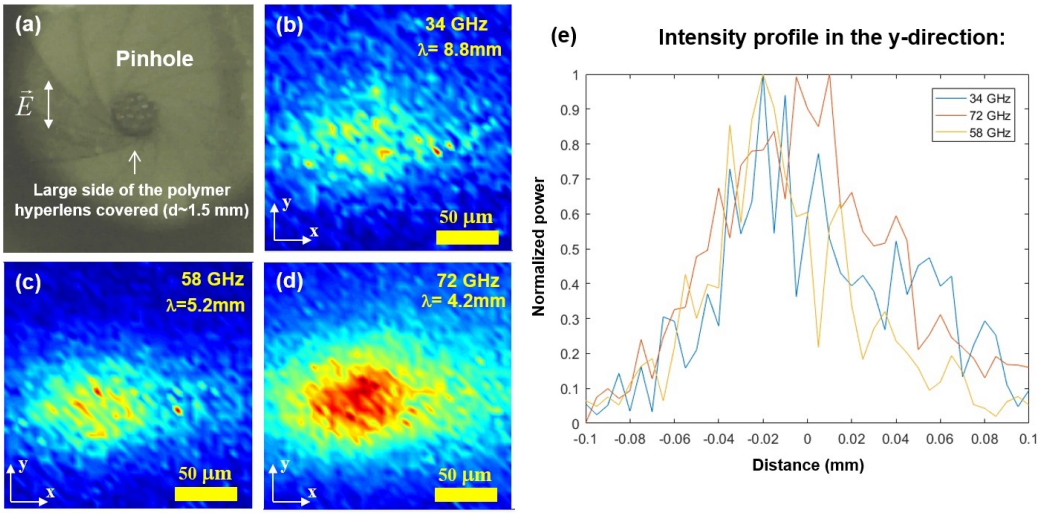

Figure 6.3: (a) Image of the large side of the polymer hyperlens covered with a 1.5 mm pinhole. Focused image of the pinhole after the hybrid hyperlens, probed with a near field antenna, for different frequencies: (b) 34 GHz ($\lambda = 8.8$ mm), (c) 58 GHz ($\lambda = 5.2$ mm), and (d) 72 GHz ($\lambda = 4.2$ mm). (e) Normalized intensity profiles in the y-direction of the focused images (b-d).

which corresponds to the ratio between the pinhole diameter and the overall magnification factor of the hybrid hyperlens. This value is in good agreement with the experimental value of 50 μm found at 34 GHz. There is a small difference of the focusing between the frequencies presented in Fig. 6.3. This is close to the experimental error of the measurement, and it could be also due to the different coupling of the various frequencies with the sub-wavelength pinhole and diffraction in the gap between the hybrid hyperlens and the near field antenna ($\sim$20 μm).

Even with the expected high optical loss of the soda-lime glass at THz, a considerable amount of power was measured after the tin/soda-lime wire array hyperlens. For comparison, no signal could be detected using the same optical components through a 200 μm pinhole, which is four times larger than the minimum focused spot achieved by the hybrid hyperlens.

A comparison between the output power after the polymer and glass hyperlenses indicates an overall loss around 15 dB due to introduction of the tin/soda-lime hyperlens in the imaging setup (at 72 GHz, $\lambda = 4.2$ mm). This experimental value takes into account the tin/soda-lime metamaterial absorption (ordinary and extraordinary modes, all wavevector components), and the back-reflection on both facets of the hyperlens, which is high due to the high refractive index of the soda-lime glass in such THz frequencies (around 2.6 at 60 GHz [211]).

Overestimating the absorption loss as 15 dB, our 3 mm length tin/soda-lime hyperlens has a loss of around 5 dB/mm at 72 GHz. According to the extinction coefficient (κ) for the soda-lime glass reported in Ref. [211] ($\kappa = 0.0318$ at 60 GHz), the expected loss due to the glass absorption is around 0.35 dB/mm. This indicates that, even at THz frequencies, the loss due to the metal is more relevant than the absorption from the glass.

As expected, due to the smaller overlap between the modal energy distribution in the metal wire, the metamaterial's optical loss is considerably lower at THz frequencies ($\approx$ 5 dB/mm) than the typical losses in the mid-infrared (around 110 dB/mm for the structure shown in Fig. 6.1(e), $d = 2.5$ μm, $\Lambda = 5$ μm, $\lambda = 3$ μm, quasi-TEM mode, $k_{\perp max}$). Note that the length of the tin/soda-lime hyperlens (3 mm) is smaller than the operation wavelength employed here (from 4.2 mm to 8.8 mm), making it a strongly resonant and far from adiabatic device. It wasn't thus straightforward that such a device would indeed work, and clearly further theoretical analysis will be required to understand it fully.

6.1.2 Conclusions and future directions

Extreme subdiffraction focusing up to $\lambda/176$ for THz frequencies using a combination of two metamaterial hyperlenses was demonstrated. This focusing could be greatly improved with the use of a glass hyperlens with higher magnification factor. Preliminary tests with our tapering setup indicate that it would be possible to scale down the wire array structure presented in Fig. 6.1(e) by 25x, resulting in a tin/soda-lime hyperlens with magnification factor of 100x. If combined with polymer hyperlens, this new hybrid hyperlens could achieve focusing of $\lambda/1600$ and would be likely limited by its overall optical loss.

Consequently, such compact configuration exhibits great potential to beat the best focusing of THz radiation achieved so far with plasmonic waveguides ($\lambda/260$) [207]. The fabrication, characterization and the modelling of such hybrid hyperlenses is currently in progress. The hybrid hyperlens also has potential to perform super-resolution imaging in the near and far field, improving the results already reported with the polymer hyperlens alone [212].

Finally, it is important to emphasize that the subdiffraction focusing presented in this Chapter is also a proof-of-concept that our tin/soda-lime wire array fibres are metamaterials (exhibit hyperbolic dispersion), and it is a strong indication that the problems seen in the mid-infrared far field experiments are related to the high overall loss of the hyperlenses at such operational frequencies.

Chapter 7

Concluding remarks and future directions

In this thesis the fabrication of the first wire array metamaterial fibres with uniform structures suitable for MIR operation was demonstrated. Wire arrays composed of tin wires embedded in soda-lime glass were reported, with wire diameters as small as 143 nm and structural fluctuation (quantified by the factor σ_d/d_{avg}) as small as 0.18 for wires with d_{avg} around 240 nm, which represents a remarkable degree of uniformity for such dimensions. Comparing the instabilities of our best structures with the ones seen in the indium/polymer system (Ref. [84] and Fig. 4.24) the level of quality $\sigma_d/d_{\text{avg}} < 0.18$ can be only obtained with wire diameters around 4.3 μm in indium/PMMA metamaterial fibres. Therefore, it is clear that our replacement of the polymer by soft-glasses and the use of the tapering process in the last fabrication step made possible the fabrication of wire structures approximately 18x smaller with an equivalent quality, which is a remarkable improvement in such a complex co-drawing process.

The fabrication, characterization and modeling of magnifying hyperlenses with tapered wire array structures suitable for MIR applications were also reported in this thesis. Far field imaging with our tin/soda-lime magnifying hyperlenses was attempted, with the conclusion that subdiffraction imaging is not feasible for short MIR wavelengths around 3 μm due to the high optical loss of the metadevices, even for samples with low magnification factor, extremely steep and short tapered transitions. Due to the tin's low melting point, the maximum input power that the metadevices withstand is also limited to a few hundred mW.

Regarding future directions, proof-of-concept far field imaging could be obtained by replacing the array camera used in this thesis with a solid-state single detector and employing a scanning technique. However, this introduces other problems related to alignment and long scanning times. Shorter tin/soda-lime hyperlenses, depending on the structural parameters selected, could exhibit overall losses in the 10-20 dB scale, which makes detection feasible. However, without an improvement in the fabrication of steeper transitions, such samples will possess a minimal magnification factor, not suitable for any subdiffraction imaging at 3 μm operational wavelength. Alternatively, preliminary modeling indicates that the hyperlenses fabricated in this thesis could also exhibit overall losses in the 10-20 dB scale at slightly larger wavelengths (for example, losses $\sim$1.4x smaller in dB at 5 μm operational wavelength, in comparison to 3 μm operational wavelength). Therefore, subdiffraction imaging at such larger wavelengths could also be feasible and will be further studied and exploited.

According to our numerical simulations, the best scenario regarding loss for this type of metamaterial concerning far field subdiffraction imaging in the short MIR is wire array fibres made of gold wires embedded in silica, since its overall loss is one-third (in dB) compared to an equivalent structure in tin/soda-lime system (at 3 μm operational wavelength). Due to the higher melting point and glass transition temperature of gold and silica, respectively, this system would also allow the use of higher input power. In this context, having a considerable amount of signal after the gold/silica "low loss hyperlens", structural parameters that lead to higher resolution and higher magnification factor could be exploited. Note that, even with a high overall loss in the 10-20 dB scale, the ideal gold/silica system would make possible the far field detection of modes with high-$k_\perp$ components, which leads to super-resolution imaging. Without the hyperlens, these high-$k_\perp$ modes would be evanescent in free-space, exhibiting much higher attenuation than 10-20 dB. In addition, other issues must be addressed, *e.g.* the filtering of the ordinary waves that leak from the wire array structure and usually have lower losses, adding considerably to the expected noise level [206].

Due to the lower penetration of the electromagnetic fields in the metal wires at THz frequencies, the overall loss of our tin/soda-lime wire array metamaterias is expected to be smaller in comparison to those at MIR frequencies. Extreme subdiffraction focusing of a THz signal down to 1/176 of its wavelength was demonstrated in this thesis using a combination of two metamaterial hyperlenses (tapered wire array tin/soda-lime hyperlens and a

polymer/indium hyperlens previous fabricated by Alessandro Tuniz).

Regarding future directions at THz frequencies, the subdiffraction focusing obtained could be greatly improved with the use of a glass hyperlens with higher magnification factor. Preliminary tests with our tapering setup indicate that it would be possible to scale down the wire array structure presented in Fig. 6.1(e) by 25x, resulting in a tin/soda-lime hyperlens with magnification factor of 100x. If combined with a polymer hyperlens, this new hybrid hyperlens could achieve focusing of $\lambda/1600$ and would be likely limited by its overall optical loss. Consequently, such compact configuration exhibits great potential to beat the best focusing of THz radiation achieved so far with plasmonic waveguides ($\lambda/260$) [207]. The fabrication, characterization and the modeling of such hybrid hyperlenses is currently in progress. The hybrid hyperlens also has potential to perform super-resolution imaging in the near and far field, improving the results already reported with the polymer hyperlens alone [212].

In conclusion, the work presented in this thesis opened several possibilities regarding metamaterial fibres for super-resolution far field imaging and lifetime engineering (discussed in Appendix A) applications in the MIR. The metamaterial structures fabricated in this thesis also offers exciting possibilities for extreme subdiffraction and far field imaging at THz frequencies.

Appendix A

Engineering lifetime with metamaterial fibres

This Appendix discusses the use of the tin/soda-lime metamaterial fibres for lifetime engineering of emitters at mid-infrared frequencies. Emitter candidates are analyzed and a proof-of-concept experiment for the lifetime engineering is suggested and discussed.

A.1 Engineering lifetime with metamaterials

A quantum system such as an atom, ion or molecule can be excited to a higher energy level by different processes such as photon absorption, heat and electrical current. This excited state is not stable and decays to its original level by the emission of a photon, in a process called spontaneous emission, as illustrated in Fig. A.1.

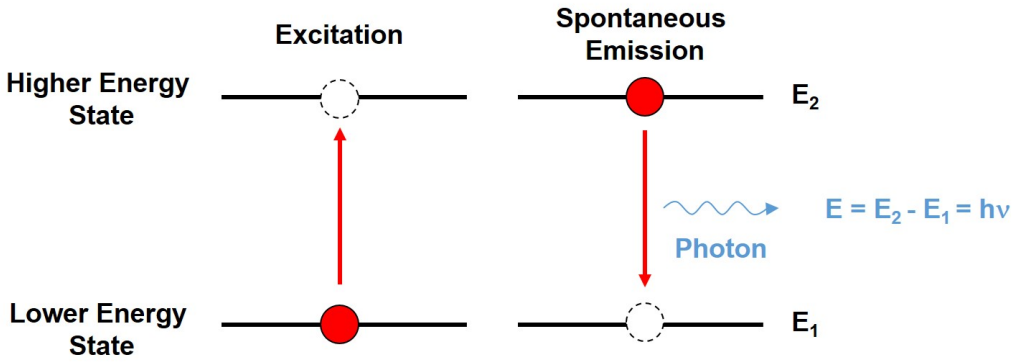

Figure A.1: Schematic of the spontaneous emission in a two level system.

When the system is excited by a large number of photons with energy compatible with its absorption energy levels, a population density in the upper energy level (N_2) is excited. The dynamics of the upper state population as a function of time, if the pump energy is turned off, is described as

$$\frac{\partial N_2(t)}{\partial t} = -\Gamma_{21} N_2(t), \tag{A.1}$$

where Γ_{21} is the rate of the spontaneous emission. Solving the differential Eq. (A.1), the temporal evolution of the upper state population is given by

$$N_2(t) = N_2(0) e^{-\Gamma_{21} t}, \tag{A.2}$$

where $N_2(0)$ is the initial population excited at the upper level. The lifetime of the transition (τ_{21}) is defined as the time required for the excited population density to decay to 1/e ($\approx 37\%$) of its initial value. From Eq. (A.2), the lifetime is the inverse of the spontaneous emission rate

$$\tau_{21} = \frac{1}{\Gamma_{21}}, \tag{A.3}$$

which is determined by the properties of the atom/molecule and the electromagnetic mode structure of the medium where it is immersed. According to Fermi's golden rule (Eq. (A.4)), this spontaneous emission rate is proportional to the local photonic density of states (ρ_{pdos}) of the surrounding

media, the angular frequency (ω), and the dipole moment associated with the transition (μ_t) [213, 214]:

$$\Gamma = \frac{1}{\tau} = \frac{2\omega}{3\hbar\epsilon_0}\rho_{pdos}|\mu_t|^2. \tag{A.4}$$

Note the prefactor in Eq. (A.4) depends on the normalization used when defining the density of states. As clearly seen in Eq. (A.4), the lifetime of a transition decreases when the emitters are placed in the near field of a medium with higher photonic density of states. In other words, more routes available for the radiative decay lead to a reduction of the emitter's lifetime.

As discussed in Chapter 2, hyperbolic metamaterials possess high photonic density of states due to their hyperbolic dispersion which allows the excitation of propagating high-k modes. Over the years, hyperbolic metamaterials have been exploited in applications related to lifetime engineering [32, 33, 39, 41]. Some of these results are summarized in Fig. A.2.

Figure A.2(a) presents the spontaneous emission lifetime of CdSe/ZnS quantum dots (normalized with the lifetime in a control sample) when the emitters are in the near field of a multilayer metamaterial composed of alternating TiO_2/silver layers (thickness of the order of 10 nm). The lifetime for a range of wavelengths around 620 nm ($\Delta\lambda$), from the wide emission band of the quantum dots, clearly shows the decrease of the emitter's lifetime in the hyperbolic regime [40]. Figure A.2(b) shows the photoluminescence kinetics of Rhodamine 800 (emission peak at 715 nm) measured with the molecules on the top (separated by a 21 nm spacer) of a dielectric (black curve), gold substrate (blue curve), and a multilayer metamaterial composed of 19 nm alternating layers of gold/Al_2O_3 (red curve) [33]. The lifetime calculated from these photoluminescence kinetics shows a reduction from 2 ns (for the dielectric case) to 1.1 ns (for the metamaterials case).

The shortening of the spontaneous emission lifetime of a laser dye emitter (IR140) embedded inside the dielectric layer of several multilayer metamaterials (Ag/PMMA) was reported in Ref. [39]. Figure A.2(c) shows the photoluminescence kinetics for different metamaterial samples in comparison with control samples (1 - glass substrate, 2 - silver substrate). From Fig. A.2(c), the lifetime of the emitters inside the metamaterials (curves 3-6) varies from 135 ps to 169 ps, while the lifetime in the near field of the control samples varies from 764 ps to 647 ps. These values indicate a shortening in the lifetime as large as 5.7x between the two configurations (inside the metamaterial and in the near field of the control sample). This reported lifetime

reduction is nearly 3-4 times larger than the values obtained for the emitter in the near field of the metamaterial reported in [33, 215].

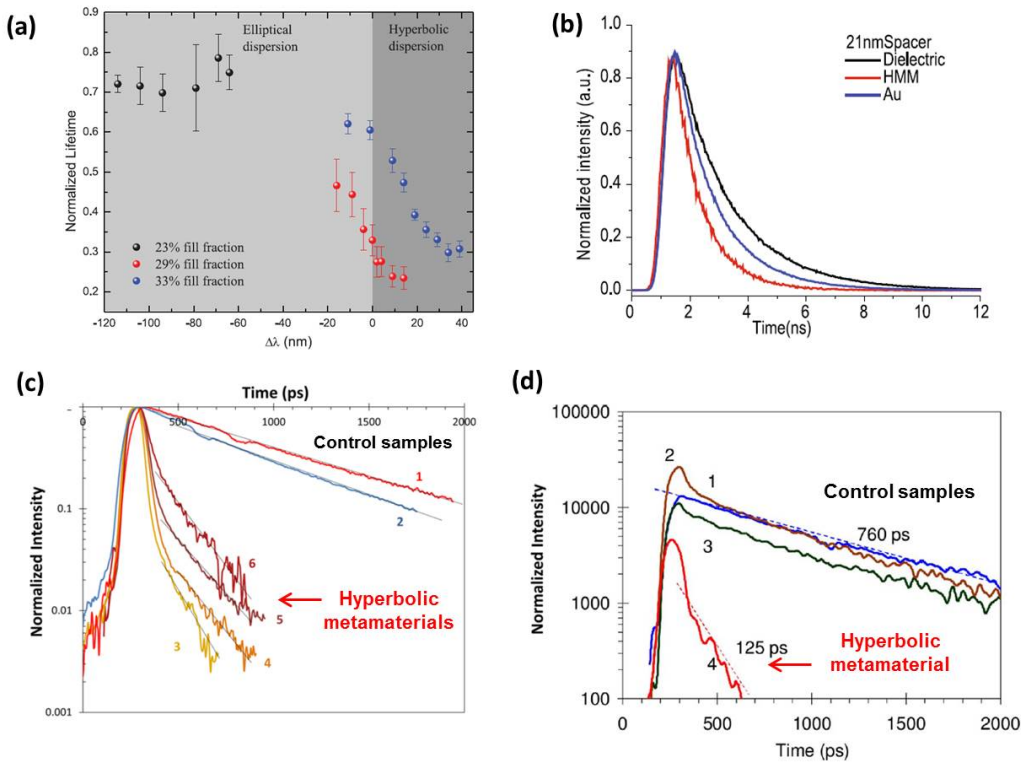

Figure A.2: Lifetime engineering with hyperbolic metamaterials: (a) spontaneous emission lifetime of CdSe/ZnS quantum dots (normalized with the lifetime in control sample) when the emitters are in the near field of a multilayer metamaterial composed of alternating TiO_2/silver layers, clearly showing the decrease of the emitter's lifetime in the hyperbolic regime (Figure extracted from Ref. [40]); (b) photoluminescence kinetics of Rhodamine 800 measured with the molecules on the top (separated by a 21 nm spacer) of a dielectric (black curve), gold substrate (blue curve), and a multilayer metamaterial (gold/Al_2O_3 layers, red curve) (Figure extracted from Ref. [33]); (c) the photoluminescence kinetics of a laser dye emitter (IR140) embedded in the PMMA layer of a multilayer metamaterial (different samples with Ag/PMMA layers) an with the emitters on the top of control samples (1 - glass substrate, 2 - silver substrate) (Figure extracted from Ref. [39]); (d) the photoluminescence kinetics of the laser dye IR140 on the top of a wire array metamaterial fibre (silver wires in Al_2O_3) and control samples (Figure extracted from Ref. [32]).

This type of lifetime engineering was also reported in wire array hyperbolic metamaterial in Ref. [32]. Figure A.2(d) shows the photoluminescence kinetics of the laser dye IR140 (emission line centered 892 nm) embedded in a PMMA film (concentration of 0.013 M) and placed on the top a wire array metamaterial composed of silver wires in Al_2O_3 (silver filling factor $\sim 15\,\%$). The lifetime obtained from the decay curves varies from 760 ps (emitter on top of the Al_2O_3 substrate) to 125 ps (emitter embedded in a PMMA film and on top of the metamaterial), which represents a reduction factor around 6x.

A more detailed overview about the physics behind the lifetime engineering with metamaterials and problems related with quenching/non-radiative decays can be found at Refs. [20, 30].

An extension of such lifetime engineering, which is currently restricted to visible and near infrared, to the MIR is quite appealing because of several interesting emitters with spontaneous emission in this wavelength range, and potential applications of lifetime engineering for fibre lasers. However, MIR operation presents experimental challenges related to the sources and detection, which will be discussed in this Appendix.

In the next section, the requirements for the MIR emitters in a lifetime engineering experiment with metamaterials are analyzed. Some options are proposed and a proof-of-concept experiment with our tin/soda-lime wire array metamaterial fibre is discussed.

A.2 MIR emitter candidates

Quantum dots made of HgTe [216] and PbSe [217] can be fabricated to exhibit an emission line through the mid-infrared, as shown in Fig. A.3. However, there are no commercial options available and they exhibit a lifetime typically in the nanosecond scale [218]. Such timescale would require the use of a single-photon correlated technique with a time response smaller than 0.1 ns to characterize the lifetime of the emitter, which is not feasible with the common MIR detectors (HgCdTe, PbSe, InAsSb).

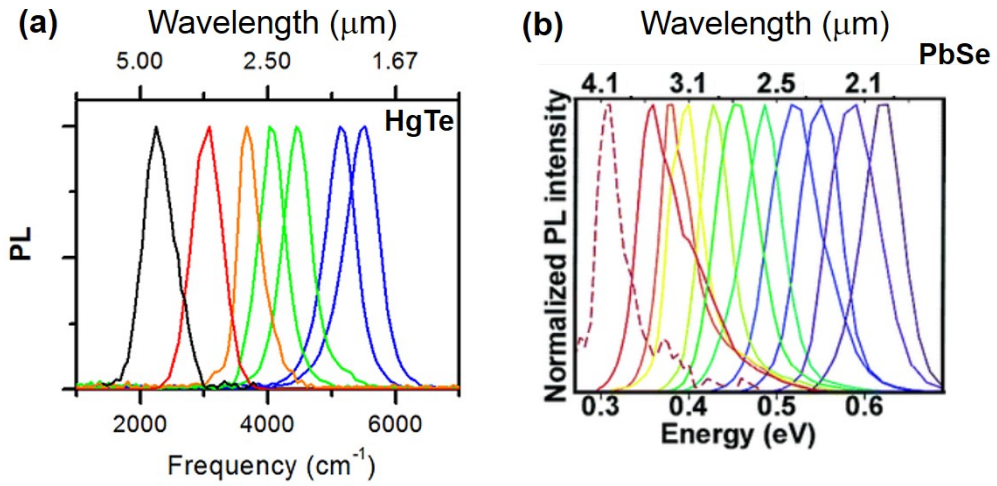

Figure A.3: Photoluminescence of the quantum dots HgTe (a) and PbSe (b) in the MIR. Figures were extracted from Refs. [216] and [217], respectively.

Alternatively, some rare-earth elements possess emission lines in the mid-infrared with lifetime typically in the order of milliseconds [219], being much more suitable for detection and characterization with the common mid-infrared detectors. Figure A.4 shows a partial energy level diagram with the emission lines of some rare-earth elements, extracted from Ref. [220]. According to Fig. A.4, Er^{3+}, Ho^{3+} and Dy^{3+} would be appropriate candidates for lifetime experiments with emission lines around $3\,\mu$m.

Apart from the emission line and the typical lifetime of the selected emitter, the characteristics of the medium in which they are embedded (dielectric host medium) is also important in a lifetime engineering experiment. The selected dielectric host medium must have low phonon energy, high rare-earth solubility and high transparency in the MIR. The low phonon energy minimizes non-radiative decays, which depopulate the excited state of the system and affect its spontaneous emission rate and lifetime. The high rare-earth solubility ensures that a medium with high concentration is achievable, which is essential to optimize the amount of spontaneous emission signal generated by a certain input power. The high transparency in the MIR minimizes any losses of the emitted signal.

Fluoride ZBLAN glass (ZrF4-BaF2-LaF3-AlF3-NaF) [219] is an interesting candidate for the dielectric host medium, since it fulfills all the requirements mentioned above and several ZBLAN fibres doped with rare-earth

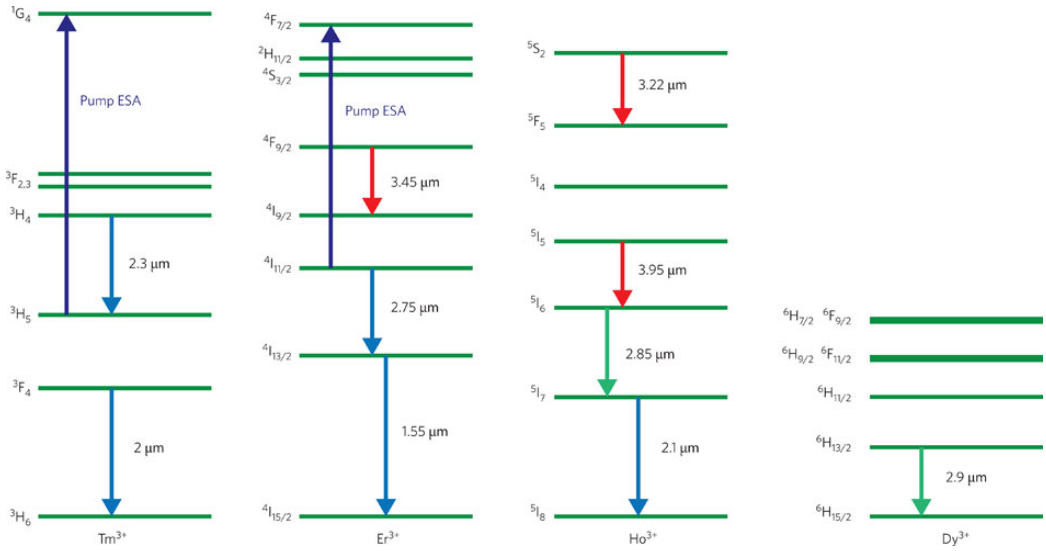

Figure A.4: Partial energy level diagram of some rare-earth elements with emission lines in the mid-infrared. Figure extracted from Ref. [220].

elements are commercially available. A slice of such ZBLAN fibres (or bulk ZBLAN glass sample) with high rare-earth concentration could be a perfect platform for our lifetime engineering studies.

The dynamics of an excited population in such systems are quite complex and several phenomenona like excited-state absorption (ESA), cross-relaxation, energy-transfer upconversion (ETU), and non-radiative decays influence the spontaneous emission rate and lifetime [219–221]. Therefore, the spontaneous emission lifetime of a specific transition/energy level must be carefully characterized before any lifetime engineering with metamaterials is attempted.

Below, an experimental setup for the study of the emission kinetics (MIR emission) of rare-earth elements embedded in ZBLAN glass is presented. The spontaneous emission lifetime of several bulk ZBLAN glass samples doped with different concentration of Ho^{3+} is characterized for the emission line around 2.85 μm.

A.3 Spontaneous emission lifetime for the 2.85 μm emission of Ho^{3+} ions embedded in bulk ZBLAN glass

According to the energy level diagram presented in Fig. A.4, Ho^{3+} ions exhibit a spontaneous emission line around 2.85 μm due to the transition between the energy levels $^5I_6$ and $^5I_7$, when the ions are excited from the ground-state ($^5I_8$) into the level $^5I_6$ with a 1150 nm pump laser.

In order to characterize this transition in Ho^{3+} doped ZBLAN samples, a high power pulsed laser with emission at 1150 nm is required. Consequently, an all-fibre Raman laser was built, as illustrated in Fig. A.5. In such system, a 980 nm pump (300 W, CW, Laserline) is launched into the first fibre laser cavity formed by 17 m of a Yb^{3+} silica double cladding fibre (Nufern) and two fibre Bragg gratings (FBG 1 and FBG2 in Fig. A.5), which generates a CW lasing signal at 1097 nm. This 1097 nm signal is then coupled into a second fibre laser cavity formed by a silica Raman gain fibre (102 m, Corning HI1060-100) and other two Bragg gratings (FBG3 and FBG4 in Fig. A.5). A cladding mode stripper (CMS) and a fibre WDM (wavelength-division multiplex) are employed to strip any residual 980 nm pump radiation in the inner cladding of the double cladding fibre before the second cavity (FBG3 and FBG4). Due to the $\sim$13 THz frequency offset of the silica Raman scattering [222], the 1097 nm signal is converted into 1150 nm. A single-mode output at 1150 nm with power as high as 5 W (CW) is achieved with a pump power of 100 W at 980 nm.

As mentioned before, several different phenomenona (ESA, ETU, cross-relaxation, non-radiative decay) affect the dynamics of the population density of the excited states in a rare-earth element and, consequently, affect their spontaneous emission lifetime. These effects are influenced by the excitation (input power, pulse duration, repetition rate) and the rare-earth concentration. For example, a higher concentration of ions could lead to a better absorption efficiency of the pump power and to stronger emission signal. However, this higher concentration of ions also increases the ion-ion interactions and affect the population densities and lifetimes of several transitions. Therefore, the selection of the ideal concentration of the rare-earth element in the ZBLAN glass and the characteristics of their excitation for the lifetime engineering experiment are not straightforward and the systems must be carefully studied.

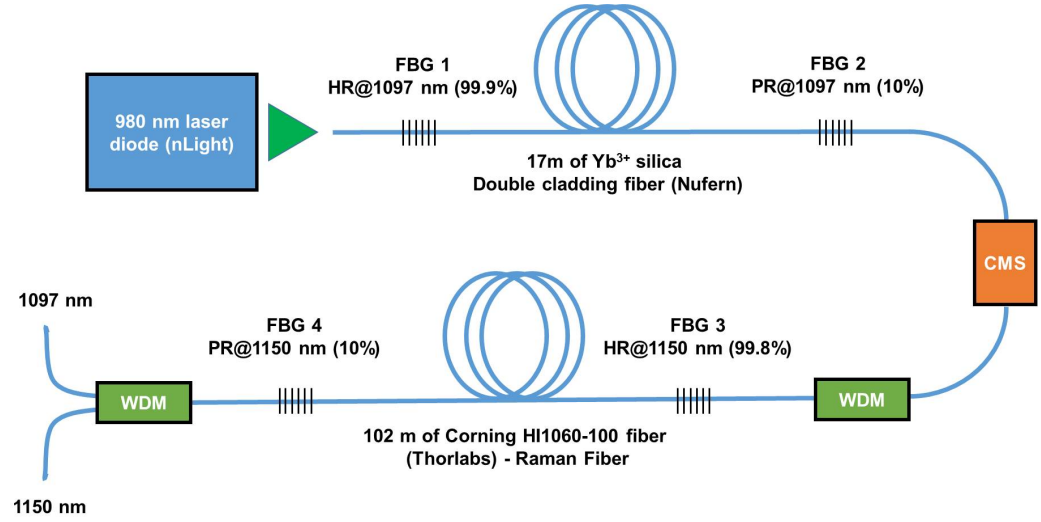

Figure A.5: Schematic of the 1150 nm all fibre Raman laser setup used to obtain the 2.85 μm spontaneous emission of Ho^{3+} ions embedded in ZBLAN samples. The system is pumped with a 980 nm laser, which is converted to 1097 nm in the first cavity (FBG1 and FBG2), and subsequently converted to 1150 nm by a Raman fibre in the second cavity (FBG3 and FBG4).

In order to have a better understanding of the spontaneous emission of Ho^{3+} ions embedded in ZBLAN glass, a study of the emission kinetics of the 2.85 μm line was performed for samples with different concentrations of Ho^{3+}. Figure A.6 illustrates the experimental setup developed for the characterization of the bulk Ho-ZBLAN samples. A chopper wheel with only one slit open is positioned close to the output fibre of the Raman fibre laser (Fig. A.5) in order to generate a pulsed signal from the CW laser. A plano convex CaF_2 lens ($f = 50$ mm) focuses the 1150 nm signal in a small region of the bulk Ho-ZBLAN sample. Another CaF_2 lens ($f = 20$ mm, transparent in the MIR) collects and focuses the spontaneous emission signal into a InAs photodetector (electrically cooled). A bandpass filter with a transmission window centered at 3 μm and with FWHM = 500 nm is placed before the detector in order to exclude wavelengths away from the 2.85 μm Ho^{3+} emission line.

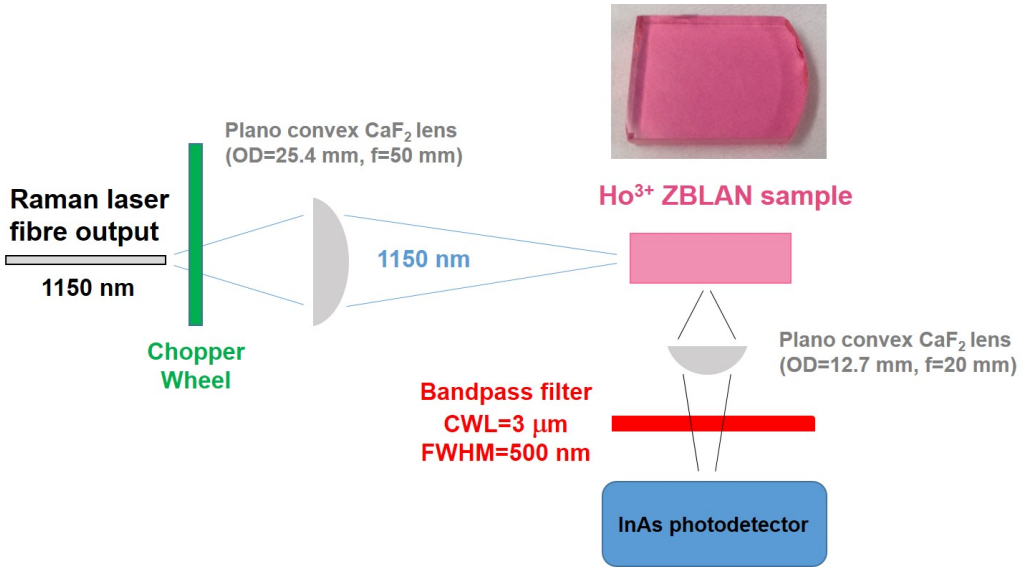

Figure A.6: Schematic of the experimental setup employed for the measurement of the emission kinetics and the lifetime of the 2.85 μm spontaneous emission line of Ho^{3+} ions embedded in bulk ZBLAN samples.

Figure A.7 shows emission kinetics of the 2.85 μm Ho^{3+} emission line for three different bulk ZBLAN samples. The Ho^{3+} doping concentration are 2 mol %, 6 mol % and 4 mol % for the samples presented in Fig. A.7(a-c), respectively. Note that the sample containing 4 mol % of Ho^{3+} is also doped with 0.3 mol % of Pr^{3+}, which is commonly employed in rare-earth based fibre lasers to quickly depopulate the energy level $^5I_7$ of the Ho^{3+} ions (bottom level of the 2.85 μm emission line) by energy-transfer processes and consecutive non-radiative decays. This energy-transfer process prevents problems with population bottleneck, which is caused by the shorter lifetime of the $^5I_6$ level (3.5 ms) in comparison to the $^5I_7$ level (12 ms) [219].

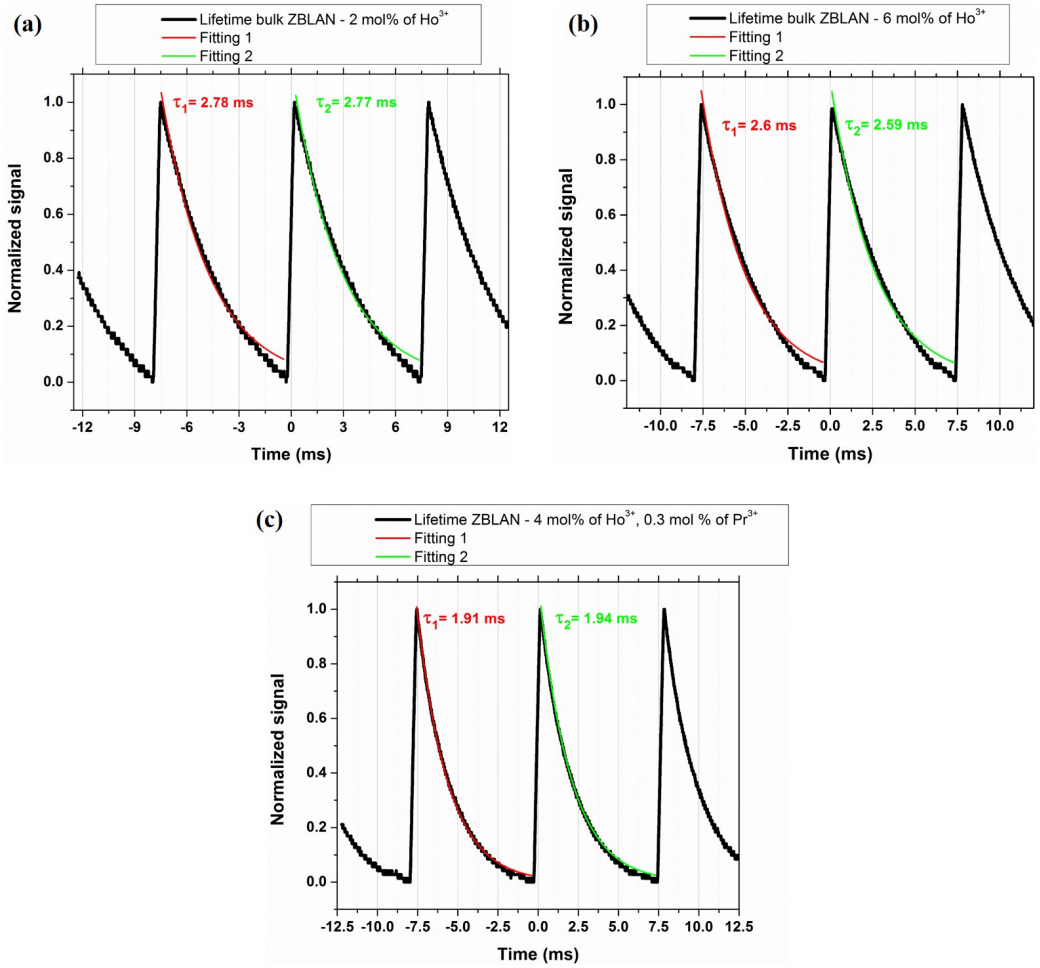

Figure A.7: Emission dynamics of the 2.85 μm spontaneous emission line of Ho^{3+} ions embedded in bulk ZBLAN samples. Concentrations: (a) 2 mol % of Ho^{3+}; (b) 6 mol % of Ho^{3+}; (c) 4 mol % of Ho^{3+} and 0.3 mol % of Pr^{3+}. Chopper wheel set to 1300 Hz (triggered from all slits), which gives a repetition rate of 125 Hz (8 ms) for the single slit opened, and an excitation pulse of 0.385 ms (determined by the size of the single open slit). The position of the incident pulses over time matches the peaks on the signal.

The lifetime of the samples were determined by a single exponential fitting as approximately 2.78 ms, 2.6 ms and 1.92 ms for the samples presented in Fig. A.7(a-c), respectively. However, note that such single exponential fittings (as expected from Eq. (A.2)), do not perfectly agree with the ex-

perimental decays, particularly for the samples with 2 mol % and 6 mol % of Ho^{3+} and the final region of the decays. As discussed before, this discrepancy is expected due to the complex population dynamics in rare-earth elements (ESA, ETU, cross-relaxation, non-radiative decays) [219, 221]. Interestingly, the sample containing 0.3 mol % of Pr^{3+} (Fig. A.7(c)) exhibits a better agreement, which indicates that the previous deviation of the other samples is likely related to the population dynamics of the energy level $^5I_7$ of the Ho^{3+} ions (bottom level of the 2.85 μm emission line). For this sample, the Pr^{3+} quickly depopulates the energy level $^5I_7$, which prevent bottlenecking and also minimize ETU from this level.

In order to avoid the influence of these other effects on the determination of the lifetime, a logarithmic plot of the emission intensity as a function of time is more appropriate, as seen in Fig. A.8. In this case, it is easier to identify the single exponential decay (a line in the ln plot) in the spontaneous decays right after the population is excited by the incident pulse, and a more precise determination of the lifetime is achieved. From Fig. A.8, the measured lifetime of the samples considering only the initial linear decay are approximately 3 ms (samples with 2 mol % of Ho^{3+}, Fig. A.8(a)), 2.8 ms (samples with 6 mol % of Ho^{3+}, Fig. A.8(b)) and 1.92 ms (sample with 4 mol % of Ho^{3+} and 0.3 mol % of Pr^{3+}, Fig. A.8(c)).

Note that the measured lifetime of 1.92 ms of the energy level $^5I_7$ for the sample with 4 mol % of Ho^{3+} and 0.3 mol % of Pr^{3+} is in excellent agreement with the value reported in [221] ($\sim$ 1.9 ms, see Fig. 3(b), measured from the 1.2 μm spontaneous emission).

According to the results presented in Fig. A.8, the lifetime of the 2.85 μm spontaneous emission does not change considerably with the rare-earth concentration, being all suitable for the lifetime engineering experiment with our metamaterial fibre. In addition, the excitation employed in our experiment (blue curve, pulse width of 0.385 ms, repetition ratio around 8 ms) also enables a trustworthy determination of the typical lifetimes.

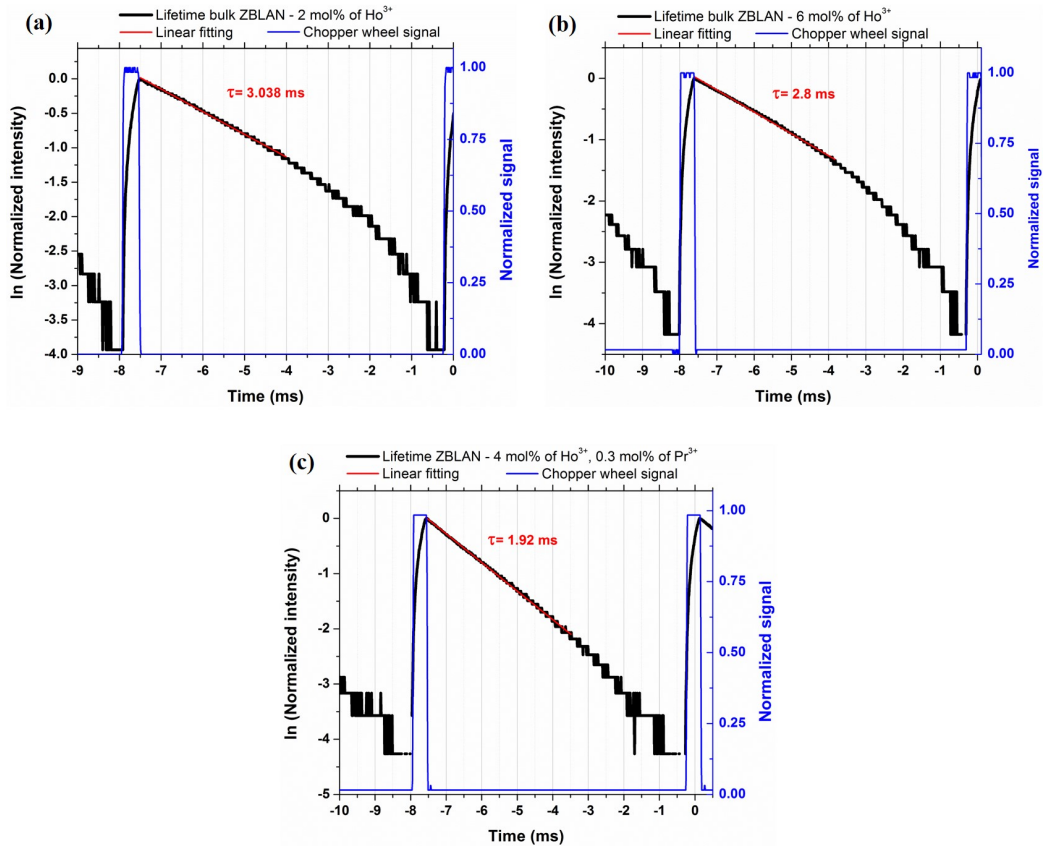

Figure A.8: Emission dynamics of the 2.85 μm spontaneous emission line of Ho^{3+} ions embedded in bulk ZBLAN samples (ln of the normalized intensity by time). Concentrations: (a) 2 mol % of Ho^{3+}; (b) 6 mol % of Ho^{3+}; (c) 4 mol % of Ho^{3+} and 0.3 mol % of Pr^{3+}. Chopper wheel set to 1300 Hz (triggered from all slits), which gives a repetition rate of 125 Hz (8 ms) for the single slit opened (blue curve), and an excitation pulse of 0.385 ms (determined by the size of the single open slit).

Below, a proof-of-concept experiment to measure the influence of the high photonic density of states of our metamaterial fibres in the lifetime of Ho^{3+} ions embedded in ZBLAN glass is proposed and discussed.

A.4 Lifetime engineering with metamaterial fibres at 2.85 μm with Ho^{3+} embedded in ZBLAN glass

The lifetime of Ho^{3+} will only be affected by the high photonic density of states of a metamaterial if the emitters are in the near field of the metamaterial. Considering this limited distance around half of the operational wavelength, ideally all the ions must be in a distance smaller than 1.5 μm to the metamaterial in a lifetime engineering experiment of the 2.85 μm emission line. If a large number of unaffected ions are present in the measured sample, their spontaneous emission will probably mask the metamaterial's influence on the few emitters that are in the near field. Consequently, the density of emitters embedded and the size of the ideal sample are greatly restricted and high doping concentration is preferable.

A bulk Ho-ZBLAN glass sample with dimensions smaller than 1.5 μm is difficult to fabricate. However, a commercial Ho-ZBLAN fibre can be easily cut in even smaller dimension with a FIB. Figure A.9 illustrates our proposed sample for the lifetime engineering experiment with the tin/soda-lime metamaterial fibre and its fabrication steps: (a) a soda-lime capillary (OD = 125 μm, ID = 30 μm) is fabricated in the drawing tower stretching a soda-lime tube. A small piece of Ho^{3+} ZBLAN fibre (OD = 125 μm, core diameter of 15 μm) is glued or spliced to the soda-lime capillary; (b) The Ho^{3+} ZBLAN fibre is cut with a FIB and only a 1.5 μm slice is left attached to the soda-lime capillary. (c) The tin/soda-lime wire array metamaterial fibre (OD $\sim$ 30 μm) is inserted into the soda-lime capillary and the final alignment (distance from the metamaterial fibre facet to the ZBLAN sample) is adjusted with a micrometer stage and a microscope.

It is important to emphasize that, due the symmetry of the capillary and the Ho-ZBLAN fibre, the wire array region of the metamaterial fibre ($\sim$ 15 μm for the metamaterial fibres with OD = 30 μm, Fig. 4.28) is perfectly aligned with the core of the ZBLAN fibre containing the Ho^{3+} ions. In addition, the proposed sample is robust, of easy handling, and allows an easy adjustment of the gap between the metamaterial and the ZBLAN sample, ideal to study the influence of such distance on the lifetime of the emitter.

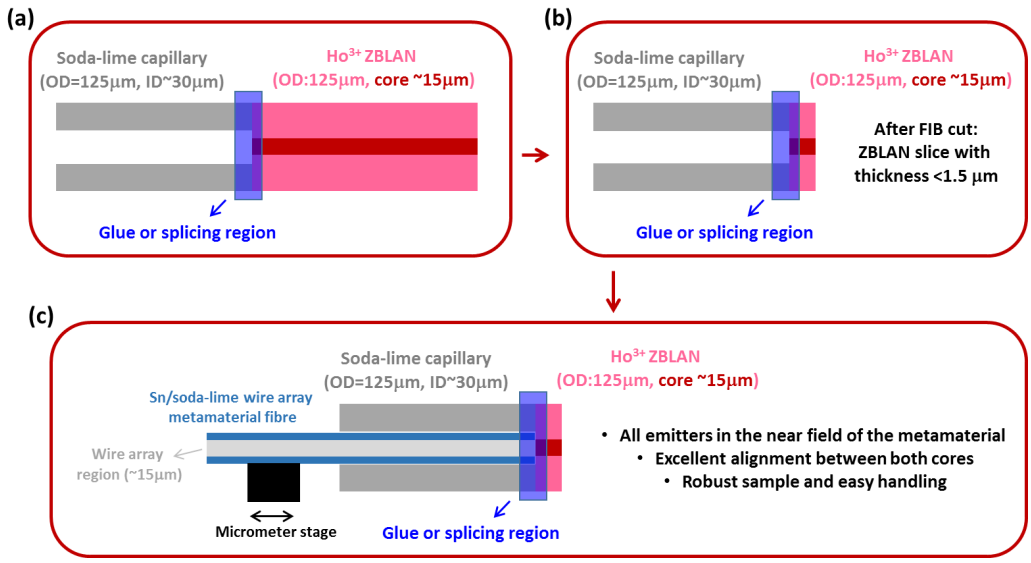

Figure A.9: Schematic of the preparation of the proposed sample for the lifetime engineering experiment with our wire array tin/soda-lime metamaterial fibre: (a) A small piece of Ho^{3+} ZBLAN fibre (OD = 125 μm, core diameter $\sim$15 μm) is glued or spliced to a soda-lime capillary (OD = 125 μm, ID = 30 μm); (b) The Ho^{3+} ZBLAN fibre is cut with a FIB and only a 1.5 μm (or even smaller) slice is left attached to the soda-lime capillary. (c) The tin/soda-lime wire array metamaterial fibre (OD $\sim$ 30 μm) is inserted into the soda-lime capillary and the final alignment (distance from the metamaterial fibre facet to the ZBLAN sample) is perform with a micrometer stage and a microscope.

The preparation of the such samples as described in Fig. A.9 and an experimental setup to measure the spontaneous emission lifetime by back-reflection are currently in progress. After the sample preparation is achieved, the emission kinetics of the 2.85 μm spontaneous emission of the Ho^{3+} present in the core of the ZBLAN fibre slice (thickness smaller than 1.5 μm) will be characterized. Once the excitation parameters are optimized (pump power, pulse width, repetition rate) and the lifetime is obtained, the metamaterial will be introduced in the soda-lime capillary and aligned with the Ho-ZBLAN slice. In this configuration, the influence of the high photonic density of states of the metamaterial on the lifetime of the emitter will be investigated as a function of distance of the metamaterial fibre facet to the ZBLAN sample.

Note that losses also decrease emission lifetime (quenching), and so to unambiguous prove lifetime is reduced because of the presence of a higher

density of propagating (not absorbed) high-k modes is more difficult, as discussed in Refs. [33, 38, 41]. An ideal experiment would be using a low-loss magnifying hyperlens, in which high-k modes can then be converted and measured in the far field - however as discussed in Chapter 5, achieving hyperlenses with low losses for the MIR is difficult and it is not clear whether losses could be low enough to get a net far field emission enhancement due to the increased density of states.

Appendix B

Simulations of the far field image of the apertures using Fourier analysis and Matlab

In this Appendix, the simulations of the far field images of the apertures presented throughout Chapter 5 using Fourier analysis with Matlab are described.

B.1 Spatial filtering

As discussed previously in Chapter 5, when the detection is performed in the far field, part of the excited spatial frequencies are not detected and the image is "diffraction limited". The evanescent waves ($|k_\perp| > |k_0| = 2\pi n/\lambda_0$ and k_z imaginary, considering $\perp$ the plane transverse to the propagation direction z) decay exponentially fast and are attenuated below the detection level, while some of the propagating spatial frequencies are filtered by the lens/objective employed to form an image in the image plane (Fig. B.1(a)). Thus, the lens/objective acts as a spatial filter, and the transmitted spatial frequencies depend on the wavelength and the numerical aperture (NA) of the out-coupling lens/objective ($|k_\perp| < |k_0|$.NA), as illustrated in Fig. B.1(b). Consequently, the resultant far field image of an aperture can be obtained filtering such transverse spatial frequencies ($|k_\perp| > |k_0|$.NA) of the original image of the aperture.

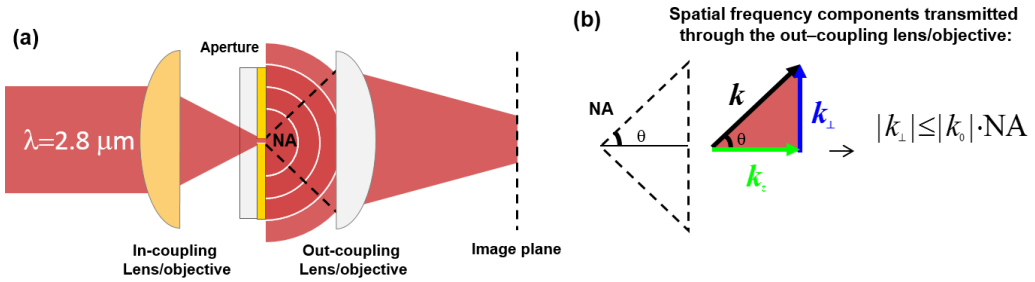

Figure B.1: (a) Schematic of the spatial filtering of the light transmitted through the out-coupling lens/objective in a far field imaging experiment. (b) Schematic of the wavevector components and the condition for the spatial frequencies transmitted through the out-coupling lens/objective.

Below, the simulation of far field images performed with a Matlab code (presented in Section B.1.2) is described step-by-step.

B.1.1 Simulation of the far field images

Firstly, a binary image of the original aperture in a background is obtained in Matlab filling a matrix with zeros (corresponding to the background) and ones (corresponding to the aperture). Figure B.2(a) shows a zoom in the binary image of a double aperture with $d = 2\,\mu$m, $\Lambda = 4\,\mu$m, in a $100\,\mu\text{m} \times 100\,\mu\text{m}$ square frame, corresponding to a matrix with 1401×1401 pixels. A fast Fourier transform is applied to the aperture image to generate its representation in the spatial frequency domain (k-space), as seen in Fig. B.2(b).

A mask representing the spatial filter in k-space is also created filling a matrix with zeros and ones, according to the filtering condition (Fig. B.2(b), 0 if $|k_\perp| > |k_0|$.NA, and 1 if $|k_\perp| \leq |k_0|$.NA), which represents a circle around the origin in k-space, as seen in Fig. B.2(d), for an out-coupling lens with NA = 0.56. The filtering is thus performed multiplying both matrices point by point. Figure B.2(d) shows the resultant image of the double aperture in k-space after this filtering. Finally the far field image is obtained transforming the filtered image in k-space back to the real space by an inverse fast Fourier transform, as seen in Fig. B.2(e).

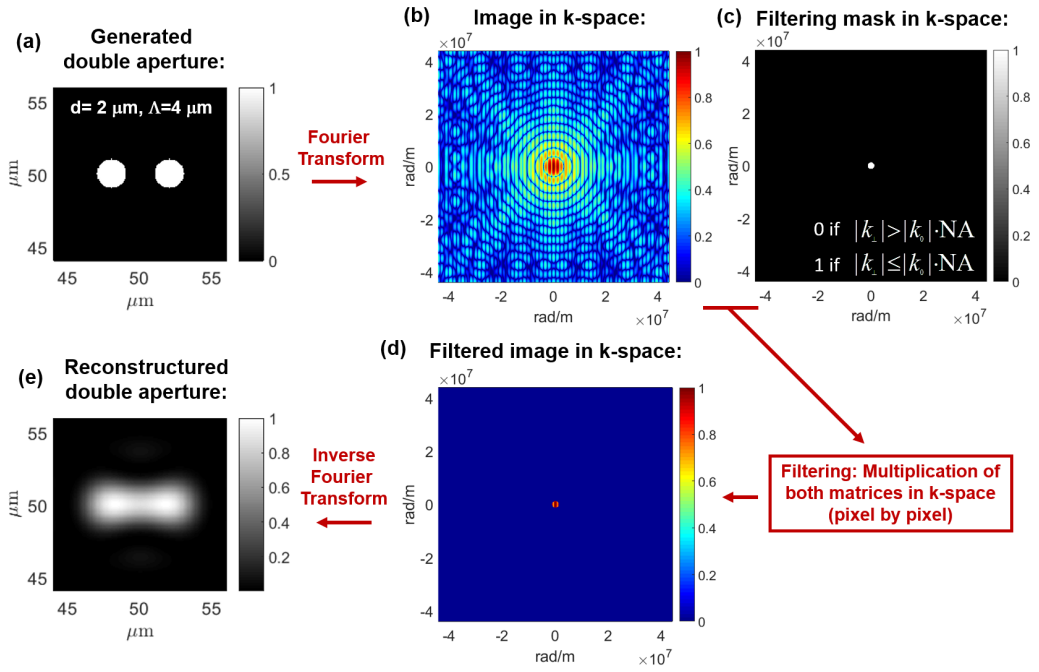

Figure B.2: (a) Double aperture generated in Matlab filling a matrix with zeros (background in black) and ones (circular apertures, white region). (b) Image of the generated aperture in k-space obtain with a fast Fourier transform in Matlab. (c) Filtering mask in k-space generated according to the filtering condition (0 if $|k_\perp| > |k_0|$.NA, and 1 if $|k_\perp| \leq |k_0|$.NA)). (d) Resultant image in k-space after the filtering (multiplication of the image by the filtering mask, point by point, in k-space). (e) Far field image of the double aperture reconstructed with an inverse fast Fourier transform of the filtered image.

Note that the original generated image formed by zeros and ones, as seen in Fig. B.2(a), corresponds to an equivalent double aperture uniformly illuminated in a transmission setup, with no phase shift in such excitation (like a incident plane wave illumination). A phase shift between the excitation of the two circular aperture can be taken into account replacing the ones in the matrix by normalized complex numbers. For example, if the simulation of a phase shift of $\pi/2$ between the two circular apertures is intended, the region in the matrix representing one circular aperture must be filled with ones, while the region corresponding to the other circular aperture must be filled with the complex number i. This approach was employed in some simulations presented in Section 5.3.3, for a phase shift of $\pi/2$ (Fig. 5.18) and

$(3/4)\pi$ (Fig. 5.19).

The script written in Matlab for the simulations of the far field images for double circular apertures is presented below, including the option of a phase shift in the excitation. The code written to simulate the anti-apertures, as discussed in Section 5.3.3, is presented in Section B.1.3.

B.1.2 Matlab code: Far field simulations of double apertures

```
1
2  %Matlab code:
3  %Simulation of the far field image of a double circular aperture - by J. Hayashi
4
5  clear all,close all
6
7  %1) Generating the image of the original double circular aperture (Amplitude and phase):
8
9  N=1401; %pixels in the x axis
10 M=1401; %pixels in the y axis
11
12 %Converting factor
13 figure_width=input('What is the width/height of the figure (um)?'); %define the width of
       the square frame
14 pixel_size_ar=(figure_width)/N; % calibration factor (um/pixel), if N=M
15
16 %Mesh for the original aperture
17 [X,Y]=meshgrid(pixel_size_ar*linspace(-(N-1)/2,(N-1)/2,N),pixel_size_ar*linspace(-(M-1)
       /2,(M-1)/2,M)); % Grid definition to generate the image
18
19 %Input parameter for the double circular aperture
20 pitch1=input('What is the distance from center of the first aperture (um)?');
21 diameter1=input('What is the diameter of the first aperture (um)?');
22 c_vector1=input('What is the complex vector defining the amplitude and phase of the
       first aperture ?');
23 pitch2=input('What is the distance from center of the second aperture (um)?');
24 diameter2=input('What is the diameter of the second aperture in (um)');
25 c_vector2=input('What is the complex vector defining the amplitude and phase of the
       second aperture ?');
26
27 % Parametrization both apertures:
28 Aperture1=sqrt((X+pitch1).^2+Y.^2)<(diameter1/2); %definition aperture 1 -> fills with 1
       s when equation is true, 0 everywhere else
29 Aperture2=sqrt((X-pitch2).^2+Y.^2)<(diameter2/2); %definition aperture 2 -> fills with 1
       s when equation is true, 0 everywhere else
30
31 F2=(c_vector1).*Aperture1/(abs(c_vector1))+(c_vector2).*Aperture2/abs(c_vector2); %
       Combination of both apertures
32 F3=angle(F2); % it returns the phase angle in radians of a matrix with complex number
33 F4=abs(F2); % it returns the amplitude
34
35 %Plotting the generated aperture:
36 figure(1) %Figure 1
37 e1=subplot(1,2,1); imshow(abs(F2)), colorbar, title('Generated aperture - Amplitude')
38 e2=subplot(1,2,2); imshow(F3), colorbar, title('Generated aperture - Phase (rad)'),
       caxis([min(min(F3)) max(max(F3))]);
39
40 %Correlation
41 lambda_um=input('What is the wavelength of the light source (um)?');
42 lambda=lambda_um*1e-6; % wavelength in m
43 k0=2*pi/lambda; %wavevector in free-space
44 NA_lens=input('What is the NA of the lens/objective?');
45 ktrans_max=k0*NA_lens; % Maximum k collected by the lens/objective (rad/m)
46
47 %%Converting factor
48 pixel_size=(figure_width)*(1e-6)/N; % calibration factor (m/pixel)
49 Ktrans_max_pixel=ktrans_max*pixel_size; % Maximum k collected by the lens/objective(rad/
       pixel)
```

```
50
51  %2) Generating the filtering mask:
52
53  %Sampling intervals
54  dx = 1; % pixel
55  dy = 1; % pixel
56
57  [Kx,Ky]=meshgrid(pi*linspace(-1/dx,1/dx,N),pi*linspace(-1/dy,1/dy,M)); % Grid definition
        to match the image in the k-space, rad/pixel
58  KF=Ktrans_max_pixel; %filtering according to the given NA (rad/pixel)
59  Filter=sqrt(Kx.^2+Ky.^2)<KF; % Definition of the filtering mask
60
61  %3) Fast Fourier Transform (FFT) of the original double aperture and filtering
62  [C]=fft2(F2); %FFT of the original double aperture -> image in k-space
63  D=fftshift(C); % Shift of the DC components to the center
64  FilteredKs=D.*Filter; % Multiplication of the image in k-space with the filtering mask
65
66  %4) Reconstruction of the filtered image (k-space -> real space)
67  FilteredImage=ifft2(FilteredKs); % inverse FFT of the filtered image in the k-space
68  E=abs(FilteredImage).^2; % Intensity image of E of the filtered image instead of the
        amplitude
69  Ephase=angle(FilteredImage); % Phase component
70
71  En=E/(max(max(E))); % normalization of the reconstructed image
72  FilterN=double(Filter); %transform matrix from logical to numeric (filtering mask)
73  Original_Picture=double(F4); %transform matrix from logical to numeric (original picture
        of the apertures)
74
75  %5) Plots
76
77  %Grid for the plots
78  [X,Y]=meshgrid(1:N,1:M); %mesh corresponding to the pixels
79  [X2,Y2]=meshgrid(0:N-1,0:M-1); % second mesh to avoid problem with surf function
80
81  % Calculation of the parameters shown in the plots
82  numberOfTrue1Pixels_OA=sum(F4(:)); % it returns the number of pixel defining the
        apertures (all 1).
83  numberOfTrue1Pixels_mask=sum(FilterN(:)); %it returns the number of pixel defining the
        filtering mask (all 1s).
84  Pitch=pitch1+pitch2; % it returns the distance between the circular apertures (center to
        center) in um
85  zoom_factor=(1/3)*figure_width/Pitch; % definition of the zoom factor according to Pitch
86  Max_phase=max(max(F3))/pi; %maximum phase shifh shown in the aperture (rad)
87  Diffraction_limit=lambda/(2*NA_lens); % Abbe diffraction limit (for incoherent
        illumination)
88
89  %%
90  %Figure 2: Original image of the double apertures (real space), image of the double
        apertures in k-space, filtering mask, phase distribution, reconstructured far field
        image and intensity profile plots
91  figure(2)
92
93  d1= subplot(2,4,1); pcolor(pixel_size*X/(1e-6),pixel_size*Y/((1e-6)),abs(F2));view(2),
        axis tight,axis square,colorbar, P1title={['\color{red}Number of pixels=' num2str(N)
        'x' num2str(M)] ['\color{red} Pixel size=', num2str(pixel_size/(1e-6),'%.2s') 'um']
        '\color{black}Generated picture - Amplitude' ''}; title(P1title),xlabel('um'),
        ylabel('um'), zoom(zoom_factor),
94  d12= subplot(2,4,5); pcolor(pixel_size*X/(1e-6),pixel_size*Y/((1e-6)),F3);view(2),axis
        tight,axis square,colorbar, P1title={['Diameters = ' num2str(diameter1) ' and '
        num2str(diameter2) ' um'] ['Pitch= ' num2str(Pitch) ' um'] ['\color{black}Generated
        picture - Phase'] ['Max phase= ', num2str(Max_phase) 'pi (rad)      (rad)']}; title(
        P1title),xlabel('um'),ylabel('um'), zoom(zoom_factor), caxis([min(min(F3)) max(max(
        F3))]),
95  b2=subplot(2,4,2); pcolor(Kx/(pixel_size),Ky/(pixel_size),log(abs(D))),view(2),axis
        tight,axis square, colorbar,caxis([0 max(max(log(abs(D))))]),P2title= {'Image in k-
        space' '' };title(P2title), xlabel('rad/m'),ylabel('rad/m')
96  b3=subplot(2,4,3); pcolor(Kx/(pixel_size),Ky/(pixel_size),FilterN),view(2),axis tight,
        axis square, colorbar,P3title={ ['\color{red}KF=',num2str(KF,'%.2s') 'rad/m' '  NA='
        , num2str(NA_lens)] ['\color{red}Number of pixels (1) defining the mask=' num2str(
        numberOfTrue1Pixels_mask)] '\color{black}Mask in the k-space' ''};title(P3title),
        xlabel('rad/m'),ylabel('rad/m')
97  a4=subplot(2,4,4); pcolor(pixel_size*X/(1e-6),pixel_size*Y/(1e-6),En),view(2),axis tight
        square,colorbar, P4title={ ['\color{red}Diffraction limit=', num2str(
        Diffraction_limit,'%.2s') 'm'] '' '\color{black}Reconstructured picture' ''};title(
        P4title),xlabel('um'),ylabel('um')
98  a5=subplot(2,4,6); pcolor(pixel_size*X/(1e-6),pixel_size*Y/(1e-6),En),view(2),axis tight
        square,colorbar, P4title={['Number of pixels (1) defining the apertures = ' num2str
```

```
    (numberOfTrue1Pixels_OA)] ['Frame width = ' num2str(figure_width) ' um'] '' '\color{
    black}Reconstructured picture' ''};title(P4title),xlabel('um'),ylabel('um'), zoom(
    zoom_factor)
99  c2=subplot(2,4,[ 7 8 ]); plot(X2(1,:)*pixel_size/(1e-6),En((end-1)/2,:),X2(1,:)*
    pixel_size/(1e-6),F4((end-1)/2,:),'r','LineWidth',2), xlabel('Distance in um'),
    ylabel('Normalized intensity'), axis([ 0 pixel_size*(M-1)/(1e-6) 0 1.1]), grid on,
    grid minor,legend('Reconstructed aperture','Original apertures','Location','
    northeastoutside'),title(['NA=', num2str(NA_lens)])
100
101 arrayfun(@(s) set(s,'EdgeColor','none'), findobj(gcf,'type','surface')), colormap(d1,
    gray), colormap(d12,gray), colormap(b2,jet), colormap(b3,gray), colormap(a4,gray),
    colormap(a5,gray)
102
103 %%
104 %Figure 3: Original image of the double apertures (real space), reconstructured far
    field image and intensity profile plots
105
106 figure(3)
107 d1= subplot(2,3,1); pcolor(pixel_size*X/(1e-6),pixel_size*Y/((1e-6)),abs(F2));view(2),
    axis tight,axis square,colorbar, P1title={['\color{red}Number of pixels=' num2str(N)
     'x' num2str(M)] ['\color{red} Pixel size=', num2str(pixel_size/(1e-6),'%.2s') 'um']
     '\color{black}Generated picture - Amplitude' ''}; title(P1title),xlabel('um'),
    ylabel('um'), zoom(zoom_factor),
108 d2= subplot(2,3,4); pcolor(pixel_size*X/(1e-6),pixel_size*Y/(1e-6),En),view(2),axis
    tight, axis square,colorbar, P4title={ ['\color{red}Diffraction limit=', num2str(
    Diffraction_limit,'%.2s') 'm'] '' '\color{black}Reconstructured picture' ['Diameters
     = ' num2str(diameter1) ' and ' num2str(diameter2) ' um'] ['Pitch= ' num2str(Pitch
    ) ' um'] };title(P4title),xlabel('um'),ylabel('um'),zoom(zoom_factor)
109 c2= subplot(2,3,[ 2 3 5 6 ]);plot(X2(1,:)*pixel_size/(1e-6),En((end-1)/2,:),X2(1,:)*
    pixel_size/(1e-6),F4((end-1)/2,:),'r','LineWidth',2), xlabel('Distance in um'),
    ylabel('Normalized intensity'), axis([ pixel_size*(M-1)*(0.45)/(1e-6) pixel_size*(M
    -1)*(0.55)/(1e-6) 0 1.1]), grid on, grid minor,legend('Reconstructed aperture','
    Original apertures','Location','northeastoutside'),title(['NA=', num2str(NA_lens)])
110 colormap(d1,gray), colormap(d2,gray), arrayfun(@(s) set(s,'EdgeColor','none'), findobj(
    gcf,'type','surface'))
111
112 %end
```

B.1.3 Matlab code: Far field simulations of anti-apertures

```
1  %Matlab code:
2  %Simulation of the far field image of an anti-aperture with inner double circular
       aperture - by J. Hayashi
3
4  clear all, close all
5  %1) Generating the image of the original anti-aperture with inner double circular
       aperture:
6
7  N=1001; %pixels in the x axis
8  M=1001; %pixels in the y axis
9
10 %%Converting factor
11 figure_width=input('What is the width of the figure (um)?'); %define the width of the
       square frame in microns
12 pixel_size_ar=(figure_width)/N; % calibration factor (um/pixel), if N=M
13
14 %Mesh for the anti-aperture
15 [X,Y]=meshgrid(pixel_size_ar*linspace(-(N-1)/2,(N-1)/2,N),pixel_size_ar*linspace(-(M-1)
       /2,(M-1)/2,M)); % Grid definition to generate the image
16
17 %Input parameter for the double circular aperture
18 diameter0=input('What is the diameter of the transmission circle of the anti-aperture(um
       )?');
19 pitch1=input('What is the distance from center of the first aperture (um)?');
20 diameter1=input('What is the diameter of the first aperture (um)?');
21 pitch2=input('What is the distance from center of the second aperture (um)?');
22 diameter2=input('What is the diameter of the second aperture in (um)');
23
24 % Parametrization of the apertures:
25 Aperture1=sqrt((X+pitch1).^2+(Y).^2)<(diameter1/2); %definition circular aperture 1 ->
       fills with 1s when equation is true, 0 everywhere else
26 Aperture2=sqrt((X-pitch2).^2+Y.^2)<(diameter2/2); %definition circular aperture 2 ->
       fills with 1s when equation is true, 0 everywhere else
27 Aperture3=sqrt(X.^2+Y.^2)<(diameter0/2); %definition of circular background of the anti-
       aperture -> fills with 1s when equation is true, 0 everywhere else
```

```
28
29 C1=-1*(Aperture1+Aperture2); % invert the signal of the double circular aperture (
       aperture 1 and 2)
30 C2=Aperture3+C1; % combine the double circular aperture with the circular baclground of
       the anti-aperture (generate the anti-aperture)
31
32 F2=abs(C2); % it returns the amplitude
33
34 figure %Figure 1
35 imshow(F2), colorbar, caxis([min(min(F2)) max(max(F2))]), title('Generated anti-aperture
       ')
36
37 %%Correlation
38 lambda_um=input('What is the wavelength of the light source (um)?');
39 lambda=lambda_um*1e-6; % wavelength in m
40 k0=2*pi/lambda; %wavevector in free-space
41 NA_lens=input('What is the NA of the lens/objective?');
42 ktrans_max=k0*NA_lens; % Maximum k collected by the lens/objective (rad/m)
43
44 Diffraction_limit=lambda/(2*NA_lens);
45
46 %%Converting factor to um
47 pixel_size=(figure_width)*(1e-6)/N; % calibration factor (m/pixel)
48 Ktrans_max_pixel=ktrans_max*pixel_size; % Maximum k collected by the lens/objective(rad/
       pixel)
49
50 %2) Generating the filtering mask:
51
52 %Sampling intervals
53 dx = 1; % pixel
54 dy = 1; % pixel
55
56 [Kx,Ky]=meshgrid(pi*linspace(-1/dx,1/dx,N),pi*linspace(-1/dy,1/dy,M)); % Grid definition
       to match the image in the k-space, rad/pixel
57 KF=Ktrans_max_pixel; %filtering according to the given NA (rad/pixel)
58 Filter=sqrt(Kx.^2+Ky.^2)<KF; % Definition of the filtering mask
59
60 %3) Fast Fourier Transform (FFT) of the anti-aperture and filtering
61 [C]=fft2(F2); %FFT of the original anti-aperture -> image in k-space
62 D=fftshift(C); % Shift of the DC components to the center
63 FilteredKs=D.*Filter; % Multiplication of the image in k-space with the filtering mask
64
65 %4) Reconstruction of the filtered image (k-space -> real space)
66 FilteredImage=ifft2(FilteredKs); % inverse FFT of the filtered image in the k-space
67 E=abs(FilteredImage).^2; % Intensity image of E of the filtered image instead of the
       amplitude
68 En=E/(max(max(E))); % normalization of the reconstructed image
69
70 FilterN=double(Filter); %transform matrix from logical to numeric (filtering mask)
71
72 %5)Plots - grids
73
74 %Grid for the plots
75 [X,Y]=meshgrid(1:N,1:M); %mesh correspond to the pixels
76 [X2,Y2]=meshgrid(0:N-1,0:M-1); % second mesh to avoid problem with surf function
77
78
79 %% Calculation of the parameters shown in the plots
80 numberOfTrue1Pixels_OA=sum(F2(:));% it returns the number of pixel defining the
       apertures (all 1s).
81 numberOfTrue1Pixels_mask=sum(FilterN(:)); %it returns the number of pixel defining the
       filtering mask (all 1s).
82 Pitch=pitch1+pitch2; % it returns the distance between the circular apertures (center to
       center) in um
83 zoom_factor=(1/5)*figure_width/Pitch; % definition of the zoom factor according to Pitch
84
85 figure(2) %Figure 2
86 %Axes in m
87 a1=subplot(2,4,1); pcolor(pixel_size*X/(1e-6),pixel_size*Y/(1e-6),F2),view(2),axis tight
       ,axis square,colorbar, P1title={['\color{red}Number of pixels=' num2str(N) 'x'
       num2str(M)] ['\color{red} Pixel size=', num2str(pixel_size/(1e-6),'%.2s') 'um'] '\
       color{black}Generated picture' ''}; title(P1title),xlabel('um'),ylabel('um')
88 a2=subplot(2,4,2); pcolor(Kx/(pixel_size),Ky/(pixel_size),log(abs(D))),view(2),axis
       tight,axis square, colorbar,caxis([0 max(max(log(abs(D))))]),P2title= {'Amplitude' '
       Image in K space' ''};title(P2title), xlabel('rad/m'),ylabel('rad/m')
89 a3=subplot(2,4,3); pcolor(Kx/(pixel_size),Ky/(pixel_size),FilterN),view(2),axis tight,
       axis square, colorbar,P3title={ ['\color{red}ktrans_{max}=',num2str(ktrans_max,'%.2s
```

APPENDIX B. SIMULATIONS OF THE FAR FIELD IMAGE OF THE APERTURES USING FOURIER ANALYSIS AND MATLAB

```
') 'rad/m'] ['NA=', num2str(NA_lens)] '\color{black}Mask in the K space' ''};title(
    P3title), xlabel('rad/m'),ylabel('rad/m')
90  a4=subplot(2,4,4); pcolor(pixel_size*X/(1e-6),pixel_size*Y/(1e-6),En),view(2),axis tight
     square,colorbar, P4title={ ['\color{red}Diffraction limit=', num2str(
    Diffraction_limit,'%.2s') 'm'] '' '\color{black}Reconstructured picture' ''};title(
    P4title),xlabel('um'),ylabel('um')
91  a5=subplot(2,4,5); pcolor(pixel_size*X/(1e-6),pixel_size*Y/(1e-6),F2),view(2),axis tight
    ,axis square,colorbar, xlabel('um'),ylabel('um'),P5title= {['\color{red}Number of
    pixels (1) defining the apertures = ' num2str(numberOfTrue1Pixels_OA)] ['Frame width
     = ' num2str(figure_width) ' um'] ['Diameters = ' num2str(diameter1) ' and '
    num2str(diameter2) ' um'] ['Pitch= ' num2str(Pitch) ' um'] ['\color{Black} Zoom -
    original aperture' ]}; title(P5title),zoom(zoom_factor)
92  a6=subplot(2,4,[6 8]); plot(X2(1,:)*pixel_size/(1e-6),En((end-1)/2,:),X2(1,:)*pixel_size
    /(1e-6),F2((end-1)/2,:),'r','LineWidth',2),P8title={['\color{red}Number of pixels
    (1) defining the mask=' num2str(numberOfTrue1Pixels_mask)] ['\color{Black} Intensity
     profile along the horizontal direction, center of the aperture'] }; title(P8title),
     xlabel('Distance in um'), ylabel('Normalized intensity'), axis([ pixel_size*(M-1)
    *0.3/(1e-6) pixel_size*(M-1)*0.7/(1e-6)  0 1.1]), grid on, legend('Reconstructed
    aperture','Original aperture','Location','northeastoutside')
93
94  colormap(a1,gray),colormap(a2,jet),colormap(a3,gray),colormap(a4,gray),colormap(a5,gray)
95  arrayfun(@(s) set(s,'EdgeColor','none'), findobj(gcf,'type','surface'))
96
97  %%
98
99
100 figure(3) %Figure 3
101 d1= subplot(2,3,1); pcolor(pixel_size*X/(1e-6),pixel_size*Y/((1e-6)),F2);view(2),axis
    tight,axis square,colorbar, P1title={['\color{red}Number of pixels=' num2str(N) 'x'
    num2str(M)] ['\color{red} Pixel size=', num2str(pixel_size/(1e-6),'%.2s') 'um'] '\
    color{black}Generated picture' ''}; title(P1title),xlabel('um'),ylabel('um'), zoom(
    zoom_factor),
102 d2= subplot(2,3,4); pcolor(pixel_size*X/(1e-6),pixel_size*Y/(1e-6),En),view(2),axis
    tight, axis square,colorbar, P4title={ ['\color{red}Diffraction limit=', num2str(
    Diffraction_limit,'%.2s') 'm'] '' '\color{black}Reconstructured picture' ['Diameters
     = ' num2str(diameter1) ' and '  num2str(diameter2) ' um'] ['Pitch= ' num2str(Pitch
    ) ' um']};title(P4title),xlabel('um'),ylabel('um'),zoom(zoom_factor)
103 c2= subplot(2,3,[ 2 3 5 6 ]);plot(X2(1,:)*pixel_size/(1e-6),En((end-1)/2,:),X2(1,:)*
    pixel_size/(1e-6),F2((end-1)/2,:),'r','LineWidth',2), xlabel('Distance in um'),
    ylabel('Normalized intensity'), axis([ pixel_size*(M-1)*(0.35)/(1e-6) pixel_size*(M
    -1)*(0.65)/(1e-6) 0 1.1]), grid on, grid minor,legend('Reconstructed aperture','
    Original aperture','Location','northeastoutside'),P7title={['NA=', num2str(NA_lens),
    ',' '  wavelength= ', num2str(lambda_um) ' um' ] ['\color{Black} Intensity profile
    along the horizontal direction, center of the aperture']};title(P7title)
104 colormap(d1,gray)
105 colormap(d2,gray)
106
107 arrayfun(@(s) set(s,'EdgeColor','none'), findobj(gcf,'type','surface'))
108 %end
```

Appendix C

Authors signatures and attributions of previously published work

The statements/signatures of the co-authors and the peer-reviewed journal which resulted in Chapter 3 are presented below:

Acknowledgment of contributions to a published work

The following signed statement is to attest that the author of this thesis has made the indicated contributions to a published work contained in this thesis.

Title of the work: Metal selection for wire array metamaterials for infrared frequencies.

Journal and issue: Optics Express 23(23), pp. 29867-29881, (2015).

Authors: Juliano G. Hayashi, Simon Fleming, Boris T. Kuhlmey and Alexander Argyros.

We, the authors of "Metal selection for wire array metamaterials for infrared frequencies," acknowledge that Juliano Grigoleto Hayashi has made the following contributions:

- Performed the simulations included in the manuscript.
- Was a principal contributor in performing the data analysis and interpretations.
- Was the principal contributor in the writing of the manuscript

_____
Simon Fleming

_____
Boris T. Kuhlmey

_____
Alexander Argyros

Date: 10/10/2017

Metal selection for wire array metamaterials for infrared frequencies

Juliano G. Hayashi,[1,*] Simon Fleming,[1] Boris T. Kuhlmey,[1,2] and Alexander Argyros[1]

[1] *Institute of Photonics and Optical Science (IPOS), School of Physics, The University of Sydney, NSW 2006, Australia*

[2] *Centre for Ultrahigh bandwidth Devices for Optical Systems (CUDOS), School of Physics, The University of Sydney, NSW 2006, Australia*

[*] *juliano.hayashi@sydney.edu.au*

Abstract: We analyze the dependence of the electromagnetic properties of wire array metamaterial media on the choice of metal, and identify promising material combinations for use in the near and mid infrared. We propose a figure of merit for the metal optical quality and consider it as a function of several parameters, such as material loss, wavelength of operation and wire diameter. Accordingly, we select promising material combinations, based on optical quality and fabrication compatibility, and simulate the loss of the quasi-TEM mode, for different wavelengths between 1 and 10 μm. We conclude that wire arrays are unlikely to deliver on their many promises at 1 μm, but should prove useful beyond 3 μm.

OCIS codes: (160.3918) Metamaterials; (160.1190) Anisotropic optical materials.

References and links

1. A. Poddubny, I. Iorsh, P. Belov, and Y. Kivshar, "Hyperbolic metamaterials," Nat. Photonics **7**(12), 948–957 (2013).
2. M. G. Silveirinha, "Nonlocal homogenization model for a periodic array of ϵ -negative rods," Phys. Rev. E Stat. Nonlin. Soft Matter Phys. **73**(4), 046612 (2006).
3. D. R. Smith and D. Schurig, "Electromagnetic wave propagation in media with indefinite permittivity and permeability tensors," Phys. Rev. Lett. **90**(7), 077405 (2003).
4. T. G. Mackay, A. Lakhtakia, and R. A. Depine, "Uniaxial dielectric media with hyperbolic dispersion relations," Microw. Opt. Technol. Lett. **48**(2), 363–367 (2006).
5. M. A. Noginov, H. Li, Y. A. Barnakov, D. Dryden, G. Nataraj, G. Zhu, C. E. Bonner, M. Mayy, Z. Jacob, and E. E. Narimanov, "Controlling spontaneous emission with metamaterials," Opt. Lett. **35**(11), 1863–1865 (2010).
6. A. N. Poddubny, P. A. Belov, and Y. S. Kivshar, "Purcell effect in wire metamaterials," Phys. Rev. B **87**(3), 035136 (2013).
7. C. L. Cortes, W. Newman, S. Molesky, and Z. Jacob, "Quantum nanophotonics using hyperbolic metamaterials," J. Opt. **14**(6), 063001 (2012).
8. W. Cai, U. K. Chettiar, A. V. Kildishev, and V. M. Shalaev, "Optical cloaking with metamaterials," Nat. Photonics **1**(4), 224–227 (2007).
9. I. S. Nefedov, D. Chicherin, and A. J. Viitanen, "Infrared cloaking based on wire media," Proc. SPIE **6987**, 698728 (2008).
10. I. Ktorza, L. Ceresoli, S. Enoch, S. Guenneau, and R. Abdeddaim, "Single frequency microwave cloaking and subwavelength imaging with curved wired media," Opt. Express **23**(8), 10319–10326 (2015).
11. G. Shvets, S. Trendafilov, J. B. Pendry, and A. Sarychev, "Guiding, focusing, and sensing on the subwavelength scale using metallic wire arrays," Phys. Rev. Lett. **99**(5), 053903 (2007).
12. P. Ikonen, C. Simovski, S. Tretyakov, P. Belov, and Y. Hao, "Magnification of subwavelength field distributions at microwave frequencies using a wire medium slab operating in the canalization regime," Appl. Phys. Lett. **91**(10), 104102 (2007).
13. D. Lu and Z. Liu, "Hyperlenses and metalenses for far-field super-resolution imaging," Nat. Commun. **3**, 1205 (2012).
14. Z. Liu, H. Lee, Y. Xiong, C. Sun, and X. Zhang, "Far-field optical hyperlens magnifying sub-diffraction-limited objects," Science **315**(5819), 1686 (2007).
15. H. Lee, Z. Liu, Y. Xiong, C. Sun, and X. Zhang, "Development of optical hyperlens for imaging below the diffraction limit," Opt. Express **15**(24), 15886–15891 (2007).
16. P. A. Belov, Y. Zhao, S. Tse, P. Ikonen, M. G. Silveirinha, C. R. Simovski, S. Tretyakov, Y. Hao, and C. Parini, "Transmission of images with subwavelength resolution to distances of several wavelengths in the microwave range," Phys. Rev. B **77**(19), 193108 (2008).

#246832 Received 27 Jul 2015; revised 29 Oct 2015; accepted 3 Nov 2015; published 6 Nov 2015

16 Nov 2015 | Vol. 23, No. 23 | DOI:10.1364/OE.23.029867 | OPTICS EXPRESS 29867

17. P. A. Belov, G. K. Palikaras, Y. Zhao, A. Rahman, C. R. Simovski, Y. Hao, and C. Parini, "Experimental demonstration of multiwire endoscopes capable of manipulating near-fields with subwavelength resolution," Appl. Phys. Lett. **97**(19), 191905 (2010).
18. A. Tuniz, K. J. Kaltenecker, B. M. Fischer, M. Walther, S. C. Fleming, A. Argyros, and B. T. Kuhlmey, "Metamaterial fibres for subdiffraction imaging and focusing at terahertz frequencies over optically long distances," Nat. Commun. **4**, 2706 (2013).
19. O. T. Naman, M. R. New-Tolley, R. Lwin, A. Tuniz, A. H. Al-Janabi, I. Karatchevtseva, S. C. Fleming, B. T. Kuhlmey, and A. Argyros, "Indefinite media based on wire array metamaterials for THz and Mid-IR," Adv. Opt. Mater. **1**(12), 971–977 (2013).
20. S. Tomotika, "On the instability of a cylindrical thread of a viscous liquid surrounded by another viscous fluid," Proc. R. Soc. Lon. A Math. **150**(870), 322–337 (1935).
21. E. Badinter, A. Ioisher, E. Monaico, V. Postolache, and I. M. Tiginyanu, "Exceptional integration of metal or semimetal nanowires in human-hair-like glass fiber," Mater. Lett. **64**(17), 1902–1904 (2010).
22. X. Zhang, Z. Ma, Z. Y. Yuan, and M. Su, "Mass-Production of vertically aligned extremely long metallic micro/nanowires using fiber drawing nanomanufacturing," Adv. Mater. **20**(7), 1310–1314 (2008).
23. S. Adachi, *The Handbook on Optical Constants of Metals: In Tables and Figures*, (World Scientific Publishing, 2012).
24. E. D. Palik, *The Handbook of Optical Constant of Solids*, (Academic, 1997).
25. J. Takahara, S. Yamagishi, H. Taki, A. Morimoto, and T. Kobayashi, "Guiding of a one-dimensional optical beam with nanometer diameter," Opt. Lett. **22**(7), 475–477 (1997).
26. S. Roberts and P. J. Dobson, "Evidence for reaction at the Al-SiO_2 interface," J. Phys. D Appl. Phys. **14**(3), L17–L22 (1981).
27. M. H. Hecht, R. P. Vasquez, F. J. Grunthaner, N. Zamani, and J. Maserjian, "A novel x-ray photoelectron spectroscopy study of the Al/SiO_2 interface," J. Appl. Phys. **57**(12), 5256 (1985).
28. F. Dadabhai, F. Gaspari, S. Zukotynski, and C. Bland, "Reduction of silicon dioxide by aluminum in metal-oxide-semiconductor structures," J. Appl. Phys. **80**(11), 6505 (1996).
29. J. Hou, D. Bird, A. George, S. Maier, B. Kuhlmey, and J. C. Knight, "Metallic mode confinement in microstructured fibres," Opt. Express **16**(9), 5983–5990 (2008).
30. L. A. B. Pilkington, "The float glass process," Proc. R. Soc. Lond. A Math. Phys. Sci. **314**(1516), 1–25 (1969).
31. T. Kloss, G. Lautenschläger, and K. Schneider, "Advances in the process of floating borosilicate glasses and some recent applications for specialty borosilicate float glasses," Glass Technol. **41**(6), 177–181 (2000).
32. Schott Borofloat 33®, general information datasheet, *http://www.us.schott.com/borofloat/english/download/borofloat33_gen_usa_web.pdf*.
33. Y. Wang, Y. Ma, X. Guo, and L. Tong, "Single-mode plasmonic waveguiding properties of metal nanowires with dielectric substrates," Opt. Express **20**(17), 19006–19015 (2012).
34. R. F. Oulton, V. J. Sorger, D. A. Genov, D. F. P. Pile, and X. Zhang, "A hybrid plasmonic waveguide for subwavelength confinement and long-range propagation," Nat. Photonics **2**(8), 496–500 (2008).
35. S. Laref, J. Cao, A. Asaduzzaman, K. Runge, P. Deymier, R. W. Ziolkowski, M. Miyawaki, and K. Muralidharan, "Size-dependent permittivity and intrinsic optical anisotropy of nanometric gold thin films: a density functional theory study," Opt. Express **21**(10), 11827–11838 (2013).
36. M. Hövel, B. Gompf, and M. Dressel, "Electrodynamics of ultrathin gold films at the insulator-to-metal transition," Thin Solid Films **519**(9), 2955–2958 (2011).
37. A. W. Snyder and J. D. Love, *Optical Waveguide Theory* (Chapman & Hall, 1983), Ch. 31.
38. R. Kitamura, L. Pilon, and M. Jonasz, "Optical constants of silica glass from extreme ultraviolet to far infrared at near room temperature," Appl. Opt. **46**(33), 8118–8133 (2007).
39. M. Rubin, "Optical properties of soda lime silica glasses," Sol. Energy Mater. **12**(4), 275–288 (1985).
40. L. G. Aio, A. M. Efimov, and V. F. Kokorina, "Refractive index of chalcogenide glasses over a wide range on compositions," J. Non-Cryst. Solids **27**(3), 299–307 (1978).
41. J. S. Brownless, B. C. P. Sturmberg, A. Argyros, B. T. Kuhlmey, and C. M. de Sterke, "Guided modes of a wire medium slab: comparison of effective medium approaches with exact calculations," Phys. Rev. B **91**(15), 155427 (2015).
42. P. A. Belov, S. A. Tretyakov, and A. J. Viitanen, "Dispersion and reflection properties of artificial media formed by regular lattices of ideally conducting wires," J. Electromagn. Waves Appl. **16**(8), 1153–1170 (2002).
43. H. K. Tyagi, H. W. Lee, P. Uebel, M. A. Schmidt, N. Joly, M. Scharrer, and P. St. J. Russell, "Plasmon resonances on gold nanowires directly drawn in a step-index fiber," Opt. Lett. **35**(15), 2573–2575 (2010).
44. M. A. Schmidt, L. N. P. Sempere, H. K. Tyagi, C. G. Poulton, and P. S. J. Russell, "Waveguiding and plasmon resonances in two-dimensional photonic lattice of gold and silver nanowires," Phys. Rev. Lett. B **77**(3), 033417 (2008).
45. H. W. Lee, M. A. Schmidt, R. F. Russell, N. Y. Joly, H. K. Tyagi, P. Uebel, and P. St. J. Russell, "Pressure-assisted melt-filling and optical characterization of Au nano-wires in microstructured fibers," Opt. Express **19**(13), 12180–12189 (2011).
46. P. Uebel, M. A. Schmidt, M. Scharrer, and P. St. J. Russell, "An azimuthally polarizing photonic crystal fibre with a central gold nanowire," New J. Phys. **13**(6), 063016 (2011).
47. Schott AR-GLAS®, technical datasheet, *http://www.schott.com/tubing/media/selector/datasheets/english/schott-tubing_datasheet_ar-glas_english.pdf*.
48. Schott Boro-8330™, technical datasheet, *http://www.schott.com/tubing/media/selector/datasheets/english/schott-tubing_datasheet_boro8330_english.pdf*.

#246832 Received 27 Jul 2015; revised 29 Oct 2015; accepted 3 Nov 2015; published 6 Nov 2015

16 Nov 2015 | Vol. 23, No. 23 | DOI:10.1364/OE.23.029867 | OPTICS EXPRESS 29868

49. Schott, IRG chalcogenide glasses technical datasheet, *http://www.schott.com/advanced_optics/english/download/schott-infrared-chalcog-glasses-family-sheet-october-2013-eng.pdf*.
50. X. Feng, A. K. Mairaj, D. W. Hewak, and T. M. Monro, "Nonsilica glasses for holey fibers," J. Lightwave Technol. **23**(6), 2046–2054 (2005).

1. Introduction

Metamaterials are metal/dielectric composites that exhibit exotic optical properties due to their subwavelength structure. The type of structure varies according to the desired electromagnetic response. In particular, hyperbolic metamaterials are one of the most interesting classes, possessing extreme anisotropy and hyperbolic (or indefinite) dispersion, where a principal component of the permittivity or permeability tensors has the opposite sign to the other components [1]. Wire arrays based on metal wires in a dielectric background behave as hyperbolic metamaterials for frequencies lower than an effective plasma frequency determined by the array's geometry [1,2], allowing extraordinary waves with a hyperbolic dispersion relation and extremely large transverse spatial frequencies to propagate [3,4]. Consequently, they have many applications such as in high electromagnetic density of states materials [5–7], cloaking [8–10] and hyperlenses [11–13].

Metamaterial hyperlenses utilize the ability to propagate high spatial frequency waves to transport subwavelength information away from the object/source, overcoming the diffraction limit. Such high spatial frequencies containing subwavelength information are evanescent in conventional isotropic materials [14,15]. Furthermore, magnifying hyperlenses can magnify subwavelength features to dimensions within the diffraction limit. Hyperlenses based on wire array media have been demonstrated in the microwave spectrum [12,16,17], and were extended to the THz spectrum using fiber drawing techniques [18]. Extending the operational wavelength range further to the infrared and visible is challenging due the subwavelength requirement of the structure and the losses of the metals at such frequencies.

The fiber drawing technique is a scalable and inexpensive method for the fabrication of subwavelength structures, particularly applicable to wire arrays and high taper ratio wire arrays as required for hyperlenses and magnifying hyperlenses. However, the scaling down of a metallic wire array metamaterial fiber is limited by rheological properties of the materials [19]. Due to the Plateau-Rayleigh instability [20], the surface tension between the molten metal and the dielectric during drawing can distort the structure or break the wires into droplets [19]. This instability has to date limited the application of this technique to metamaterials for wavelengths longer than 20 μm. However, considering the size of wires that have been drawn with this technique [21,22], it should be possible to produce subwavelength wire array metamaterial fibers for the infrared and visible using glass as the dielectric medium.

In this paper, we identify promising metal/dielectric combinations for the fabrication of wire array metamaterial fibers for the near and mid-infrared (NIR and MIR, respectively). Firstly, in Section 2, we propose a figure of merit for the optical quality of metals specific to wire arrays. Based on optical quality and fabrication feasibility, we identify interesting material combinations for operation around 1, 3 and 10 μm wavelengths. In Section 3, we extend our loss study to parameters such as wire diameter (d), operational wavelength (λ) and the index of the dielectric host (n_d). Finally, in Section 4, we study the loss of high-spatial frequency quasi-TEM modes for hexagonal wire array structures with specific material combinations, varying wire diameter, wire spacing and index of the dielectric, in the NIR and MIR.

2. Bulk metal losses and figure of merit

The optical loss of a wave reflecting from, or propagating along, a bulk metal is determined by the imaginary and real part of the metal's permittivity (ε_i and ε_r), which vary with free space wavelength (λ). The dielectric constant ε_i is related to the metal's absorption, while the ε_r is related to the penetration of the wave in the bulk metal. Figures 1(a) and 1(b) show experimental values of ε_i and ε_r, respectively, for several metals in the NIR and MIR (data

#246832 Received 27 Jul 2015; revised 29 Oct 2015; accepted 3 Nov 2015; published 6 Nov 2015

16 Nov 2015 | Vol. 23, No. 23 | DOI:10.1364/OE.23.029867 | OPTICS EXPRESS 29869

from Refs [23,24].). For all the metals presented, except Bi, ε_i and the absolute value of ε_r increases with λ. In a wire array, or even in a single metal wire plasmonic waveguide, ε_i is also not sufficient to estimate propagation loss of waves in these structures. The optical loss of each mode is also strongly related to the energy distribution between the metal and the surrounding dielectric, meaning that the real part of permittivity (ε_r) of both materials and the geometry also influence the loss.

An appropriate figure of merit for this type of structure is the loss of the fundamental TM mode in a single metal wire waveguide. While these losses also depend on the wire diameter used, setting a nominal diameter enables comparison between metals. The mode condition equation for the 0th order TM mode of a single wire can be found analytically as [25],

$$\frac{\gamma_2 I_1(\gamma_1 a) K_0(\gamma_2 a)}{\gamma_1 I_0(\gamma_1 a) K_1(\gamma_2 a)} = -\frac{\varepsilon_2}{\varepsilon_1} \tag{1}$$

where I_m and K_m are the modified Bessel functions of order m, a is the radius of the metal wire, and ε_1 and ε_2 are the complex permittivities of the metal and dielectric, respectively. The factor γ is defined by

$$\gamma_j = k_0 (n_{\text{eff}}{}^2 - \varepsilon_j)^{1/2} \tag{2}$$

where n_{eff} is the effective index of the mode, k_0 is vacuum wavenumber ($k_0 = 2\pi/\lambda$). The root of the transcendental Eq. (1) can be found numerically and provides the n_{eff} of the TM mode, which can be used to calculate the loss in dB/μm using

$$\alpha = \frac{40\pi \cdot \kappa}{\lambda \cdot \ln(10)} \tag{3}$$

where κ is the imaginary part of n_{eff} and λ is the wavelength in microns.

Figures 1(c) and 1(d) illustrate the loss of the lowest order TM mode calculated using Eqs. (1)-(3), for wire diameters of 250 nm and 500 nm, respectively, embedded in vacuum, as a function of wavelength. The representative metals were chosen for their good optical properties (Au, Ag, Al, Cu) or their convenience for fabrication due to availability and relatively low melting temperature (Bi, Sn, In). As expected, Figs. 1(c) and 1(d) show that the absolute value of the loss changes with wire diameter but the relative loss of the different metals is not qualitatively affected. Consequently, the loss for a nominal diameter is a good figure of merit for a metal's optical quality. As such, Figs. 1(c) and 1(d) show that loss decreases for longer wavelengths and Au, Ag, Al and Cu are clearly the best metals as far as loss is concerned for the wavelength range between 1 to 10 μm.

#246832 Received 27 Jul 2015; revised 29 Oct 2015; accepted 3 Nov 2015; published 6 Nov 2015

16 Nov 2015 | Vol. 23, No. 23 | DOI:10.1364/OE.23.029867 | OPTICS EXPRESS 29870

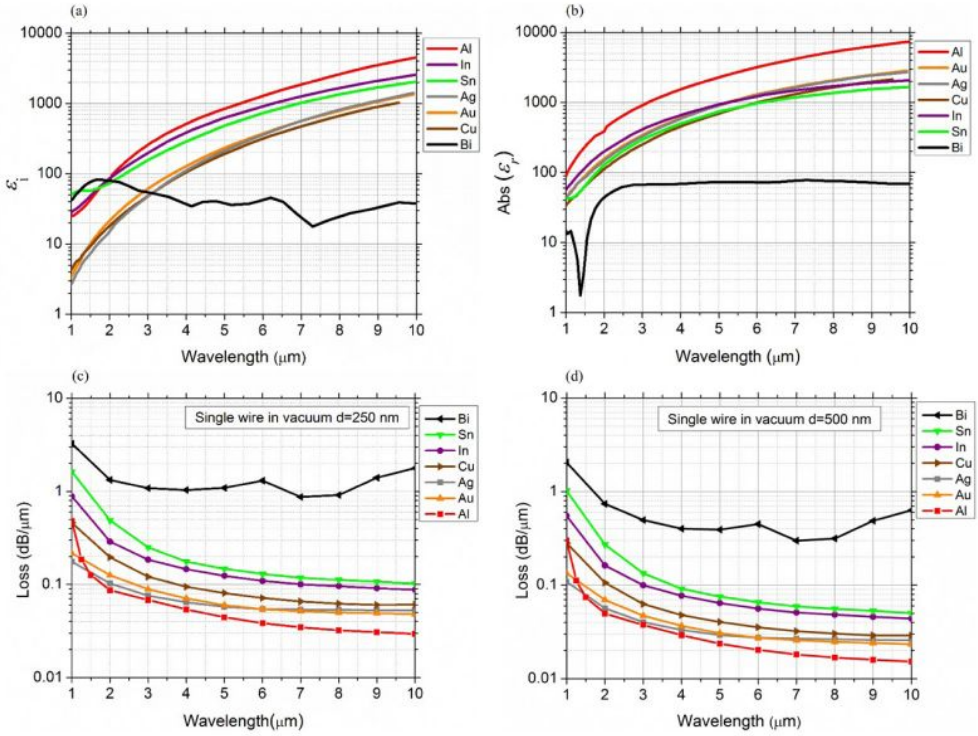

Fig. 1. Measured values of (a) the imaginary and (b) the real part of the permittivity for bulk metals [23,24], in the NIR and MIR. Figure of merit: the 0th order TM mode loss of a single metal wire waveguide embedded in vacuum for wire diameters of (c) d = 250 nm, (d) d = 500 nm.

Apart from optical loss, fabrication feasibility is another extremely important criterion in the selection of materials for wire array metamaterial media. When fiber drawing is used, the co-drawing of metal and glass is only possible if the materials are chemically compatible and the rheological properties match. The components must not react and the metal must be liquid at the drawing temperature. In addition, the potential formation of solid oxides during drawing can be extremely detrimental to the fabrication.

Considering Fig. 1(c), Al is the best metal in terms of optical quality over almost all the wavelength range considered. However, experimental tests with common silica-based glasses (borosilicate, soda-lime and SiO_2) showed high reactivity resulting in the production of Si, through the reaction [26–28]

$$4Al+3SiO_2 \rightarrow 2Al_2O_3+3Si. \quad (4)$$

Cu is compatible with glass and Cu/SiO_2 fibers have been reported in the literature [29], however its strong tendency to oxidize when molten can be a problem, especially during preform fabrication. According to our figure of merit, both Au and Ag have similar and high optical quality, but Ag presents higher reactivity. Therefore, among the metals with lowest losses, Au remains the best option once compatibility with the glass drawing process is considered.

The second group of metals, having poorer optical quality, is considered for practicality. Of these, Sn presents low oxidation when molten and high compatibility with common glasses, especially with soda-lime and borosilicate. This compatibility is commercially employed in the fabrication of float soda-lime and borosilicate by the Pilkington process or microfloat process [30–32]. This feature, combined with low cost and low melting point, motivates a deeper analysis of its use in drawn wire arrays. We thus focus further analysis on

#246832 Received 27 Jul 2015; revised 29 Oct 2015; accepted 3 Nov 2015; published 6 Nov 2015

16 Nov 2015 | Vol. 23, No. 23 | DOI:10.1364/OE.23.029867 | OPTICS EXPRESS 29871

Au and Sn, as cases of high optical quality (Au) and practicality (Sn). Figures 1(c) and 1(d) show that losses for wire arrays using other interesting metals (Ag and Cu) are expected to lie between these two cases.

In the next section, we extend our loss study of the 0th order TM mode of the single wire waveguide to other parameters such as wire diameter (d), wavelength, and the refractive index of the dielectric host (n_d), before studying losses of the full wire array in Section 4.

3. Single metal wire waveguide

The loss of the TM mode of a single metal wire depends on the wire diameter, the wavelength and the index of the surrounding dielectric. Figures 2(a) and 2(b) present this loss for Au and Sn wires with several diameters (from 10 nm to 2.5 μm), in the wavelength region between 1 to 10 μm, calculated with Eqs. (1)-(3) using the complex permittivity of the metals from Figs. 1(a) and 1(b). Vacuum is selected as the dielectric medium in order to analyze, in the first instance, the influence of the metal in isolation.

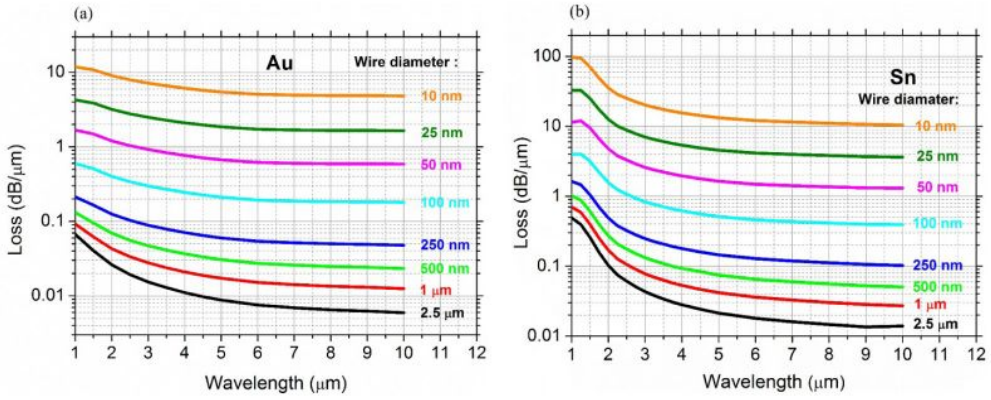

Fig. 2. Loss as a function of wavelength for several wire diameters. (a) Au, (b) Sn.

Figure 2 shows that the losses are higher for the Sn wires, as expected from the figure of merit and because Sn has larger ε_i (Fig. 1(a)). In addition, the optical losses decrease with longer wavelength and larger wire diameter. This is somewhat counterintuitive in that ε_i increases with wavelength (Fig. 1(a)), and one could naively expect losses to diminish with wire diameter, as the amount of metal is reduced. In order to clarify this behavior, we calculate the field distribution in the metal.

The fractional energy in the metal is defined as

$$\eta = \iint_{metal} W(r)dA \Big/ \iint_{All} W(r)dA \tag{5}$$

where W is the mode energy density given by [33,34]

$$W(r) = \frac{1}{2}\left(\frac{d(\varepsilon(r)\omega)}{d\omega} |\mathbf{E}(r)|^2 + \mu_0 |\mathbf{H}(r)|^2 \right) \tag{6}$$

and μ_0 is the vacuum permeability, ε is the complex permittivity, and ω is the angular frequency.

Figure 3(a) illustrates how fractional energy in the wire varies with wire diameter for Au and Sn wires embedded in vacuum, for a fixed wavelength of 3 μm. As seen in Fig. 3(a), smaller wire diameters lead to an extremely confined mode, which increases loss [33]. This behavior is consistent with Figs. 1(c) and 1(d). We note that we use the bulk permittivity of the metals for this calculation, which becomes increasingly inapplicable for very thin wires with diameters below tens of nanometers [35,36]. Thus, these results should be treated as an approximation.

#246832 Received 27 Jul 2015; revised 29 Oct 2015; accepted 3 Nov 2015; published 6 Nov 2015

16 Nov 2015 | Vol. 23, No. 23 | DOI:10.1364/OE.23.029867 | OPTICS EXPRESS 29872

The fractional energy analysis cannot be used to explain the wavelength dependence of loss as it does not take into account the dispersion and group velocity. From perturbation theory [37], the difference in the imaginary part of the mode effective index for the TM mode of a single wire with and without the metallic loss can be expressed to first order as

$$\Delta\kappa = \left(\frac{\varepsilon_0}{\mu_0}\right)^{1/2} \frac{\int_{metal} \varepsilon_i |\mathbf{E}|^2 \, da}{\int_{All} 2(|E_r H_\phi|) da} \tag{7}$$

where E_r and H_ϕ are the radial and azimuthal components of the electric and magnetic field, respectively. Figure 3(b) shows the factor $\Delta\kappa/\lambda$, which is proportional to the loss per unit length, for 250 nm Au and Sn wires in vacuum, as a function of wavelength. This is consistent with the loss calculated directly from the complex mode effective index in Figs. 1(c) and 1(d), showing again that loss decreases for longer wavelengths and that Sn is lossier than Au.

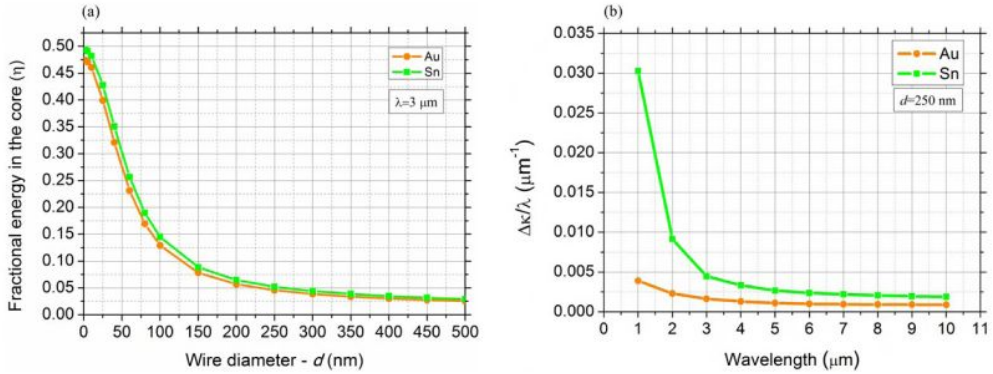

Fig. 3. (a) Fractional energy in the metal for the lowest order TM mode in the single wire waveguide in vacuum, as a function of the wire diameter, for Au and Sn, at λ = 3 μm. (b) Difference in the imaginary part of the mode effective index for the TM mode of a single wire with and without the metallic loss, normalized by the wavelength.

The refractive index of the dielectric surrounding the metal also influences the mode energy distribution. For this reason, for a specific material combination, any loss analysis as a function of wavelength must include the dispersion of the complex dielectric index. However, for a fixed wavelength, it is interesting to understand how the loss behaves if only n_d varies, which simulates a change of the dielectric. Figure 4 illustrates the loss of the Au and Sn wire with d = 250 nm, at λ = 3 μm, for n_d varying from 1 to 3. This range covers the indices of SiO_2 (1.41925 [38]), soda-lime (1.4849 [39]), borosilicate (around 1.5), and some chalcogenide glasses (up to 3 [40]) commonly used for the wavelengths in the range of 1-10 μm. In order to simplify the analysis, the loss of the dielectric was omitted, as with appropriate choice of dielectrics the loss of the metal should dominate.

#246832 Received 27 Jul 2015; revised 29 Oct 2015; accepted 3 Nov 2015; published 6 Nov 2015

16 Nov 2015 | Vol. 23, No. 23 | DOI:10.1364/OE.23.029867 | OPTICS EXPRESS 29873

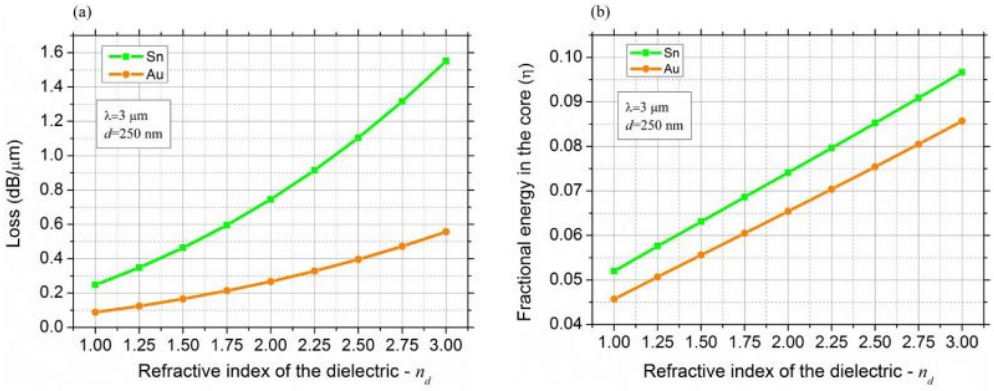

Fig. 4. (a) Loss and (b) fractional energy in the metal core as a function of the refractive index of the dielectric for Au and Sn wires (d = 250 nm), at λ = 3 μm.

As seen in Fig. 4, the loss and fractional energy in the metal increase for higher dielectric index n_d. Consequently, the selection of the dielectric must not only consider its transparency but also the real part of its refractive index. As the loss of the metal is usually much higher than that of the dielectric, the selection of an optically poorer dielectric could result in a lower modal loss if the real part of the dielectric index is low, through reducing the fractional energy in the metal.

In the next section, we study the loss of the high-spatial frequency quasi-TEM mode for the full hexagonal wire array metamaterial media. We propose some material combinations for operational wavelengths in the NIR and MIR, and consider the effect of varying structure parameters such as wire diameter and wire spacing (Λ).

4. Indefinite wire array metamaterial media

The indefinite wire array metamaterial media constitutes a spatially dispersive hyperbolic medium for frequencies below the effective plasma frequency of the structure [1], and has three types of modes: TE, TM and quasi-TEM (a second TM mode) [2]. When this hyperbolic metamaterial is considered for super resolution imaging, it is the propagation of high spatial frequency modes that is most important, as these contain the subwavelength information usually restricted to the near field. In the absence of spatial dispersion, the extraordinary mode of hyperbolic media has the dispersion relation [1,3,4,18]

$$\frac{k_{\parallel}^2}{\varepsilon_{\perp}} - \frac{|k_{\perp}|^2}{|\varepsilon_{\parallel}|} = \left(\frac{\omega}{c}\right)^2 \tag{8}$$

where $k_{\perp}$, $k_{\parallel}$, $\varepsilon_{\perp}$ and $\varepsilon_{\parallel}$, are the wave vector and permittivity components transverse and parallel to the wires, respectively, and c is the speed of light. The isofrequency surface generated by Eq. (8) is hyperbolic, and has no high spatial frequency cut-off, enabling sub-diffraction imaging. However, because of spatial dispersion not one but two extraordinary modes exist (the TM and quasi–TEM), and isofrequency surfaces are best calculated numerically. Figure 5(a) shows isofrequency curves for the modes in a hexagonal wire array shown in Fig. 5(b), based on Sn and soda-lime, with d = 100 nm, wire spacing Λ = 600 nm and λ = 3 μm, calculated using a commercial finite element solver (COMSOL). As can be seen, the quasi-TEM mode (black dots) allows propagation of high transverse spatial frequencies with $(k_{\perp}/k_0)>n_d$, which can enable imaging beyond the diffraction limit. Figure 5(c) shows an example of a calculated quasi-TEM mode with high spatial frequency, where the white arrows represent the **E** field distribution in the xy plane and the color scale represents the normalized time averaged energy flow in the wire direction.

#246832 Received 27 Jul 2015; revised 29 Oct 2015; accepted 3 Nov 2015; published 6 Nov 2015

16 Nov 2015 | Vol. 23, No. 23 | DOI:10.1364/OE.23.029867 | OPTICS EXPRESS 29874

From homogenization theory [2], the TE mode (red dots) in this structure does not have a hyperbolic dispersion of the form of Eq. (8) because its polarization is transverse to the anisotropy axis, corresponding to an ordinary wave. As a result, the wire array behaves like a dielectric and the dispersion relation is given by [41]

$$k_{\perp}^2 + k_{\parallel}^2 = \varepsilon_{\mathrm{d}} \left(\frac{\omega}{c} \right)^2 \tag{9}$$

where ε_{d} is the permittivity of the dielectric host. The isofrequency curves are thus circles, matching the numerical results in Fig. 5(a). The TE mode is evanescent for $(k_{\perp}/k_0)>n_{\mathrm{d}}$, which corresponds to $k_{\perp}/k_0>1.4849$ in Fig. 5(a). The dispersion relation of the TM modes (blue dots), can be approximated from spatially dispersive homogenization models as [41]

$$k_{\perp}^2 + k_{\parallel}^2 + k_{\mathrm{p}}^2 = \varepsilon_{\mathrm{d}} \left(\frac{\omega}{c} \right)^2 \tag{10}$$

where k_{p} is the effective plasma frequency of the wire array [19,42]. According to Eq. (10), the TM mode is evanescent for all $k_{\perp}$ when $k_{\mathrm{p}}^2>\varepsilon_{\mathrm{d}}*(\omega/\mathrm{c})^2$, a condition that is fulfilled in the structure of Fig. 5.

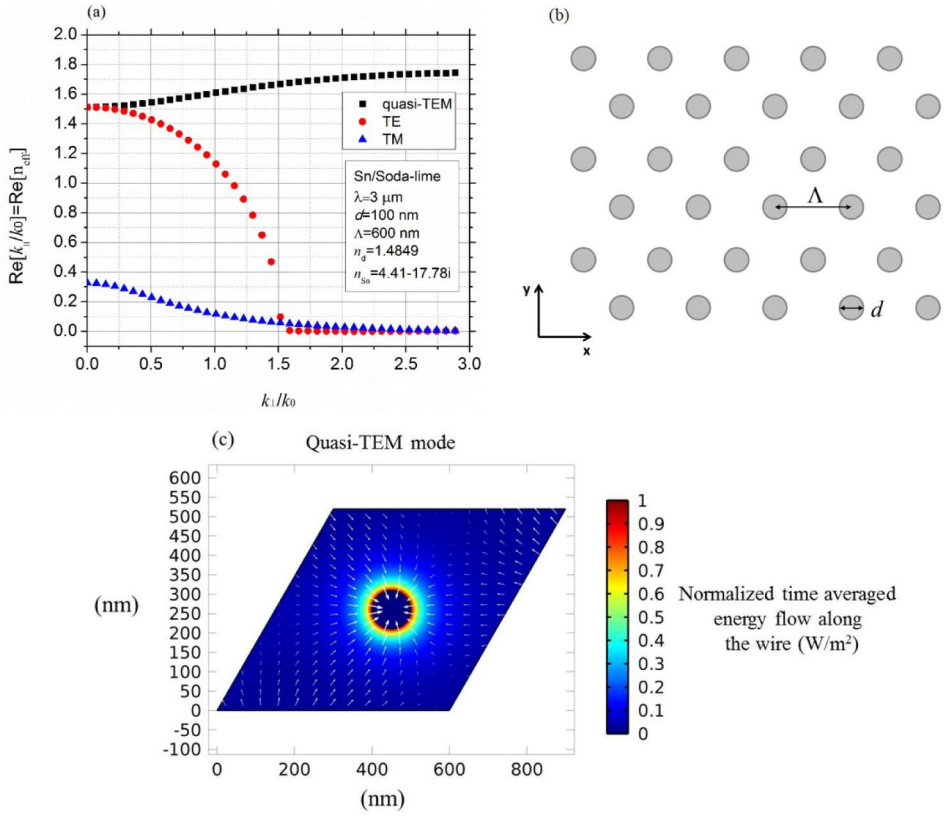

Fig. 5. (a) Isofrequency curves of the modes in the wire array, Sn/soda-lime system, d = 100 nm, L = 600 nm and λ = 3 μm. (b) Schematic of the hexagonal wire array (c) Field distribution of the calculated quasi-TEM mode with high spatial frequency ($k_{\perp} = (\pi/\Lambda)*(2/\sqrt{3})$).

The wire array is more complex than the single wire waveguide as the propagation loss also depends on the distance between the wires Λ and the mode field distribution, in addition to the other parameters already discussed. In the following subsections, we discuss some

#246832 Received 27 Jul 2015; revised 29 Oct 2015; accepted3 Nov 2015; published 6 Nov 2015

16 Nov 2015 | Vol. 23, No. 23 | DOI:10.1364/OE.23.029867 | OPTICSEXPRESS 29875

possible material combinations for wire arrays in the MIR and NIR and analyze their loss for a range of structural parameters. Any effect relying on the hyperbolic nature of the material (e.g. density of states enhancement, sub-diffraction imaging), will require low loss for high transverse spatial frequencies ($k_\perp/k_0$)>n_d.

We used COMSOL to calculate the isofrequency curves, loss and modal fields of the wire array with a hexagonal lattice as in Fig. 5(b), using Bloch-Floquet boundary conditions. From the complex effective index (n_{eff}) of the simulated quasi-TEM mode, Eq. (3) is used to calculate the propagation loss. For each specific structure and material combination, two cases of the quasi-TEM mode were considered, $k_\perp = 0$ being the lowest transverse spatial frequency, corresponding to k oriented along the wires, and $k_\perp = (\pi/\Lambda)*(2/\sqrt{3}) = k_{\perp max}$ which corresponds to the edge of the Brillouin zone for the wire array, and thus the highest transverse spatial frequency that can propagate. Consequently, $k_{\perp max}$ corresponds to the highest resolution possible with the structure for a given Λ. The range of the geometric parameters (d and Λ) for each material combination varies with the operational wavelength and the refractive index of the dielectric host. We limit our study to structures capable of sub-diffraction propagation and thus keep the distance between the wires below the diffraction limit ($\Lambda<\lambda/2n_d$). The wire diameters are selected in order to achieve d/Λ between 0.1 and 0.9. The mesh size in the metal wire was set as $d/100$, while the mesh in the dielectric was set smaller than $\Lambda/50$.

4.1 – Near infrared (1μm), System: Au/SiO_2

We consider Au wires in SiO_2 as the case study for the NIR. Au was shown to be favorable above, and SiO_2 is chosen for its high transmission at 1 μm and known compatibility with Au with both co-drawing techniques [43] and the pressure-assisted melt-filling method [44–46].

Figure 6 presents the loss in dB/μm of the quasi-TEM mode with lowest loss as a function of L, for λ = 1 μm and different wire diameters. In Figs. 6(a) and 6(b), the modes have $k_\perp = 0$ and $k_{\perp max}$, respectively. The indices used were 1.45042 [38] for SiO_2 and 0.25-6.66i [23] for Au, considering its bulk complex permittivity from Figs. 1(a) and 1(b). It is important to emphasize that this becomes increasingly inapplicable for very thin wires with diameters below tens of nanometers. According to the literature, the loss of thin gold films is expected to increase or decrease as a function of thickness, depending on the type of film [35,36]. Thus, further work will be required and these simulations at 1 μm wavelength must be treated as an approximation. We limited our study to structures with Λ<345 nm, which corresponds to the diffraction limit ($\lambda/2n_d$).

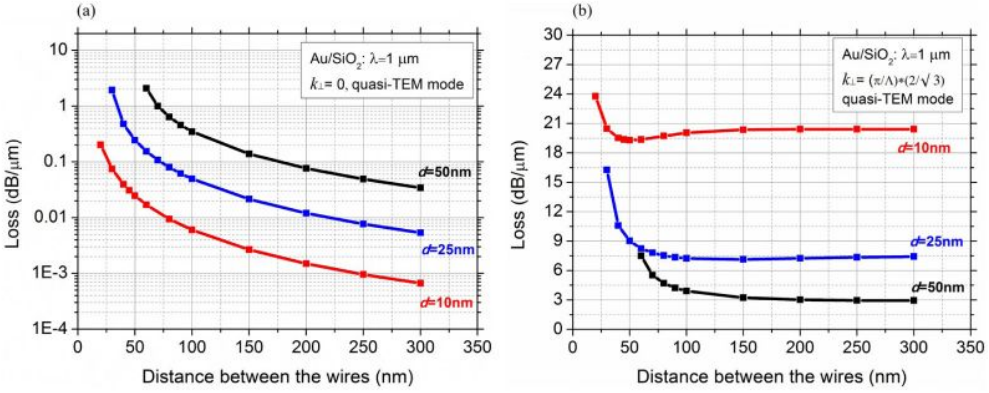

Fig. 6. Quasi-TEM mode loss for the wire array (Au/SiO_2 system) as a function of d and L, at λ = 1 μm, for (a) $k_\perp = 0$, and (b) $k_{\perp max}$ (corresponding to the edge of the Brillouin zone).

As shown in Fig. 6(a), the loss of the quasi-TEM mode decreases with increasing Λ for $k_\perp = 0$. This is expected since the metal fraction in the unit cell decreases for a fixed wire diameter. When the distance between the wires is constant, the loss increases for larger wire

#246832 Received 27 Jul 2015; revised 29 Oct 2015; accepted 3 Nov 2015; published 6 Nov 2015

16 Nov 2015 | Vol. 23, No. 23 | DOI:10.1364/OE.23.029867 | OPTICS EXPRESS 29876

diameters, showing the opposite behavior compared to the single wire case (Figs. 2(a) and 2(b)). This indicates that, for $k_\perp = 0$, the influence of the metal fraction on the loss is more significant than the influence of the mode confinement when d is changed. On the other hand, the modes with $k_\perp = k_\perp max$ follow the behavior of the single wire waveguide, presenting higher loss for smaller wire diameter. This indicates that, for $k_\perp max$, the variation on the mode confinement is more significant than the change in metal fraction when d increases. Indeed, for $k_\perp = 0$ the quasi-TEM modal fields are predominantly between wires, while for large $k_\perp$ fields localize more strongly at the wire interface.

Figure 7 (a) shows the profile of the normalized electric field across the small diagonal of the unit cell (red line of the inset) of the quasi-TEM modes with $k_\perp = 0$ and $k_\perp max$, for the cases with d = 10 nm (Figs. 7(b) and 7(c)) and d = 25 nm (Figs. 7(d) and 7(e)), for Λ = 40 nm, Au/SiO_2 system, at λ = 1 μm.

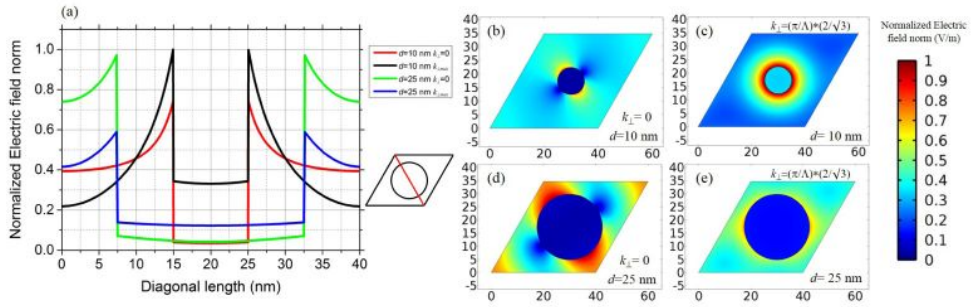

Fig. 7. (a) Profile of the normalized electric field norm across the small diagonal of the unit cell (red line of the inset) from the four quasi-TEM modes showed in (b-e), Au/SiO_2 system, L = 40 nm, at λ = 1 μm. Normalized electric field norm for the quasi-TEM modes with $k_\perp = 0$ and $k_{\perp max}$, d = 10 nm (b,c) and d = 25 nm (d,e), respectively.

According to Figs. 7(a)-7(e), the concentration of electric field in the metal wire for the modes with $k_\perp max$ is higher than their respective modes with $k_\perp = 0$, which explains the difference in the losses between Fig. 6(a) and 6(b). In addition, Fig. 7(a) also shows that, for $k_\perp = 0$, there is slightly more electric field in the metal for the case with d = 25 nm than the one with d = 10 nm. This explains the unusual behavior presented in Fig. 6(a), where the loss increase for larger wire diameters. From the **E** and **H** field distributions and using Eqs. (5)-(6), we calculated the energy density inside the metal for the all the four cases presented in Figs. 7(b)-7(d). The fractional energies in the metal found were 0.004 (Fig. 7(b)), 0.242 (Fig. 7(c)), 0.0325 (Fig. 7(d)) and 0.229 (Fig. 7(e)), which are also in agreement with the losses presented in Fig. 6.

Importantly our results show that while the loss of the quasi-TEM mode with k oriented parallel to the wires ($k_\perp = 0$) can be low enough to propagate over hundreds of wavelengths, this is not the case for modes with $k_\perp > n_d k_0$, which are the modes most relevant to any sub-diffraction physics such as hyperlenses and density of states enhancement.

For an imaging application, considering 20 dB as the maximum acceptable propagation loss, Fig. 6(b) shows that the maximum propagation length for the Au/SiO_2 system at λ = 1 μm is around 1, 3 and 7 μm for wire diameters of 10, 25 and 50 nm, respectively. These maximum propagation lengths of approximately 1, 3, and 7 wavelengths make wire array based metamaterial hyperlenses unlikely to be of use at 1 μm wavelength.

4.2 – Mid infrared (3 μm), Systems: Au/SiO_2 and Sn/soda-lime

For the MIR we consider the Au/SiO_2 system again, and also consider Sn for the metal. Its low melting point (232 °C) makes possible the use of drawing methods using common soft-glasses such as soda-lime (drawing temperature around 700 °C), and borosilicate (800 °C). Both have similar optical quality at 3 μm, with a transmission around 50% for 1 mm thickness

#246832 Received 27 Jul 2015; revised 29 Oct 2015; accepted 3 Nov 2015; published 6 Nov 2015

16 Nov 2015 | Vol. 23, No. 23 | DOI:10.1364/OE.23.029867 | OPTICS EXPRESS 29877

[47,48]. We select soda-lime for our simulations because of its lower drawing temperature and well known compatibility with Sn [30–32].

Figures 8(a) and 8(b) present the loss for the Au/SiO_2 system at λ = 3 μm, for the quasi-TEM modes with $k_\perp$ = 0 and for $k_{\perp max}$. Similarly, Figs. 8(c) and 8(d) show the equivalent results for the Sn/soda-lime system. The indices used were 1.41925 [38] for SiO_2, 1.63-18.6i [23] for Au, 1.4849 [39] for soda-lime and 4.41-17.78i [24] for Sn. The structure is limited to L<1 μm, which corresponds to the diffraction limit for λ = 3 μm, given the indices of the glasses.

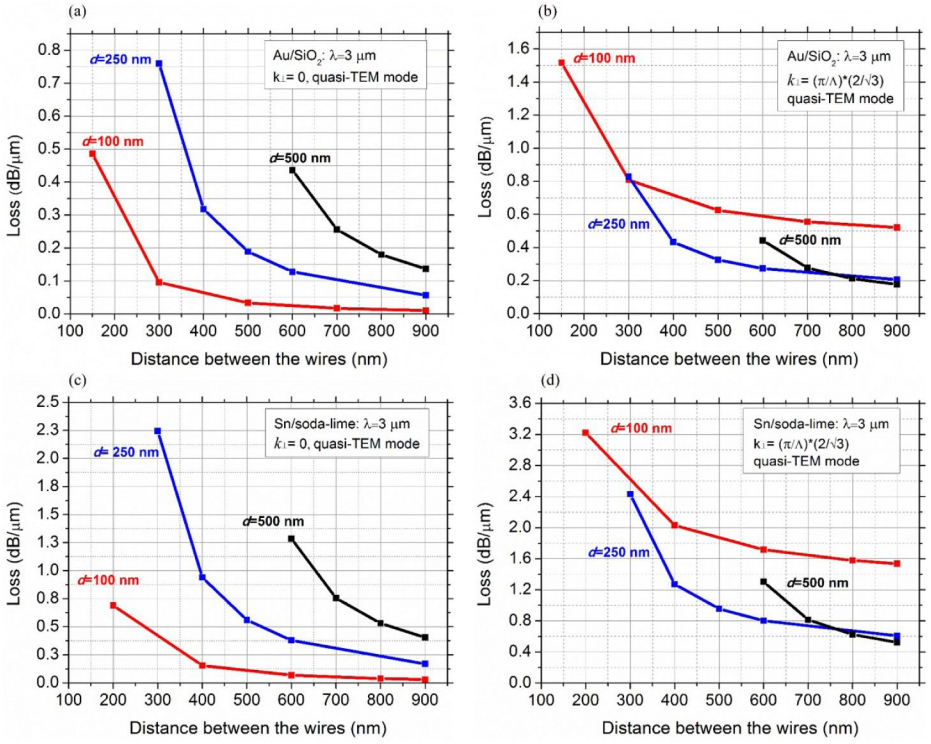

Fig. 8. Quasi-TEM mode loss for wire arrays as functions of *d* and L, at 3 μm wavelength, for (a,c) $k_\perp$ = 0 and (b,d) $k_{\perp max}$ (corresponding to the edge of the Brillouin zone). (a,b) Au/SiO_2 and (c,d) Sn/soda-lime.

As shown in Figs. 8(a) and 8(b), the loss of the quasi-TEM modes at 3 μm for both $k_\perp$ = 0 and $k_{\perp max}$, present the same behavior as the modes at 1 μm when wire diameter and separation are varied. Considering again 20 dB as the maximum acceptable loss, Fig. 8(b) shows that the maximum propagation lengths of the high $k_\perp$ mode for the Au/SiO_2 system at λ = 3 μm are around 33 μm (*d* = 100 nm), 100 μm (*d* = 250 nm) and 110 μm (*d* = 500 nm), when the distance between the wires approaches the diffraction limit. These maximum propagation lengths of approximately 10, 30, and 36 wavelengths make the use of wire arrays much more compelling at 3 μm than at 1 μm wavelength. In this regime, depending on the combination of *d* and L, even distances between the wires around half of the diffraction limit have reasonable propagation lengths. For instance, for L = 500 nm and *d* = 250 nm, the 20 dB propagation length is around 50 μm.

Regarding the Sn/soda-lime system, Fig. 8(d) shows that the maximum propagation length at λ = 3 μm is around 13 μm (*d* = 100 nm), 33 μm (*d* = 250 nm), and 40 μm (*d* = 500 nm). As expected from the single wire waveguide analysis, Au is optically better than Sn. However, the propagation lengths of approximately 4, 11 and 13 wavelengths described above make this an interesting option for large wire diameters and wire separation.

#246832 Received 27 Jul 2015; revised 29 Oct 2015; accepted 3 Nov 2015; published 6 Nov 2015

16 Nov 2015 | Vol. 23, No. 23 | DOI:10.1364/OE.23.029867 | OPTICS EXPRESS 29878

4.3 – Mid infrared (10 μm), Systems: Au and Sn embedded in a glass with n_d = 2.8

At the operational wavelength of 10 μm, the loss of the dielectric also needs to be taken into account in the selection of the materials. Because of their low transparency, silica-based glasses must be excluded. Chalcogenide glasses such as IRG 22 (Schott, $Ge_{33}As_{12}Se_{55}$) [49], GLS (Gallium Lanthanum Sulphide) [50], As_2Se_3 and As_2S_3 are better choices because they have a transmission higher than 50% at λ = 10 μm, for 2 mm samples. Therefore, we consider a material with n_d = 2.8 as the dielectric, which is representative of the above examples.

The low minimum drawing temperature of the chalcogenide glasses, between 300 to 700°C, makes the co-drawing of these glasses with high melting point metals such as Au, Al, Cu and Ag impossible. This limitation emerges from the fabrication requirement that the minimum drawing temperature of the dielectric must be higher than the melting point of metal. According to our figure of merit (Fig. 1(c)), apart from these high melting point metals, the best options at λ = 10 μm are Sn and In. Because their optical quality is very similar, Sn was selected due its low oxidation and low cost. Even though it is impossible to co-draw chalcogenide glasses with molten Au, we nevertheless consider Au as an ideal scenario for comparison.

Figures 9(a) and 9(b) present the loss for Sn wires at λ = 10 μm, for the quasi-TEM modes with $k_\perp = 0$ and for $k_{\perp max}$, respectively. Figures 9(c) and 9(d) show the equivalent results for Au wires. The indices used were 22-46.41i [24] for Sn and 12.36-55.04i [23] for Au. The structure is limited to L<1.785 μm, which corresponds to the diffraction limit for λ = 10 μm in a dielectric with n_d = 2.8.

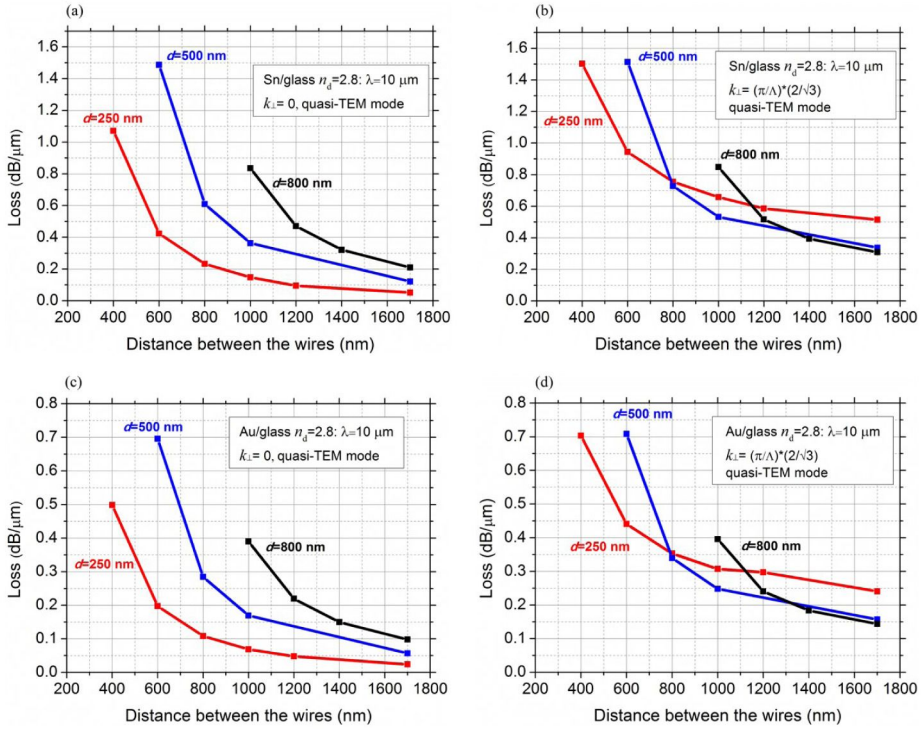

Fig. 9. Quasi-TEM mode loss for wire array as functions of *d* and L, at 10 μm wavelength, for (a,c) $k_\perp = 0$ and (b,d) $k_{\perp max}$ (corresponding to the edge of the Brillouin zone). (a,b) Sn and (c,d) Au embedded in a glass with n_d = 2.8.

Considering again 20 dB as the maximum acceptable loss of the high $k_\perp$ modes, Fig. 9(b) shows that the maximum propagation lengths for the Sn/glass with n_d = 2.8 system at λ = 10 μm are around 38 μm (*d* = 250 nm), 60 μm (*d* = 500 nm), and 65 μm (*d* = 800 nm). These

#246832 Received 27 Jul 2015; revised 29 Oct 2015; accepted 3 Nov 2015; published 6 Nov 2015

16 Nov 2015 | Vol. 23, No. 23 | DOI:10.1364/OE.23.029867 | OPTICS EXPRESS 29879

propagation lengths of approximately 3.8, 6 and 6.5 wavelengths are not as encouraging as the propagation lengths at λ = 3 μm.

Regarding the Au wires, Fig. 9(d) shows that the maximum propagation lengths are around 83 μm (8 wavelengths, d = 100 nm), 127 μm (12 wavelengths, d = 250 nm), and 140 μm (14 wavelengths, d = 500 nm). As expected by the single wire waveguide analysis, Au is optically better than Sn for the wire array at λ = 10 μm, presenting a factor of 2 improvement on the loss. Although the metals have lower loss at this wavelength compared to 3 μm, the higher index of the dielectric results in an overall increase in the loss due to higher confinement in the metal.

4.4 – Loss as a function of n_d

The refractive index of the dielectric (n_d) influences the mode energy distribution in the wire array and, consequently, also affects the mode loss. Therefore, the best dielectric in terms of the metamaterial optical performance is not necessarily the one with the lowest extinction coefficient (i.e. the highest transparency).

Figure 10(a) illustrates the loss of the quasi-TEM modes ($k_\perp$ = 0 and $k_{\perp max}$) as functions of n_d at λ = 3 μm, for a fixed structure with Sn wires (d = 250 nm, L = 500 nm). The refractive index of the dielectric is varied from 1 to 3, covering SiO_2 (1.41925 [38]), soda-lime (1.4849 [39]), borosilicate (around 1.5), and some chalcogenide glasses (up to 3 [40]).

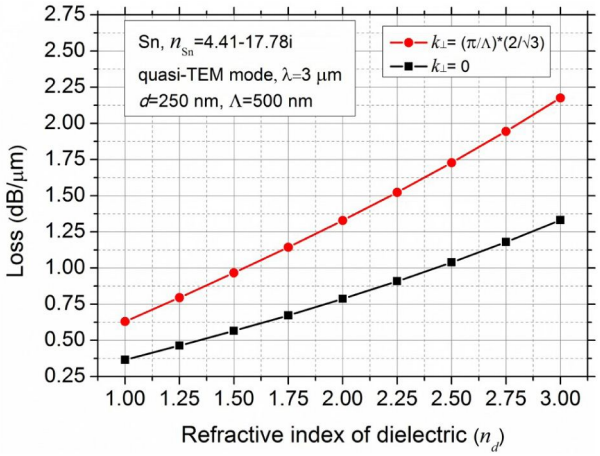

Fig. 10. Quasi-TEM mode loss for a wire array with Sn wires as a function of the refractive index of the dielectric n_d, d = 250 nm and L = 500 nm, at 3 μm wavelength, for $k_\perp$ = 0 (red curve) and for $k_{\perp max}$ (black curve), corresponding to the edge of the Brillouin zone.

Figure 10 shows the loss increasing for larger n_d for both modes. This behavior is in agreement with the single wire waveguide (Figs. 4(a) and 4(b)) and indicates that larger n_d increases the mode confinement in the metal. As a result, if the transparency of the glass candidates is equivalent, the best option is the dielectric with the lower refractive index n_d.

Since lower refractive indices lower losses, it is tempting to artificially reduce the effective refractive index of the glass e.g. by adding holes between wires. Simulations to that effect (adding a hole between wires in the unit cell) shows this only reduces loss by ~1%, because electric fields are weakest at the half-way point between wires, where it would be practical to add holes in the structure. Further simulations showed that reducing the amount of metal by replacing wires by metallic coated holes do not reduce loss at all, but rather lead to an increase in losses when the metal thickness is below the skin depth – which can be understood in that the effective resistance increases when reducing the metal cross section.

#246832 Received 27 Jul 2015; revised 29 Oct 2015; accepted 3 Nov 2015; published 6 Nov 2015

16 Nov 2015 | Vol. 23, No. 23 | DOI:10.1364/OE.23.029867 | OPTICS EXPRESS 29880

4. Conclusion

We have investigated promising metal/glass combinations considering optical quality and drawing feasibility for the fabrication of wire array metamaterial media for the MIR and NIR. The figure of merit based on the 0th-order TM mode loss of a single metal wire waveguide provides a qualitative comparison between the optical quality of the metals. The single wire analysis shows that loss decreases for longer wavelengths, larger wire diameter and smaller refractive index of the surrounding dielectric due to the variations in the mode confinement. Simulations of the full wire arrays show that the loss for the quasi-TEM mode varies greatly with transverse spatial frequency. While it is the high spatial frequency modes that give hyperbolic media their most interesting properties, the propagation loss of the highest spatial frequency (at the Brillouin zone edge) can be orders of magnitude higher than for propagation parallel to the wire. At $\lambda = 1$ μm the loss of high spatial frequency modes are high for all material combinations considered. With 20 dB-propagation lengths of a few microns at most among all configurations simulated, wire media are unlikely to yield many applications in the NIR.

The situation is considerably better at longer wavelengths. At $\lambda = 3$ μm, Au is optically the best option yielding 20 dB-propagation lengths for high spatial frequency modes up to 110μm, depending on the wire diameter and the distance between the wires. Reasonable losses are still achieved for distances between the wires smaller than half of the diffraction limit, so that sub-diffraction limited wire-array based hyperlenses are in principle feasible at this wavelength. Sn is optically poorer but still usable for large wire diameters and distance between the wires, with maximum 20 dB-propagation lengths up to 40 μm in this limit.

For an optical wavelength of 10 μm, losses are relatively higher, even for Au wire arrays, because of the increased refractive index of suitable host dielectrics. At this wavelength, Sn wire arrays with relatively large wire diameters and distance between the wires marginally below the diffraction limit could also prove useful, with maximum propagation lengths up to 65 μm.

In all cases, the loss of the high spatial frequency modes diminishes rapidly with increased wire diameter and wire-to-wire spacing. Magnifying hyperlenses based on tapered wire arrays will thus suffer much lower losses than those calculated here – as long as the taper angle is steep from the outset. Such configurations require further study.

Our study shows the practical spectral limits of wire array metamaterial media, considering the properties of feasible material combinations, and assuming the need to propagate distances of multiple wavelengths. We conclude there is little possibility for operation wavelengths of 1 μm or shorter for applications relying on transmission of high spatial frequencies, but have identified material combinations that will permit operation in the near infrared to wavelengths as short as 3 μm.

Acknowledgments

This research was supported by the Australian Research Council (ARC) under the Discovery Project scheme number DP120103942 and DP140104116, and it was performed in part at the Optofab node of the Australian National Fabrication Facility (ANFF) using Commonwealth and NSW State Government funding. The author Juliano Hayashi would like to thank the Science without Borders Program by CAPES (Brazil) for the financial support under grant 9468/13-7.

#246832 Received 27 Jul 2015; revised 29 Oct 2015; accepted 3 Nov 2015; published 6 Nov 2015

APPENDIX C. AUTHORS SIGNATURES AND ATTRIBUTIONS OF PREVIOUSLY PUBLISHED WORK

Appendix D

List of publications

The currently publications that resulted from this thesis are listed below (January/2018):

Peer-reviewed publications

1. Juliano G. Hayashi, Simon Fleming, Boris T. Kuhlmey and Alexander Argyros, *"Metal selection for wire array metamaterials for infrared frequencies,"* Optics Express 23(23), pp. 29867-29881, 2015.

2. Lin Huang, Honglin An, Juliano G. Hayashi, Guobin Ren, Alessio Stefani, and Simon Fleming, *"Thermal poling of multi-wire array optical fiber,"* Optics Express 26(2), pp. 674-679, 2018.

The preparation of other peer-reviewed publications with the content of Chapter 4, Chapter 5 and Chapter 6 are in progress.

Review paper

1. Shaghik Atakaramians, Alessio Stefani, Haisu Li, Md. Samiul Habib, Juliano Grigoleto Hayashi, Alessandro Tuniz, Xiaoli Tang, Jessienta Anthony, Richard Lwin,Alexander Argyros, Simon C. Fleming, Boris T. Kuhlmey, *"Fiber-Drawn Metamaterial for THz Waveguiding and Imaging"*, Journal of Infrared, Millimeter, and Terahertz Waves, Springer, pp.1-17, 2017.

Conference proceedings and presentations

1. Juliano G. Hayashi, Richard Lwin, Simon Fleming, Boris T. Kuhlmey, and Alexander Argyros, *"Wire array metamaterial fibers based on soft-glass"*, European Quantum Electronics Conference (CLEO Europe 2015), EH P 13, Optical Society of America, Germany (21-25 June 2015).

2. J.G. Hayashi, R. Lwin, Alessio Stefani, S. Fleming, A. Argyros, and B.T. Kuhlmey, *"Metamaterial hyperlens for the MIR"*, 41st International Conference on Infrared, Millimeter, and Terahertz waves (IRMMW-THz), IEEE, Denmark (25-30 September 2016).

3. A. Stefani, J. Grigoleto Hayashi, X.L. Tang and A. Argyros, *"Soft-glass scalable metamaterials: fiber drawn split ring resonators"*, Paper ID 5138, META16, the 7th International Conference on Metamaterials, Photonic Crystals and Plasmonics, Spain (25-28 July 2016).

4. Simon C. Fleming, Alexander Argyros, Juliano Hayashi, Shicheng Xue, Geoff Barton, Boris Kuhlmey, *"Metamaterials and Hyperlenses: Practical Fabrication by Fibre Drawing"*, Invited Paper CI7, TecnoLaser 2016, Cuba (29 March - 1 April 2016).

5. Simon C. Fleming, Alexander Argyros, Juliano Hayashi, Shicheng Xue, Geoff Barton, Boris Kuhlmey, *"Metamaterial Fibres"*, Paper WW2A.3 (Invited) at Workshop on Specialty Optical Fibers and Their Applications (WSOF 2015), Hong Kong (4-6 November 2015).

6. Simon C. Fleming, Alexander Argyros, Juliano Hayashi, Shicheng Xue, Geoff Barton and Boris Kuhlmey, *"Metamaterials: Practical Fabrication by Fibre Drawing"*, Invited Paper at 8th International Conference for Advanced Infocomm Technology (ICAIT 2015), Hangzhou, China (25-27 October 2015).

7. Simon Fleming, Alexander Argyros, Juliano Grigoleto, Shicheng Zhu, Geoff Barton and Boris Kuhlmey, *"Fibre Technology for Realising Metamaterials"*, Invited Paper E3-1, p.67. 8th International Conference on Materials for Advanced Technologies (ICMAT) and 4th Photonics Global Conference (PGC), Singapore (28 June - 3 July 2015).

8. Alessio Stefani, Juliano Grigoleto Hayashi, Simon Fleming, Alexander Argyros and Boris T. Kuhlmey, *"Split-ring resonators hyperlens for undistorted sub-wavelength imaging"*, Paper EH-P.22, CLEO Europe, Germany (23-27 June 2017).

9. S. Fleming, A. Stefani, J. Grigoleto Hayashi, B. Kuhlmey, *"Metamaterials Fabricated by Fibre Drawing"*, (Invited paper) Paper S1009 / 1-3A-3, Proceedings of 12th Conference on Lasers and Electro-Optics Pacific Rim (CLEO-PR 2017), 22nd OptoElectronics and Communications Conference (OECC 2017) and 5th Photonics Global Conference 2017 (PGC 2017), Singapore (31 July - 4 August 2017).

10. Wu Shengling, Simon Fleming, Boris T. Kuhlmey, Juliano G. Hayashi, Heike Ebendorff-Heidepriem, and Alessio Stefani, *"Fabrication of $Ge_{28}Sb_{12}Se_{60}$ chalcogenide glass microstructured optical fiber with stack-and-draw method"*, accepted (3 Oct 2017) for Australia New Zealand Conference on Optics and Photonics (ANZCOP), Queenstown, New Zealand (4-7 December 2017).

11. J.G. Hayashi, R. Lwin, A. Argyros, S. Fleming, B.T. Kuhlmey and A. Stefani, *"Extreme sub-diffraction focusing of THz radiation with magnifying metamaterial hyperlenses"*, accepted (3 Oct 2017) for Australia New Zealand Conference on Optics and Photonics (ANZCOP), Queenstown, New Zealand (4-7 December 2017).

Bibliography

[1] Yongmin Liu and Xiang Zhang. Metamaterials: a new frontier of science and technology. *Chemical Society Reviews*, 40(5):2494–2507, 2011.

[2] John David Jackson. *Classical electrodynamics*. John Wiley & Sons, 2007.

[3] Mark Fox. *Optical properties of solids*. Oxford University Press, 2001.

[4] Hiroyuki Fujiwara. *Spectroscopic ellipsometry: principles and applications*. John Wiley & Sons, 2007.

[5] Edward D. Palik. *The Handbook of Optical Constant of Solids*. Academic press, 1998.

[6] Sadao Adachi. *The Handbook on Optical Constants of Semiconductors: In Tables and Figures*. World Scientific Publishing, 2012.

[7] Lev Davidovich Landau, J.S. Bell, M.J. Kearsley, L.P. Pitaevskii, E.M. Lifshitz, and J.B. Sykes. *Electrodynamics of continuous media*, volume 8. Elsevier, 2013.

[8] D.J. Barber and Ian C. Freestone. An investigation of the origin of the colour of the lycurgus cup by analytical transmission electron microscopy. *Archaeometry*, 32(1):33–45, 1990.

[9] Graeme W. Milton. *The theory of composites*. Cambridge University Press, 2002.

[10] Russell J. Gehr and Robert W. Boyd. Optical properties of nanostructured optical materials. *Chemistry of Materials*, 8(8):1807–1819, 1996.

[11] Ross C. McPhedran, Ilya V. Shadrivov, Boris T. Kuhlmey, and Yuri S. Kivshar. Metamaterials and metaoptics. *NPG Asia Materials*, 3:100, 2011.

[12] John B. Pendry, A.J. Holden, W.J. Stewart, and I. Youngs. Extremely low frequency plasmons in metallic mesostructures. *Physical Review Letters*, 76(25):4773, 1996.

[13] John B. Pendry, A.J. Holden, D.J. Robbins, and W.J. Stewart. Magnetism from conductors and enhanced nonlinear phenomena. *IEEE Transactions on Microwave Theory and Techniques*, 47(11):2075–2084, 1999.

[14] Viktor G. Veselago. The electrodynamics of substances with simultaneously negative values of ϵ and μ. *Soviet Physics Espekhi*, 10(4):509, 1968.

[15] David R. Smith, Willie J. Padilla, D.C. Vier, Syrus C. Nemat-Nasser, and Seldon Schultz. Composite medium with simultaneously negative permeability and permittivity. *Physical Review Letters*, 84(18):4184, 2000.

[16] Richard A. Shelby, David R. Smith, and Seldon Schultz. Experimental verification of a negative index of refraction. *Science*, 292(5514):77–79, 2001.

[17] Wenshan Cai and Vladimir Shalaev. *Optical metamaterials: fundamentals and applications*. Springer Science & Business Media, 2009.

[18] Tie Jun Cui, David R. Smith, and R.P. Liu. *Metamaterials*. Springer, 2010.

[19] Filippo Capolino. *Metamaterials handbook*. CRC Press, 2009.

[20] A. Poddubny, I. Iorsh, P. Belov, and Y. Kivshar. Hyperbolic metamaterials. *Nature Photonics*, 7(12):948–957, 2013.

[21] Nikolay I. Zheludev and Yuri S. Kivshar. From metamaterials to metadevices. *Nature Materials*, 11(11):917, 2012.

[22] Dylan Lu and Zhaowei Liu. Hyperlenses and metalenses for far-field super-resolution imaging. *Nature Communications*, 3:1205, 2012.

[23] Saman Jahani and Zubin Jacob. All-dielectric metamaterials. *Nature Nanotechnology*, 11(1):23, 2016.

[24] Huanyang Chen, Che Ting Chan, and Ping Sheng. Transformation optics and metamaterials. *Nature Materials*, 9(5):387, 2010.

[25] Nina Meinzer, William L. Barnes, and Ian R. Hooper. Plasmonic meta-atoms and metasurfaces. *Nature Photonics*, 8(12):889–898, 2014.

[26] D.R. Smith and D. Schurig. Electromagnetic wave propagation in media with indefinite permitivitty and permeability tensors. *Physical Review Letters*, 90(7):077405, 2003.

[27] T.G. Mackay, A. Lakhtakia, and R.A. Depine. Uniaxial dielectric media with hyperbolic dispersion relations. *Microwave and Optical Technology Letters*, 48(2):363–367, 2006.

[28] Ismo V. Lindell, S.A. Tretyakov, K.I. Nikoskinen, and S. Ilvonen. Bw mediamedia with negative parameters, capable of supporting backward waves. *Microwave and Optical Technology Letters*, 31(2):129–133, 2001.

[29] Leonid V. Alekseyev, Viktor A. Podolskiy, and Evgenii E. Narimanov. Homogeneous hyperbolic systems for terahertz and far-infrared frequencies. *Advances in OptoElectronics*, 2012, 2012.

[30] Yu Guo, Ward Newman, Cristian L. Cortes and Jacob Zubin. Applications of hyperbolic metamaterial substrates. *Advances in OptoElectronics*, 2012, 2012.

[31] Zubin Jacob, Leonid V. Alekseyev and Evgenii Narimanov. Optical hyperlens: Far-field imaging beyond the diffraction limit. *Optics Express*, 14(18):8247–8256, 2006.

[32] M.A. Noginov, H. Li, Y.A. Barnakov, D. Dryden, G. Nataraj, G. Zhu, C.E. Bonner, M. Mayy, Z. Jacob, and E.E. Narimanov. Controlling spontaneous emission with metamaterials. *Optics Letters*, 35(11):1863–1865, 2010.

[33] Zubin Jacob, J.Y Kim, Gururaj V. Naik, Alexandra Boltasseva, Evgenii E. Narimanov, and Vladimir M. Shalaev. Engineering photonic density of states using metamaterials. *Applied Physics B: Lasers and Optics*, 100(1):215–218, 2010.

[34] John D. Joannopoulos, Steven G. Johnson, Joshua N. Winn, and Robert D. Meade. *Photonic crystals: molding the flow of light*. Princeton University Press, 2011.

[35] Igor I. Smolyaninov and Evgenii E. Narimanov. Metric signature transitions in optical metamaterials. *Physical Review Letters*, 105(6):067402, 2010.

[36] Igor I. Smolyaninov and Vera N. Smolyaninova. Hyperbolic metamaterials: Novel physics and applications. *Solid-State Electronics*, 136:102–112, 2017.

[37] Tengfei Li and Jacob B. Khurgin. Hyperbolic metamaterials: beyond the effective medium theory. *Optica*, 3(12):1388–1396, 2016.

[38] Prashant Shekhar, Jonathan Atkinson, and Zubin Jacob. Hyperbolic metamaterials: fundamentals and applications. *Nano Convergence*, 1(1):14, 2014.

[39] T. Tumkur, G. Zhu, P. Black, Yu A. Barnakov, C.E. Bonner, and M.A. Noginov. Control of spontaneous emission in a volume of functionalized hyperbolic metamaterial. *Applied Physics Letters*, 99(15):151115, 2011.

[40] Harish N.S. Krishnamoorthy, Zubin Jacob, Evgenii Narimanov, Ilona Kretzschmar, and Vinod M. Menon. Topological transitions in metamaterials. *Science*, 336(6078):205–209, 2012.

[41] J. Kim, V.P. Drachev, Z. Jacob, G.V. Naik, A. Boltasseva, E.E. Narimanov and V.M. Shalaev. Improving the radiative decay rate for dye molecules with hyperbolic metamaterials. *Optics Express*, 20(7):8100–8116, 2012.

[42] Xiaodong Yang, Jie Yao, Junsuk Rho, Xiaobo Yin, and Xiang Zhang. Experimental realization of three-dimensional indefinite cavities at the nanoscale with anomalous scaling laws. *Nature Photonics*, 6(7):450–454, 2012.

[43] C.L. Cortes, W. Newman, S. Molesky, and Z. Jacob. Quantum nanophotonics using hyperbolic metamaterials. *Journal of Optics*, 14(6):063001, 2012.

[44] Yu Guo, Cristian L. Cortes, Sean Molesky, and Zubin Jacob. Broadband super-planckian thermal emission from hyperbolic metamaterials. *Applied Physics Letters*, 101(13):131106, 2012.

[45] S.A Biehs, Maria Tschikin, and Philippe Ben-Abdallah. Hyperbolic metamaterials as an analog of a blackbody in the near field. *Physical Review Letters*, 109(10):104301, 2012.

[46] Igor S. Nefedov and Constantin R. Simovski. Giant radiation heat transfer through micron gaps. *Physical Review B*, 84(19):195459, 2011.

[47] Belov A. Pavel, George K. Palikaras, Yan Zhao, Atiqur Rahman, Constantin R. Simovski, Yang Hao and Clive Parini. Experimental demonstration of multiwire endoscopes capable of manipulating near-fields with subwavelength resolution. *Applied Physics Letters*, 97(19), 2010.

[48] Zhaowei Liu, Hyesog Lee, Yi Xiong, Cheng Sun, and Xiang Zhang. Far-field optical hyperlens magnifying sub-diffraction-limited objects. *Science*, 315(5819):1686–1686, 2007.

[49] Junsuk Rho, Ziliang Ye, Yi Xiong, Xiaobo Yin, Zhaowei Liu, Hyeunseok Choi, Guy Bartal, and Xiang Zhang. Spherical hyperlens for two-dimensional sub-diffractional imaging at visible frequencies. *Nature Communications*, 1:143, 2010.

[50] A. Tuniz, K.J. Kaltenecker, B.M. Fischer, M. Walther, S.C. Fleming, A. Argyros and B.T. Kuhlmey. Metamaterial fibres for subdiffraction imaging and focusing at terahertz frequencies over optically long distances. *Nature Communications*, 4:2706, 2013.

[51] Satoshi Ishii, Alexander V. Kildishev, Evgenii Narimanov, Vladimir M. Shalaev, and Vladimir P. Drachev. Sub-wavelength interference pattern from volume plasmon polaritons in a hyperbolic medium. *Laser & Photonics Reviews*, 7(2):265–271, 2013.

[52] David R. Smith, David Schurig, Jack J. Mock, Pavel Kolinko, and Patrick Rye. Partial focusing of radiation by a slab of indefinite media. *Applied Physics Letters*, 84(13):2244–2246, 2004.

[53] Keith G. Balmain, A.A.E. Luttgen, and Peter C. Kremer. Resonance cone formation, reflection, refraction, and focusing in a planar

anisotropic metamaterial. *IEEE Antennas and Wireless Propagation Letters*, 1(1):146–149, 2002.

[54] Eudenilson L. Albuquerque and Michael G. Cottam. *Polaritons in periodic and quasiperiodic structures*. Elsevier, 2004.

[55] D.L. Mills and E. Burstein. Polaritons: the electromagnetic modes of media. *Reports on Progress in Physics*, 37(7):817, 1974.

[56] J.S. Nkoma. Phonon polariton modes in semiconductor superlattices. *Solid State Communications*, 64(11):1383–1386, 1987.

[57] Gabriele F. Giuliani and J.J. Quinn. Charge-density excitations at the surface of a semiconductor superlattice: a new type of surface polariton. *Physical Review Letters*, 51(10):919, 1983.

[58] Jie Yao, Xiaodong Yang, Xiaobo Yin, Guy Bartal, and Xiang Zhang. Three-dimensional nanometer-scale optical cavities of indefinite medium. *Proceedings of the National Academy of Sciences*, 108(28):11327–11331, 2011.

[59] Bing Wang, Xiang Zhang, Francisco J. García-Vidal, Xiaocong Yuan, and Jinghua Teng. Strong coupling of surface plasmon polaritons in monolayer graphene sheet arrays. *Physical Review Letters*, 109(7):073901, 2012.

[60] Ivan V. Iorsh, Ivan S. Mukhin, Ilya V. Shadrivov, Pavel A. Belov, and Yuri S. Kivshar. Hyperbolic metamaterials based on multilayer graphene structures. *Physical Review B*, 87(7):075416, 2013.

[61] Andrei Andryieuski, Andrei V. Lavrinenko, and Dmitry N. Chigrin. Graphene hyperlens for terahertz radiation. *Physical Review B*, 86(12):121108, 2012.

[62] Jason Valentine, Shuang Zhang, Thomas Zentgraf, Erick Ulin-Avila, Dentcho A. Genov, Guy Bartal, and Xiang Zhang. Three-dimensional optical metamaterial with a negative refractive index. *Nature*, 455(7211):376, 2008.

[63] Sergey S. Kruk, David A. Powell, Alexander Minovich, Dragomir N. Neshev, and Yuri S. Kivshar. Spatial dispersion of multilayer fishnet metamaterials. *Optics Express*, 20(14):15100–15105, 2012.

[64] V.M. Agranovich and V.E. Kravtsov. Notes on crystal optics of superlattices. *Solid State Communications*, 55(1):85–90, 1985.

[65] A.A. Orlov, P.M. Voroshilov, P.A. Belov, and Y.S. Kivshar. Engineered optical nonlocality in nanostructured metamaterials. *Physical Review B*, 84(4):045424, 2011.

[66] Slobodan M. Vukovic, Ilya V. Shadrivov, and Yuri S. Kivshar. Surface bloch waves in metamaterial and metal-dielectric superlattices. *Applied Physics Letters*, 95(4):041902, 2009.

[67] Robyn Wangberg, Justin Elser, Evgenii E. Narimanov, and Viktor A Podolskiy. Nonmagnetic nanocomposites for optical and infrared negative-refractive-index media. *JOSA B*, 23(3):498–505, 2006.

[68] A.V. Chebykin, A.A. Orlov, A.V. Vozianova, Stanislav I. Maslovski, Y.S. Kivshar, and Pavel A. Belov. Nonlocal effective medium model for multilayered metal-dielectric metamaterials. *Physical Review B*, 84(11):115438, 2011.

[69] A.V. Chebykin, A.A. Orlov, C.R. Simovski, Y.S. Kivshar, and Pavel A. Belov. Nonlocal effective parameters of multilayered metal-dielectric metamaterials. *Physical Review B*, 86(11):115420, 2012.

[70] Gururaj V. Naik, Jongbum Kim, and Alexandra Boltasseva. Oxides and nitrides as alternative plasmonic materials in the optical range. *Optical Materials Express*, 1(6):1090–1099, 2011.

[71] Dmitriy Korobkin, Burton Neuner, Chris Fietz, Nikoletta Jegenyes, Gabriel Ferro, and Gennady Shvets. Measurements of the negative refractive index of sub-diffraction waves propagating in an indefinite permittivity medium. *Optics Express*, 18(22):22734–22746, 2010.

[72] Anthony J. Hoffman, Leonid Alekseyev, Scott S. Howard, Kale J. Franz, Dan Wasserman, Viktor A. Podolskiy, Evgenii E. Narimanov, Deborah L. Sivco, and Claire Gmachl. Negative refraction in semiconductor metamaterials. *Nature Materials*, 6(12):946–950, 2007.

[73] P.A. Belov, R. Marques, S.I. Maslovski, I.S. Nefedov, M. Silveirinha, C.R. Simovski, and S.A. Tretyakov. Strong spatial dispersion

in wire media in the very large wavelength limit. *Physical Review B*, 67(11):113103, 2003.

[74] Constantin R. Simovski, Pavel A. Belov, Alexander V. Atrashchenko and Yuri S. Kivshar. Wire metamaterials: Physics and applications. *Advanced Materials*, 24(31):4229–4248, 2012.

[75] Manju Singh and Gobind Das. Highly ordered anodic porous alumina membrane and its surface modification approaches for biomedical application. *IOSR Journal of Applied Chemistry*, 7(1):17–34, 2014.

[76] Paul Evans, W.R. Hendren, Ron Atkinson, G.A. Wurtz, Wayne Dickson, A.V. Zayats, and R.J. Pollard. Growth and properties of gold and nickel nanorods in thin film alumina. *Nanotechnology*, 17(23):5746, 2006.

[77] A.V. Kabashin, P. Evans, S. Pastkovsky, W. Hendren, G.A. Wurtz, R. Atkinson, R. Pollard, V.A. Podolskiy, and A.V. Zayats. Plasmonic nanorod metamaterials for biosensing. *Nature Materials*, 8(11):867, 2009.

[78] M.A. Noginov, Yu A. Barnakov, G. Zhu, T. Tumkur, H. Li, and E.E. Narimanov. Bulk photonic metamaterial with hyperbolic dispersion. *Applied Physics Letters*, 94(15):151105, 2009.

[79] Jing-Feng Li, Shuji Tanaka, Toshiya Umeki, Shinya Sugimoto, Masayoshi Esashi, and Ryuzo Watanabe. Microfabrication of thermoelectric materials by silicon molding process. *Sensors and Actuators A: Physical*, 108(1):97–102, 2003.

[80] Lloyd R. Harriott. Limits of lithography. *Proceedings of the IEEE*, 89(3):366–374, 2001.

[81] Alessandro Tuniz, B.T. Kuhlmey, R. Lwin, A. Wang, Jessienta Anthony, Rainer Leonhardt, and S.C. Fleming. Drawn metamaterials with plasmonic response at terahertz frequencies. *Applied Physics Letters*, 96(19):191101, 2010.

[82] Alessandro Tuniz, Richard Lwin, Alexander Argyros, Simon C. Fleming, Elise M. Pogson, Evan Constable, Roger A. Lewis, and Boris T.

Kuhlmey. Stacked-and-drawn metamaterials with magnetic resonances in the terahertz range. *Optics Express*, 19(17):16480–16490, 2011.

[83] Neetesh Singh, Alessandro Tuniz, Richard Lwin, Shaghik Atakaramians, Alexander Argyros, Simon C Fleming, and Boris T Kuhlmey. Fiber-drawn double split ring resonators in the terahertz range. *Optical Materials Express*, 2(9):1254–1259, 2012.

[84] O.T. Naman, M.R. New-Tolley, R. Lwin, A. Tuniz, A.H. Al-Janabi, I. Karatchevtseva, S.C. Fleming, B.T. Kuhlmey and A. Argyros. Indefinite media based on wire array metamaterials for THz and Mid-IR. *Advanced Optical Materials*, 1(12):971–977, 2013.

[85] Jie Yao, Zhaowei Liu, Yongmin Liu, Yuan Wang, Cheng Sun, Guy Bartal, Angelica M. Stacy, and Xiang Zhang. Optical negative refraction in bulk metamaterials of nanowires. *Science*, 321(5891):930–930, 2008.

[86] J. Brown. Artificial dielectrics. *Progress in Dielectrics*, 2:195–225, 1960.

[87] Walter Rotman. Plasma simulation by artificial dielectrics and parallel-plate media. *IRE Transactions on Antennas and Propagation*, 10(1):82–95, 1962.

[88] R. King, D. Thiel, and K. Park. The synthesis of surface reactance using an artificial dielectric. *IEEE Transactions on Antennas and propagation*, 31(3):471–476, 1983.

[89] J.M. Pitarke, F.J. Garcia-Vidal, and J.B. Pendry. Effective electronic response of a system of metallic cylinders. *Physical Review B*, 57(24):15261, 1998.

[90] J.B. Pendry, A.J. Holden, D.J. Robbins, and W.J. Stewart. Low frequency plasmons in thin-wire structures. *Journal of Physics: Condensed Matter*, 10(22):4785, 1998.

[91] John Brian Pendry. Negative refraction makes a perfect lens. *Physical Review Letters*, 85(18):3966, 2000.

[92] Igor S. Nefedov and Ari J. Viitanen. Guided waves in uniaxial wire medium slab. *Progress In Electromagnetics Research*, 51:167–185, 2005.

[93] M.G. Silveirinha. Nonlocal homogenization model for a periodic array of ϵ-negative rods. *Physical Review E*, 73(4):046612, 2006.

[94] Mário G. Silveirinha, Pavel A. Belov, and Constantin R. Simovski. Subwavelength imaging at infrared frequencies using an array of metallic nanorods. *Physical Review B*, 75(3):035108, 2007.

[95] John Brown and Willis Jackson. The properties of artificial dielectrics at centimetre wavelengths. *Proceedings of the IEE-Part B: Radio and Electronic Engineering*, 102(1):11–16, 1955.

[96] P.A. Belov, S.A. Tretyakov and A.J. Viitanen. Dispersion and reflection properties of artificial media formed by regular lattices of ideally conducting wires. *Journal of Electromagnetic Waves and Applications*, 16(8):1153–1170, 2002.

[97] S.I. Maslovski, S.A. Tretyakov, and P.A. Belov. Wire media with negative effective permittivity: A quasi-static model. *Microwave and Optical Technology Letters*, 35(1):47–51, 2002.

[98] Stanislav I. Maslovski and Mário G. Silveirinha. Nonlocal permittivity from a quasistatic model for a class of wire media. *Physical Review B*, 80(24):245101, 2009.

[99] N.A. Nicorovici, R.C. McPhedran, and L.C. Botten. Photonic band gaps for arrays of perfectly conducting cylinders. *Physical Review E*, 52(1):1135, 1995.

[100] Mário G. Silveirinha and Carlos A. Fernandes. Efficient calculation of the band structure of artificial materials with cylindrical metallic inclusions. *IEEE Transactions on Microwave Theory and Techniques*, 51(5):1460–1466, 2003.

[101] Philip Russell. Photonic crystal fibers. *Science*, 299(5605):358–362, 2003.

[102] Jonathan C. Knight. Photonic crystal fibres. *Nature*, 424(6950):847–851, 2003.

[103] Philip St.J. Russell. Photonic-crystal fibers. *Journal of Lightwave Technology*, 24(12):4729–4749, 2006.

[104] A.F. Abouraddy, M. Bayindir, G. Benoit, S.D. Hart, K. Kuriki, N. Orf, O. Shapira, F. Sorin, B. Temelkuran, and Y. Fink. Towards multimaterial multifunctional fibres that see, hear, sense and communicate. *Nature Materials*, 6(5):336, 2007.

[105] Xian Feng, Arshad K. Mairaj, Daniel W. Hewak and Tanya M. Monro. Nonsilica glasses for holey fibers. *Journal of Lightwave Technology*, 23(6):2046, 2005.

[106] Heike Ebendorff-Heidepriem and Tanya M. Monro. Extrusion of complex preforms for microstructured optical fibers. *Optics Express*, 15(23):15086–15092, 2007.

[107] Maryanne Large, Joseph Zagari, John Canning, Tom Ryan, Martin van Eijkelenborg, Nilmini Goringe, and Nader Issa. Casting preforms for optical fibres, July 22 2002. US Patent App. 10/484,219.

[108] Yani Zhang, Kang Li, Lili Wang, Liyong Ren, Wei Zhao, Runcai Miao, Maryanne C.J. Large, and Martijn A. van Eijkelenborg. Casting preforms for microstructured polymer optical fibre fabrication. *Optics Express*, (12):5541–5547, 2006.

[109] Anders Bjarklev, Jes Broeng, and Araceli Sanchez Bjarklev. Fabrication of photonic crystal fibres. In *Photonic Crystal Fibres*, pages 115–130. Springer, 2003.

[110] Alexis Méndez and Ted F. Morse. *Specialty optical fibers handbook*. Academic Press, 2011.

[111] Geoff Barton, Martijn A. van Eijkelenborg, Geoffrey Henry, Maryanne C.J. Large, and Joseph Zagari. Fabrication of microstructured polymer optical fibres. *Optical Fiber Technology*, 10(4):325–335, 2004.

[112] G.F. Taylor. A method of drawing metallic filaments and a discussion of their properties and uses. *Physical Review*, 23(5):655, 1924.

[113] S. Tomotika. On the instability of a cylindrical thread of a viscous liquid surrounded by another viscous fluid. *Proceedings of the Royal Society of London. Series A, Mathematical and Physical Sciences*, 150(870):322–337, 1935.

[114] E. Badinter, A. Ioisher, E. Monaico, V. Postolache and I.M. Tiginyanu. Exceptional integration of metal or semimetal nanowires in human-hair-like glass fiber. *Materials Letters*, 64(17):1902–1904, 2010.

[115] X. Zhang, Z. Ma, Z.Y. Yuan, and M. Su. Mass-production of vertically aligned extremely long metallic micro/nanowires using fiber drawing nanomanufacturing. *Advanced Materials*, 20(7):1310–1314, 2008.

[116] Durdu Ö. Güney, Thomas Koschny, and Costas M. Soukoulis. Reducing ohmic losses in metamaterials by geometric tailoring. *Physical Review B*, 80(12):125129, 2009.

[117] S. Adachi. *The Handbook on Optical Constants of Metals: In Tables and Figures*. World Scientific Publishing, 2012.

[118] J. Takahara, S. Yamagishi, H. Taki, A. Morimoto, and T. Kobayashi. Guiding of a one-dimensional optical beam with nanometer diameter. *Optics Letters*, 22(7):475–477, 1977.

[119] S. Roberts and P.J. Dobson. Evidence for reaction at the Al-SiO_2 interface. *Journal of Physics D: Applied Physics*, 14(3):L17–22, 1981.

[120] M.H. Hecht, R.P. Vasquez, F.J. Grunthaner, N. Zamani and J. Maserjian. A novel x–ray photoelectron spectroscopy study of the Al/SiO_2 interface. *Journal of Applied Physics*, 57(12):5256–5261, 1985.

[121] Ferhad Dadabhai, Franco Gaspari, Stefan Zukotynski, and Colby Bland. Reduction of silicon dioxide by aluminum in metaloxidesemiconductor structures. *Journal of Applied Physics*, 80(11):6505–6509, 1996.

[122] Jing Hou, David Bird, Alan George, Stefan Maier, Boris T. Kuhlmey, and J.C. Knight. Metallic mode confinement in microstructured fibres. *Optics Express*, 16(9):5983–5990, 2008.

[123] L.A.B. Pilkington. Review lecture. the float glass process. *Proceedings of the Royal Society of London. Series A, Mathematical and Physical Sciences*, 314(1516):1–25, 1969.

[124] T. Kloss, G. Lautenschläger and K. Schneider. Advances in the process of floating borosilicate glasses and some recent applications for specialty borosilicate float glasses. *Glass Technology*, 41(6):177–181, 2000.

[125] Schott Borofloat 33®, general information datasheet. http://www.us.schott.com/borofloat/english/download/borofloat33_gen_usa_web.pdf.

[126] Yipei Wang, Yaoguang Ma, Xin Guo and Limin Tong. Single-mode plasmonic waveguiding properties of metal nanowires with dielectric substrates. *Optics Express*, 20(17):19006–19015, 2012.

[127] Rupert F. Oulton, Volker J. Sorger, D.A. Genov, D.F.P. Pile and X. Zhang. A hybrid plasmonic waveguide for subwavelength confinement and long-range propagation. *Nature Photonics*, 2(8):496–500, 2008.

[128] Slimane Laref, Jiangrong Cao, Abu Asaduzzaman, Keith Runge, Pierre Deymier, Richard W. Ziolkowski, Mamoru Miyawaki and Krishna Muralidharan. Size-dependent permittivity and intrinsic optical anisotropy of nanometric gold thin films: a density functional theory study. *Optics Express*, 21(10):11827–11838, 2013.

[129] Martin Hövel, Bruno Gompf and Martin Dressel. Electrodynamics of ultrathin gold films at the insulator-to-metal transition. *Thin Solid Films*, 519(9):2955 – 2958, 2011.

[130] Allan W. Snyder and John Love. *Optical Waveguide Theory*. Springer Science & Business Media, 2012.

[131] Rei Kitamura, Laurent Pilon and Miroslaw Jonasz. Optical constants of silica glass from extreme ultraviolet to far infrared at near room temperature. *Applied Optics*, 46(33):8118–8133, 2007.

[132] M. Rubin. Optical properties of soda lime silica glasses. *Solar Energy Materials*, 12(4):275 – 288, 1985.

[133] L.G Aio, A.M Efimov, and V.F Kokorina. Refractive index of chalcogenide glasses over a wide range of compositions. *Journal of Non-Crystalline Solids*, 27(3):299 – 307, 1978.

[134] J. Scott Brownless, Björn C.P. Sturmberg, Alexander Argyros, Boris T. Kuhlmey and C. Martijn de Sterke. Guided modes of a wire medium slab: Comparison of effective medium approaches with exact calculations. *Physical Review B*, 91:155427, 2015.

[135] H.K. Tyagi, H.W. Lee, P. Uebel, M.A. Schmidt, N. Joly, M. Scharrer and P. St.J. Russell. Plasmon resonances on gold nanowires directly drawn in a step-index fiber. *Optics Letters*, 35(15):2573–2575, 2010.

[136] M.A. Schmidt, L.N. Prill Sempere, H.K. Tyagi, C.G. Poulton and P.St.J. Russell. Waveguiding and plasmon resonances in two-dimensional photonic lattices of gold and silver nanowires. *Physical Review B*, 77(3):033417, 2008.

[137] H.W. Lee, M.A. Schmidt, R.F. Russel, N.Y. Joly, H.K. Tyagi, P. Uebel, and P.St.J. Russell. Pressure-assisted melt-filling and optical characterization of Au nano-wires in microstructured fibers. *Optics Express*, 19(13):12180–12189, 2011.

[138] Patrick Uebel, Markus A. Schmidt, Michael Scharrer, Philip St.J. Russell. An azimuthally polarizing photonic crystal fibre with a central gold nanowire. *New Journal of Physics*, 13(6):063016, 2011.

[139] Schott AR-GLAS®, technical datasheet. `http://www.schott.com/tubing/media/selector/datasheets/english/schott-tubing_datasheet_ar-glas_english.pdf`.

[140] Schott Boro-8330™, technical datasheet. `http://www.schott.com/tubing/media/selector/datasheets/english/schott-tubing_datasheet_boro8330_english.pdf`.

[141] Schott, IRG22 chalcogenide glasses technical datasheet. `http://www.schott.com/d/advanced_optics/2642c34e-bc86-418f-a55d-022c58c1cb26/1.0/schott-infrared-chalcog-glasses-irg22-january-2016-eng.pdf`.

[142] Tingye Li. *Optical fiber communications: fiber fabrication*. Elsevier, 2012.

[143] Schott Technical Glasses - Physical and technical properties, general information datasheet. `http://www.us.schott.com/newsfiles/com/20100705105802_TechnGlas_USA.pdf`.

[144] Jas Sanghera and Ishwar D. Aggarwal. *Infrared fiber optics*. CRC Press, 1998.

[145] Guangming Tao, Alexander M. Stolyarov, and Ayman F. Abouraddy. Multimaterial fibers. *International Journal of Applied Glass Science*, 3(4):349–368, 2012.

[146] Guangming Tao, Ayman F. Abouraddy, Alexander M. Stolyarov, and Yoel Fink. Multimaterial fibers. In *Lab-on-Fiber Technology*, pages 1–26. Springer, 2015.

[147] S.P. Logvinenko, G.F. Mikhina, and G.T. Mende. Low temperature indium resistance thermometer. *Cryogenics*, 24(8):421–422, 1984.

[148] Erwin Eggert, H. Schmidt, and Gert Shuckle. Small axial thermocouple, June 25 1974. US Patent 3,819,420.

[149] Evgeni Sorkine. Micro-thermocouple, December 7 2011. US Patent App. 13/313,901.

[150] G.K.T. Conn. A thermocouple-bolometer detector. *Transactions of the Faraday Society*, 41:192–196, 1945.

[151] J.G. Wistreich. The fundamentals of wire drawing. *Metallurgical Reviews*, 3(1):97–142, 1958.

[152] I.W. Donald. Production, properties and applications of microwire and related products. *Journal of Materials Science*, 22(8):2661–2679, 1987.

[153] G.F. Taylor. Process and apparatus for making filaments. February 24 1931. US Patent 1,793,529.

[154] J.D. Ayers. Glass fibres with fine conducting cores. *Journal of Materials Science*, 28(9):2337–2346, 1993.

[155] S. Roy Choudhury and Y. Jaluria. Practical aspects in the drawing of an optical fiber. *Journal of Materials Research*, 13(2):483–493, 1998.

[156] S. Shabahang, J.J. Kaufman, D.S. Deng, and A.F. Abouraddy. Observation of the plateau-rayleigh capillary instability in multi-material optical fibers. *Applied Physics Letters*, 99(16):161909, 2011.

[157] S. Tomotika. Breaking up of a drop of viscous liquid immersed in another viscous fluid which is extending at a uniform rate. *Proceedings of the Royal Society of London. Series A, Mathematical and Physical Sciences*, 153(879):302–318, 1936.

[158] Pierre-Gilles De Gennes, Françoise Brochard-Wyart, and David Quéré. *Capillarity and wetting phenomena: drops, bubbles, pearls, waves*. Springer Science & Business Media, 2013.

[159] Maryanne Large. *Microstructured polymer optical fibres*. Springer, 2008.

[160] Thomas W. Chapman. The viscosity of liquid metals. *AIChE Journal*, 12(2):395–400, 1966.

[161] Dora Juan Juan Hu and Ho Pui Ho. Recent advances in plasmonic photonic crystal fibers: design, fabrication and applications. *Advances in Optics and Photonics*, 9(2):257–314, 2017.

[162] H.W. Lee, M.A. Schmidt, H.K. Tyagi, L. Prill Sempere, and P.St.J. Russell. Polarization-dependent coupling to plasmon modes on submicron gold wire in photonic crystal fiber. *Applied Physics Letters*, 93(11):111102, 2008.

[163] Yan Hong, Zeyu Ma, Chaoming Wang, Liyuan Ma, and Ming Su. 3d ordered assemblies of semiconductive micro/nanowires using microscale fibrous building blocks. *ACS Applied Materials & Interfaces*, 1(2):251–256, 2009.

[164] Joseph R. Davis. *Copper and copper alloys*. ASM international, 2001.

[165] Mecit Yaman, Tural Khudiyev, Erol Ozgur, Mehmet Kanik, Ozan Aktas, Ekin O. Ozgur, Hakan Deniz, Enes Korkut, and Mehmet Bayindir. Arrays of indefinitely long uniform nanowires and nanotubes. *Nature Materials*, 10(7):494–501, 2011.

[166] Joshua J. Kaufman, Guangming Tao, Soroush Shabahang, Daosheng S. Deng, Yoel Fink, and Ayman F. Abouraddy. Thermal drawing of high-density macroscopic arrays of well-ordered sub-5-nm-diameter nanowires. *Nano Letters*, 11(11):4768–4773, 2011.

[167] U.C. Paek and R.B. Runk. Physical behavior of the neck-down region during furnace drawing of silica fibers. *Journal of Applied Physics*, 49(8):4417–4422, 1978.

[168] Subhasish Roy Choudhury, Yogesh Jaluria, and Steve H.K Lee. Generation of neck-down profile for furnace drawing of optical fiber. Technical report, American Society of Mechanical Engineers, New York, NY (United States), 1995.

[169] S. Roy Choudhury. A computational method for generating the free-surface neck-down profile for glass flow in optical fiber drawing. *Numerical Heat Transfer: Part A: Applications*, 35(1):1–24, 1999.

[170] E.V. Rozhitsina, S. Gruner, I. Kaban, W. Hoyer, V.E. Sidorov, and P.S. Popel. Dynamic viscosities of pure tin and Sn-Ag, Sn-Cu, and Sn-Ag-Cu eutectic melts. *Russian Metallurgy (Metally)*, 2011(2):118, 2011.

[171] Joonho Lee, Wataru Shimoda, and Toshihiro Tanaka. Surface tension and its temperature coefficient of liquid Sn-X (X= Ag, Cu) alloys. *Materials Transactions*, 45(9):2864–2870, 2004.

[172] Toshihiro Tanaka, Masashi Nakamoto, Ryosuke Oguni, Joonho Lee, and Shigeta Hara. Measurement of the surface tension of liquid Ga, Bi, Sn, In and Pb by the constrained drop method. *Zeitschrift für Metallkunde*, 95(9):818–822, 2004.

[173] A. Amirfazli, D. Chatain, and A.W. Neumann. Drop size dependence of contact angles for liquid tin on silica surface: line tension and its correlation with solid–liquid interfacial tension. *Colloids and Surfaces A: Physicochemical and Engineering Aspects*, 142(2):183–188, 1998.

[174] George Biddell Airy. On the diffraction of an object-glass with circular aperture. *Transactions of the Cambridge Philosophical Society*, 5:283, 1835.

[175] Max J. Riedl. *Optical design fundamentals for infrared systems*, volume 48. SPIE press, 2001.

[176] Marcel A. Lauterbach. Finding, defining and breaking the diffraction barrier in microscopy–a historical perspective. *Optical Nanoscopy*, 1(1):8, 2012.

[177] Ernst Abbe. Beiträge zur theorie des mikroskops und der mikroskopischen wahrnehmung. *Archiv für mikroskopische Anatomie*, 9(1):413–418, 1873.

[178] Siegfried Weisenburger and Vahid Sandoghdar. Light microscopy: an ongoing contemporary revolution. *Contemporary Physics*, 56(2):123–143, 2015.

[179] Hermann von Helmholtz. Die theoretische grenze für die leistungsfähigkeit der mikroskope. *Annalen der Physik und Chemie, Jubelband J. C. Poggendorff gewidmet*, pages 557–584, 1874.

[180] Eric Betzig and Jayk Trautman. Near-field optics - microscopy, spectroscopy, and surface modification beyond the diffraction limit. *Science*, 257(5067):189–195, 1992.

[181] Stefan W. Hell. Far-field optical nanoscopy. *Science*, 316(5828):1153–1158, 2007.

[182] Bo Huang, Wenqin Wang, Mark Bates, and Xiaowei Zhuang. Three-dimensional super-resolution imaging by stochastic optical reconstruction microscopy. *Science*, 319(5864):810–813, 2008.

[183] Scott Marshall Mansfield and G.S. Kino. Solid immersion microscope. *Applied Physics Letters*, 57(24):2615–2616, 1990.

[184] Xiang Zhang and Zhaowei Liu. Superlenses to overcome the diffraction limit. *Nature Materials*, 7(6):435, 2008.

[185] Minkyung Kim and Junsuk Rho. Metamaterials and imaging. *Nano Convergence*, 2(1):22, 2015.

[186] Nicholas Fang, Hyesog Lee, Cheng Sun, and Xiang Zhang. Sub–diffraction-limited optical imaging with a silver superlens. *Science*, 308(5721):534–537, 2005.

[187] Zhaowei Liu, Stéphane Durant, Hyesog Lee, Yuri Pikus, Nicolas Fang, Yi Xiong, Cheng Sun, and Xiang Zhang. Far-field optical superlens. *Nano Letters*, 7(2):403–408, 2007.

[188] Yi Xiong, Zhaowei Liu, Cheng Sun, and Xiang Zhang. Two-dimensional imaging by far-field superlens at visible wavelengths. *Nano Letters*, 7(11):3360–3365, 2007.

[189] C.G. Parazzoli, R.B. Greegor, J.A. Nielsen, M.A. Thompson, K. Li, A.M. Vetter, M.H. Tanielian, and D.C. Vier. Performance of a negative index of refraction lens. *Applied Physics Letters*, 84(17):3232–3234, 2004.

[190] Changbao Ma and Zhaowei Liu. A super resolution metalens with phase compensation mechanism. *Applied Physics Letters*, 96(18):183103, 2010.

[191] Changbao Ma, Marco A. Escobar, and Zhaowei Liu. Extraordinary light focusing and fourier transform properties of gradient-index metalenses. *Physical Review B*, 84(19):195142, 2011.

[192] Fabrice Lemoult, Geoffroy Lerosey, Julien de Rosny, and Mathias Fink. Resonant metalenses for breaking the diffraction barrier. *Physical Review Letters*, 104(20):203901, 2010.

[193] Fabrice Lemoult, Mathias Fink, and Geoffroy Lerosey. Far-field subwavelength imaging and focusing using a wire medium based resonant metalens. *Waves in Random and Complex Media*, 21(4):614–627, 2011.

[194] Fabrice Lemoult, Mathias Fink, and Geoffroy Lerosey. Revisiting the wire medium: an ideal resonant metalens. *Waves in Random and Complex Media*, 21(4):591–613, 2011.

[195] Nanfang Yu and Federico Capasso. Flat optics with designer metasurfaces. *Nature Materials*, 13(2):139, 2014.

[196] Alexander Y. Zhu, Arseniy I. Kuznetsov, Boris Lukyanchuk, Nader Engheta, and Patrice Genevet. Traditional and emerging materials for optical metasurfaces. *Nanophotonics*, 6(2):452–471, 2017.

[197] Philippe Lalanne and Pierre Chavel. Metalenses at visible wavelengths: past, present, perspectives. *Laser & Photonics Reviews*, 11(3), 2017.

[198] Juliano G. Hayashi, Simon Fleming, Boris T. Kuhlmey and Alexander Argyros. Metal selection for wire array metamaterials for infrared frequencies. *Optics Express*, 23:29867–29881, 2015.

[199] J.D. Love, W.M. Henry, W.J. Stewart, R.J. Black, S. Lacroix, and F. Gonthier. Tapered single-mode fibres and devices. part 1: Adiabaticity criteria. *IEE Proceedings J (Optoelectronics)*, 138(5):343–354, 1991.

[200] R.J. Black, S. Lacroix, F. Gonthier, and J.D. Love. Tapered single-mode fibres and devices. ii. experimental and theoretical quantification. *IEE Proceedings J-Optoelectronics*, 138(5):355–364, 1991.

[201] Sutter Instruments - Pipette Coolbook 2015, P-97 and P-1000 Micropipette pullers - Rev. E. `https://www.sutter.com/PDFs/pipette_cookbook.pdf`.

[202] Spiricon - Pyrocam IV datasheet (OPHIR Photonics). `http://www.ophiropt.com/laser--measurement/sites/default/files/Pyrocam.pdf`.

[203] Steve Reyntjens and Robert Puers. A review of focused ion beam applications in microsystem technology. *Journal of Micromechanics and Microengineering*, 11(4):287, 2001.

[204] Fatin Syazana Jamaludin, Mohd Faizul Mohd Sabri, and Suhana Mohd Said. Controlling parameters of focused ion beam (FIB) on high aspect ratio micro holes milling. *Microsystem Technologies*, 19(12):1873–1888, 2013.

[205] Mercury Cadmium Telluride solid state detector datasheet (Horiba Scientific), model DSS-MCT(14)020L. `http://www.horiba.com/fileadmin/uploads/Scientific/Documents/OSD/OBB/detectors/DSS-MCT_14_-020.pdf`.

[206] Md. Samiul Habib, Alessandro Tuniz, Korbinian J. Kaltenecker, Quentin Chateiller, Isadora Perrin, Shaghik Atakaramians, Simon C. Fleming, Alexander Argyros, and Boris T. Kuhlmey. Removing image artefacts in wire array metamaterials. *Optics Express*, 24(16):17989–18002, 2016.

[207] Hui Zhan, Rajind Mendis, and Daniel M. Mittleman. Superfocusing terahertz waves below $\lambda/250$ using plasmonic parallel-plate waveguides. *Optics Express*, 18(9):9643–9650, 2010.

[208] M. Awad, M. Nagel, and H. Kurz. Tapered sommerfeld wire terahertz near-field imaging. *Applied Physics Letters*, 94(5):051107, 2009.

[209] Victoria Astley, Rajind Mendis, and Daniel M. Mittleman. Characterization of terahertz field confinement at the end of a tapered metal wire waveguide. *Applied Physics Letters*, 95(3):031104, 2009.

[210] D. Grischkowsky, Søren Keiding, Martin Van Exter, and C. Fattinger. Far-infrared time-domain spectroscopy with terahertz beams of dielectrics and semiconductors. *JOSA B*, 7(10):2006–2015, 1990.

[211] T. Manabe, K. Sato, and T. Ihara. Measurement of complex refractive index of soda-lime glass at 60 ghz by vector-network-analyser-based scatterometer. *Electronics Letters*, 28(14):1354–1355, 1992.

[212] Shaghik Atakaramians, Alessio Stefani, Haisu Li, Md Samiul Habib, Juliano Grigoleto Hayashi, Alessandro Tuniz, Xiaoli Tang, Jessienta Anthony, Richard Lwin, Alexander Argyros, et al. Fiber-drawn metamaterial for thz waveguiding and imaging. *Journal of Infrared, Millimeter, and Terahertz Waves*, pages 1–17, 2017.

[213] B.H. Bransden and C.J. Joachain. *Physics of atoms and molecules*. Addison-Wesley, 1983.

[214] Kaizad Rustomji, Redha Abdeddaim, C. Martijn de Sterke, Boris Kuhlmey, and Stefan Enoch. Measurement and simulation of the polarization-dependent purcell factor in a microwave fishnet metamaterial. *Physical Review B*, 95(3):035156, 2017.

[215] Harish N.S. Krishnamoorthy, Zubin Jacob, Evgenii Narimanov, Ilona Kretzschmar, and Vinod M. Menon. Metamaterial based broadband engineering of quantum dot spontaneous emission. *arXiv:0912.2454*, 2009.

[216] Sean Keuleyan, Emmanuel Lhuillier and Philippe Guyot-Sionnest. Synthesis of colloidal HgTe quantum dots for narrow mid-IR emission and detection. *Journal of the American Chemical Society*, 133(41):16422–16424, 2011.

[217] Jeffrey M. Pietryga, Richard D. Schaller, Donald Werder, Michael H. Stewart, Victor I. Klimov and Jennifer A. Hollingsworth. Pushing the

band gap envelope: mid-infrared emitting colloidal PbSe quantum dots. *Journal of the American Chemical Society*, 126(38):11752–11753, 2004.

[218] Randy J. Ellingson, Matthew C. Beard, Justin C. Johnson, Pingrong Yu, Olga I. Micic, Arthur J. Nozik, Andrew Shabaev, and Alexander L. Efros. Highly efficient multiple exciton generation in colloidal pbse and pbs quantum dots. *Nano Letters*, 5(5):865–871, 2005.

[219] Xiushan Zhu and N. Peyghambarian. High-power ZBLAN glass fiber lasers: review and prospect. *Advances in OptoElectronics*, 2010, 2010.

[220] Stuart D. Jackson. Towards high-power mid-infrared emission from a fibre laser. *Nature Photonics*, 6(7):423–431, 2012.

[221] André Felipe Henriques Librantz, Stuart D. Jackson, Fabio Henrique Jagosich, Laércio Gomes, Gaël Poirier, Sidney José Lima Ribeiro, and Younes Messaddeq. Excited state dynamics of the Ho^{3+} ions in holmium singly doped and holmium, praseodymium-codoped fluoride glasses. *Journal of Applied Physics*, 101(12):123111, 2007.

[222] Q. Lin and Govind P. Agrawal. Raman response function for silica fibers. *Optics Letters*, 31(21):3086–3088, 2006.